UNIVERSITY OF CALIFORNIA SAN DIEGO

Thermomechanical Properties of Medium- and High-Entropy Oxides and Their Interaction with Molten Salts

A dissertation submitted in partial satisfaction of the
requirements for the degree Doctor of Philosophy

in

Chemical Engineering

by

Andrew J. Wright

Committee in charge:

Professor Jian Luo, Chair
Professor Renkun Chen
Professor Olivia Graeve
Professor Kenneth Vecchio
Professor Kesong Yang

2020

The dissertation of Andrew Wright is approved, and it is acceptable in quality and form for publication on microfilm and electronically:

_____

_____

_____

_____

_____

Chair

University of California San Diego

2020

TABLE OF CONTENTS

LIST OF FIGURES

LIST OF TABLES

ACKNOWLEDGEMENTS

First, I would to acknowledge the chair of my committee and my principal investigator, Professor Jian Luo. This work would have not come to fruition if it were not for his countless hours of editing, revision, and guidance for the past few years on our several works.

Professor Renkun Chen, an expert in thermal transport, has collaborated on a majority of my doctoral work and has been invaluable in resource in my development and understanding of thermal processes at low and elevated temperatures. His doctoral students, Prof. Qingyang Wang and Ka Man Chung, have not only provided numerous hours of their time to collect data I have presented here, but have also shared insightful knowledge that have shaped my work and understanding, and consequently, deserve endless gratitude.

Professor Vecchio and NE-MRC has granted me to use their laboratory space and much of their equipment. My other committee members, Prof. Olivia Graeve and Prof. Kesong Yang, have contributed their advice and instigated thoughtful discussions that were helpful.

I would also like to thank all my colleagues: Prof. Qingyang Wang, Chuying Huang, Shu-Ting Ko, Ka Man Chung, and Yi-Ting Yeh. My gratitude begins with their assistance in gathering data, providing useful discussions, and helping all this come together, but also extends beyond words I am able describe. My other group members, Dr. Jiajia Huang, Dr. Naixie Zhou, Dr. Mojtaba Samiee, Prof. Shengfeng Yang, Sicong Jiang, Dr. Joshua Gild, Dr. Jiuyuan Nie, Mingde Qin, Chongze Hu, Qizhang Yan, Dawei Zhang, Haoyang Leng, Siyuan Shao, Yi Liu, Tyler Harrington, Kevin Kauffman, William Mellor, and any others who I apologetically may have forgotten, have also shaped me by our endless discussions in and out of meetings.

My collaborators at the Army Research Lab (ARL), Dr. Anindya Ghoshal, Dr. Michael Walock, Dr. Muthuvel Murugan, Prof. Andy Nieto, and Dr. Daniel Cole, deserve numerous

recognition for putting up with me for two summer internships and allowing me to use their facilities. They have assisted tremendously in the progression of my doctoral work and career development.

Additionally, I would like to thank various other supporters and funding sources such as, Dr. Youyang Zhou from NREL for the supply of chloride salt, a Vannevar Bush Faculty Fellowship (via ONR Grant No. N00014-16-1-2569), an associated DoD Laboratory-University Collaboration Initiative (LUCI) Fellowship, and the U.S. Department of Energy's Office of Energy Efficiency and Renewable Energy (EERE) under Solar Energy Technologies Office (SETO) Agreement Number EE0008529, since this work would not have been able to completed without them.

Lastly, my parents, sister, and loved ones have continued to push and motivate me through all times, which I am indebted to.

Chapter 2, in full, is a reprint of the material as it appears in Journal of the European Ceramic Society 2020. A.J. Wright, Q. Wang, C. Huang, A. Nieto, R. Chen, J. Luo, From high-entropy ceramics to compositionally complex ceramics: A case study of fluorite oxides. *J. Eur. Ceram. Soc.*, 2020, 40, 5. The dissertation author was the primary investigator and author of this paper.

Chapter 3, in full, is currently being prepared for submission. A.J. Wright, Q. Wang, Y.T. Yeh, R. Chen, J. Luo, Origin of the Insulative Property in Rare-Earth Niobates/Tantalates. The dissertation author was the primary investigator and author of this paper.

Chapter 4, in full, is a reprint of the material as it appears in Scripta Materialia 2020. A.J. Wright, Q. Wang, S.T. Ko, K.M. Chung, R. Chen, J. Luo, Size disorder as a descriptor for predicting reduced thermal conductivity in medium- and high-entropy pyrochlore oxides. *Scripta*

Mater., 2020, 181. The dissertation author was the primary investigator and author of this paper.

Chapter 5, in full, is currently being prepared for submission. A.J. Wright, Q. Wang, C. Hu, Y.T. Yeh, R. Chen, J. Luo, Single-phase duodenary high-entropy fluorite/pyrochlore oxides with an order-disorder transition. The dissertation author was the primary investigator and author of this paper.

Chapter 6, in full, is a reprint of the material as it appears in Journal of the American Ceramic Society 2020. A.J. Wright, C. Huang, M.J. Walock, A. Ghoshal, M. Murugan, J. Luo, Sand corrosion, thermal expansion, and ablation of medium- and high-entropy compositionally-complex fluorite oxides. *J. Am. Ceram. Soc*., 2020.The dissertation author was the primary investigator and author of this paper.

Chapter 7, in full, is currently being prepared for submission. A.J. Wright, K.M. Chung, Q. Wang, Y.T. Yeh, R. Chen, J. Luo, Molten $KMgCl_3$ salt corrosion in high entropy oxides. The dissertation author was the primary investigator and author of this paper.

VITA

2016	Bachelor of Science, Chemical Engineering, Washington State University
2018	Master of Science, Chemical Engineering, University of California San Diego
2020	Doctor of Philosophy, Chemical Engineering, University of California San Diego

PUBLICATIONS

A.J. Wright, K.M. Chung, Q. Wang, Y.T. Yeh, R. Chen, J. Luo, Molten $KMgCl_3$ salt corrosion in high entropy oxides. ***(In preparation)***.

A.J. Wright, Q. Wang, Y.T. Yeh, R. Chen, J. Luo, Origin of the Insulative Property in Rare-Earth Niobates/Tantalates. ***(In preparation)***.

A.J. Wright, Q. Wang, C. Hu, Y.T. Yeh, R. Chen, J. Luo, Single-phase duodenary high-entropy fluorite/pyrochlore oxides with an order-disorder transition. ***(Submitted)***.

A.J. Wright, C. Huang, M.J. Walock, A. Ghoshal, M. Murugan, J. Luo, Sand corrosion, thermal expansion, and ablation of medium- and high-entropy compositionally-complex fluorite oxides. *J. Am. Ceram. Soc*., **2020**.

A.J. Wright, J. Luo, A step forward from high-entropy ceramics to compositionally complex ceramics: A new perspective. *J. Mater. Sci.*, **2020**, 55.

A.J. Wright, Q. Wang, S.T. Ko, K.M. Chung, R. Chen, J. Luo, Size disorder as a descriptor for predicting reduced thermal conductivity in medium- and high-entropy pyrochlore oxides. *Scripta Mater.*, **2020**, 181.

A.J. Wright, Q. Wang, C. Huang, A. Nieto, R. Chen, J. Luo, From high-entropy ceramics to compositionally complex ceramics: A case study of fluorite oxides. *J. Eur. Ceram. Soc.*, **2020**, 40, 5.

J. Gild, **A.J. Wright**, K. Quiambao-Tomko, M. Qin, J.A. Tomko, M. Shafkat bin Hoque, J.L. Braun, B. Bloomfield, D. Martinez, T. Harrington, K. Vecchio, P.E. Hopkins, and J. Luo, Thermal conductivity and hardness of three single-phase high-entropy metal diborides fabricated by borocarbothermal reduction and spark plasma sintering. *Ceram. Int.*, **2020**, 46, 5.

ABSTRACT OF THE DISSERTATION

Thermomechanical Properties of Medium- and High-Entropy Oxides and Their Interaction with Molten Salts

by

Andrew J. Wright

Doctor of Philosophy in Chemical Engineering

University of California San Diego, 2020

Professor Jian Luo, Chair

Thermal/environmental barrier coatings are a gradually important field of research arising from the growing desire to increase the temperature, and hence energy, of processes such as gas-turbine engines and solar energy storage tanks. These materials need to not only be thermally insulating but also inert in various harsh environments. This challenge is approached by using a relatively new class of materials, high entropy oxides (circa 2015), which typically have five cations in equimolar

proportions randomly distributed within a lattice site. High entropy oxides inherently have low thermal conductivities compared to their constituents and compositionally simpler compounds due to the increased disorder. We explore for the first time in high-entropy ceramics into vast compositional space of non-equimolar ratios (medium-entropy). To tackle this near limitless and complex space, we screened numerous novel compositions (> 100) across multiple different (yet related) families. Their thermomechanical properties are measured, and trends are fit to the data to predict, provide guidance, and reduce effort on searching for future/promising materials in this vast compositional space. Key descriptors such as size disorder, oxygen vacancy concentration, and short-range ordering will be discussed. A similar approach is pursued to examine the stability of the oxides in contact with molten silicate and chloride salts. The difference in optical basicity (proportional to the tendency of oxygen to donate electrons) between the oxide and corrosive medium was found to be a reasonable predictor of performance. Additionally, the high-entropy oxides proved to be more stable in chloride salts than a Ni-superalloy reference above $100\ h$ due to a passivating layer that forms. This likely represents the largest dataset provided to the high-entropy ceramic field so far and is to serve as a stepping-stone for future experimental and modeling efforts. Overall, high entropy oxides prove to be a promising route for innovating thermal/environmental barrier coatings by providing improved thermomechanical properties and a vast compositional space poised for further tuning to provide superior performance in various areas.

INTRODUCTION

1.1 BACKGROUND

In practically all fields of research, thermal protection systems are in place to protect and maintain the process in question. Generally, these are coatings with a thickness on the order of $100\ \mu m$ and are able to reduce the temperature by 25 % on a Kelvin scale. Technological progress has been dramatically rising at an ever-increasing rate in all fields with resemblance to Moore's Law. Consequently, the demand for more efficient gas-turbine engines and faster flight transport, achieved through higher operating temperatures, continues to grow. The main limitation in increasing the inlet temperature of the turbine lies, expectedly, on the temperature reductions of the top coat material of the thermal barrier coating (TBC). The turbines are fabricated from a nickel-based superalloy and are able to operate up to $1150℃$ with no dramatic changes in the material—amazingly, $\sim$88 % of the melting temperature on a Kelvin scale [1]. Currently, the inlet temperature of turbines currently is about $1300℃$. The gold-standard material in protecting the metal is 7 wt. % (4 mol. %) yttria doped into zirconia or yttria-stabilized zirconia (YSZ). Further increases in temperature are limited because YSZ undergoes an undesirable phase transformation and has poor sintering resistance [2,3].

Another common issue with increased temperature, is the increase in chemical reactivity. YSZ also has poor chemical stability with contaminants or particulates in the gas inlet. These particulates are lumped together under the broad name of calcia-magnesia-alumina-silicates (CMAS). The stoichiometry of these constituents along with any other minor compounds drastically change the behavior of the material, but the melting temperature tends to be $\sim 1200℃$. Under typical flight conditions, CMAS concentration is generally small; however, the concentration and effects can be very significant in ash or sand laden areas—such as from recent

volcanic activity or in Southwest Asia [4–6]. CMAS-induced corrosion can very easily compromise a YSZ coating by penetrating through pores and grain boundaries and then dissolving the grains [7–9].

Newer generation aircrafts have begun using turbine components made from C/SiC ceramic matrix composites (CMCs) as these have higher strength tolerances and temperature capabilities compared to a Ni-based superalloy. However, these materials tend to have worse oxidation resistance and thus, this is the primary concern when designing coatings for these materials. Consequently, the coatings on these materials are typically called environmental barrier coatings (EBCs) as their main goal is to limit catastrophic effects from oxidation and CMAS (environmental effects). The top coat materials are usually rare-earth (RE) silicates (RE_2SiO_5 or $Re_2Si_2O_7$) because these have low oxygen diffusivity and are relatively stable in CMAS and H_2O laden environments compared to TBC top coat materials—although they have lower thermal conductivities. Both TBCs and EBCs are strong in either thermal conductivity or corrosion resistance, but tend to weak in the other; however, this may be able to solve by mixing or making compositions more complex.

The field of high entropy alloys (HEAs) emerged in 2004 with the seminal works of Yeh et al. [10] and Cantor et al. [11], which involved mixing at least five elements in a range of 5 – 35 at. %. The Gibbs free energy of mixing (ΔG_{mix}) thermodynamically governs phase stability and is shown in Equation 1.

$$\Delta G_{mix} = \Delta H_{mix} - T\Delta S_{mix} \quad (1)$$

The hypothesis is that compounds would be more stable or may prefer a solid solution if the positive enthalpic barrier (ΔH_{mix}) was overcome due to a significant increase in configurational entropy (ΔS_{mix}) that should increase with increasing temperature. For an N-

component system, the configurational entropy is maximized when all the constituents are in an equimolar ratio, which is then determined by $\Delta S_{mix} = RlnN$ where R is the gas component and N is the number of components. High entropy is loosely defined as $\Delta S_{mix} > 1.6R$ [12]. This was the most common condition as the most studied HEA is the Cantor alloy, $Co_{20}Cr_{20}Fe_{20}Mn_{20}Ni_{20}$ [13,14]. These initial studies and the plethora that shortly followed were able to show that HEAs increased phase stability and unique performance benefits, which was mainly focused on mechanical behavior initially, compared to their constituents [12,15]. Shortly after, several papers began to explore non-equimolar compositions and low/medium entropy and found further improvements in mechanical properties such as fracture toughness [16–18].

Work continued and expanded quickly on high HEAs (metals), and eventually incorporated high entropy ceramics (HECs) with the first publication generally attributed to Rost et al. [19]. In this study, it was demonstrated that an equimolar mixture of MgO, CoO, NiO, CuO, and ZnO on a metal cation basis formed a single crystalline phase while any 4-component mixture in equimolar ratios resulted in multiple phases. This demonstrates the potential strong effect entropy has on a system. Since this initial study, reports on HECs have come out at a near exponential rate on a wide range of systems such as borides [20–23], carbides [24–28], silicates [29–32], silicides [33–35], aluminides [36], fluorides [37,38], and phosphates [39,40]. This has led to an array of improvements such as electrochemical performance in oxides [41–45] and oxidation resistance and mechanical property improvements in borides and carbides [20–22,26,28,46–51]. However, one phenomenon that appears to be consistent across all HECs is a decrease in thermal conductivity compared to its constituents [27,30,33,39,51–62].

Thermal conductivity (k) measures the effectiveness of a material to transport heat primarily through either electronic or vibrational means. In this dissertation, only vibrational

contributions will be considered as the electronic conductivity of the specimens investigated is negligible. In electrically insulating specimens, thermal conductivity is largely governed by the characteristics of phonons (or propagons) and occasionally by diffusons, and locons in extremely insulating scenarios [63–65]. Phonons are quantum quasiparticles embodying lattice vibrations. The lattice vibrations follow a sinusoidal wave that allows the phonons to propagate through the lattice and have a large mean free path. Diffusons and locons are typically used in discussion of glasses but can be relevant in ultralow thermal conductivity specimens. Diffusons follow a diffusive characteristic based on a random-walk model so they are non-propagating. Locons are highly localized and non-propagating vibrations, however, these particles are still speculative.

Vibrational waves, or phonons, can travel quickly in a material when the lattice is highly symmetrical and defects are minimal, such as in diamond or copper. However, phonon-phonon interactions and the presence of defects can severely depress thermal conductivity by scattering the phonons. The main scattering mechanisms are grain boundary, phonon-displacement (atomic size disorder), phonon-impurity (atomic mass disorder), phonon-isotope impurity, phonon-electron, and phonon-phonon scattering (three phonon), which includes normal and Umklapp scattering [66–68]. Normal scattering occurs when the momentum from the collision of two phonons is conserved in the first Brillouin zone while in Umklapp scattering, this momentum lies outside the first Brillouin zone. A large emphasis will be placed on phonon scattering from size and mass disorder in this dissertation.

High entropy ceramics can thus be expected to have low thermal conductivity because the significant atomic substitution on lattice sites that gives rise to significant mass and size disorder, which is effective at scattering phonons [69–71]. In 2020, Wright et al. found size disorder to be a more effective descriptor than ideal mixing entropy itself in describing thermal

conductivity in medium- and high-entropy pyrochlores [72], which agrees with previous theoretical work conducted by Schelling et al [73].

While mass and size disorder are the typical mechanisms of low thermal conductivity in high entropy materials, others have been revealed in HECs that potentially further reduce the conductivity. Braun et al. used a virtual crystal approximation model to investigate the thermal conduction mechanism in the rocksalt-structured ESO, $(Mg_{1/5}Co_{1/5}Ni_{1/5}Cu_{1/5}Zn_{1/5})O$, and they showed that ~50% reduction in thermal conductivity could be achieved when adding another cation in the ESO derivatives [54]. The authors ruled out mass and size disorder (by using nearby elements in the periodic table) and anharmonicity (via adopting components with similar thermal expansion coefficients as MgO). Consequently, they attributed the temperature-independent (amorphous or glass-like) thermal conductivity to disorder in the interatomic force constants. This claim was further supported by an extended X-ray absorption fine structure analysis, which revealed a highly strained anion sublattice that presumably led to the suppressed thermal conductivity.

Additionally, Wright et al. showed on another occasion that ideal mixing entropy may not be the best descriptor in predicting low thermal conductivity as they found low- and medium-entropy compositions can have lower thermal conductivities [69,72,74]. This observation was attributed to the concentration of oxygen vacancies because oxygen vacancies in the defect-fluorite structure tend to cluster when the nominal oxygen vacancy concentration is greater than 5 %. The low-, medium-, and high-entropy compositions had 1.45 %, 3.7 %, and 10 %. The clustering of these vacancies effectively reduces the configurational entropy and point defect scattering, thereby increasing conductivity.

Corrosion resistance in T/EBCs is difficult because of the extreme temperatures involved ($> 800℃$). However, improvements have quickly been realized by studying the reactions of oxides with CMAS. One concept that has been used successfully is based on optical basicity (OB, Λ) first proposed by Duffy in 1971 [75]. This theory is an extension of Lewis acids and bases and relates the reactivity of a glass or oxide to the electron density around the oxygen atoms [76–78]. According to this, the optical basicity of two oxides/glasses can be determined and the difference between the two ($\Delta\Lambda$) can be correlated to the degree of reactivity, with a higher difference corresponding to increased reactivity [79].

TBCs and EBCs differ in that TBCs are typically more porous as low thermal conductivity is most important while EBCs are typically denser so to reduce the rate corrosion. Both systems have heeded corrosion of CMAS, however, in different ways. EBCs are designed so that their $\Delta\Lambda$ is small and reaction is thus minimized. Successful examples include rare-earth silicates such as $Sc_2Si_2O_7$. TBCs approach this in contrast to EBCs by focusing on a large $\Delta\Lambda$ because reactive crystallization will occur that creates a dense layer thud inhibiting further attack. Successful examples of this include zirconates such as $Gd_2Zr_2O_7$.

HECs have a potential unique advantage as they are theoretically more stable compared to “simpler” compositions because of the lowered Gibbs free energy. This may allow HECs to be more resistant to CMAS attack. Furthermore, the abundance of elements in the composition allows for limitless tuning of the atomic ratios to better select the desired optical basicity of the material.

A few reports in recent literature began the investigation of CMAS and water vapor attack on the HECs, however, none have applied the concept of optical basicity yet. Dong et al. systemically studied the corrosive behavior of water vapor on $(Yb_{0.2}Y_{0.2}Lu_{0.2}Sc_{0.2}Gd_{0.2})_2Si_2O_7$

and found there to be excellent corrosion resistance and strength retention compared to the individual rare-earth disilicates, which they attribute to the increased phase stability of the high entropy phase [80]. Ren et al. similarly investigated the water vapor corrosion on $(Y_{1/4}Ho_{1/4}Er_{1/4}Yb_{1/4})SiO_5$ and observed a 3.2 % reduction in mass loss compared to rule-of-mixtures average of the constituents [30]. Lastly, Sun et al. studied the high temperature water vapor and CMAS corrosion on $(Er_{0.25}Tm_{0.25}Yb_{0.25}Lu_{0.25})_2Si_2O_7$ at 1400℃ and 1500℃, respectively [31]. Both tests found superior corrosion resistance of the high entropy composition compared the constituents, which attributed to the increase in phase stability.

1.2 OVERVIEW

The hypothesis of this research is that HECs are likely to perform as superior T/EBC materials because the inherently reduced thermal conductivity from the increased disorder and increased corrosion resistance from the increased stability by increased configurational entropy. To approach this I (and collaborators) fabricated a myriad of compositions (> 100) by solid state reaction across multiple different families: compositionally-complex fluorite oxides (CCFOs, low-/medium-entropy), high-entropy fluorite oxides, medium-/high-entropy pyrochlore oxides, and high-entropy niobate/tantalates. The thermal conductivity and Young's modulus of all the compositions were measured by laser flash analysis and acoustic sonic resonance, respectively. Molten sand/salt stability was also carried out for several specimens. Additionally, trends are related between the thermomechanical properties and performance and (mass and size) disorder and optical basicity.

In chapter two, the thermomechanical properties of the CCFOs are discussed, where it is highlighted that the oxygen vacancy concentration is critical to the properties. The thermomechanical properties of the ultralow thermal conductivity, high-entropy niobate/tantalate

system, another fluorite system, is revealed in Chapter three. It was found the insulative nature originates from severe short-range ordering. Chapter four, discusses the thermomechanical properties of the high-entropy pyrochlores and reveals that size disorder is the predominant factor affecting thermal conductivity. The niobates/tantalates were then mixed with the pyrochlores in chapter five and show a unique increase in modulus above the linear rule-of-mixtures. In chapter six and seven, the corrosion resistance of the specimens with respect to molten CMAS and Carnallite salt ($KMgCl_3$) are investigated. For the CMAS corrosion, the CCFOs show minor improvements compared to our standard YSZ at moderate temperatures ($1200℃ - 1300℃$), however, perform significantly worse at higher temperatures due to increased reactivity (from higher $\Delta\Lambda$) . To test the stability of our specimens against molten salt, we sealed numerous specimens (42) from all the previously mentioned studies in glass ampoules under Ar with salt and annealed at $800℃$ for 24 h. Trends were drawn relating performance to optical basicity and found the lowest $\Delta\Lambda$ to perform better, in general. Furthermore, all the HECs display parabolic rate constants while a reference Haynes 230 alloy shows a linear one.

2. FROM HIGH-ENTROPY CERAMICS TO COMPOSITIONALLY COMPLEX CERAMICS: A CASE STUDY OF FLUORITE OXIDES

2.1 INTRODUCTION

High-entropy alloys (HEAs) have been developed since 2004 with the seminal works of Yeh et al. [1] and Cantor et al. [2]. A key advantage of HEAs is a vast compositional space to enable improved and tailorable properties. The initial focus is on equiatomic compositions, where the configurational entropy is maximized as $\Delta S_{conf} = RlnN$ per mole, where N (typically ≥ 5) is the number of elements and R is gas constant. In the physical metallurgy community, HEAs have been expanded to multi-principal element alloys (MPEAs) and complex-concentrated or compositionally-complex alloys (CCAs) to include medium-entropy and non-equiatomic compositions, which display excellent strength and ductility that can outperform their equiatomic counterparts [3–5].

Since 2015, high-entropy ceramics (HECs) have been made in bulk form, including various high-entropy oxides [6–10], borides [11,12], carbides [13–15], nitrides [16], and silicides [17,18]. Unlike metallic HEAs of simple FCC, BCC or HCP structures, HECs typically only have high-entropy mixing at one (or multiple) cation sublattice(s). Interestingly, single-phase high-entropy aluminides (intermetallic compounds with high-entropy mixing in only one of the two metal sublattices, albeit substantial anti-site defects and disorder in the other Al-rich sublattice) have also been made [19], thereby bridging the gap between HEAs and HECs. The HECs have been demonstrated on multiple occasions to exhibit lower thermal conductivities than their constituents because of stronger phonon scattering [9,20,21]. In some sense, HECs exhibit amorphous-like thermal conductivity or “phonon glass” behavior.

Yttria-stabilized zirconia (YSZ) with different yttria contents has been widely used [22,23] because of its superior properties, such as ionic conductivity [24] and fracture toughness [23]. Particularly, YSZ has been used as thermal barrier coatings (TBCs) for gas-turbine engines due to low thermal conductivity [25]. In general, there are great interests to search for new materials with low thermal conductivity and yet high stiffness for potential applications as thermally-insulating protective coatings. In this regard, it is natural to explore "high-entropy" versions of YSZ, which can offer further reduced thermal conductivities. High-entropy fluorite oxides (HEFOs) have been made on three occasions. Djenadic et al. made single-phase high-entropy rare earth oxide powders such as $(Ce_{0.2}La_{0.2}Pr_{0.2}Sm_{0.2}Y_{0.2})O_2$ [7]. Gild et al. first reported the fabrication of a series of eight densified bulk YSZ-like HEFOs, e.g., $(Zr_{0.2}Ce_{0.2}Hf_{0.2})(Y_{0.2}Gd_{0.2})O_2$, with equimolar HfO_2-ZrO_2-CeO_2 as the matrix plus one or two stabilizers (selected from Y_2O_3, $Yb2O_3$, Gd_2O_3, and CaO) [9]. Chen et al. also reported a high-entropy $(Zr_{0.2}Hf_{0.2}Ce_{0.2}Sn_{0.2}Ti_{0.2})O_2$ (albeit some compositional inhomogeneity indicated by EDS mapping, particularly for Ce) with low thermal conductivity [26]. Moreover, Gild et al. showed 25 – 50 % reductions in the thermal conductivity of the YSZ-like HEFOs in comparison with YSZ. To date, all studies of HECs (including all HEFOs) only explored equimolar or near equimolar compositions.

In this study, we further expand the work to non-equimolar compositions to achieve better performance such as lower thermal conductivity for TBCs, which represent a new direction to further broaden the compositional space. A somewhat surprising (but fully explainable) and scientifically interesting result is that the thermal conductivity can be reduced further by exploring non-equimolar compositions.

2.2 FROM HIGH-ENTROPY CERAMICS (HECs) TO COMPOSITIONALLY-COMPLEX CERAMICS (CCCs)

HEAs were initially defined as alloys containing five or more elements in equimolar ratios by Jien-Wei Yeh in 2004 [1]. This definition has been broadened to MPEAs or CCAs to include alloys containing multiple principal elements of 5 at. % to 35 at. % [27,28]. Alternatively, Yeh et al. also propose to classify alloys based on their ideal molar mixing entropies as low-entropy ($\Delta S_{conf} < 0.69R$), medium-entropy ($0.69R \leq \Delta S_{conf} < 1.61R$), and high-entropy ($\Delta S_{conf} \geq 1.61R$) alloys [29]. Others proposed medium-entropy alloys to have $R < \Delta S_{conf} < 1.5R$ (so that $\Delta S_{conf} \geq 1.5R$ per mole for HEAs) [30]. The latter seems to be a more realistic classification of medium- and high-entropy compositions that we adopt. Note that here ΔS_{conf} is calculated assuming ideal random mixing, albeit clustering and local ordering in the real solid solutions can reduce the actual mixing entropy.

Moreover, the concept of entropy-stabilized phases was proposed [31]. A system is said to be entropy stabilized if the mixing entropy alone can overcome the positive enthalpic barrier to stabilize the solid-solution phase. In 2015, Rost et al. reported an entropy-stabilized oxide, $(Mg_{1/5}Ni_{1/5}Co_{1/5}Cu_{1/5}Zn_{1/5})O$, of the rocksalt structure [6]. The entropy-stabilized ceramics are generally a subset of HECs, but entropy stabilization can also occur in cases that are not officially "high entropy" based on the above definitions, as schematically shown in Figure 2.1.

It is worth noting that (medium-entropy) multi-cation ceramics have already been studied by the ceramic community, e.g., $BaZr_{0.1}Ce_{0.7}Y_{0.2-x}Yb_xO_{3-\delta}$ for solid oxide fuel cell applications [32], albeit that they are typically not near equimolar compositions. However, efforts to develop HECs have so far been focused on equimolar or near equimolar compositions. Similar to the expansion from HEAs to MEPAs and CCAs in the physical metallurgy community, there is a

potential benefit to broaden the realm of HECs to explore non-equimolar and/or medium-entropy compositions, which represent an even large compositional space.

Following the definitions of metallic HEAs, HECs typically refer to equimolar or near-equimolar compositions of five or more principal cations, which usually produce $> 1.5R$ per mol. ideal configuration entropy ΔS_{conf}, on at least one sublattice. However, like in the metallic HEAs, some researchers [13] also consider equimolar, four-cation compositions (with $1.39R$ per mol. ΔS_{conf}) as HECs.

Here, we propose to loosely define a class of medium- to high-entropy compositionally-complex ceramics (CCCs or C^3) as single-phase ceramic solid solutions with at least three principal (meaning typically 5%-35% on a sublattice) cations (mixing on at least one sublattice, if there are more than one cation sublattice), which should generally have $> R$ per mole of metal cations in the ideal ΔS_{conf} (on at least one sublattice). Thus, the well-established HECs and entropy-stabilized ceramics [33,34] are a subset of CCCs (Figure 2.1). It is important to note that the definitions of high- and medium-entropy compositions are most subjective; thus, the respective boundaries are only loosely defined (so that different approaches based on the configuration entropy or the number and percentages of principal cations will lead to somewhat different cutoffs of the classifications). We should note that most non-equimolar and/or medium-entropy ceramics (based on the above definitions) also represent a largely unexplored compositional space.

Pursuing along the line to broaden HECs to CCCs to include medium-entropy non-equimolar compositions using fluorite oxides as an exemplar, this study explores the fabrication, phase stability, mechanical properties, and thermal conductivities of nine compositions of compositionally-complex fluorite oxides (CCFOs). These CCFOs have the general formula of

$(Hf_{1/3}Zr_{1/3}Ce_{1/3})_{1-x}(Y_{1/2}X_{1/2})_xO_{2-\delta}$ where X = Yb, Ca, and Gd, respectively, and x = 0.4, 0.148, and 0.058, respectively. Notably, the medium-entropy non-equimolar CCFOs exhibit even lower thermal conductivity (k) and higher modulus-to thermal conductivity (E/k) ratios than their equimolar high-entropy counterparts. Thus, this study suggests a new direction to design, fabricate, and test stiff and insulative CCFOs (or explore CCCs in general) via exploring non-equimolar and/or medium-entropy compositions that also represent a largely unexplored compositional space (in addition to HECs).

2.3 EXPERIMENTAL PROCEDURE

2.3.1 MATERIALS AND SYNTHESIS

Three variants of three different cation combinations (i.e., nine compositions) of CCFOs were explored in this study. The "H" variant represents high cubic stabilizer concentration and equimolar composition of the maximum configurational entropy, i.e., $(Hf_{1/5}Zr_{1/5}Ce_{1/5}Y_{1/5}X_{1/5})_xO_{2-\delta}$, where X = Yb for Cation Combination #4, Ca for Cation Combination #5, and Gd for Cation Combination #7 (based on the numerical series used in the prior report by Gild et al. [9]). The "M" and "L" variants represent medium and low stabilizer concentrations, and their total concentration of the two stabilizers (Y and X) matches those in 8 mol. % YSZ and 3 mol. % YSZ, respectively, while equimolar Hf, Zr, and Ce: i.e., $(Hf_{1/3}Zr_{1/3}Ce_{1/3})_{1-x}(Y_{1/2}X_{1/2})_xO_{2-\delta}$, where x = 0.148 for the "M" variant and x = 0.058 for the "L" variant, respectively. The nine CCFO compositions, along with 3YSZ and 8YSZ, are shown in Table 2.1.

Each CCFO was synthesized from commercially-purchased HfO_2 (99.99 %, 61 – 80 nm, US Research Nanomaterials, Inc.), ZrO_2 (99 %, 15 – 25 nm, Alfa Aesar), CeO_2 (99.5 %, 15 – 30 nm, Alfa Aesar), Y_2O_3 (99.995 %, 25 – 50 nm, Alfa Aesar), Yb_2O_3 (99.9 %, < 50 nm, MTI Corporation), CaO (98 %, ≤ 160 nm, Sigma-Aldrich), and Gd_2O_3 (99.99 %, 20 – 40 nm, Alfa

Aesar) nanopowders. The powders were weighed based on the targeted stoichiometries and placed inside a YSZ planetary mill jar with ethanol. YSZ grinding media was also added to the jar with the ball-to-powder mass ratio of approximately 10:1. The powders were then wet-milled in a planetary mill (Across International PQ-N04, NJ, USA) operating at 300 RPM for 24 hours. The milled slurry was transported to an 85°C drying oven to dry overnight. After drying, the powders were lightly ground using a mortar and pestle to break up any agglomerates that formed during the drying process.

The powders were consolidated into pellets by using a 10 mm diameter graphite die inside a spark plasma sintering (SPS) machine (Thermal Technologies, CA, USA) to sinter at 1650°C for 5 min under 50 MPa, with a heating ramp rate of 100°C/min. The powder was loaded into a 10 mm graphite die that was internally lined with 125 μm thick graphite foil. The die was then insulated by covering all surfaces with graphite felt. The chamber was pumped down to at least 20 mTorr. The chamber was under this vacuum until approximately 700°C, when argon was filled into the chamber and remain for the rest of the sintering process. After the five-minute dwell at 1650°C, the pressure was immediately released and power supply was turned off. Following cooling, the pellets were decarburized and homogenized at 1500°C for 24 hours and allowed to naturally cool in the furnace. The same fabrication procedure was used to sinter 3YSZ and 8YSZ as our benchmark specimens.

2.3.2 CHARACTERIZATION

2.3.2.1 SCANNING ELECTRON MICROSCOPY (SEM)

A scanning electron microscope (SEM, FEI Apreo, OR, USA) equipped with an energy dispersive X-ray spectroscopy (EDS) detector was used to investigate the microstructure and homogeneity of polished samples. Before SEM examination, the samples were mounted and

polished to a fineness of 40 nm and then coated with a thin layer of iridium to minimize charging.

2.3.2.2 X-RAY DIFFRACTION (XRD), DENSITY, AND PHASE STABILITY

Following the homogenization step, each sample was pulverized into a powder with a mortar and pestle. The crystal structure of the sample was examined through an XRD (Rigaku Miniflex II, Tokyo, Japan) operating at 30 kV and 15 mA with a scan step of 0.01° 2θ and a dwell time of 3 s. The XRD was calibrated (peak position and breadth) with LaB6 purchased from NIST (SRM 660b). XRD analysis was conducted through MDI Jade 6. It is assumed that the material exhibits the stoichiometric amount of oxygen vacancies and that Ce is in 4+ oxidation state. The microstrain of each material was calculated by Williamson-Hall analysis [35].

The bulk density was calculated by both the ASTM C373-18 Standard boil method [36] and digital image threshold processing (ImageJ) of SEM micrographs, which were in close agreements.

Phase stability was tested by long furnace annealing (for 24 h) followed by rapid air quenching. After air quenching to room temperature, the pellets were ground into a powder and examined by XRD.

2.3.2.3 RAMAN SPECTROSCOPY

A confocal Raman microscope (Renishaw inVia, England, UK) equipped with a 40 mW, 488 nm Ar^+ laser, and a 1 μm spot size was used to characterize the tetragonality of the selected specimens. The power was kept below 2 mW to avoid local heating. The experiments were performed on compacted powder samples after decarburization. The data were collected for 10 seconds and averaged over 10 scans.

2.3.2.4 MECHANICAL PROPERTIES

The Young's modulus was determined through a pulse-echo sonic resonance setup by an oscilloscope (TDS 420A, Tektronix, USA) following the ASTM C1198-09 Standard [37]. The material's longitudinal (u_L) and transverse (u_T) wave speeds were determined from the measurements and then were used to calculate Poisson's ratio (ν) and Young's Modulus (here we used "$E_{measured}$" to represented the directly measured modulus with minor porosity) according to the following Eqs. (1) and (2) below:

$$\nu = \frac{u_L^2 - 2u_T^2}{2(u_L^2 - u_T^2)} \tag{1}$$

$$E_{measured} = 2u_T^2\rho(1+\nu). \tag{2}$$

Subsequently, Young's modulus was corrected for porosity by:

$$E_{measured} = E(1 - 2.9P), \tag{3}$$

where E (i.e., E_0 in the equations in Ref. [38]) is the corrected Young's modulus for a fully-dense specimen [38] that we report in Table 2.1 and used for all discussion.

The mechanical property of the CCFOs was also probed by nanoindentation by using a Hysitron TI 950 nanoindenter (MA, USA) and nanohardness was calculated based on the widely accepted Oliver-Pharr method [39,40]. A 150 nm diamond Berkovich tip was used. The max loading force for indentation was 9 mN. This value was chosen because it provided a large enough depth so that the Oliver-Pharr equations were applicable.

All measurements were performed at room temperature on polished surfaces. The indentation procedure followed a 10-5-10 setup. Specifically, the max force was reached over 10 s, dwelled for 5 seconds, and then released over 10 s. A 5 × 5 grid with 5 μm spacing between each point was used for the indent locations. This grid was selected for three nearby areas on the

sample for a total of 75 indents. Obvious outliers (e.g., an indentation on pores or grain boundaries) were removed from the analysis after inspection.

2.3.2.5 THERMAL CONDUCTIVITY

Thermal conductivity measured from room temperature to 1000°C was determined by the product of thermal diffusivity (α), density (ρ), and specific heat capacity (c_p) based on the following equation:

$$k_{measured} = \alpha \rho c_p \tag{4}$$

The thermal diffusivity was measured by laser flash analysis (LFA 467 HT HyperFlash, NETZSCH, Germany). The heat capacity was estimated through Neumann-Kopp rule by the rule of mixtures of the constituent oxides [41]. Finally, the conductivity was corrected for porosity based on the following equation:

$$k_{measured} = k(1 - P)^{3/2} \tag{5}$$

Here, k (i.e. k_0 in equations in Ref. [42]) is the corrected thermal conductivity for a fully-dense specimen [42]. Again, here we adopt $k_{measured}$ to represent the measured thermal conductivity of specimens with minor porosity and reserve k for the corrected value reported in Table 2.1 and discussed in all places.

2.4 RESULTS AND DISCUSSION

2.4.1 XRD

XRD was performed on all 11 compositions and the results are shown in Figure 2.2. The CCFOs are compared to 8YSZ and 3YSZ that were fabricated by the same procedure.

8YSZ shows the expected cubic fluorite structure. 3YSZ shows a mixture of the tetragonal, cubic, and monoclinic phases. After annealing at 1500°C for 24 hours, 3YSZ exhibits the metastable tetragonal phase; however, it is known that this phase can transform into

tetragonal and cubic phases after prolonged high-temperature annealing [43]. The tetragonal phase could then transform into the monoclinic phase during cooling. Due to the presence of multiple phases, the properties of 3YSZ were not measured (because we are interested in the intrinsic properties of the single-phase material).

For the nine CCFOs annealed at 1500°C for 24 hours (furnace-cooled), all the "H" and "M" compositions, except for 5H, possess a single cubic fluorite phase ($Fm\bar{3}m$, space group #225). Composition 5H still predominantly contains a fluorite phase; however, there is a secondary $Ca(Hf/Zr)O_3$ perovskite phase.

Among the "L" variants annealed at 1500°C for 24 hours, 4L and 7L show a single body-centered tetragonal (BCT) phase, similar to the tetragonal YSZ (P42/nmc, space group #137). Composition 5L (with Y and Ca as the stabilizers) exhibits a single cubic fluorite phase. The addition of every Ca^{2+} cation generates an O^{2-} oxygen vacancy, doubling that produced by adding a 3+ cation. Since it is known that the formation of the cubic fluorite structure strongly depends on the concentration of oxygen vacancies [44], the additional oxygen vacancies in 5L with Ca^{2+} stabilizers likely stabilize this cubic phase.

On examination of the XRD spectra, the peaks widen as the stabilizer concentration decreases. In general, peak broadening can arise from small crystallite/domain size, residual strains, and inhomogeneity. The residual strains and small crystallite size effects can be excluded in this case based on the Williamson-Hall analysis and long annealing times. Furthermore, our samples are compositionally homogeneous (as shown by the EDS analysis later). Thus, we propose that the peak broadening observed here is likely resulted from partial/initial phase transformation. Specifically, an FCC to BCT transition will result in peak splitting when the *c/a*

ratio in the BCT cell deviates from the $\sqrt{2}$ of the cubic phase. However, due to XRD instrumental broadening, the initial small splitting will appear as peak broadening.

Here, the microstrain parameter (ε) extracted from the Williamson-Hall plot can be used as a proxy for the degree of broadening due to the presence of the tetragonal phase, in which the effects can be seen in variant "L". As the stabilizer concentration increases, the broadening parameter decreases, suggesting that the tetragonality of the sample decreases.

Table 2.1 summarizes the relevant data obtained from XRD. Compositions 5H and 3YSZ were not single phases (so their properties were not further measured). Compositions 4L and 7L were classified as BCT. The *c/a* ratio for 4L and 7L are 1.423 and 1.421, respectively. When *c/a* $= \sqrt{2} \approx 1.414$, the phase is equivalent to FCC (fluorite). Thus, 4L and 7L only exhibit moderate tetragonality. The rest of the CCFOs exhibit the cubic fluorite structure according to XRD (albeit some trace tetragonality that results in peak broadening). The lattice parameter for each composition increases with the increasing stabilizer concentration due to the larger sizes of the stabilizer atoms compared to the host atoms. Assuming XRD peak broadening is due to the initial FCC to BCT phase transition, ε increases as the stabilizer concentration decreases. The tetragonality at lower stabilizer concentrations is expected, similar to that observed in YSZ [43].

2.4.2 RAMAN SPECTROSCOPY

Raman spectroscopy was used to investigate the presence of moderate tetragonality, which is more sensitive than XRD. This technique is susceptible to local short-range ordering. Figure 2.3 shows the Raman spectra for 8YSZ, 4L, 4M, and 4H. A pure cubic specimen should exhibit a single sharp peak around 465 cm^{-1} [45–47]. In the specimens measured, there are six peaks which correspond to the tetragonal symmetry [48–50]. Although nearly all the XRD spectra show a strong cubic structure, the short-range order suggests some tetragonality in all

specimens, which decreases as the stabilizer concentration increases. Other researchers have suggested that this tetragonality may arise from distorted C-type/pyrochlore micro/nanodomains within the system [51–53]. The broadened peaks are likely due to both the decreasing tetragonality and a highly disordered structure. It is important to note that in this case (excluding the composition series 5), variants "H" and "M" are cubic, and "L" is tetragonal according to XRD. Although Raman spectra indicate some tetragonality in all nominally cubic phase, we used XRD as our primary criterion to differentiate cubic and tetragonal phases (as the tetragonality revealed by Raman is small, yet universal). To sum up, we believe 4L exhibits long-range tetragonal order while both 4M and 4H exhibits long-range cubic order (according to XRD), but short-range tetragonal order (according to Raman spectroscopy). In fact, 8YSZ is commonly known as a cubic phase. However, it is also known, and verified here, that the Raman spectra can also reveal some tetragonality even in the well-known cubic 8YSZ [48–51].

2.4.3 PHASE STABILITY

The stability of 4L, 4M, and 4H (or $(Hf_{1/3}Zr_{1/3}Ce_{1/3})_{1-x}(Y_{1/2}Yb_{1/2})_xO_{2-\delta}$) was examined further by utilizing specimens quenched from different temperatures. Here, each sample was first annealed at 1500°C for approximately 24 h and then rapidly air quenched to preserve the crystal structure. XRD revealed that all variants exhibited sharp fluorite peaks, including 4L that exhibited tetragonal phase in the slow furnace cooled specimen (Figure 2.1 for slow furnace cooling vs. Figure 2.4 for air-quenched specimen). This indicates that 4L underwent a cubic to tetragonal phase change during furnace cooling.

After quenching at 1500°C to form a single cubic phase, each sample was then annealed again at 1200°C – 1400°C for 24 h – 48 h. It was found that variants "H" and "M" remained cubic with sharp peaks for all temperatures examined and are shown in Figure S2.1 in Suppl.

Data. Variant “L”, however, underwent a BCT to FCC phase transition around 1400°C – 1500°C. The XRD spectra for quenched 4L from all temperatures are shown in Figure 2.4(a). The expanded spectra in Figure 2.4(b) shows that at 1200°C, the sample is a single tetragonal phase. As the temperature increases to 1300°C, the gap between the two tetragonal peaks decreases and the two peaks eventually merge at 1400°C. However, the presence of the tetragonal structure is still noticeable in the peak. It is not until 1500°C that the structure becomes a single cubic fluorite phase. The volume expansion from the fluorite phase to body-centered tetragonal is approximately 0.7 %. It is evident that the transformation was not destructive to the specimen on the macroscale.

The phase stability of the CCFOs is now compared to YSZ. The phase transition temperature (~ 1400°C) of 4L (stabilizer concentration = 5.8 at. %) is significantly lower than its 3YSZ counterpart (~ 2200°C). Also, the tetragonal phase is stable in 8YSZ from 600°C to 1300°C. Within the CCFOs, no phase change was detected down to 1200°C. Thus, the cubic phase stable region is enlarged in CCFOs in comparison with YSZ.

A proposed phase diagram of the $(Hf_{1/3}Zr_{1/3}Ce_{1/3})_{1-x}(Y_{1/2}Yb_{1/2})_xO_{2-\delta}$ CCFOs is shown in Figure 2.5. The phase diagram resembles the YSZ phase diagram [43]. Interestingly, no two-phase region is observed between the tetragonal and cubic single-phase regions the $(Hf_{1/3}Zr_{1/3}Ce_{1/3})_{1-x}(Y_{1/2}Yb_{1/2})_xO_{2-\delta}$ CCFOs, differing from the YSZ system. It is possible that such a two-phase region is too narrow (to be detected by our experiments) in this CCFO system.

In comparison with the YSZ phase diagram [43], it appears that the cubic fluorite phase is stabilized in $(Hf_{1/3}Zr_{1/3}Ce_{1/3})_{1-x}(Y_{1/2}Yb_{1/2})_xO_{2-\delta}$ CCFOs to a significantly greater degree by pushing the tetragonal envelope inward by at least a few hundred degrees at all temperatures. It is also known that Ce may enhance the stability of the cubic phase [54,55]. However, the HfO_2-

CeO_2-ZrO_2 ternary phase diagram shows the three-phase region (monoclinic + tetragonal + cubic) for the equimolar composition at 1500°C [56]. It appears that the cubic stabilizers in this system affects the phase stability to a more considerable degree in this CCFO system than yttria does in the zirconia system. We should note that entropy stabilization of higher symmetry phases is seen in other reports [57,58]. This is consistent with the enhanced stability of the high-symmetry cubic phase in this CCFO system at lower stabilizer concentrations compared to YSZ.

2.4.4. SEM-EDS

Polished cross-sections were examined by SEM-EDS to investigate the microstructure and homogeneity on the microscale. All the compositions following the furnace anneal were solid compacts free of cracks with a random distribution of (low) porosity. All specimens are chemically homogeneous. SEM micrograph and the corresponding EDS maps on 4L, 4M, and 4H were selected as an example and shown in Figure 2.6. SEM-EDS analysis results of other compositions are shown in Figure S2.2 in Suppl. Data. All the CCFOs exhibited homogeneously distributed elements besides 5H (and 7L to a minor extent).

2.4.5 MECHANICAL PROPERTIES

The Young's modulus (E) and nanohardness data are shown in Table 2.1. Our measurements of our 8YSZ system agree well with literature values on both properties [59,60]. The composition series 5 ($(Hf_{1/3}Zr_{1/3}Ce_{1/3})_{1-x}(Y_{1/2}Ca_{1/2})_xO_{2-\delta}$) specimens had significantly lower modulus while the rest of the CCFOs had similar values. Calcium is a large ion (ionic radius = 1.12 Å) with a different charge (2+) than the rest of the cations investigated (3+/4+), which may result in the different modulus.

Nanoindentation revealed similar nanohardness values of all compositions to be 16-20 GPa, on par with that of 8YSZ (17.3 ± 1.5 GPa). Specimen 5M $(Hf_{0.284}Zr_{0.284}Ce_{0.284}Y_{0.074}Ca_{0.074})_xO_{2-\delta}$ is the hardest (19.6 ± 0.6 GPa), despite its lowest modulus.

2.4.6 THERMAL CONDUCTIVITY

One of the most attractive properties of YSZ is its low thermal conductivity (k). Thermal conductivity measurements were performed from room temperature to 1000°C and are shown in Figure 2.7, with the raw diffusivity and heat capacity data shown in Figures S2.3 and S2.4 in Suppl. Data. Noting that the measured room-temperature k values for 4H and 7H are greater than those previously reported [9]. The differences may arise from differences in measurement methods (laser flash analysis vs. time-domain thermoreflectance). The measured temperature-dependent thermal conductivity of 8YSZ is in an excellent agreement with literature [61]. For some specimens (e.g., 8YSZ, 4H and 7H), thermal conductivity initially decreases but then slightly increases with temperature above around 800°C. This increasing trend is presumably due to radiation heat transfer, as also observed and speculated in the literature [62–64]. If the radiation thermal conductivity is significant, the data reduction method used in the laser flash analysis is no longer fully valid. Therefore, the data shown in the high-temperature range (e.g., above ~800°C) should be taken as an approximation only.

The temperature-dependent thermal conductivity values give insight into the thermal conduction mechanism. 8YSZ exhibits a constant k around 2 W m^{-1} K^{-1} but increases slightly at T ≥ 800°C due to radiation heat transfer. From room temperature to 1000°C, the reduction in k for the CCFOs compared to 8YSZ is about 20 %. This reduction of the thermal conductivity is likely originated from the increased phonon scattering. Both equimolar 4H and 7H show the

classical 1/*T* relationship representative of Umklapp scattering at low temperatures, which then rise at higher temperatures from radiative effects (like 8YSZ).

Notably, at lower stabilizer concentrations, the temperature dependency changes to an amorphous-like or disordered trend [65], where the thermal conductivity increases slowly with temperature or nearly temperature-independent. Disordered trends arise when the propagating phonon modes are severely suppressed, and the main heat conduction mode becomes non-propagating diffusons [66,67]. It is interesting to note that the equimolar compositions, which have the most disorder on the cation sublattice, do not display this trend. Thus, this amorphous-like behavior is probably a result of oxygen vacancies. Oxygen vacancies are known to cluster in the fluorite structure to form bi- and tri-vacancies when the oxygen vacancy concentration increases above 5 % [51,53,68,69]. The clustering of the vacancies, in turn, lowers the configurational entropy on the anion sublattice and phonon scattering of the system. Thus, equimolar 4H and 7H display a crystalline-like conductivity that has a 1/*T* dependency with temperature, while other compositions exhibit amorphous-like behaviors.

This also explains an important finding of this study that the non-equimolar medium-entropy CCFOs exhibit even lower (and temperature-independent) thermal conductivities than their equimolar high-entropy counterparts. This is clearly demonstrated, e.g., in Figure 2.8 for the composition 4 series $(Hf_{1/3}Zr_{1/3}Ce_{1/3})_{1-x}(Y_{1/2}Yb_{1/2})_xO_{2-\delta}$ as an example.

The thermal conductivities of 5L and 5M $(Hf_{1/3}Zr_{1/3}Ce_{1/3})_{1-x}(Y_{1/2}Ca_{1/2})_xO_{2-\delta}$ specimens are lower than those of the composition 7 series $(Hf_{1/3}Zr_{1/3}Ce_{1/3})_{1-x}(Y_{1/2}Gd_{1/2})_xO_{2-\delta}$ specimens, which are slightly lower than that of the composition 4 series $(Hf_{1/3}Zr_{1/3}Ce_{1/3})_{1-x}(Y_{1/2}Yb_{1/2})_xO_{2-\delta}$ specimens. The introduction of Ca^{2+} reduced the conductivity of the system further. As shown in Figure 2.7, Composition 5M approaches the minimum thermal conductivity limit (e.g., Cahill

limit [70]) at high temperature but there is still room for further reduction. A factor may be the size disorder. Composition series 5, 7, and 4 contain Ca^{2+}, Gd^{3+}, and Yb^{3+}, which have Shannon effective ionic radii of 1.12 Å, 1.053 Å, and 0.985 Å, respectively [71]. This suggests size disorder as a possible factor in controlling thermal conductivity. In this case, the different charge state of Ca^{2+} plays an indirect effect.

2.4.7 STIFFNESS TO CONDUCTIVITY (*E/K*) RATIO

Interestingly, the mechanical properties of the CCFOs are reasonably similar to YSZ, but the thermal conductivity is reduced. Traditionally, the modulus and conductivity are directly related as strong bonding increases both [21]. The room temperature k, E, and E/k for the composition 4 series $(Hf_{1/3}Zr_{1/3}Ce_{1/3})_{1-x}(Y_{1/2}Yb_{1/2})_xO_{2-\delta}$ are shown in Figure 2.8. Here, there is a clear improvement in the E/k ratio when we move from equimolar high-entropy 4H to non-equimolar concentrations. A sharp drop in modulus in 4L and consequently E/k may be due to the relatively weaker tetragonal structure compared to cubic. Thus, the highest E/k ratio of 133.6 ± 4.3 GPa·m·K·W^{-1} is achieved for 4M $Hf_{0.284}Zr_{0.284}Ce_{0.284}Y_{0.074}Yb_{0.074})_xO_{2-\delta}$.

The properties of all CCFOs are summarized in Table 2.1. The same trend stated above is seen in the other composition series as well, where the non-equimolar CCFOs (variant "M") are generally more thermally-insulative (with lower thermal conductivity) compared to their equimolar high-entropy counterparts (variant "H").

Generally, as the concentration of oxygen vacancy concentration increases (from "L" to "H"), so does the thermal conductivity and modulus to an extent. The k appears to reach a minimum (and E/k reaches a maximum) around the composition of variant "M" which has a nominal oxygen vacancy percentage of 3.7 %. However, this trend is not upheld in the composition 5 series $(Hf_{1/3}Zr_{1/3}Ce_{1/3})_{1-x}(Y_{1/2}Ca_{1/2})_xO_{2-\delta}$ specimens because Ca^{2+} introduces more

oxygen vacancies in comparison with Yb^{3+} and Gd^{3+}. Note that 5L $Hf_{0.314}Zr_{0.314}Ce_{0.314}Y_{0.029}Ca_{0.029})_xO_{2-\delta}$ has a nominal oxygen vacancy concentration of 2.2 %, while 5M $Hf_{0.284}Zr_{0.284}Ce_{0.284}Y_{0.074}Ca_{0.074})_xO_{2-\delta}$ has 5.6 %. Overall, an oxygen vacancy concentration around 3 % should display the most improved properties in terms of the E/k ratio. This shows the importance of oxygen vacancies to the thermal properties of this new class of CCFOs.

Notably, most CCFOs display a 5 – 30 % increase in E/k ratio compared to YSZ. This study further showed that one can explore medium non-equimolar CCFOs to reduce k (beyond their equimolar high-entropy counterparts) while retaining the modulus (at least to certain concentration) and hardness to achieve higher E/k ratio. This allows for a new direction to design stiff and insulative ceramics. It is important to note not only HECs represent a new compositional space, but also most medium-entropy and/or non-equimolar compositions are largely unexplored by any prior studies (i.e., investigated in neither the traditional ceramic research nor in the most recent HEC studies).

2.5 CONCLUSION

This study broadens high-entropy ceramics (HECs) to compositionally-complex ceramics (CCCs) to explore medium-entropy non-equimolar compositions using compositionally-complex fluorite oxides (CCFOs) as an exemplar. Nine compositions CCFOs with the general formula of $(Hf_{1/3}Zr_{1/3}Ce_{1/3})_{1-x}(Y_{1/2}X_{1/2})_xO_{2-\delta}$ (where X = Yb, Ca, and Gd) have been fabricated and eight of exhibit single solid-solution phases at 1500 °C.

In comparison with YSZ, these CCFOs exhibit increased cubic stability and lower thermal conductivity, while retaining comparable modulus and hardness. Moreover, the

temperature-dependent thermal conductivity in the non-equimolar CCFOs shows an amorphous-like behavior.

Most notably, the medium-entropy non-equimolar CCFOs exhibit even lower thermal conductivity (k) and higher E/k ratios than their equimolar high-entropy counterparts. Thus, these results suggest a new direction to design, fabricate, and test insulative yet stiff CCFOs specifically, as well as other high-performance CCCs in general, via exploring non-equimolar and/or medium-entropy compositions beyond HECs.

This study has also demonstrated the importance of oxygen vacancies, particularly their clustering, in influencing the thermal conductivity, which is the underlying reason that non-equimolar medium-entropy CCFOs outperform their equimolar high-entropy counterparts.

Chapter 2, in full, is a reprint of the material as it appears in Journal of the European Ceramic Society 2020. A.J. Wright, Q.Y. Wang, C.Y. Huang, A. Nieto, R.K. Chen, J. Luo, From high-entropy ceramics to compositionally complex ceramics: A case study of fluorite oxides. *J. Eur. Ceram. Soc.*, 2020, 40, 5. The dissertation author was the primary investigator and author of this paper.

Table 2.1. Summary of properties measured at room temperature for all single-phase specimens annealed at 1500°C for 24 hours. Specimen 3YSZ and 5H have multiple phases, so their properties were not measurements. Nanohardness was not measured for 4H due to an experimental issue.

Identifier	Composition	a_c (Å)	a_t (Å)	c_t (Å)	Microstrain (%)	Theoretical Density (g/cm^3)	Relative Density (%)	Nanohardness (GPa)	$E\ (GPa)$	$k\left(\frac{W}{m \cdot K}\right)$	$E/k\left(\frac{GPa \cdot m \cdot K}{W}\right)$
3YSZ	$Zr_{0.942}Y_{0.058}O_{2-\delta}$	—	—	—	—	—	—	—	—	—	—
8YSZ	$Zr_{0.852}Y_{0.148}O_{2-\delta}$	5.134	—	—	0.15	5.97	97.3 ± 0.6	17.3 ± 1.5	219.2 ± 2.6	2.19 ± 0.07	100.3 ± 3.2
4L	$Hf_{0.314}Zr_{0.314}Ce_{0.314}Y_{0.029}Yb_{0.029}O_{2-\delta}$	—	3.682	5.238	0.19	7.85	96.9 ± 0.6	17.1 ± 1.8	201.2 ± 2.2	1.78 ± 0.05	113.0 ± 3.6
4M	$Hf_{0.284}Zr_{0.284}Ce_{0.284}Y_{0.074}Yb_{0.074}O_{2-\delta}$	5.210	—	—	0.16	7.83	97.5 ± 0.6	17.7 ± 1.7	232.8 ± 2.2	1.74 ± 0.05	133.6 ± 4.3
4H	$Hf_{0.2}Zr_{0.2}Ce_{0.2}Y_{0.2}Yb_{0.2}O_{2-\delta}$	5.227	—	—	0.08	7.59	98.2 ± 0.6	—	232.6 ± 2.4	2.23 ± 0.07	104.4 ± 3.3
5L	$Hf_{0.314}Zr_{0.314}Ce_{0.314}Y_{0.029}Ca_{0.029}O_{2-\delta}$	5.214	—	—	0.16	7.67	97.3 ± 0.6	18.4 ± 1.3	180.1 ± 4.8	1.65 ± 0.05	109.4 ± 4.4
5M	$Hf_{0.284}Zr_{0.284}Ce_{0.284}Y_{0.074}Ca_{0.074}O_{2-\delta}$	5.218	—	—	0.10	7.30	95.4 ± 0.6	19.6 ± 0.6	153.8 ± 2.3	1.54 ± 0.05	99.6 ± 3.4
5H	$Hf_{0.2}Zr_{0.2}Ce_{0.2}Y_{0.2}Ca_{0.2}O_{2-\delta}$	—	—	—	—	—	—	—	—	—	—
7L	$Hf_{0.314}Zr_{0.314}Ce_{0.314}Y_{0.029}Gd_{0.029}O_{2-\delta}$	—	3.690	5.245	0.17	7.78	96.1 ± 0.6	18.5 ± 1.4	199.4 ± 2.0	1.74 ± 0.05	114.3 ± 3.6
7M	$Hf_{0.284}Zr_{0.284}Ce_{0.284}Y_{0.074}Gd_{0.074}O_{2-\delta}$	5.225	—	—	0.08	7.70	96.9 ± 0.6	18.2 ± 1.7	218.9 ± 2.3	1.70 ± 0.05	128.4 ± 4.2
7H	$Hf_{0.2}Zr_{0.2}Ce_{0.2}Y_{0.2}Gd_{0.2}O_{2-\delta}$	5.265	—	—	0.07	7.28	98.2 ± 0.6	16.3 ± 1.2	238.9 ± 2.7	2.19 ± 0.06	106.3 ± 3.3

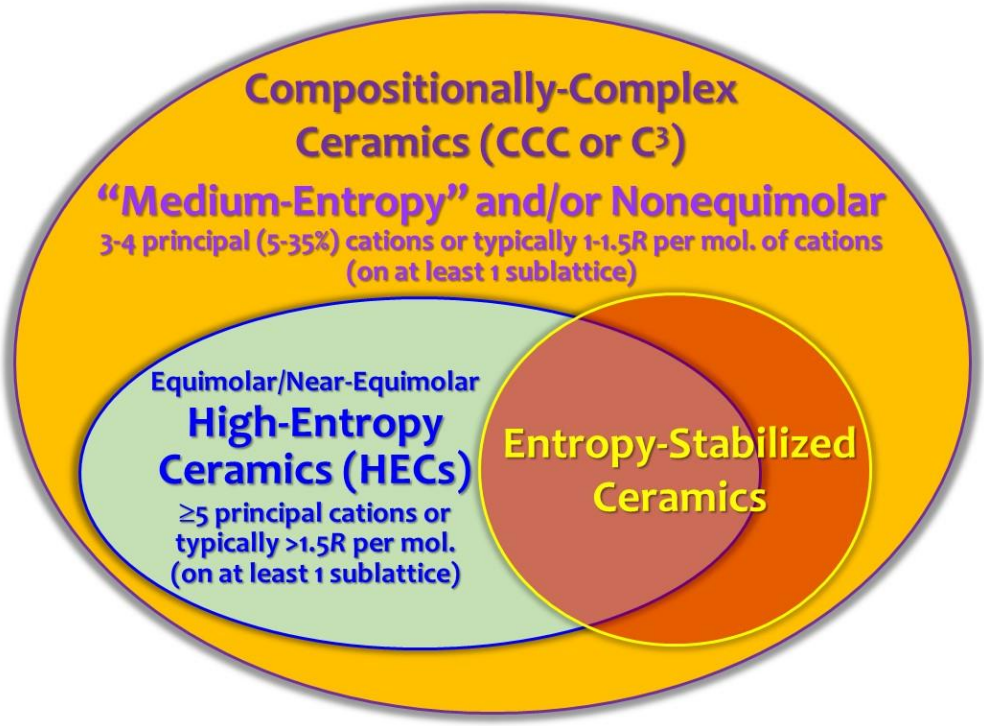

Figure 2.1 . Schematic of proposed compositionally-complex ceramics (CCC or C^3), which include high-entropy ceramics (HECs) and entropy-stabilized ceramics as subsets. Following the definitions of metallic high-entropy alloys (HEAs), HECs typically refer to equimolar or near-equimolar compositions of five or more principal cations (usually producing > 1.5 R per mol. of cations ideal configuration entropy) on at least one sublattice. We propose to broaden HECs to CCCs to further include non-equimolar and/or medium-entropy compositions of three or four principal (typically 5%-35%) cations or generally 1-1.5 R per mol. ideal configuration entropy on at least one sublattice. Note that different (mostly subjective) criteria exist so that the boundaries of high- or medium-entropy compositions are only loosely defined. We should further note that most non-equimolar and/or medium-entropy ceramics (based on the above definitions) also represent a largely unexplored compositional space (in addition to HECs).

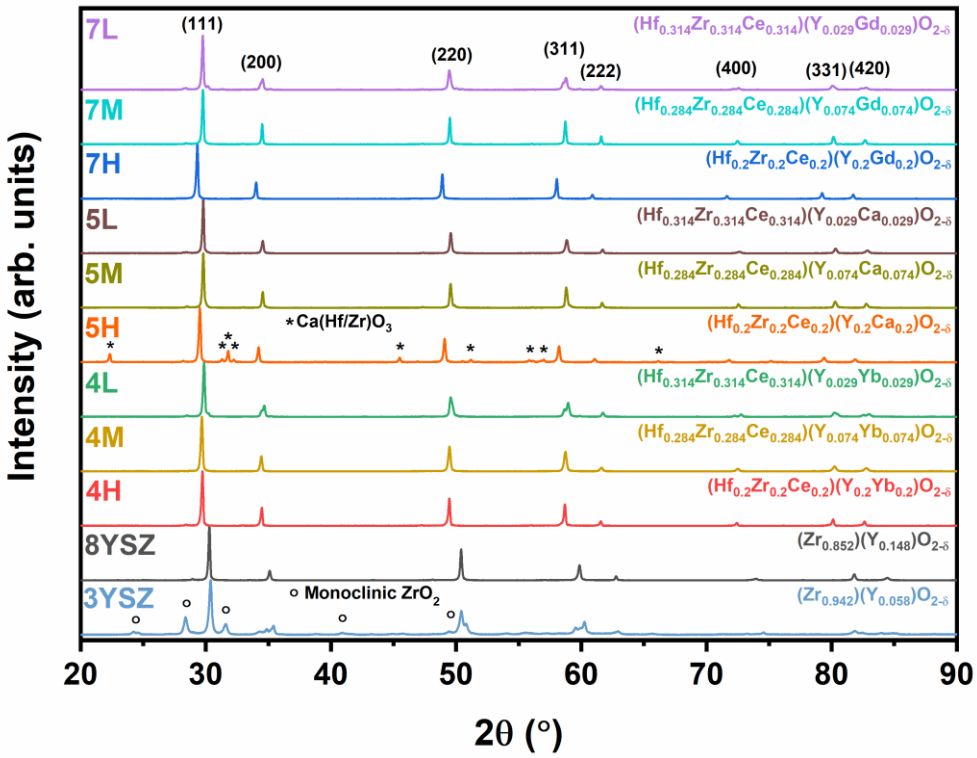

Figure 2.2. XRD patterns of all 11 specimens (nine CCFOs, along with 8YSZ and 3YSZ) annealed at 1500°C for 24 hours and furnace cooled. All variants "M" and "H" specimens, except 5H, exhibit single solid-solution phases of the fluorite structure. In variant "L" specimens, both 4L and 7L exhibit the tetragonal structure, while 5L retains the cubic fluorite structure.

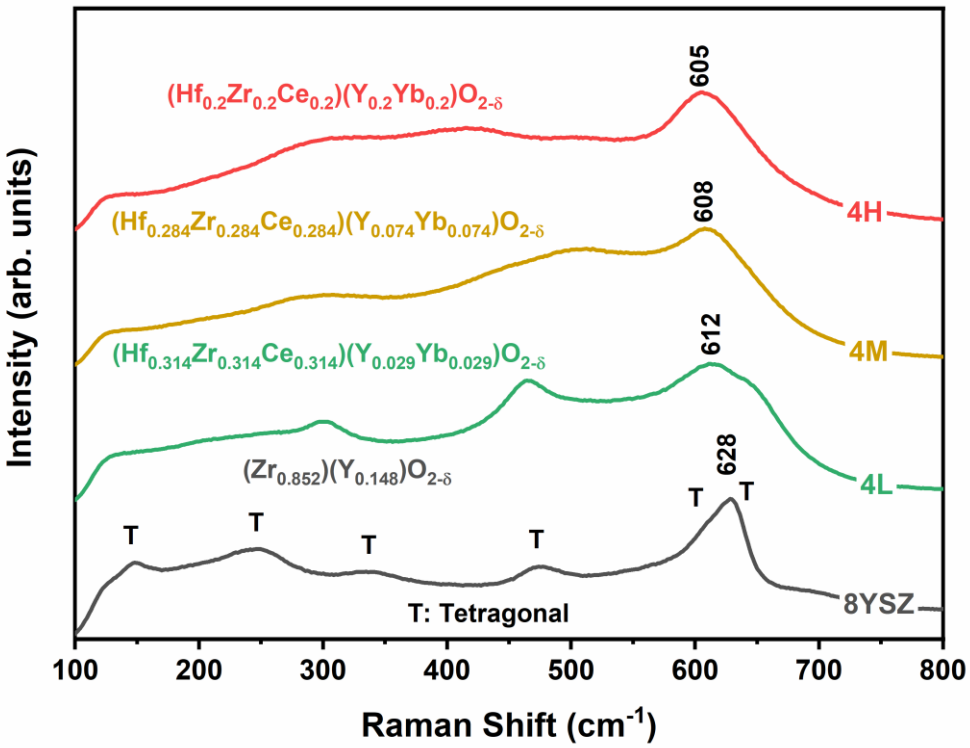

Figure 2.3. Raman spectra showing some degrees of tetragonality present in selected specimens annealed at 1500°C (albeit that some are shown as cubic fluorite by XRD). As the stabilizer concentration is increased, the degree of the tetragonality decreases.

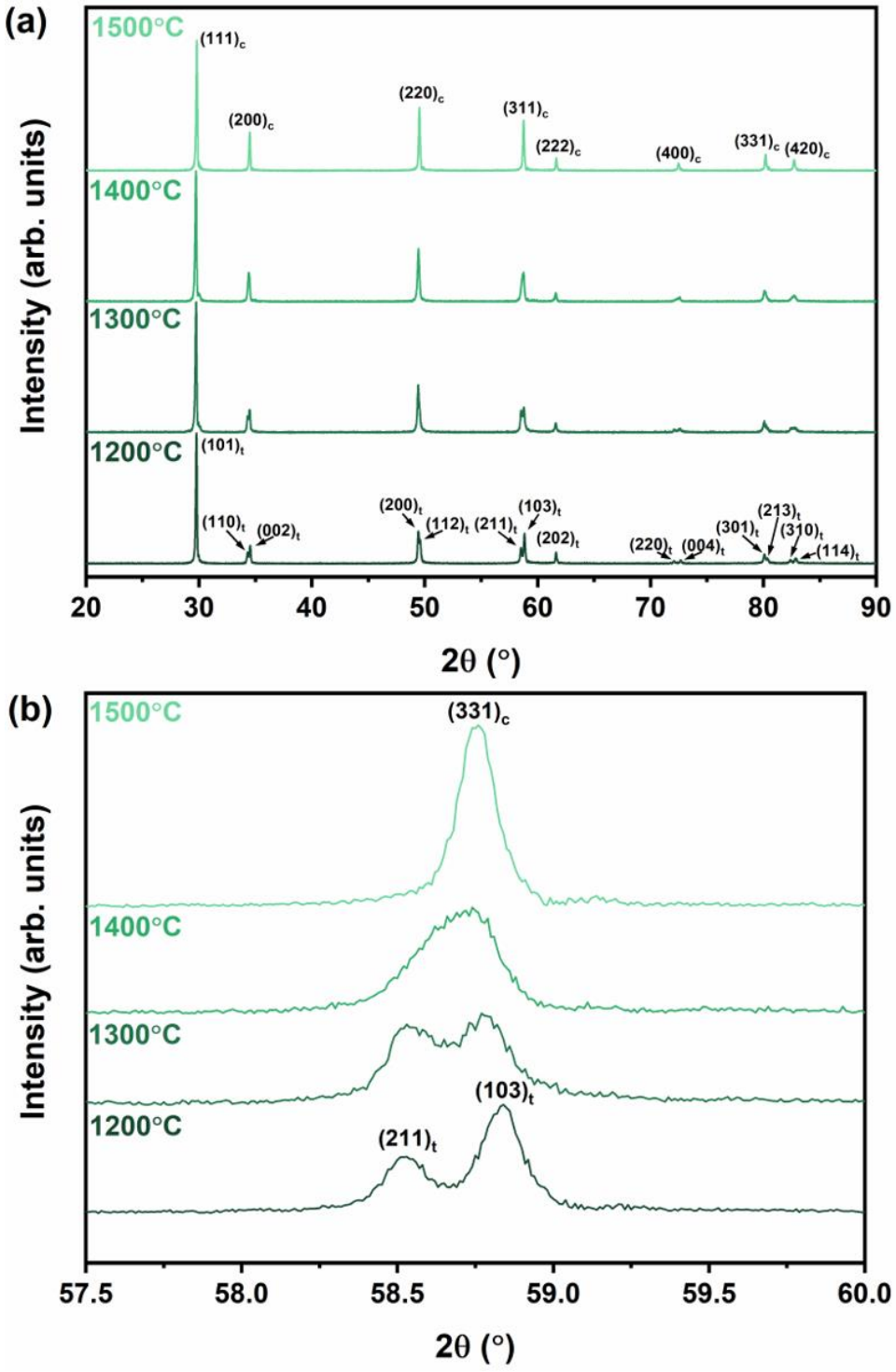

Figure 2.4. (a) XRD spectra of four 4L ($Hf_{0.314}Zr_{0.314}Ce_{0.314}Y_{0.029}Yb_{0.029}O_{2-\delta}$) specimens produced by 24-hour annealing at different temperatures (labeled in the figure) and subsequent quenching. A phase transformation occurs around 1400°C and completes at 1500°C. (b) Expanded views of the XRD spectra showing the transition from two tetragonal peaks to a single cubic peak.

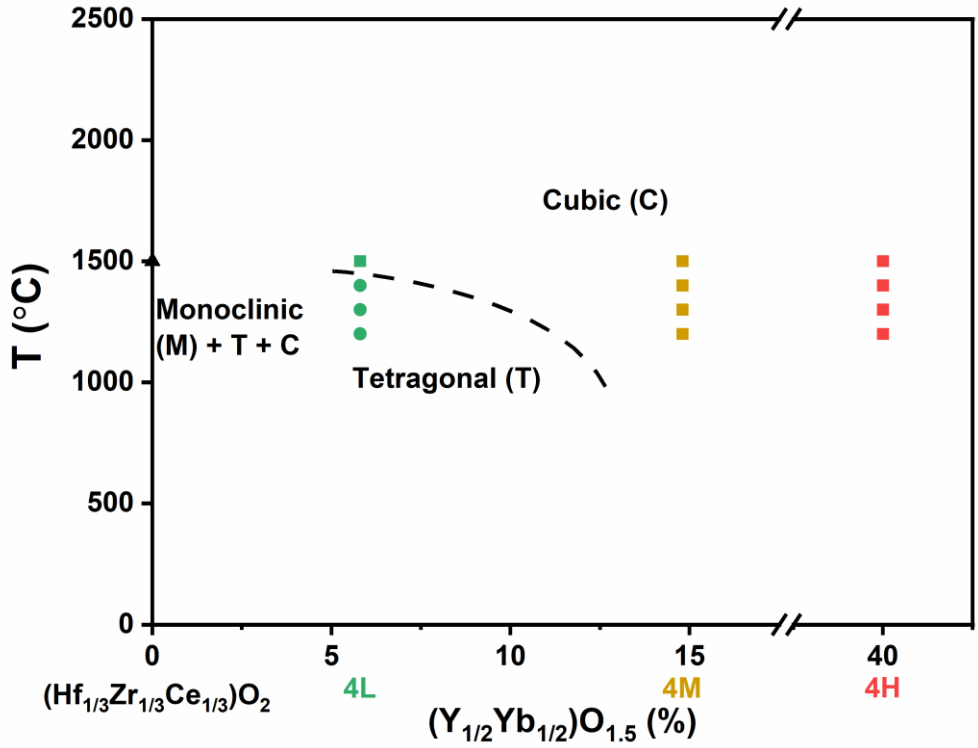

Figure 2.5. Proposed phase diagram of specimens $(Hf_{1/3}Zr_{1/3}Ce_{1/3})_{1-x}(Y_{1/2}Yb_{1/2})_xO_{2-\delta}$ (4L, 4M, and 4H). Composition 4L undergoes a transformation from the tetragonal to cubic phase at ~1400°C – 1500°C while 4M and 4H remained in the cubic fluorite phase from 1200°C to 1500°C. All specimens were annealed at the respective temperatures for 24 h and subsequently quenched. The composition $(Hf_{1/3}Zr_{1/3}Ce_{1/3})O_2$ exhibits three phases according to Andrievskaya et al.[56]. (Legends: ▲ = 3 phase; ● = tetragonal; ■ = cubic.)

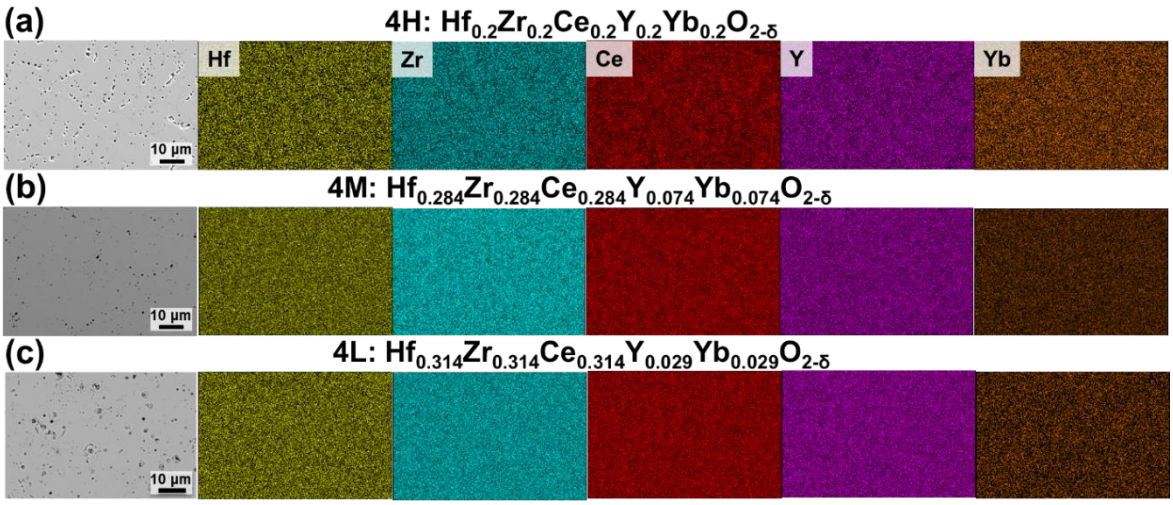

Figure 2.6. SEM images and corresponding EDS elemental maps on the cross sections of (a) 4H, (b) 4M, (c) and 4L annealed at 1500°C for 24 hours. The cation distributions are uniform in all specimens at the microscale.

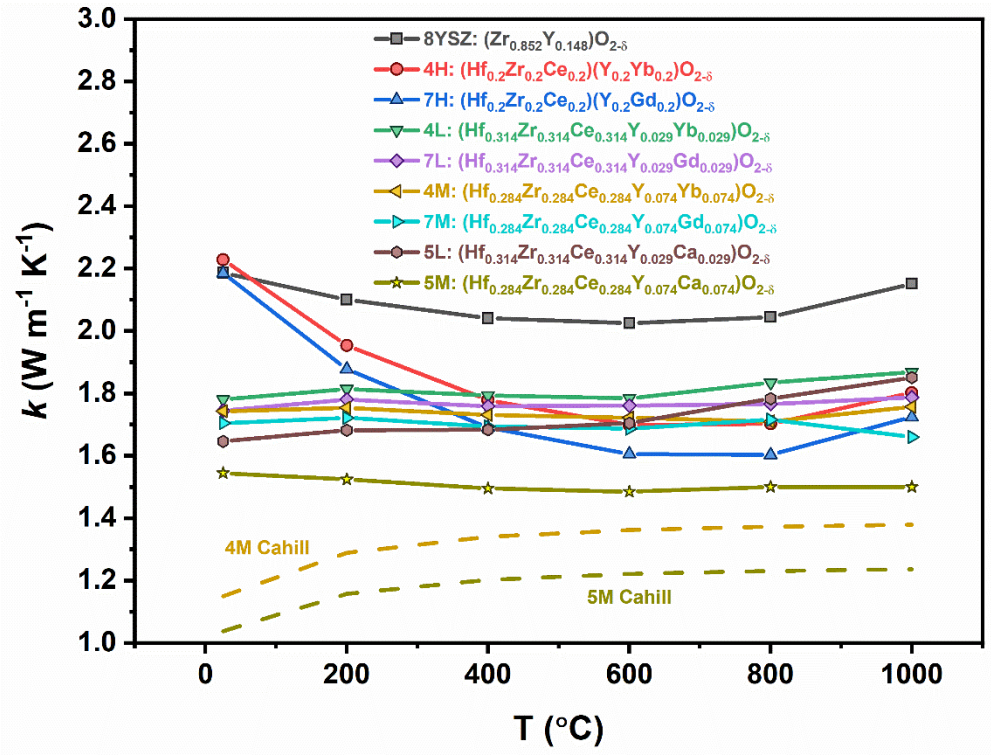

Figure 2.7. Measured thermal conductivity vs. temperature curves for all single-phase specimens from room temperature to 1000°C. The calculated phonon limits for 4M and 5M by using the Cahill [70] model are shown by the dashed lines. All specimens were annealed at 1500°C for 24 hours prior to the thermal conductivity measurements.

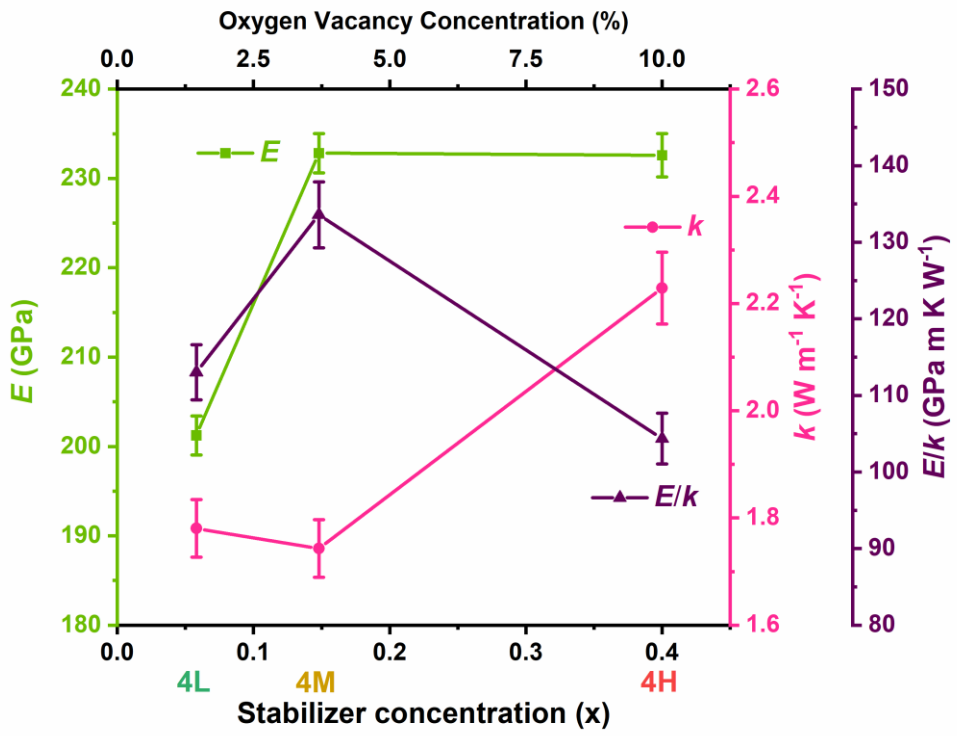

Figure 2.8. Room-temperature Young's modulus (E), thermal conductivity (k), and E/k ratio for $(Hf_{1/3}Zr_{1/3}Ce_{1/3})_{1-x}(Y_{1/2}Yb_{1/2})_xO_{2-\delta}$ series of specimens 4L, 4M, and 4H. 4M exhibits the lowest thermal conductivity and the highest E/k ratio. All specimens were annealed at 1500°C for 24 hours.

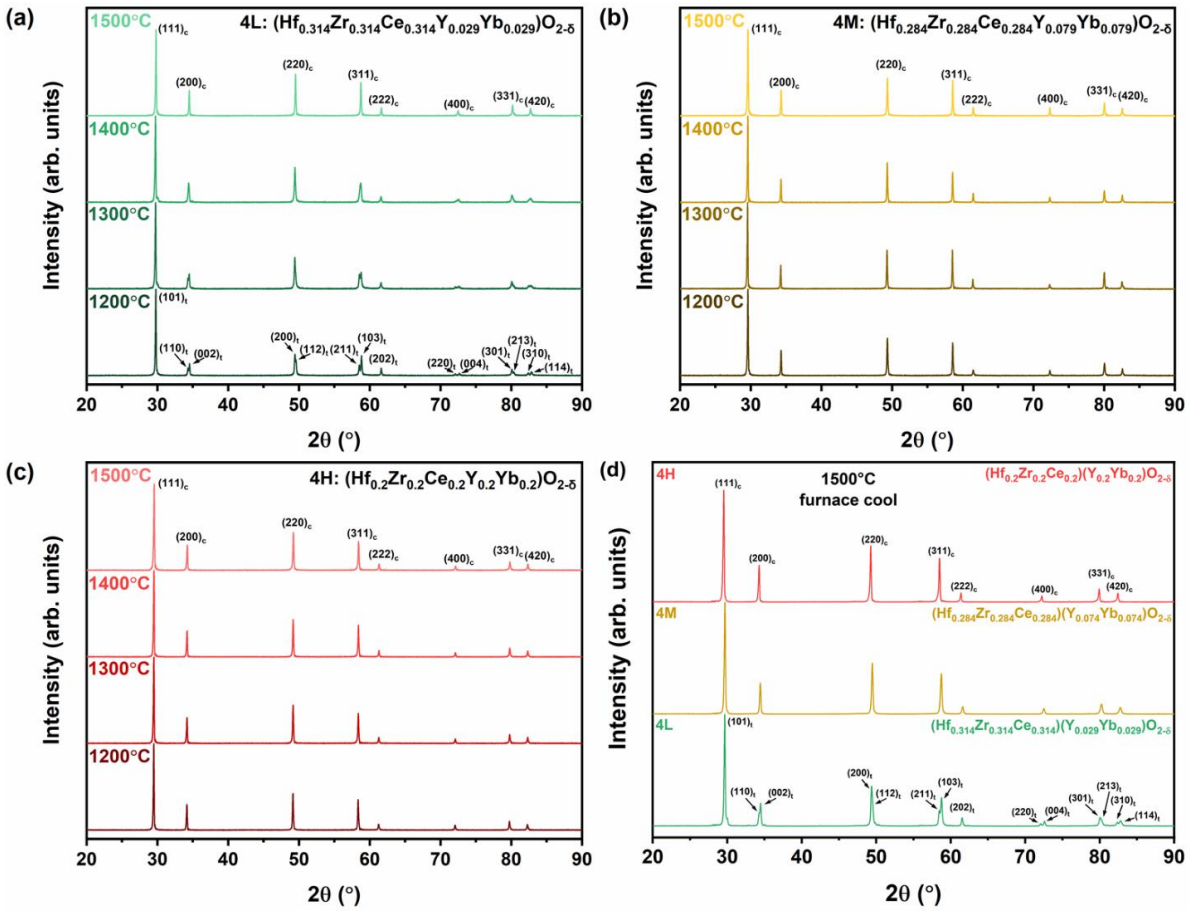

Figure 2.9. XRD patterns of the specimens air-quenched from 1200°C - 1500°C for compositions (a) 4L, (b) 4M, and (c) 4H. (d) The XRD patterns of three specimens of 4L, 4M, and 4H furnace-cooled from 1500°C as reference.

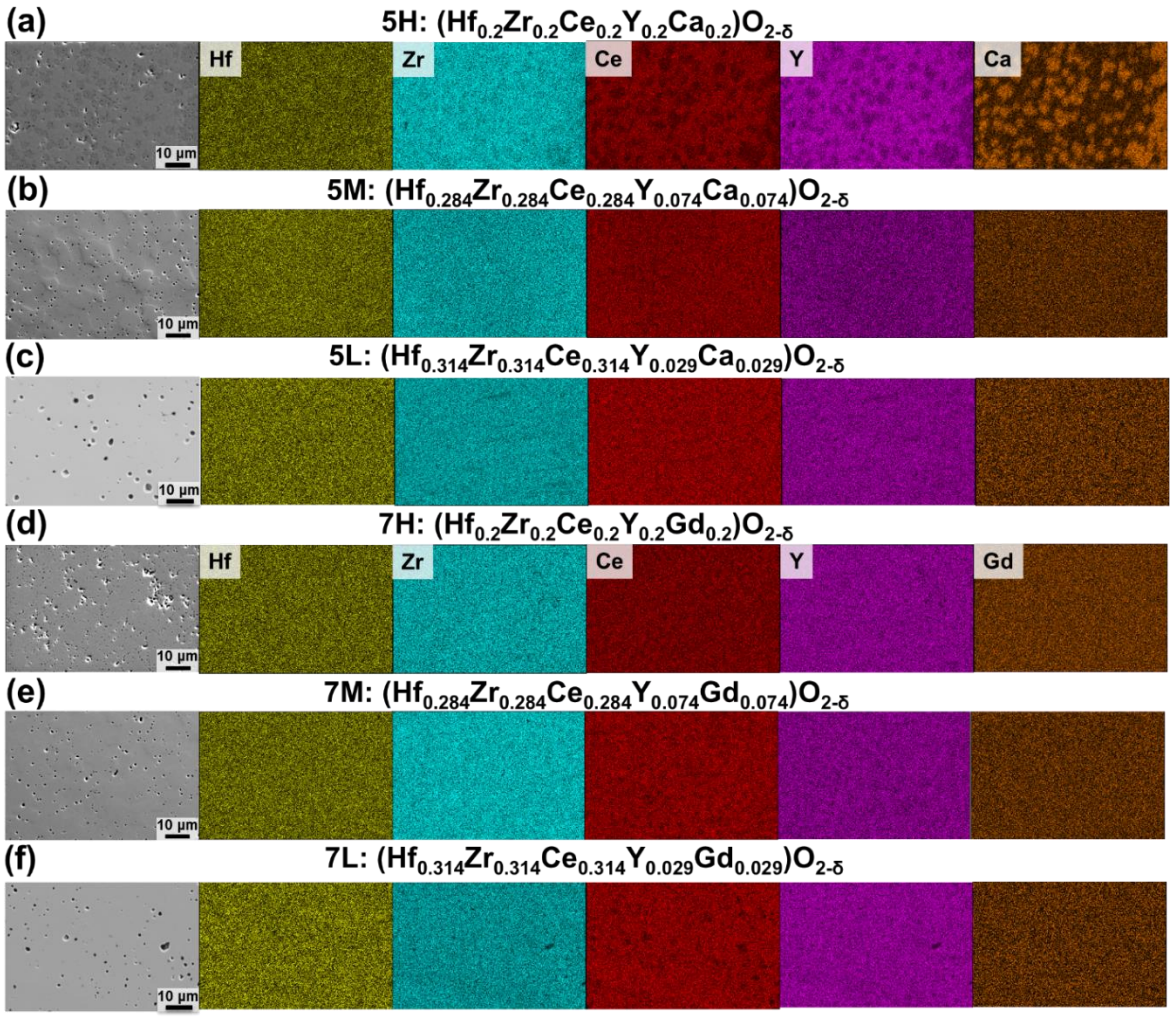

Figure 2.10. SEM images and EDS elemental maps of specimens (a) 5H, (b) 5M, (c) 5L, (d) 7H, (e) 7M, and (f) 7L furnace-cooled from 1500°C.

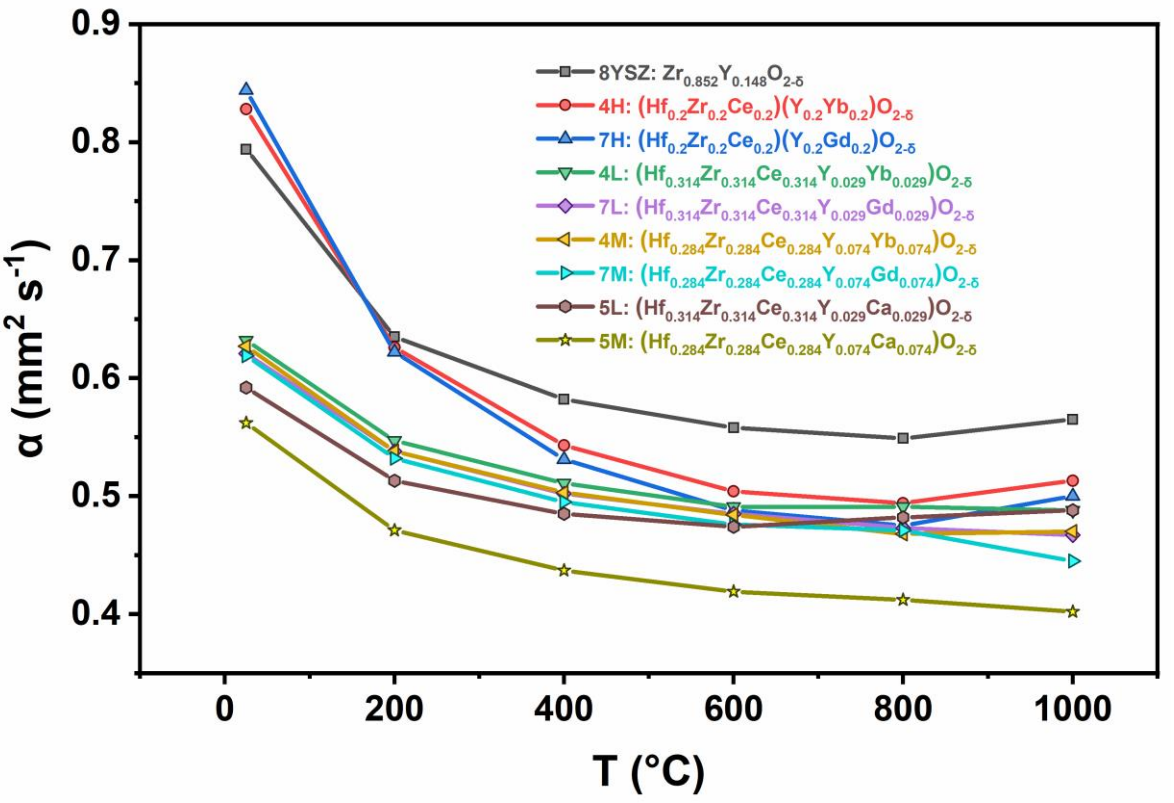

Figure 2.11. Measured thermal diffusivity vs. temperatures curves for all single-phase specimens from room temperature to 1000°C.

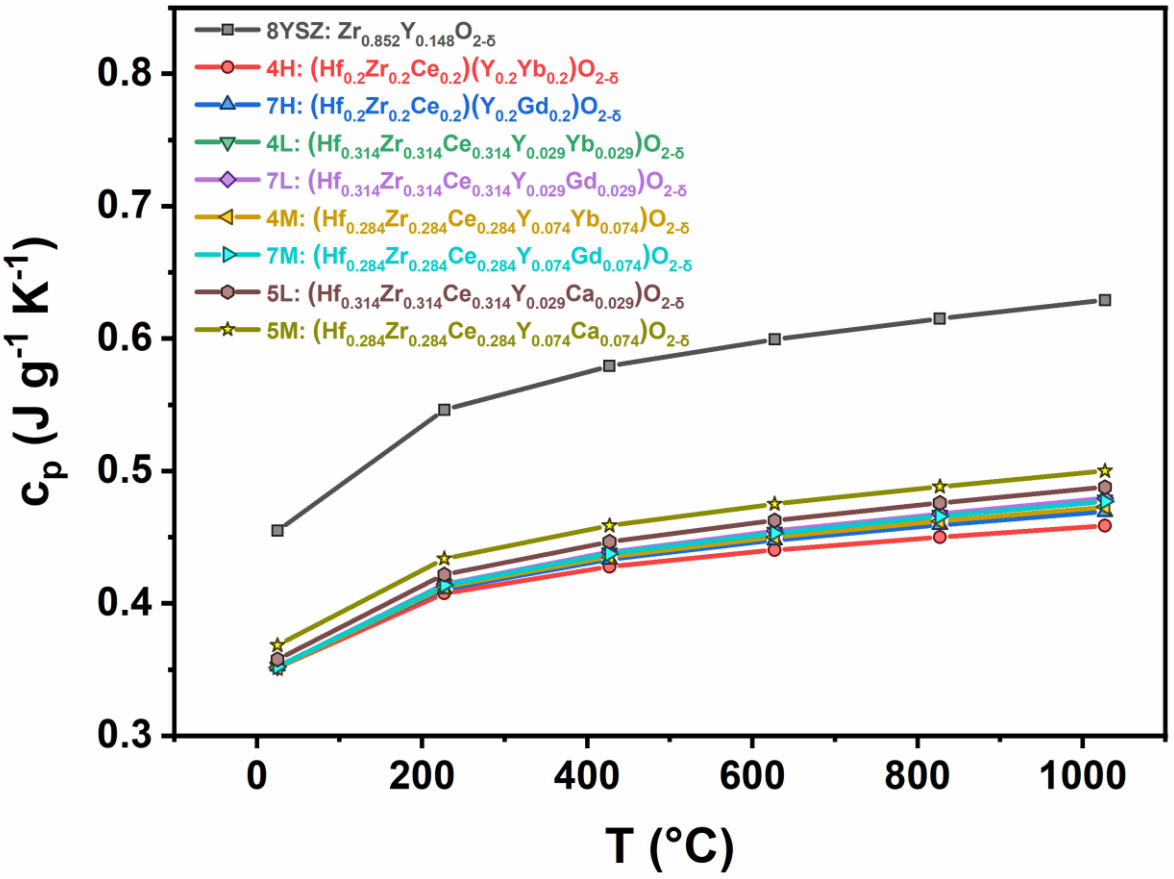

Figure 2.12. Calculated temperature-dependent heat capacity based on Neumann-Kopp law using the heat capacities of the constituent oxides from I. Barin, Thermochemical Data of Pure Substances, VCH, Weinheim, 1995.

2.6 REFERENCES

[1] J.W. Yeh, S.K. Chen, S.J. Lin, J.Y. Gan, T.S. Chin, T.T. Shun, C.H. Tsau, S.Y. Chang, Nanostructured high-entropy alloys with multiple principal elements: novel alloy design concepts and outcomes, Adv. Eng. Mater. 6 (2004) 299–303. doi:10.1002/adem.200300567.

[2] B. Cantor, I.T.H. Chang, P. Knight, A.J.B. Vincent, Microstructural development in equiatomic multicomponent alloys, Mater. Sci. Eng. A. 375 (2004) 213–218. doi:10.1016/j.msea.2003.10.257.

[3] A. Gali, E.P. George, Tensile properties of high- and medium-entropy alloys, Intermetallics. 39 (2013) 74–78. doi:10.1016/j.intermet.2013.03.018.

[4] B. Gludovatz, A. Hohenwarter, K.V.S. Thurston, H. Bei, Z. Wu, E.P. George, R.O. Ritchie, Exceptional damage-tolerance of a medium-entropy alloy CrCoNi at cryogenic temperatures, Nat. Commun. 7 (2016) 10602. doi:10.1038/ncomms10602.

[5] Z. Li, K.G. Pradeep, Y. Deng, D. Raabe, C.C. Tasan, Metastable high-entropy dual-phase alloys overcome the strength-ductility trade-off, Nature. 534 (2016) 227–230. doi:10.1038/nature17981.

[6] C.M. Rost, E. Sachet, T. Borman, A. Moballegh, E.C. Dickey, D. Hou, J.L. Jones, S. Curtarolo, J.P. Maria, Entropy-stabilized oxides, Nat. Commun. 6 (2015) 8485. doi:10.1038/ncomms9485.

[7] R. Djenadic, A. Sarkar, O. Clemens, C. Loho, M. Botros, V.S.K. Chakravadhanula, C. Kübel, S.S. Bhattacharya, A.S. Gandhi, H. Hahn, Multicomponent equiatomic rare earth oxides, Mater. Res. Lett. 5 (2017) 102–109. doi:10.1080/21663831.2016.1220433.

[8] S. Jiang, T. Hu, J. Gild, N. Zhou, J. Nie, M. Qin, T. Harrington, K. Vecchio, J. Luo, A new class of high-entropy perovskite oxides, Scr. Mater. 142 (2018) 116–120. doi:10.1016/j.scriptamat.2017.08.040.

[9] J. Gild, M. Samiee, J.L. Braun, T. Harrington, H. Vega, P.E. Hopkins, K. Vecchio, J. Luo, High-entropy fluorite oxides, J. Eur. Ceram. Soc. 38 (2018) 3578–3584. doi:10.1016/j.jeurceramsoc.2018.04.010.

[10] M.R. Chellali, A. Sarkar, S.H. Nandam, S.S. Bhattacharya, B. Breitung, H. Hahn, L. Velasco, On the homogeneity of high entropy oxides: An investigation at the atomic scale, Scr. Mater. 166 (2019) 58–63. doi:10.1016/j.scriptamat.2019.02.039.

[11] J. Gild, Y. Zhang, T. Harrington, S. Jiang, T. Hu, M.C. Quinn, W.M. Mellor, N. Zhou, K. Vecchio, J. Luo, High-Entropy Metal Diborides: A New Class of High-Entropy Materials and a New Type of Ultrahigh Temperature Ceramics, Sci. Rep. 6 (2016) 37946. doi:10.1038/srep37946.

[12] Y. Zhang, W.M. Guo, Z. Bin Jiang, Q.Q. Zhu, S.K. Sun, Y. You, K. Plucknett, H.T. Lin, Dense high-entropy boride ceramics with ultra-high hardness, Scr. Mater. 164 (2019) 135–139. doi:10.1016/j.scriptamat.2019.01.021.

[13] P. Sarker, T. Harrington, C. Toher, C. Oses, M. Samiee, J.P. Maria, D.W. Brenner, K.S. Vecchio, S. Curtarolo, High-entropy high-hardness metal carbides discovered by entropy descriptors, Nat. Commun. 9 (2018) 1–10. doi:10.1038/s41467-018-07160-7.

[14] T.J. Harrington, J. Gild, P. Sarker, C. Toher, C.M. Rost, O.F. Dippo, C. McElfresh, K. Kaufmann, E. Marin, L. Borowski, P.E. Hopkins, J. Luo, S. Curtarolo, D.W. Brenner, K.S. Vecchio, Phase stability and mechanical properties of novel high entropy transition metal carbides, Acta Mater. 166 (2019) 271–280. doi:10.1016/j.actamat.2018.12.054.

[15] X. Yan, L. Constantin, Y. Lu, J.F. Silvain, M. Nastasi, B. Cui, (Hf0.2Zr0.2Ta0.2Nb0.2Ti0.2)C high-entropy ceramics with low thermal conductivity, J. Am. Ceram. Soc. 101 (2018) 4486–4491. doi:10.1111/jace.15779.

[16] T.K. Chen, T.T. Shun, J.W. Yeh, M.S. Wong, Nanostructured nitride films of multi-element high-entropy alloys by reactive DC sputtering, Surf. Coatings Technol. 188 (2004) 193–200. doi:10.1016/j.surfcoat.2004.08.023.

[17] J. Gild, J. Braun, K. Kaufmann, E. Marin, T. Harrington, P. Hopkins, K. Vecchio, J. Luo, A high-entropy silicide: (Mo0.2Nb0.2Ta0.2Ti0.2W0.2)Si2, J. Mater. (2019). doi:10.1016/j.jmat.2019.03.002.

[18] Y. Qin, J.X. Liu, F. Li, X. Wei, H. Wu, G.J. Zhang, A high entropy silicide by reactive spark plasma sintering, J. Adv. Ceram. 8 (2019) 148–152. doi:10.1007/s40145-019-0319-3.

[19] N. Zhou, S. Jiang, T. Huang, M. Qin, T. Hu, J. Luo, Single-phase high-entropy intermetallic compounds (HEICs): bridging high-entropy alloys and ceramics, Sci. Bull. 64 (2019) 856–864. doi:10.1016/j.scib.2019.05.007.

[20] A. Giri, J.L. Braun, P.E. Hopkins, Reduced dependence of thermal conductivity on temperature and pressure of multi-atom component crystalline solid solutions, J. Appl. Phys. 123 (2018) 015106. doi:10.1063/1.5010337.

[21] J.L. Braun, C.M. Rost, M. Lim, A. Giri, D.H. Olson, G.N. Kotsonis, G. Stan, D.W. Brenner, J.P. Maria, P.E. Hopkins, Charge-Induced Disorder Controls the Thermal Conductivity of Entropy-Stabilized Oxides, Adv. Mater. 30 (2018) 1805004. doi:10.1002/adma.201805004.

[22] R.C. Garvie, R.H. Hannink, R.T. Pascoe, Ceramic steel?, Nature. 258 (1975) 703–704. doi:10.1038/258704a0.

[23] T.K. Gupta, F.F. Lange, J.H. Bechtold, Effect of stress-induced phase transformation on the properties of polycrystalline zirconia containing metastable tetragonal phase, J. Mater. Sci. 13 (1978) 1464–1470. doi:10.1007/BF00553200.

[24] J.A. Kilner, Ionic conductors: Feel the strain, Nat. Mater. 7 (2008) 838–839. doi:10.1038/nmat2314.

[25] W. Pan, S.R. Phillpot, C. Wan, A. Chernatynskiy, Z. Qu, Low thermal conductivity oxides, MRS Bull. 37 (2012) 917–922. doi:10.1557/mrs.2012.234.

[26] K. Chen, X. Pei, L. Tang, H. Cheng, Z. Li, C. Li, X. Zhang, L. An, A five-component entropy-stabilized fluorite oxide, J. Eur. Ceram. Soc. 38 (2018) 4161–4164. doi:10.1016/j.jeurceramsoc.2018.04.063.

[27] D.B. Miracle, Critical Assessment: Critical Assessment 14: High entropy alloys and their development as structural materials, Mater. Sci. Technol. (United Kingdom). 31 (2015) 1142–1147. doi:10.1179/1743284714Y.0000000749.

[28] D.B. Miracle, O.N. Senkov, A critical review of high entropy alloys and related concepts, Acta Mater. 122 (2017) 448–511. doi:10.1016/j.actamat.2016.08.081.

[29] J.W. Yeh, Y.L. Chen, S.J. Lin, S.K. Chen, High-entropy alloys - A new era of exploitation, Mater. Sci. Forum. 560 (2007) 1–9. doi:10.4028/www.scientific.net/MSF.560.1.

[30] D. Miracle, J. Miller, O. Senkov, C. Woodward, M. Uchic, J. Tiley, Exploration and Development of High Entropy Alloys for Structural Applications, Entropy. 16 (2014) 494–525. doi:10.3390/e16010494.

[31] X. Yang, Y. Zhang, Prediction of high-entropy stabilized solid-solution in multi-component alloys, Mater. Chem. Phys. 132 (2012) 233–238. doi:10.1016/j.matchemphys.2011.11.021.

[32] M. Liu, L. Yang, S. Wang, K. Blinn, M. Liu, Z. Liu, Z. Cheng, Enhanced sulfur and coking tolerance of a mixed ion conductor for SOFCs: BaZr 0.1 Ce 0.7 y 0.2 - X Yb x O 3 -δ, Science (80-.). 326 (2009) 126–129. doi:10.1126/science.1174811.

[33] R.-Z. Zhang, M.J. Reece, Review of high entropy ceramics: design, synthesis, structure and properties, J. Mater. Chem. A. 7 (2019) 22148–22162. doi:10.1039/C9TA05698J.

[34] A. Sarkar, Q. Wang, A. Schiele, M.R. Chellali, S.S. Bhattacharya, D. Wang, T. Brezesinski, H. Hahn, L. Velasco, B. Breitung, High-Entropy Oxides: Fundamental Aspects and Electrochemical Properties, Adv. Mater. 31 (2019) 1806236. doi:10.1002/adma.201806236.

[35] G.K. Williamson, W.H. Hall, X-ray line broadening from filed aluminium and wolfram, Acta Metall. 1 (1953) 22–31. doi:10.1016/0001-6160(53)90006-6.

[36] ASTM International, ASTM C373-18: Standard Test Methods for Determination of Water Absorption and Associated Properties by Vacuum Method for Pressed Ceramic Tiles and

Glass Tiles and Boil Method for Extruded Ceramic Tiles and Non-tile Fired Ceramic Whiteware Products, Annu. B. ASTM Stand. (2018) 7. doi:10.1520/C0373-16.2.

[37] ASTM International, ASTM C1198-09 Standard Test Method for Dynamic Young's Modulus, Shear Modulus, and Poisson's Ratio for Advanced Ceramics by Sonic Resonance, Annu. B. ASTM Stand. 09 (2013) 1–11. doi:10.1520/C1198-09R13.2.

[38] E.A. Dean, J.A. Lopez, Empirical dependence of elastic moduli on porosity for ceramic materials, J. Am. Ceram. Soc. 66 (1983) 366–370. doi:10.1111/j.1151-2916.1983.tb10051.x.

[39] W.C. Oliver, F.R. Brotzen, On the generality of the relationship among contact stiffness, contact area, and elastic modulus during indentation, J. Mater. Res. 7 (1992) 613–617. doi:10.1557/JMR.1992.0613.

[40] W.C. Oliver, G.M. Pharr, Measurement of hardness and elastic modulus by instrumented indentation: Advances in understanding and refinements to methodology, J. Mater. Res. 19 (2004) 3–20. doi:10.1557/jmr.2004.19.1.3.

[41] I. Barin, Thermochemical data of pure substances, VCH, Weinheim, 1995. doi:10.1016/s0165-2427(96)05632-2.

[42] R.W. Rice, Porosity of Ceramics: properties and applications, CRC Press, Boca Raton, FL, 1998. doi:10.1017/CBO9781107415324.004.

[43] H.G. Scott, Phase relationships in the zirconia-yttria system, J. Mater. Sci. 10 (1975) 1527–1535. doi:10.1007/BF01031853.

[44] K. Matsui, H. Yoshida, Y. Ikuhara, Review: microstructure-development mechanism during sintering in polycrystalline zirconia, Int. Mater. Rev. 63 (2018) 375–406. doi:10.1080/09506608.2017.1402424.

[45] J.R. McBride, K.C. Hass, B.D. Poindexter, W.H. Weber, Raman and x-ray studies of Ce1-xRExO2-y, where RE=La, Pr, Nd, Eu, Gd, and Tb, J. Appl. Phys. 76 (1994) 2435–2441. doi:10.1063/1.357593.

[46] M. Guo, J. Lu, Y. Wu, Y. Wang, M. Luo, UV and visible Raman studies of oxygen vacancies in rare-earth-doped ceria, Langmuir. 27 (2011) 3872–3877. doi:10.1021/la200292f.

[47] B. Choudhury, A. Choudhury, Ce 3+ and oxygen vacancy mediated tuning of structural and optical properties of CeO 2 nanoparticles, Mater. Chem. Phys. 131 (2012) 666–671. doi:10.1016/j.matchemphys.2011.10.032.

[48] C. Mercer, J.R. Williams, D.R. Clarke, A.G. Evans, On a ferroelastic mechanism governing the toughness of metastable tetragonal-prime (t′) yttria-stabilized zirconia, Proc. R. Soc. A Math. Phys. Eng. Sci. 463 (2007) 1393–1408. doi:10.1098/rspa.2007.1829.

[49] A.M. Limarga, D.R. Clarke, Piezo-spectroscopic coefficients of tetragonal-prime yttria-stabilized zirconia, J. Am. Ceram. Soc. 90 (2007) 1272–1275. doi:10.1111/j.1551-2916.2007.01622.x.

[50] C. Viazzi, J.P. Bonino, F. Ansart, A. Barnabé, Structural study of metastable tetragonal YSZ powders produced via a sol-gel route, J. Alloys Compd. 452 (2008) 377–383. doi:10.1016/j.jallcom.2006.10.155.

[51] J.T.S. Irvine, A.J. Feighery, D.P. Fagg, S. García-Martín, Structural studies on the optimization of fast oxide ion transport, Solid State Ionics. 136–137 (2000) 879–885. doi:10.1016/S0167-2738(00)00568-3.

[52] L. Lõpez-Conesa, J.M. Rebled, M.H. Chambrier, K. Boulahya, J.M. González-Calbet, M.D. Braida, G. Dezanneau, S. Estradé, F. Peirõ, Local structure of rare earth niobates (RE3NbO7, RE = Y, Er, Yb, Lu) for proton conduction applications, Fuel Cells. 13 (2013) 29–33. doi:10.1002/fuce.201200136.

[53] K.N. Clausen, W. Hayes, Defect structure of yttria-stabilized zirconia and its influence on the ionic conductivity at elevated temperatures, Phys. Rev. B - Condens. Matter Mater. Phys. 59 (1999) 14202–14219. doi:10.1103/PhysRevB.59.14202.

[54] E. Tani, M. Yoshimura, S. Somiya, Revised Phase Diagram of the System ZrO2-CeO2 Below 1400°C, J. Am. Ceram. Soc. 66 (1983) 506–510. doi:10.1111/j.1151-2916.1983.tb10591.x.

[55] P. Duran, M. Gonzalez, C. Moure, J.R. Jurado, C. Pascual, A new tentative phase equilibrium diagram for the ZrO2-CeO2 system in air, J. Mater. Sci. 25 (1990) 5001–5006. doi:10.1007/BF00580121.

[56] E.R. Andrievskaya, G.I. Gerasimyuk, O.A. Kornienko, A. V. Samelyuk, L.M. Lopato, V.P. Red'ko, Phase equilibria in the system HfO 2-ZrO 2-CeO 2 at 1500°C, Powder Metall. Met. Ceram. 45 (2006) 448–456. doi:10.1007/s11106-006-0105-y.

[57] R. Liu, H. Chen, K. Zhao, Y. Qin, B. Jiang, T. Zhang, G. Sha, X. Shi, C. Uher, W. Zhang, L. Chen, Entropy as a Gene-Like Performance Indicator Promoting Thermoelectric Materials, Adv. Mater. 29 (2017) 1702712. doi:10.1002/adma.201702712.

[58] K. Zhao, P. Qiu, X. Shi, L. Chen, Recent Advances in Liquid-Like Thermoelectric Materials, Adv. Funct. Mater. (2019) 1903867. doi:10.1002/adfm.201903867.

[59] J.W. Adams, R. Ruh, K.S. Mazdiyasni, Young's Modulus, Flexural Strength, and Fracture of Yttria-Stabilized Zirconia versus Temperature, J. Am. Ceram. Soc. 80 (2005) 903–908. doi:10.1111/j.1151-2916.1997.tb02920.x.

[60] M. Fujikane, D. Setoyama, S. Nagao, R. Nowak, S. Yamanaka, Nanoindentation examination of yttria-stabilized zirconia (YSZ) crystal, J. Alloys Compd. 431 (2007) 250–255. doi:10.1016/j.jallcom.2006.05.058.

[61] K.W. Schlichting, N.P. Padture, P.G. Klemens, Thermal conductivity of dense and porous yttria-stabilized zirconia, J. Mater. Sci. 36 (2001) 3003–3010. doi:10.1023/A:1017970924312.

[62] M.R. Winter, D.R. Clarke, Oxide materials with low thermal conductivity, J. Am. Ceram. Soc. 90 (2007) 533–540. doi:10.1111/j.1551-2916.2006.01410.x.

[63] T. Li, Z. Ma, L. Liu, S.Z. Zhu, Thermal properties of Sm2Zr2O7-NiCr 2O4 composites, Ceram. Int. 40 (2014) 11423–11426. doi:10.1016/j.ceramint.2014.03.093.

[64] S. Shin, Q. Wang, J. Luo, R. Chen, Advanced Materials for High-Temperature Thermal Transport, Adv. Funct. Mater. (2019) 1904815. doi:10.1002/adfm.201904815.

[65] J. Yang, X. Qian, W. Pan, R. Yang, Z. Li, Y. Han, M. Zhao, M. Huang, C. Wan, Diffused Lattice Vibration and Ultralow Thermal Conductivity in the Binary Ln–Nb–O Oxide System, Adv. Mater. 31 (2019) 1808222. doi:10.1002/adma.201808222.

[66] W. Zhou, Y. Cheng, K. Chen, G. Xie, T. Wang, G. Zhang, Thermal Conductivity of Amorphous Materials, Adv. Funct. Mater. (2019) 1903829. doi:10.1002/adfm.201903829.

[67] F. DeAngelis, M.G. Muraleedharan, J. Moon, H.R. Seyf, A.J. Minnich, A.J.H. McGaughey, A. Henry, Thermal Transport in Disordered Materials, Nanoscale Microscale Thermophys. Eng. 23 (2019) 81–116. doi:10.1080/15567265.2018.1519004.

[68] A. Bogicevic, C. Wolverton, G.M. Crosbie, E.B. Stechel, Defect ordering in aliovalently doped cubic zirconia from first principles, Phys. Rev. B - Condens. Matter Mater. Phys. 64 (2001). doi:10.1103/PhysRevB.64.014106.

[69] E.D. Wachsman, Effect of oxygen sublattice order on conductivity in highly defective fluorite oxides, J. Eur. Ceram. Soc. 24 (2004) 1281–1285. doi:10.1016/S0955-2219(03)00509-0.

[70] D.G. Cahill, S.K. Watson, R.O. Pohl, Lower limit to the thermal conductivity of disordered crystals, Phys. Rev. B. 46 (1992) 6131–6140. doi:10.1103/PhysRevB.46.6131.

[71] R.D. Shannon, Revised effective ionic radii and systematic studies of interatomic distances in halides and chalcogenides, Acta Crystallogr. Sect. A. 32 (1976) 751–767. doi:10.1107/S0567739476001551.

3. ORIGIN OF THE INSULATIVE PROPERTY IN RARE-EARTH NIOBATES/TANTALATES

3.1 INTRODUCTION

The work developed in high-entropy ceramics is developing rapidly due to their attractive properties [1–4]. The majority of work has been focused on borides [5–8], carbides [9–13], and rocksalt- [14–16] and fluorite-structured oxides [17–22]. However, recent work is beginning to expand into other systems such as silicates [23–26], silicides [27–29], aluminides [30], fluorides [31,32], and phosphates [33,34]. Notable properties include enhanced electrochemical [3,35–38] and mechanical performance [5–7,11,13,39–42] and increased phase stability [19,43]. Significant modeling efforts have also helped guide experiments and confirmed their results [11,42,44–46].

Perhaps the most interesting and useful property high-entropy ceramics possess, across nearly all systems, is low thermal conductivity. This arises from the inherent disorder in high entropy materials, and oxides tend to have the lowest thermal conductivity [12,18–20,24,47–51]. However, the extent of low thermal conductivity can either be suppressed or enhanced depending on variables unique to individual systems. For example, Braun et al. attributed low thermal conductivity in high entropy rocksalt oxides to valency disorder inducing unit cell distortions [49]. Wright et al. attributed low thermal conductivity in fluorite and pyrochlore oxides to be due to the concentration of oxygen vacancies and the size disorder, respectively [19,48]. Although developing a unifying expression that governs thermal conductivity trends across all high entropy ceramics is more challenging, further understanding of critical parameters within systems is crucial in further developing these materials for insulative applications.

3.2 EXPERIMENTAL PROCEDURES

3.2.1 MATERIALS AND SYNTHESIS

In this report, we will report on an emerging class of defect-fluorites that show amorphous-like thermal conductivity [20,52]. We aim to further the understanding of this class of materials by reporting on several new compositions. The rare-earth-based (RE) niobates/tantalates (RE3(Nb,Ta)O7) have room temperature thermal conductivities approaching $1\ W\ m^{-1}\ K^{-1}$ and have moderate moduli (~ 200-250 GPa). This makes them the highest Young's modulus to thermal conductivity ratio (E/k) reported to-date [52]. We examined the influence of the ratio of Nb and Ta and also the effects of aliovalent doping. Furthermore, we considered the influence of mass disorder by introducing light elements into a dense matrix. Promising compositions and temperature-dependent thermal conductivity trends are also included. Lastly, in addition to reporting on 29 new HEC compositions, we have also narrowed down a simple parameter (weighted average ionic radius) that can be used as a first-order approximation in predicting low thermal conductivity niobate/tantalate-based fluorite oxides.

Constituent rare-earth oxide, Al_2O_3, and MgO powders were purchased from US Research Nanomaterials and were approximately 5 μm. CaO (particle size < 160 nm), Nb_2O_5 (particle size ~ 500 nm), and Ta_2O_5 powders were purchased from Sigma-Aldrich, SkySpring Nanomaterials, and Inframat Advanced Materials, respectively. Stoichiometric amounts were weighed out with a 0.01 mg precision for a total of 2 g. The powders along with 2 wt. % stearic acid was added to a poly(methyl methacrylate) tube with tungsten carbide endcaps and one Ø5/16" tungsten carbide ball. The powders were high-energy ball milled for 100 minutes (SPEX 8000D, SPEX SamplePrep, USA). The powders were then pressed under 100 MPa in a 0.5" die stainless steel die and placed on Pt foil to undergo sintering at 1600℃ or 1700℃ for 24 h. Both

surfaces of the specimens were then ground with a 30 μm diamond disc to remove any surface contamination obtained during sintering. Pellets were ground into a powder with an agate mortar and pestle for diffraction experiments.

3.2.2 CHARACTERIZATION

3.2.2.1 X-RAY DIFFRACTION (XRD) AND DENSITY (ρ)

X-ray diffraction (XRD, Miniflex II, Rigaku, Japan) determined the crystal structure and theoretical density. Data was collected over 2 seconds per step with 0.02° 2θ steps. The bulk density was determined through the boil method (ASTM Standard C373-18 [53]). The relative density of the specimens ranged from 90 – 100 %.

3.2.2.2 NEUTRON DIFFRACTION

Neutron diffraction experiments were carried out at Oak Ridge National Laboratory on the Nanoscale-Ordered MAterials Diffractometer (NOMAD, BL-1B) at the Spallation Neutron Source (SNS). Powders were loaded into a 2 mm diameter quartz capillary to a height of 3 cm (~ 0.7 g). The diffraction experiments were carried out at 290 K for approximately 25 minutes. The data from all six detector banks were background-subtracted (from an empty quartz capillary) and normalized to the intensity of vanadium prior to being combined to produce the total scattering function, S(Q). This function was then Fourier-transformed with a Q_{max} of 50.0 $Å^{-1}$ to obtain the partial distribution functions, G(r). The momentum transfer, Q, is given as $Q=4\pi\sin\theta/\lambda$, where θ and λ are the scattering angle and neutron wavelength.

3.2.2.3 YOUNG'S MODULUS (E)

The Young's modulus was determined through an oscilloscope operating in pulse-echo mode (TDS 420A, Tektronix, USA). The longitudinal and transverse wave speeds and thus,

Poisson's ratio and Young's modulus were calculated by the same method used by our group in a previous publication [19].

3.2.2.4 THERMAL CONDUCTIVITY (k)

The thermal conductivity (k) was calculated through the product of thermal diffusivity (α), density (ρ), and heat capacity (c_p). Laser flash analysis (LFA 467 HT HyperFlash, NETZSCH, Germany) determined the thermal diffusivity. Before measurement, the specimens were coated with carbon to maximize laser absorption. The heat capacity was determined through the weighted average of the heat capacity of the constituents [54] according to the Neumann-Kopp rule. Both Young's modulus and thermal conductivity were corrected for porosity according to $E = \frac{E_{measured}}{1-2.9P}$ and $k = \frac{k_{measured}}{(1-P)^{3/2}}$, where P is the pore fraction [55,56].

3.2.3 NEUTRON DIFFRACTION MODELING

3.2.3.1 PDFgui

A small-box modeling approach was carried out with the PDFgui software [57]. A cif file was created in VESTA for each composition based on a A_4O_7 fluorite (space group 225, $Fm\bar{3}m$) and A_3BO_7 weberite (space group 20, $C222_1$) unit cell [58]. The Q_{damp} and Q_{broad} values were $0.017659\ \text{Å}^{-1}$ and $0.0191822\ \text{Å}^{-1}$. The fluorite cell had the lattice parameter, scale, correlated atomic motion (delta2), and the isotropic atomic displacement parameter (ADP) for the cation and anion site refined. The weberite cell had 27 parameters refined: lattice parameters, scale, correlated atomic motion (delta2), eight ADPs corresponding to the eight distinct lattice sites, and 14 lattice position parameters. The fitting range was selected to be from $0.02\ \text{Å} - 70\ \text{Å}$ and then the upper bound was reduced in 5 Å steps until the final fitting range of $0.02\ \text{Å} - 5\ \text{Å}$. After each fitting window, the converged parameters were used as initial values for the following fit.

3.2.3.2 REVERSE MONTE CARLO (RMC)

A large-box modeling approach was carried out with the RMCprofile program [59]. Only the weberite cell was investigated using this technique as it was found that the weberite cell fit better in our PDFgui analysis and previous researchers have also stated unsuccessful attempts in modeling Yb_3TaO_7 from a fluorite cell starting point [60]. A 6×8×8 supercell was constructed for reverse Monte Carlo (RMC) analysis. Bank 2 from NOMAD was fitted in GSAS-II to provide an initial structure for the RMC simulation [61]. A Chebyshev background was manually determined so to not capture the diffuse scattering. The lattice parameters, scale, atomic positions, ADPs, domain size, and microstrain were all refined.

Minimum bond lengths were selected for each atom-atom pair, but no maximum was set. The cations were allowed to move up to 0.05 Å per translational move while O atoms were allowed up to 0.1 Å. The rare earth cations all had an equal probability of swapping as did Nb and Ta (in compositions NT5-50 and NT5-50 4L). The probability for the simulation to generate translational or atomic swapping moves was approximately 50 %. The Bragg pattern from bank 2, $S(Q)$ ($F(Q)$ or $i(Q)$ in RMCprofile notation), and $G(r)$ ($D(r)_{normalized}$ in RMCprofile notation) were all fit simultaneously. The simulation ran for $24\ h$ with no scaling, and then continued for another $24\ h$ with scaling. Post-analysis of the generated structure was carried out using CrystalMaker® 10.5 [62].

3.3 RESULTS AND DISCUSSION

3.3.1 INFLUENCE OF Nb:Ta RATIO ON E AND k

All 29 compositions examined in this study revealed a single fluorite phase according to benchtop XRD analysis. Of these, 26 can be classified as novel HECs. Every specimen along

with their room temperature thermal conductivity and Young's modulus are available in Table 3.1.

Yang et al. reported on Dy_3NbO_7 in 2019 stating the highest E/k of a material to-date, $235\ GPa\ m\ K\ W^{-1}$ and a thermal conductivity of $1\ W\ m^{-1}\ K^{-1}$ [52]. An interesting and quick experiment is to see how the influence of substituting Nb with Ta affects the thermomechanical properties as they have the same ionic radius (0.64 Å) [63], yet Ta is approximately twice the mass of Nb. Recently, a group has investigated this with $Dy_3(Ta_{1-x}Nb_x)O_7$ [64]. They found that both the modulus and thermal conductivity decrease as more Nb is added. However, Dy_3TaO_7 has a long-range weberite structure that may play a role in the observations. Although both Nb and Ta are the same size, yet Dy_3NbO_7 has a fluorite structure while Dy_3TaO_7 has a weberite structure suggests Ta has a stronger preference for ordering.

We conducted a similar experiment with $(Dy_{0.25}Er_{0.25}Ho_{0.25}Nb_{0.25-x}Ta_x)_4O_7$. Within this composition, there is no long-range weberite phase transition as all specimens show a single fluorite phase in Figure 3.1(a). The E, k, and E/k are shown in Figure 3.1(b). Both the modulus and conductivity increase as more Nb is substituted for Ta, similar to the compositionally simpler compound $Dy_3(Ta_{1-x}Nb_x)O_7$. Interestingly, there is a strong change in both the conductivity and modulus when there is approximately three times more Ta than Nb. This is also in agreement with the observations in $Dy_3(Ta_{1-x}Nb_x)O_7$, however, there is a long-range order phase transition that accompanies this in their study, but this is absent in our specimens. This suggests there may be some atomic scale rearrangement.

3.3.2 THERMAL CONDUCTIVITY TREND

We plotted the room temperature thermal conductivity versus multiple parameters to reveal a simple linear trend that may be utilized by the community to assist in screening efforts

and selecting promising compositions. Figure 3.2(a) has k_{RT} plotted against $\bar{r}^{3+}/\bar{r}^{5+}$, which we found to be the best fit. Here, $\bar{r}$ is the weighted average effective ionic radius assuming a coordination number of VII according to Shannon [63]. Plots with other examined parameters (size disorder, mass disorder, density, and entropy) are available in the Supplementary Information (SI). A strong negative relationship (PCC $= -0.77$) is found between thermal conductivity and the average size of the rare earth cations (since $\bar{r}^{5+}$ is a constant of 0.69 Å). This has a direct relationship to the stable phases of the RE_3NbO_7 and RE_3TaO_7 compositions of which three stable phases exist depending on the radius of the rare-earth cations [65,66]. These two systems have the relationship that the larger rare cations form an ordered orthorhombic structure while the smaller cations (Dy in RE_3NbO_7 and Ho in RE_3TaO_7) form the disordered (chemically) fluorite phase. This appears to go against the intuitive thought that the specimen that has a stronger preference of ordering should have a higher thermal conductivity.

Figure 3.2(b) expands panel (a) to include compositions from literature with a couple being high entropy [52,67–70]. Although there is not much thermal conductivity data for these materials, our data agrees well with previous reports. The data reported from Ref. [68] on a few ternary RE_3NbO_7 and a couple of high-entropy compounds appears to be lower than expected, which may be due to the difference in thermal conductivity determination (laser flash vs. hot-wire). Regardless, the noticeable trend is that the long-range order fluorites show significantly reduced thermal conductivities compared to the ordered orthorhombic materials. This trend can be expected since the atoms in the orthorhombic structure (weberite and perovskite) are ordered compared to fluorite, but this does not hold up within the fluorite regime. The five specimens selected in Figure 3.2(a) were chosen for further study due to their varying conductivity and average size to help explain the observed phenomenon.

3.3.3 TEMPERATURE-DEPENDENT THERMAL CONDUCTIVITY

Figure 3.3 shows the thermal conductivity up to 1000℃. All five specimens show identical amorphous-like conductivity trends indicative of poor phonon-like conductivity and strong diffuson-like conductivity [71–74]. This observation has been noted in simpler composition such as Dy_3NbO_7 and appears to be common in fluorite-structured niobates and tantalates [52]. The phonon (or propagon) limit was computed for each specimen according to the model developed by Cahill, Watson, and Pohl [75]. Practically all specimens lie below the phonon limit at intermediate temperatures (200-600℃). This shows significant diffused vibration modes transporting heat as opposed to the typical acoustic modes. This occurs when the mean free path of the phonon approaches the interatomic spacing (Ioffe-Regel limit) and is usually prevalent in highly disordered materials (chemically, structurally, or electronically) [72,76,77]. Since the k_{RT} are similar to the simpler ternary compositions with identical charge distribution, we propose the conductivity is largely driven by structural disorder.

3.3.4 LONG-RANGE ORDER AND DIFFUSED SCATTERING

Preliminary benchtop XRD was carried out to determine the long-range phase. The Bragg peaks in Figure 3.4(a) correspond to a fluorite structure as expected. However, on closer inspection of the background, we noticed significant diffuse scattering occurring in all specimens around 40°,46°, and 55° 2θ. We have shown this in Figure 3.4(b) on a logarithmic intensity scale for our five specimens with distinctly different conductivities and size. We also found that the magnitude of these broad peaks correlated with k_{RT}. Specifically, that the smaller peaks had lower conductivities and the more prevalent peaks had higher conductivities.

These same powders were also used in neutron diffraction experiments. Neutron diffraction is more sensitive to O compared to X-rays and makes it a great complement in

diffraction studies. The total scattering function S(Q) is provided in Figure 3.4(c) and reveals more noticeable broad peaks in the background. A close-up of the background in Figure 3.4(d) reveals these same broad diffuse scattering peaks with higher clarity. The same trend discerned from XRD is also noticed here when examining the same peaks (more thermally insulative specimens have smaller diffuse peak intensities), however, we were also able to identify additional features in the neutron diffraction pattern that were not distinguishable in benchtop XRD. Firstly, a large diffuse peak is found around $1\ \text{Å}^{-1}$ in Q-space in a three of the specimens, but not two. A quick look at the composition reveals each of these materials contain Dy and Ho, relatively large cations. This peak was missed in XRD as it would have been near $15°\ 2\theta$, which was below our scanning range. Secondly, the diffuse peak near $4.5\ \text{Å}^{-1}$ consists of two peaks in NT25, NT5-50, and NT5-50 4L (all containing Dy and Ho), but was found to exist as one broad peak in NT4 and NT8. It seems that the materials with Dy and Ho have a stronger tendency for general ordering as seen by the increase in the number of peaks. In contrast, the materials without these cations (NT4 and NT8) seem to have a higher degree of ordering along certain orientations. However, in all specimens, it was found that the frequently overlooked background is rich with information.

This phenomenon of diffuse scattering in rare-earth niobates and tantalates has been realized by researchers dating back to the 1979 with Allpress and Rossell studying electron diffraction patterns [78]. It was proposed then and confirmed later that the diffuse scattering corresponded to an orthorhombic weberite structure. Suggesting that although the materials show a long-range fluorite structure, there is still a tendency for ordering on the atomic scale.

3.3.5 SHORT-RANGE ORDERING AND PARTIAL DISTRIBUTION FUNCTION (PDF)

Figure 3.5 shows the PDF, G(r) for all five specimens and provides insight into the structure on the atomic scale by providing a histogram of the atom-atom distances. A general observation revealed that each pattern had the same peaks and general shape alluding to the same general structure. On closer observation, it was found that the specimens containing Dy and Ho displayed a more ordered structure evident by the sharper peaks, especially around 3 Å. Specimen NT8, in particular, showed a very disordered structure with little distinguishable fine features. This agrees with the consensus that the larger the size difference between the 3+ and 5+ cations, the higher the tendency for ordering. This similar to the relationship between the pyrochlore and fluorite structure in rare-earth zirconates and hafnates, for example [79–81]. This trend is not followed for NT25 and NT4 since NT4 has a larger size ratio than NT25 (1.356 versus 1.337) yet has a more disordered PDF. This may suggest a tendency for chemical short-range ordering among the 3+ cations.

3.3.6 SMALL-BOX MODELING WITH PDFgui

The PDFgui software was used to, one, provide insight on the local structure, and two, on a possible transition between the fluorite and weberite structures. We approached this by first fitting the PDF to a fluorite and weberite structure over a large radial distance (70 Å). This was to provide general lattice parameters that serve as an average over a relatively large number of unit cells (~ 13 for fluorite and ~ 8 for weberite). The maximum bound was decreased in 5 Å steps. This approached was followed to avoid any local minimums that may have resulted if this procedure was followed in reverse (i.e., increasing the maximum bound from 5 Å in 5 Å steps. The R_w factor given in Equation (1) was used to evaluate the fitting.

$$R_w = \sum_{i=0}^{n} \left(\frac{w_i \left(Y_i^{obs} - Y_i^{calc} \right)^2}{\sum_{i=0}^{n} w_i \left(Y_i^{obs} \right)^2} \right)^{1/2} \times 100\% \quad (1)$$

Additionally, the percent difference between the fluorite and weberite fitting factors were evaluated as a function of the fitting window.

Figure 3.6(a-e) shows the R_w factor for the weberite and fluorite cells for each specimen. Across all materials, the weberite structure fit best at all observed fitting windows. This is likely due to two reasons. First, the weberite structure has been found to be a better fit for fluorite in the niobate and tantalate fluorite structure previously in short fitting windows [60]. Second, there are more degrees of freedom in the weberite structure, however, they should approach each other at sufficiently high radial distances.

In the most disordered specimen, NT8 (Fig. 3.6(a)), the weberite structure fit better than fluorite and the two structures gradually approached each other. As the average size of the 3+ cations increase, the fitting by the weberite cell becomes stronger at small radial distances (5-10 Å) and the approach to the fluorite becomes quicker. This trend is not consistent for NT5-50 4L (Fig. 3.6(e)). While there is still a strong preference for the weberite structure, it does not fit as well as NT5-50. We believe this may be due to the addition of La into the structure makes the rare-earth niobate/tantalate become non-stoichiometric (RE^{3+}:(Nb, Ta)$^{5+}$ ≠ 3:1). This deviation from stoichiometry likely creates oxygen vacancies and promotes anti-site mixing, thus giving rise to more disordering than expected.

The percent difference between the fluorite and weberite fits are shown in Figure 3.6(f-j). These assist in showing the strong preference for weberite ordering in materials with larger rare-earth cations and a quicker approach to the fluorite fit. There is no strict cutoff for the weberite-to-fluorite transition. We arbitrarily define one as 20%. In other words, the weberite cell persists

and is a good model until the R_w factor is within 20% of the fluorite cell. The radial distance where the 20% crossover occurs can also be regarded as the domain size of the weberite cell. However, we make the distinction that this nanodomain is not a traditional nanodomain where a structure different from the bulk may be stabilized on the atomic scale. Instead, the fluorite-structured RE_3NbO_7 and RE_3TaO_7 are proposed to be of the weberite structure, but these orthorhombic cells average out to a cubic cell at some characteristic length (here proposed to be when the fitting factors are within 20%). This distinction has also been proposed recently by researchers studying the fluorite $Ho_2Zr_2O_7$ [79,80,82,83].

Using this definition, the domain sizes for NT8, NT25, NT4, NT5-50, and NT5-50 4L are 60,25,50,15, and 20 Å. This concept still applies to thermal conduction as the vibrational density of states generated by this local weberite domain will be different than the outside bulk fluorite domain and attribute to phonon scattering. The domain size becomes increasingly small as the $\bar{r}^{3+}$ increases. Notably, in NT5-50, the domain size approaches the distance of one weberite unit cell (~10.5×~7.5×~7.5), which is where the definition of a phonon no longer becomes applicable [72,77]. At the Ioffe-Regel limit (phonon mean free path ~ a), the heat transfer is better described by a diffuson model where heat is carried through a random-walk model. This provides direct evidence as to why the thermal conductivity approaches and lies below the phonon limit. It is noted that the trend does not hold up for NT25 and NT4, which helps make clear that it is unlikely to find one parameter perfectly predicting thermal conduction in these complex materials and other established phenomenon are still important. Here, we believe that the Sc present in NT25 provides a higher thermal conductivity than predicted by our domain size trend because Sc is a very light element and can transfer heat very efficiently due to high vibrational frequency it can achieve. In fact, all of the compositions that contained Sc had the

highest thermal conductivities among the niobates as seen in Table 3.1. Lastly, additional effects such as anti-site defects and oxygen vacancies likely play a role in the reduced conductivity of NT5-50 4L although it has a larger predicted domain size than NT5-50.

An example of the fluorite and weberite fitting NT5-50 to a 10 Å limit using PDFgui is shown in Figure 3.7(a, b). The fluorite model is too simple an unable to capture peaks around 3 Å. The resulting R_w was 29.0%. The weberite model improves this to 23.6% by capturing the general feature of nearest-neighbor region, but still fails to pick up on the fine features. PDFgui, in general, is a very simplified approach since it uses average parameters for a unit cell to model data. This has strong limitations in simple ternary niobates such as Yb_3TaO_7 [60]. This is expected to be exacerbated as the complexity of the composition increases, thus requiring the use of more in-depth simulations.

3.3.7 LARGE-BOX MODELING WITH RMCprofile

The reverse Monte Carlo method for fitting PDFs is highly revered as its ethos remains as a purely data-driven technique. The only restriction applied was that each atomic pair had a minimum distance. A 6×8×8 weberite supercell (16896 atoms) was constructed with each cation randomly distributed among their sites. The fit using this method is shown in Figure 3.7(c). The fit improves dramatically to a R_w of 12.1% and can qualitatively capture the peaks around 3 Å, albeit not quantitatively.

An examination into the nearest neighbor region along with the partial PDFs ($G_{ij}(r)$) for each specimen is shown in Figure 3.8. We found some difficulty in modeling the PDFs using this method due to the abundance of elements. This creates rather sharp peaks in the partial PDFs but produces a smoother total PDF that fits well to experiments. We had comparable results when we tried using the bond valence sum method as well, which is provided in the SI.

The first interactions in each composition is predominantly composed of Nb-O, Ta-O, and Sc-O while the RE-O interactions comprise of the large first peak. We found the peaks near the 3 Å region to correspond to O-O interactions. Thus, demonstrating that the larger cations induce more ordered oxygen sites such as in NT5-50 (Fig. 3.8(d)) respective of an ordered weberite structure, whereas this is absent in NT8 (Fig. 3.8(a)).

3.3.8 ATOMIC DENSITY VARIATIONS

The 6×8×8 converged supercells were collapsed back down to one unit cell while retaining each atomic position to see the degree of disorder. A reference Dy3TaO7 from the ICSD database (collection code 191963) is provided in Figure 3.9(a) while each HEC is provided in Figure 3.9(b-d) in the [001] viewing direction. There are a few distinct observations to made here. First is that NT25, NT5-50, and NT5-50 4L show numerous O atoms occupying the interstitials while this is minimal in NT8 and NT4. The location of these O atoms is random but tend to be localized to the region with the O-O nearest neighbor space. Second, specimens NT8 and NT4 show correlated disorder with the atomic positions. Both cation and (some) anion positions show stretching in the general direction of the (010) plane while this is not observable in the other specimens. It is also interesting to note that this stretching observed in the anion sublattice is asymmetrical along the y-axis. This feature likely arose from the absence of the low index diffuse scattering peak in Figure 3.4(d) at $1\ \text{Å}^{-1}$ that both NT8 and NT4 did not exhibit. The main weberite peak contributing to that diffuse scattering peak is the (110) plane, which is closely related to the stretching direction. Considering all of the specimens, it is clear that there is extreme disorder in the O sublattice while the cations are relatively ordered. This further supports the evidence that the diffuse scattering peaks are enhanced by neutron diffraction in contrast to X-rays.

A heatmap of the atomic density was calculated for each model (including the reference) for the atoms in the [001] plane at z=0.25 in Figure 3.9(g-l). The transition from zero to maximum intensity is denoted by dark blue to white. Again, in specimens NT8 and NT4 (Figure 3.9(h, j)), a couple of the O sites are displaced along a direction similar to the (010) but not exactly. The sites appeared to be more ordered in the other specimens. While NT25, NT5-50, and NT5-50 4L have less displacement within the sites, they instead have population of O within interstitials and can be distinguish in some of the heatmaps, particularly NT25 (Figure 3.9(i)).

The weberite structure is identical to the fluorite structure when $a/c = \sqrt{2}$ and $c = b$. The lattice parameters along with these two ratios are provided next to the heatmaps in Figure 3.9. All materials are very close to the cubic conditions, but the small deviations are what give rise to the diffuse scattering and weberite short-range ordering. While we do believe this is inherent to the material system and not high-entropy [60], we would like to note that it is unlikely for any high-entropy system to highly-symmetrical cubic system. There should always remain a tendency for short-range ordering and deviations from cubic systems as each atom has slightly different affinities and size [82,87].

Our key finding here is that the presence of larger cations such as Dy and Ho drastically affect the structure of the O sublattice. The smaller cations composed within NT8 and NT4 demonstrate a structure resembling ordered sites, but highly anisotropic displacements (stretched) near the (010) direction. The specimens containing larger cations such as Dy and Ho (NT25, NT5-50, and NT5-50 4L) induce more of isotropically displaced O sublattice but has some O atoms occupying interstitials. We are unsure how this affects the thermal properties. While the structure of the O sublattice seems to be highly dependent on large cations such as Dy and Ho, it does not correlate well the measured thermal conductivity. However, the radius ratio,

$\bar{r}^{3+}/\bar{r}^{5+}$, appears to be a suitable descriptor that possibly accounts for all of these effects in a simple approximation. This is similar to how the radius ratio describing the fluorite-to-pyrochlore transition, r_A^{3+}/r_B^{4+}, embodies the complex phenomenon of anti-site mixing energetics [84]. Inelastic neutron scattering experiments are proposed to obtain the phonon dispersion curves to see how the observed correlated disorder versus random disorder affects phonon broadening.

3.4 CONCLUSION

Overall, 29 (26 new high-entropy) niobates/tantalates were synthesized to further the understanding in this emerging class of ultralow thermal conductivity materials. It was found that the pure niobates appear to have the lowest thermal conductivities and consequently the highest E/k ratios. A promising trend appears when relating the average size of the 3+ cations to Nb and Ta to the room temperature thermal conductivity. A select few of these compositions with varying sizes and thermal conductivities were chosen for further study. The temperature-dependent thermal conductivity confirms the glass-like trend with value approaching or slightly falling below the phonon limit. XRD revealed a long-range order fluorite structure but showed diffuse scattering peaks representative of the orthorhombic weberite structure in the background. Neutron diffraction increased the clarity of these diffuse scattering peaks suggesting they are sensitive to O atoms. The PDFs showed the lowest thermal conductivity specimens (which had the largest cations) were more ordered than the low thermal conductivity specimens with smaller cations. A small-box modeling approach on these PDFs reveal the lower thermal conductivity materials fit much stronger to a weberite structure in the nearest-neighbor region compared to the fluorite structure, but was quickly comparable to the fluorite cell once the fitting window was increased. This picture is consistent with a small weberite domain size approaching the Ioffe-

Regel limit (i.e., phonon limit). A reverse Monte Carlo approach was also tested and fit the PDFs better while also producing a supercell structure. The materials containing Dy and Ho were found to have ordered O sites with isotropic displacement, but also some O occupying forbidden regions. The materials without these elements showing ordered sites with no occupation of interstitials but displayed highly anisotropic displacement within the cation and some anion sites. While the structure is highly correlated on the presence of certain elements, it does not correlate well with the thermal conductivity likely due to the numerous factors affecting the thermal properties. Instead, it is suggested that a simple descriptor, $\bar{r}^{3+}/\bar{r}^{5+}$, may embody all the varying factors into a simple parameter to predict thermal conductivity in this class of materials.

Chapter 3, in full, is currently being prepared for submission. A.J. Wright, Q. Wang, Y.T. Yeh, R. Chen, J. Luo, Origin of the Insulative Property in Rare-Earth Niobates/Tantalates. The dissertation author was the primary investigator and author of this paper.

Table 3.1. The thermomechanical properties of each high-entropy (although a few are low-entropy) niobate/tantalate synthesized in this study sorted from smallest $\bar{r}^{3+}/\bar{r}^{5+}$ to highest. * denotes specimens explorer further using neutron diffraction.

Identifier	Composition	$\bar{r}^{3+}/\bar{r}^{5+}$	$k_{RT}\left(\frac{W}{m\cdot K}\right)$	E_{RT} (GPa)	E/k $(GPa\ m\ K\ W^{-1})$
NT8*	$(Sc_{0.25}Yb_{0.25}Lu_{0.25}Nb_{0.25})_4O_7$	1.281	1.28 ± 0.04	225.2 ± 2.3	176.3 ± 2.6
NT20	$(Sc_{0.168}Er_{0.234}Tm_{0.183}Yb_{0.165}Nb_{0.25})_4O_7$	1.316	1.24 ± 0.02	211.4 ± 1.9	170.7 ± 2.8
NT21	$(Sc_{0.2}Dy_{0.186}Tm_{0.185}Yb_{0.18}Nb_{0.25})_4O_7$	1.316	1.24 ± 0.02	214.1 ± 1.9	172.1 ± 2.6
NT24	$(Sc_{0.185}Dy_{0.21}Er_{0.182}Yb_{0.173}Nb_{0.25})_4O_7$	1.324	1.21 ± 0.05	217.9 ± 1.8	179.9 ± 2.9
NT25*	$(Sc_{0.165}Dy_{0.191}Ho_{0.197}Tm_{0.197}Nb_{0.25})_4O_7$	1.337	1.21 ± 0.03	217.8 ± 1.7	180.4 ± 3.2
NT10-2A	$(Er_{0.245}Tm_{0.245}Yb_{0.245}Al_{0.02}Ta_{0.245})_4O_7$	1.343	1.18 ± 0.04	209.0 ± 2.7	179.6 ± 3.4
NT10-2M	$(Er_{0.245}Tm_{0.245}Yb_{0.245}Mg_{0.02}Ta_{0.245})_4O_7$	1.347	1.20 ± 0.04	207.4 ± 2.7	177.6 ± 3.0
NT26	$(Sc_{0.15}Dy_{0.279}Ho_{0.171}Er_{0.15}Nb_{0.25})_4O_7$	1.347	1.16 ± 0.03	222.9 ± 1.9	191.4 ± 3.2
NT4*	$(Er_{0.25}Tm_{0.25}Yb_{0.25}Nb_{0.25})_4O_7$	1.356	1.15 ± 0.04	217.9 ± 2.5	190.1 ± 3.2
NT10	$(Er_{0.25}Tm_{0.25}Yb_{0.25}Ta_{0.25})_4O_7$	1.356	1.22 ± 0.04	226.5 ± 3.1	185.4 ± 3.4
NT6	$(Y_{0.25}Tm_{0.25}Yb_{0.25}Nb_{0.25})_4O_7$	1.363	1.19 ± 0.04	215.6 ± 2.5	180.8 ± 2.9
NT10-2C	$(Er_{0.245}Tm_{0.245}Yb_{0.245}Ca_{0.02}Ta_{0.245})_4O_7$	1.365	1.15 ± 0.03	204.1 ± 2.3	182.7 ± 2.8
NT2	$(Dy_{0.25}Er_{0.25}Yb_{0.25}Nb_{0.125}Ta_{0.125})_4O_7$	1.372	1.10 ± 0.03	223.9 ± 2.7	202.8 ± 3.3
NT5	$(Dy_{0.25}Ho_{0.25}Er_{0.25}Nb_{0.25})_4O_7$	1.388	1.09 ± 0.03	214.2 ± 2.4	196.0 ± 3.9
NT5-25	$(Dy_{0.25}Ho_{0.25}Er_{0.25}Nb_{0.188}Ta_{0.063})_4O_7$	1.388	1.11 ± 0.01	202.9 ± 2.2	182.4 ± 3.0
NT5-100	$(Dy_{0.25}Ho_{0.25}Er_{0.25}Ta_{0.25})_4O_7$	1.388	1.21 ± 0.01	222.4 ± 3.5	183.9 ± 3.4
NT5-75	$(Dy_{0.25}Ho_{0.25}Er_{0.25}Nb_{0.063}Ta_{0.188})_4O_7$	1.388	1.19 ± 0.01	224.2 ± 3.1	187.8 ± 3.2
NT5-50*	$(Dy_{0.25}Ho_{0.25}Er_{0.25}Nb_{0.125}Ta_{0.125})_4O_7$	1.388	1.12 ± 0.01	207.6 ± 2.7	184.8 ± 3.0
NT1	$(Y_{0.25}Dy_{0.25}Er_{0.25}Nb_{0.125}Ta_{0.125})_4O_7$	1.389	1.11 ± 0.03	226.5 ± 2.6	204.1 ± 3.1
NT5-50 2L	$(Dy_{0.245}Ho_{0.245}Er_{0.245}La_{0.02}Nb_{0.123}Ta_{0.123})_4O_7$	1.393	1.09 ± 0.01	222.7 ± 2.7	204.6 ± 3.3
NT3	$(Y_{0.25}Dy_{0.25}Ho_{0.25}Nb_{0.25})_4O_7$	1.395	1.14 ± 0.03	208.8 ± 2.2	182.7 ± 2.8
NT5-50 4L*	$(Dy_{0.24}Ho_{0.24}Er_{0.24}La_{0.04}Nb_{0.12}Ta_{10.12})_4O_7$	1.399	1.06 ± 0.01	220.6 ± 2.5	209.0 ± 3.4
NT32	$(Y_{0.143}Dy_{0.587}Ho_{0.02}Nb_{0.143}Ta_{0.107})_4O_7$	1.403	1.15 ± 0.06	226.7 ± 3.0	196.4 ± 3.4
NT5-50 6L	$(Dy_{0.235}Ho_{0.235}Er_{0.235}La_{0.06}Nb_{0.118}Ta_{0.118})_4O_7$	1.404	1.10 ± 0.01	218.9 ± 3.0	198.6 ± 3.7
NT0-0	$(Dy_{0.75}Nb_{0.25})_4O_7$	1.406	1.10 ± 0.03	201.8 ± 2.2	183.8 ± 2.8
NT0-25	$(Dy_{0.75}Nb_{0.188}Ta_{0.063})_4O_7$	1.406	1.11 ± 0.01	209.4 ± 2.4	188.4 ± 3.0
NT0-50	$(Dy_{0.75}Nb_{0.125}Ta_{0.125})_4O_7$	1.406	1.10 ± 0.01	207.6 ± 2.3	189.1 ± 2.9
NT5-50 8L	$(Dy_{0.23}Ho_{0.23}Er_{0.23}La_{0.08}Nb_{0.115}Ta_{0.115})_4O_7$	1.409	1.12 ± 0.01	201.3 ± 2.2	179.3 ± 2.7
NT5-50 10L	$(Dy_{0.225}Ho_{0.225}Er_{0.225}La_{0.1}Nb_{0.113}Ta_{0.113})_4O_7$	1.415	1.12 ± 0.01	208.8 ± 2.6	187.1 ± 3.0

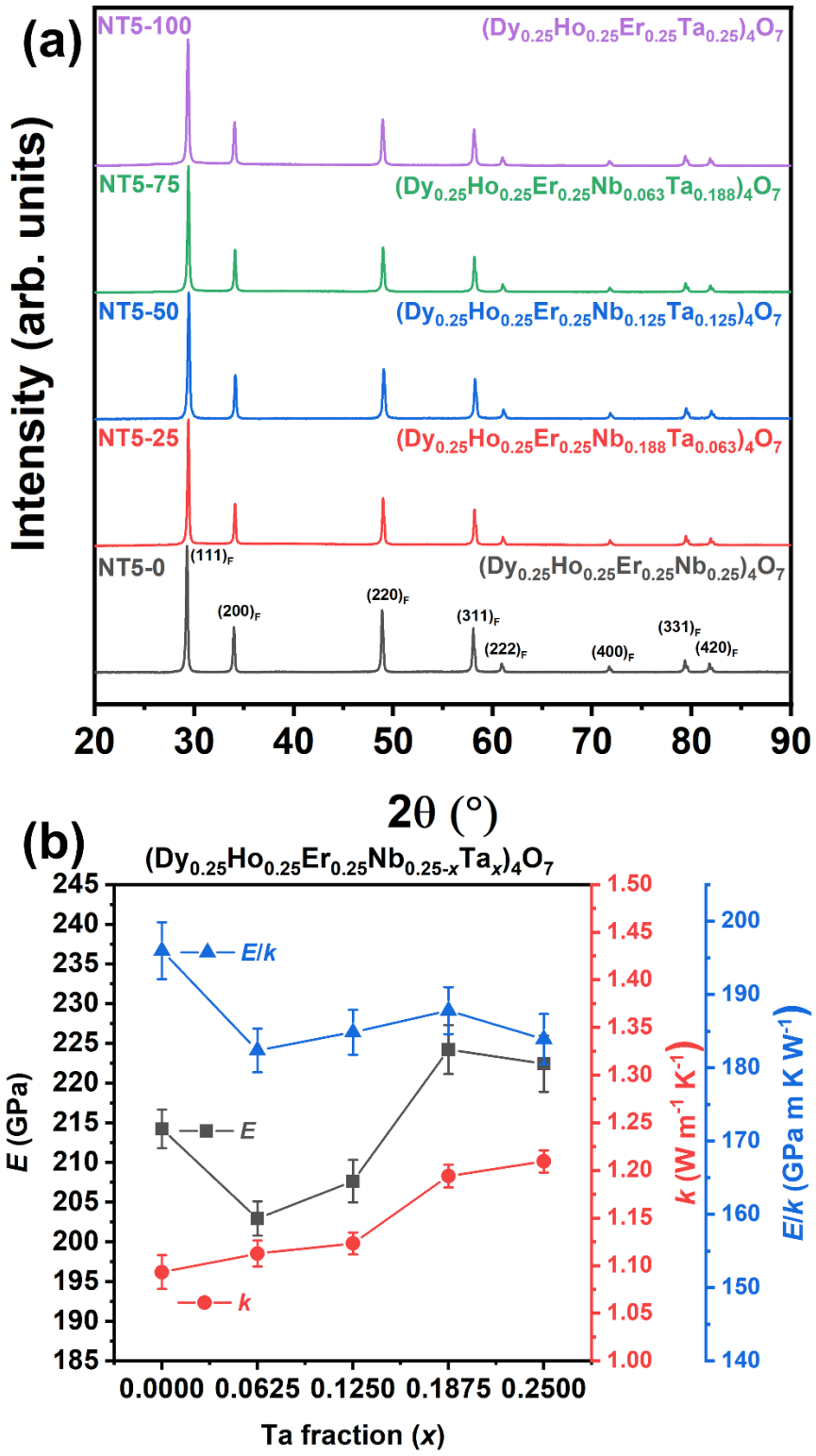

Figure 3.1. **(a)** XRD pattern evolution from $(Dy_{0.25}Er_{0.25}Ho_{0.25}Nb_{0.25})_4O_7$ to $(Dy_{0.25}Er_{0.25}Ho_{0.25}Ta_{0.25})_4O_7$. **(b)** The Young's modulus (E), thermal conductivity (k), and E/k ratio for $(Dy_{0.25}Er_{0.25}Ho_{0.25}Nb_{0.25-x}Ta_x)_4O_7$ series.

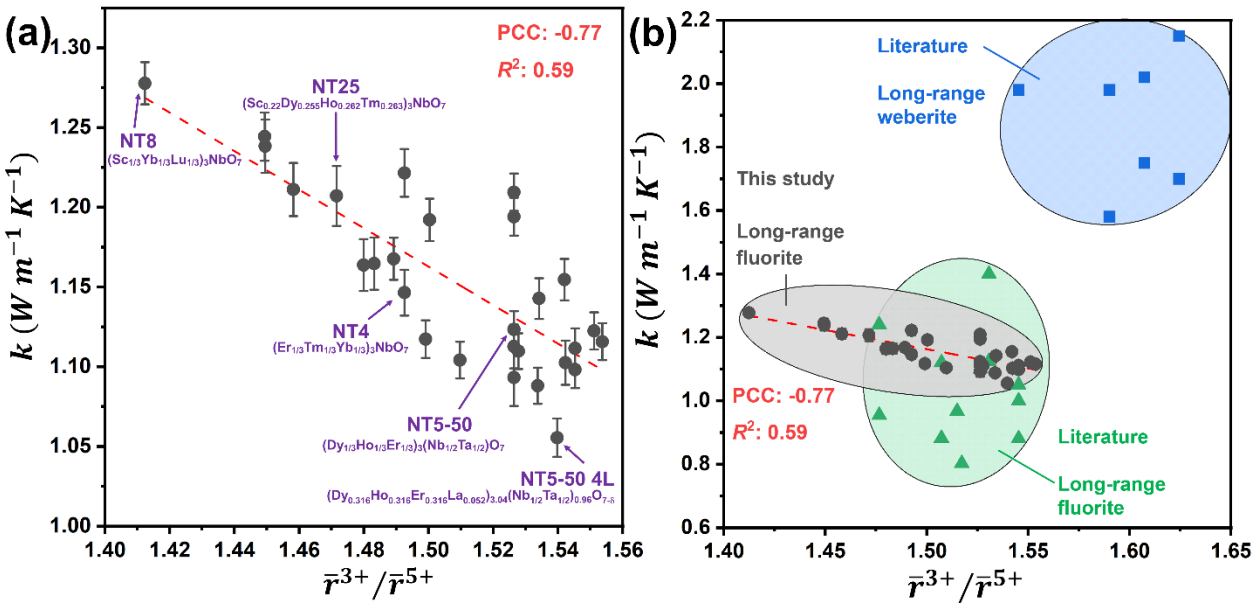

Figure 3.2. (a) Room temperature thermal conductivity trend regarding the radius ratio of the 3+ cations to the 5+ cations. The highlighted specimens were selected for further study. **(b)** Data in panel (A) expanded to include data of long-range fluorite and weberite structures from Refs. [52,67-70].

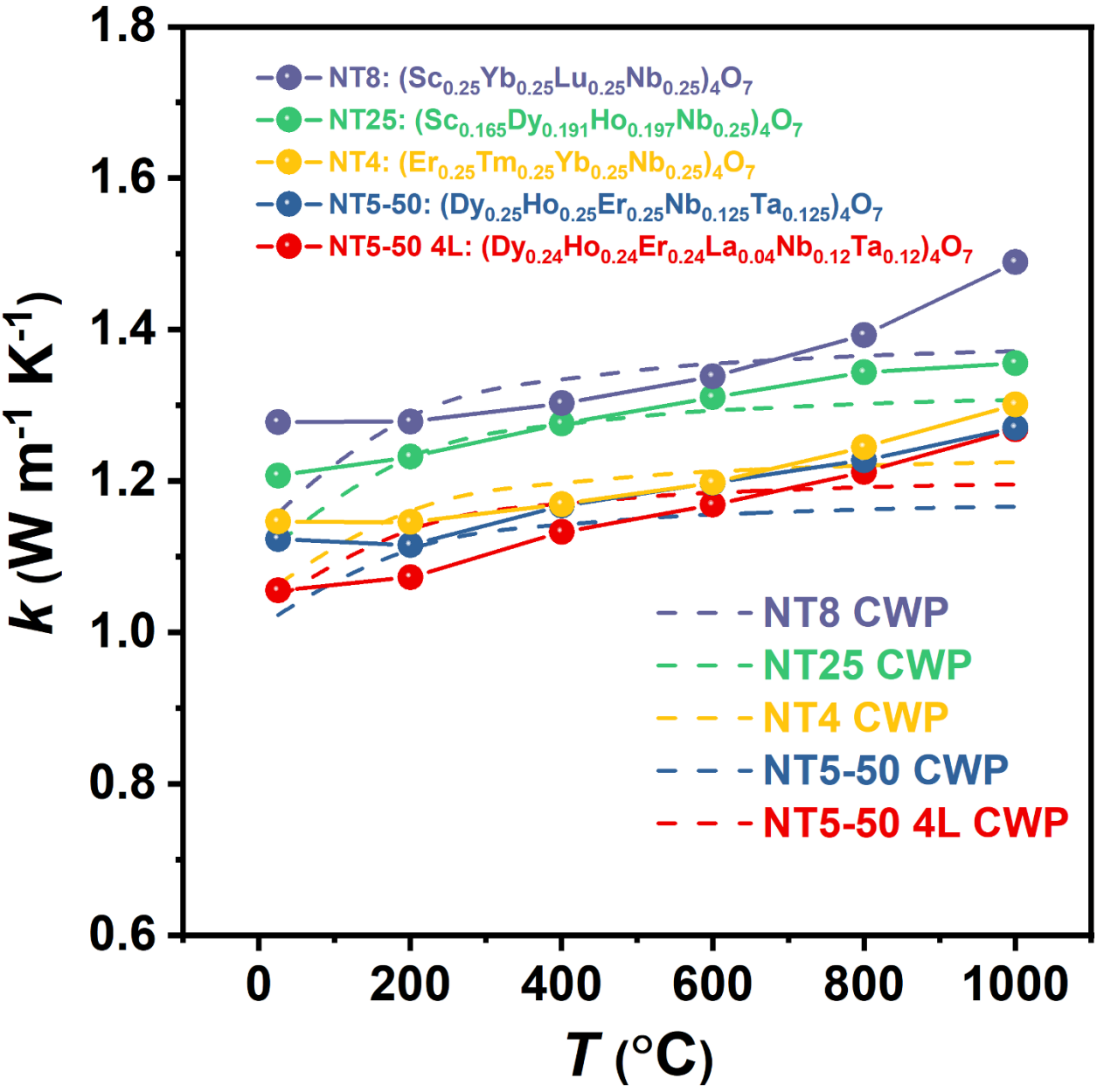

Figure 3.3. (a) Temperature-dependent thermal conductivity of NT8, NT25, NT4, NT5-50, and NT5-50 4L from room temperature to 1000℃. The phonon limit as described by Cahill, Watson, Pohl is shown as a dashed line [75].

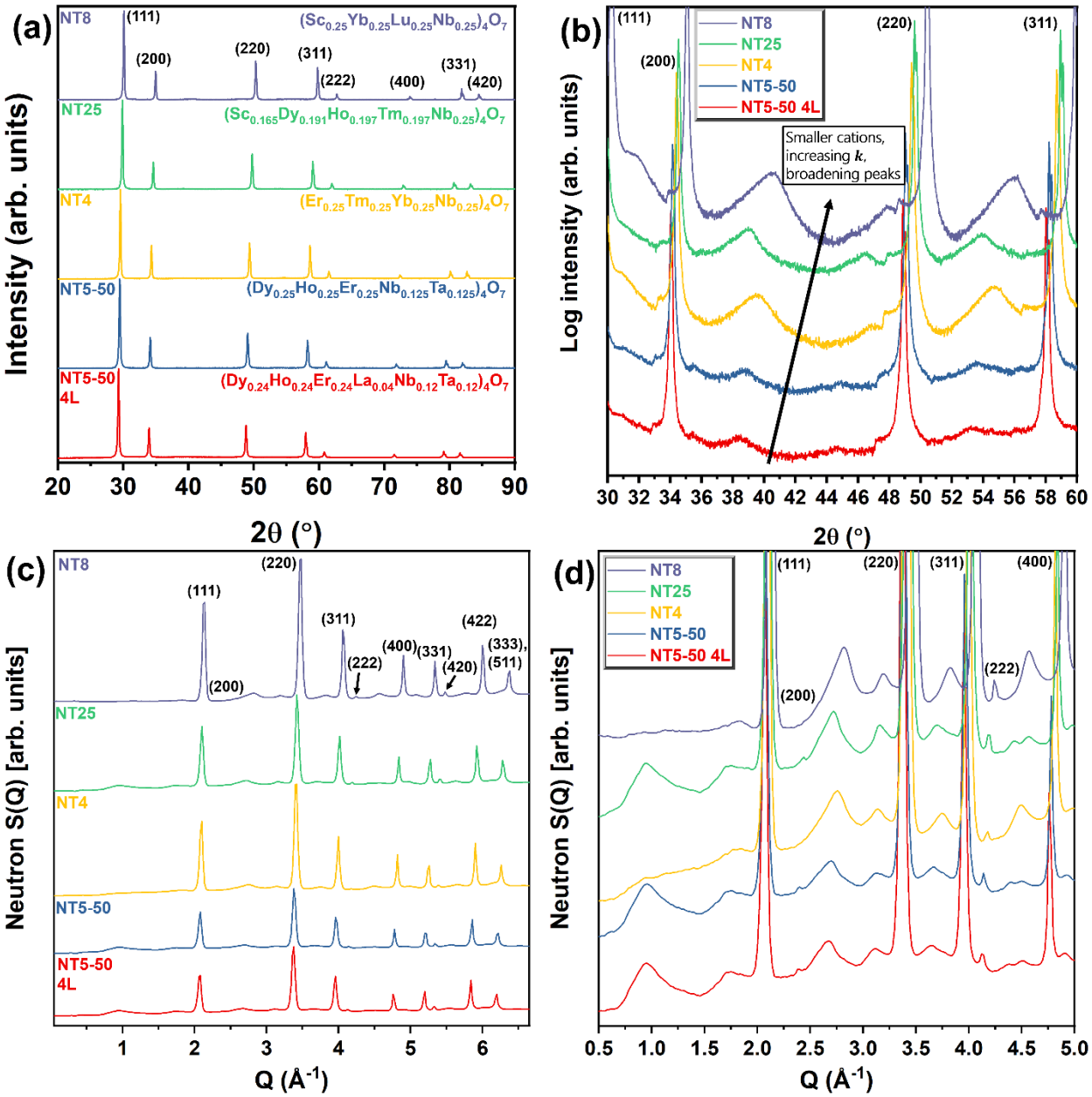

Figure 3.4. Benchtop X-ray diffraction patterns of each specimen on a **(a)** linear intensity scale and **(b)** a close-up of diffuse scattering present on a logarithmic intensity scale. specimen **(c)** Neutron diffraction total scattering patterns of each specimen and **(d)** the diffuse scattering at higher magnification.

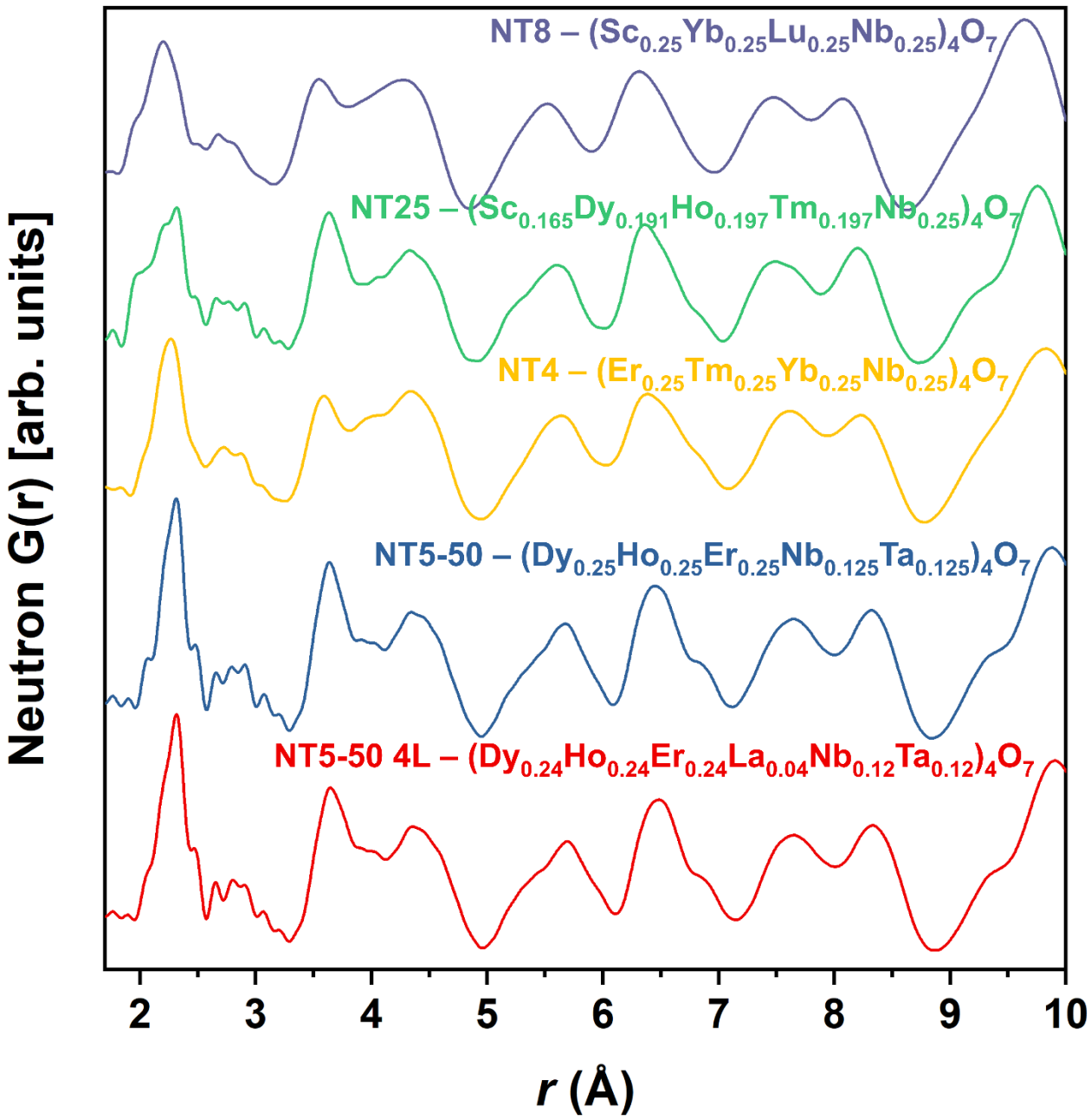

Figure 3.5. The partial distribution functions (PDFs, $G(r)$) of each specimen up to 10 Å.

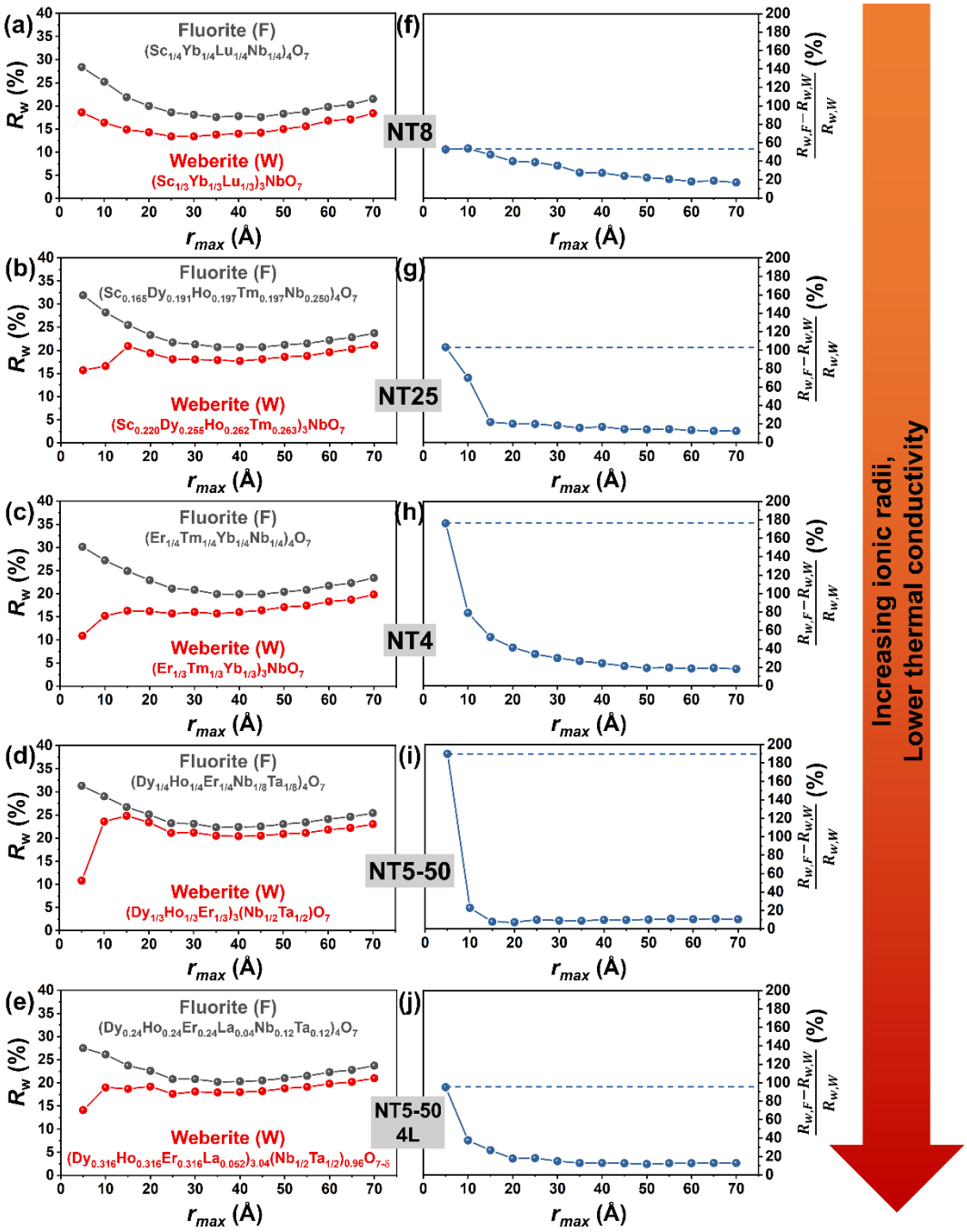

Figure 3.6. (a-e) The fitting parameter R_w based on the upper bound of the fitting window for both the fluorite and weberite structures. The fitting began from $0.02 - 70$ Å and then was decreased in 5 Å steps to $0.02 - 5$ Å. After each step, the converged parameters from the previous step was used as the initial guess. **(f-j)** Percent difference between the fluorite and weberite R_w factors. A stronger fit is found for the lower thermal conductivity specimens while also showing a steeper decline suggesting a smaller domain size for the weberite structure.

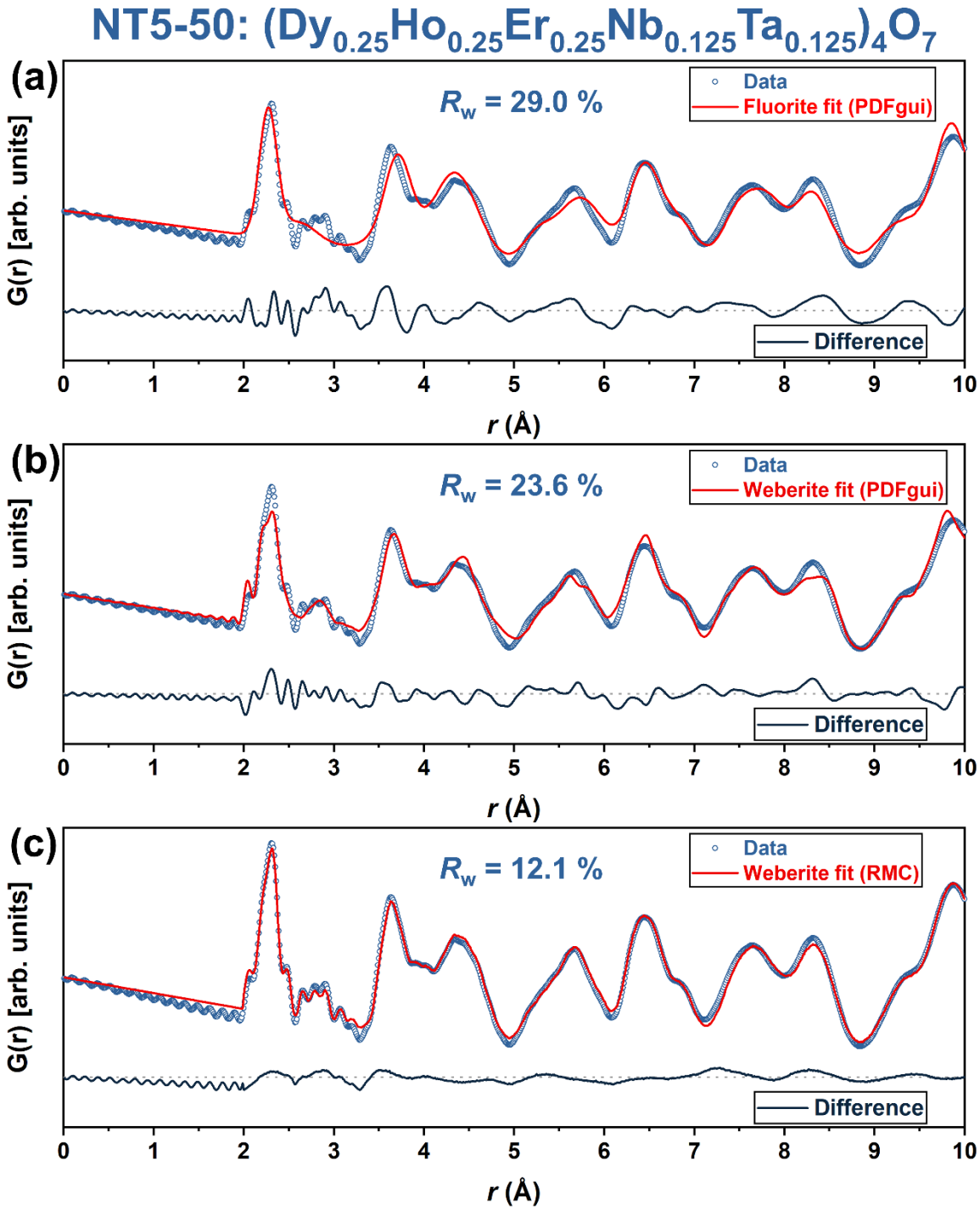

Figure 3.7. The fitting and difference curve up to 10 Å of NT5-50 ($(Dy_{0.25}Er_{0.25}Ho_{0.25}Nb_{0.125}Ta_{0.125})_4O_7$) using a **(a)** fluorite and **(b)** weberite structure within the PDFgui software [57]. **(c)** The reverse Monte Carlo fitting results under the same conditions achieved with RMCprofile [59].

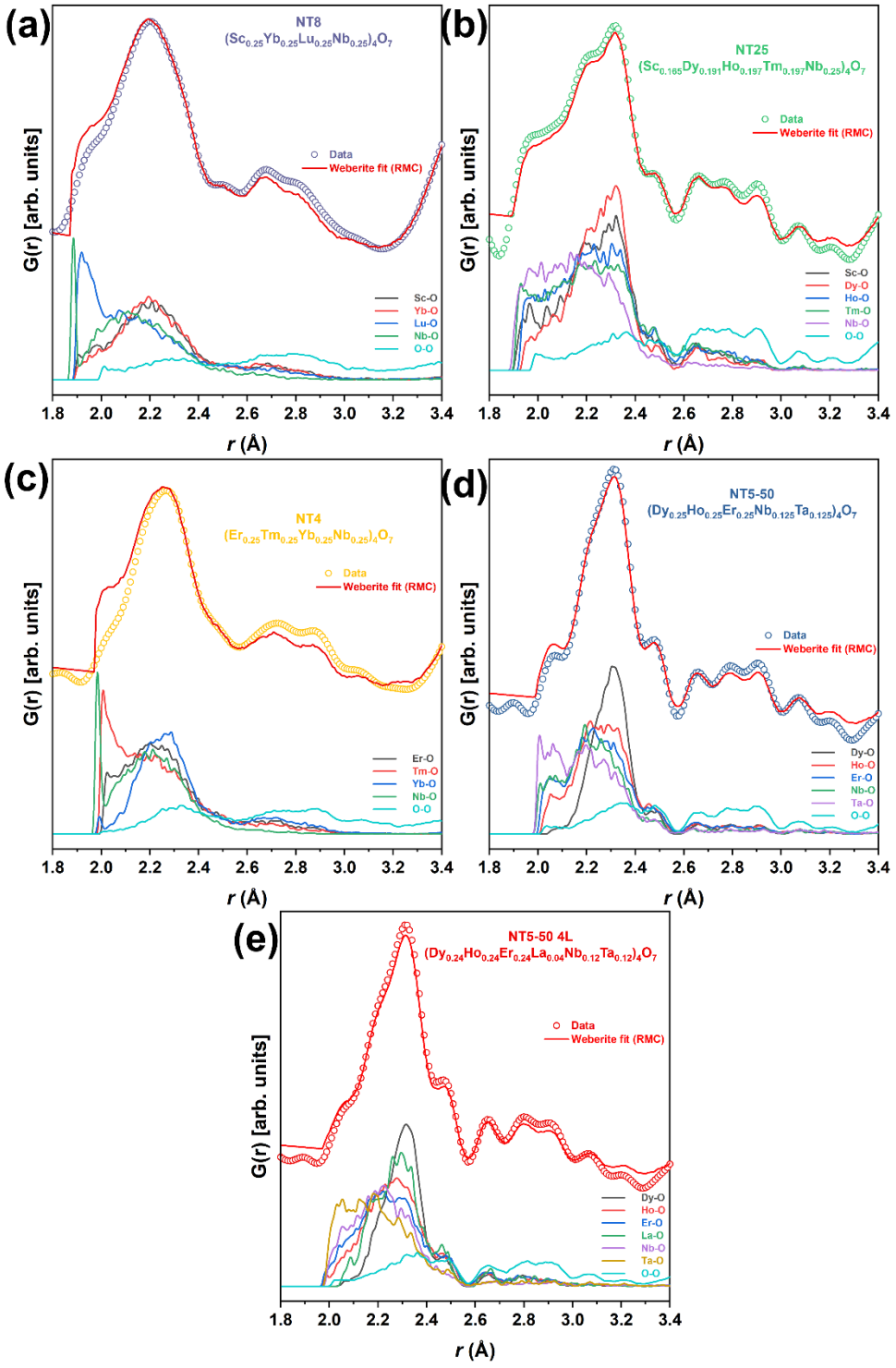

Figure 3.8. The fitting and the partial $G_{ij}(r)$ for each bonded pair and O-O of **(a)** NT8, **(b)** NT25, **(c)** NT4, **(d)** NT5-50, and **(e)** NT5-50 4L. All the specimens with Dy and Ho (NT25, NT5-50, and NT5-50) were found to have a stronger affinity for O ordering discernible by the sharper O-O interactions compared to NT8 and NT4.

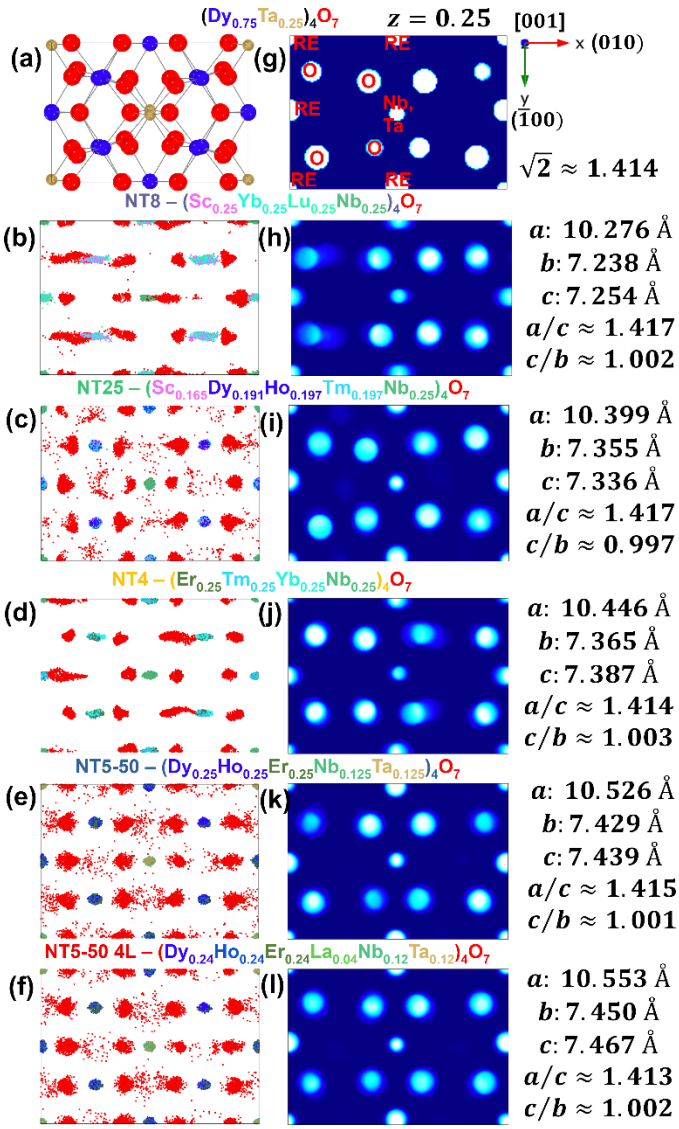

Figure 3.9. (a) Structural template (Dy_3TaO_7) of the weberite looking down the [001] plane. The collapsed unit cell of the converged reverse Monte Carlo simulation for **(b)** NT8, **(c)** NT25, **(d)** NT4, **(e)** NT5-50, and **(f)** NT5-50 4L in the [001] viewing direction. **(g)** Atomic density of Dy_3TaO_7 looking down the [001] plane at $z = 0.25$. **(h-l)** The atomic density heatmap of each specimen in the [001] viewing direction where $z = 0.25$ along with the converged lattice parameters. The compositions containing the larger Dy and Ho cations (NT25, NT5-50, and NT5-50 4L) have a more ordered O sublattice with some O atoms occupying interstitials while the compositions in absence of these larger cations shown stretched cation and anion positions in the (010) direction. The presence of large cations drastically affects the O sublattice but does not correlate well with the measured thermal conductivity.

3.5 REFERENCES

[1] C. Oses, C. Toher, S. Curtarolo, High-entropy ceramics, Nat. Rev. Mater. (2020) 1–15. doi:10.1038/s41578-019-0170-8.

[2] R.-Z. Zhang, M.J. Reece, Review of high entropy ceramics: design, synthesis, structure and properties, J. Mater. Chem. A. 7 (2019) 22148–22162. doi:10.1039/C9TA05698J.

[3] A. Sarkar, Q. Wang, A. Schiele, M.R. Chellali, S.S. Bhattacharya, D. Wang, T. Brezesinski, H. Hahn, L. Velasco, B. Breitung, High-entropy oxides: Fundamental aspects and electrochemical properties, Adv. Mater. 31 (2019) 1806236. doi:10.1002/adma.201806236.

[4] A.J. Wright, J. Luo, A step forward from high-entropy ceramics to compositionally complex ceramics: a new perspective, J. Mater. Sci. (2020) 1–16. doi:10.1007/s10853-020-04583-w.

[5] J. Gild, Y. Zhang, T. Harrington, S. Jiang, T. Hu, M.C. Quinn, W.M. Mellor, N. Zhou, K. Vecchio, J. Luo, High-entropy metal diborides: A new class of high-entropy materials and a new type of ultrahigh temperature ceramics, Sci. Rep. 6 (2016) 37946. doi:10.1038/srep37946.

[6] Y. Zhang, Z. Bin Jiang, S.K. Sun, W.M. Guo, Q.S. Chen, J.X. Qiu, K. Plucknett, H.T. Lin, Microstructure and mechanical properties of high-entropy borides derived from boro/carbothermal reduction, J. Eur. Ceram. Soc. 39 (2019) 3920–3924. doi:10.1016/j.jeurceramsoc.2019.05.017.

[7] Y. Zhang, W.M. Guo, Z. Bin Jiang, Q.Q. Zhu, S.K. Sun, Y. You, K. Plucknett, H.T. Lin, Dense high-entropy boride ceramics with ultra-high hardness, Scr. Mater. 164 (2019) 135–139. doi:10.1016/j.scriptamat.2019.01.021.

[8] J. Gild, K. Kaufmann, K. Vecchio, J. Luo, Reactive flash spark plasma sintering of high-entropy ultrahigh temperature ceramics, Scr. Mater. 170 (2019) 106–110. doi:10.1016/j.scriptamat.2019.05.039.

[9] J. Zhou, J. Zhang, F. Zhang, B. Niu, L. Lei, W. Wang, High-entropy carbide: A novel class of multicomponent ceramics, Ceram. Int. 44 (2018) 22014–22018. doi:10.1016/j.ceramint.2018.08.100.

[10] X. Han, V. Girman, R. Sedlák, J. Dusza, E.G. Castle, Y. Wang, M. Reece, C. Zhang, Improved creep resistance of high entropy transition metal carbides, J. Eur. Ceram. Soc. (2019).

[11] T.J. Harrington, J. Gild, P. Sarker, C. Toher, C.M. Rost, O.F. Dippo, C. McElfresh, K. Kaufmann, E. Marin, L. Borowski, P.E. Hopkins, J. Luo, S. Curtarolo, D.W. Brenner, K.S. Vecchio, Phase stability and mechanical properties of novel high entropy transition metal carbides, Acta Mater. 166 (2019) 271–280. doi:10.1016/j.actamat.2018.12.054.

[12] X. Yan, L. Constantin, Y. Lu, J.F. Silvain, M. Nastasi, B. Cui, (Hf0.2Zr0.2Ta0.2Nb0.2Ti0.2)C high-entropy ceramics with low thermal conductivity, J. Am. Ceram. Soc. 101 (2018) 4486–4491. doi:10.1111/jace.15779.

[13] E. Castle, T. Csanádi, S. Grasso, J. Dusza, M. Reece, Processing and properties of high-entropy ultra-high temperature carbides, Sci. Rep. 8 (2018) 8609. doi:10.1038/s41598-018-26827-1.

[14] C.M. Rost, Z. Rak, D.W. Brenner, J.P. Maria, Local structure of the MgxNixCoxCuxZnxO(x=0.2) entropy-stabilized oxide: An EXAFS study, J. Am. Ceram. Soc. 100 (2017) 2732–2738. doi:10.1111/jace.14756.

[15] C.M. Rost, E. Sachet, T. Borman, A. Moballegh, E.C. Dickey, D. Hou, J.L. Jones, S. Curtarolo, J.P. Maria, Entropy-stabilized oxides, Nat. Commun. 6 (2015) 1–8. doi:10.1038/ncomms9485.

[16] D. Bérardan, S. Franger, D. Dragoe, A.K. Meena, N. Dragoe, Colossal dielectric constant in high entropy oxides, Phys. Status Solidi - Rapid Res. Lett. 10 (2016) 328–333. doi:10.1002/pssr.201600043.

[17] K. Chen, X. Pei, L. Tang, H. Cheng, Z. Li, C. Li, X. Zhang, L. An, A five-component entropy-stabilized fluorite oxide, J. Eur. Ceram. Soc. 38 (2018) 4161–4164. doi:10.1016/j.jeurceramsoc.2018.04.063.

[18] J. Gild, M. Samiee, J.L. Braun, T. Harrington, H. Vega, P.E. Hopkins, K. Vecchio, J. Luo, High-entropy fluorite oxides, J. Eur. Ceram. Soc. 38 (2018) 3578–3584. doi:10.1016/j.jeurceramsoc.2018.04.010.

[19] A.J. Wright, Q. Wang, C. Huang, A. Nieto, R. Chen, J. Luo, From high-entropy ceramics to compositionally-complex ceramics: A case study of fluorite oxides, J. Eur. Ceram. Soc. 40 (2020) 2120–2129. doi:10.1016/j.jeurceramsoc.2020.01.015.

[20] Z. Zhao, H. Chen, H. Xiang, F.Z. Dai, X. Wang, W. Xu, K. Sun, Z. Peng, Y. Zhou, High entropy defective fluorite structured rare-earth niobates and tantalates for thermal barrier applications, J. Adv. Ceram. 9 (2020) 303–311. doi:10.1007/s40145-020-0368-7.

[21] R. Djenadic, A. Sarkar, O. Clemens, C. Loho, M. Botros, V.S.K. Chakravadhanula, C. Kübel, S.S. Bhattacharya, A.S. Gandhi, H. Hahn, Multicomponent equiatomic rare earth oxides, Mater. Res. Lett. 5 (2017) 102–109. doi:10.1080/21663831.2016.1220433.

[22] A. Sarkar, C. Loho, L. Velasco, T. Thomas, S.S. Bhattacharya, H. Hahn, R. Djenadic, Multicomponent equiatomic rare earth oxides with a narrow band gap and associated praseodymium multivalency, Dalt. Trans. 46 (2017) 12167–12176. doi:10.1039/c7dt02077e.

[23] C. Heng, X. Huimin, D. Fu-Zhi, L. Jiachen, Z. Yanchun, High entropy (Yb0.25Y0.25Lu0.25Er0.25)2SiO5 with strong anisotropy in thermal expansion, J. Mater. Sci. Technol. (2019). doi:10.1016/j.jmst.2019.07.022.

[24] X. Ren, Z. Tian, J. Zhang, J. Wang, Equiatomic quaternary (Y1/4Ho1/4Er1/4Yb1/4)2SiO5 silicate: A perspective multifunctional thermal and environmental barrier coating material, Scr. Mater. 168 (2019) 47–50. doi:10.1016/j.scriptamat.2019.04.018.

[25] Y. Dong, K. Ren, Y. Lu, Q. Wang, J. Liu, Y. Wang, High-entropy environmental barrier coating for the ceramic matrix composites, J. Eur. Ceram. Soc. 39 (2019) 2574–2579. doi:10.1016/j.jeurceramsoc.2019.02.022.

[26] L. Sun, Y. Luo, X. Ren, Z. Gao, T. Du, Z. Wu, J. Wang, A multicomponent γ-type (Gd1/6Tb1/6Dy1/6Tm1/6Yb1/6Lu1/6)2Si2O7 disilicate with outstanding thermal stability, Mater. Res. Lett. 8 (2020) 424–430. doi:10.1080/21663831.2020.1783007.

[27] J. Gild, J. Braun, K. Kaufmann, E. Marin, T. Harrington, P. Hopkins, K. Vecchio, J. Luo, A high-entropy silicide: (Mo0.2Nb0.2Ta0.2Ti0.2W0.2)Si2, J. Mater. 5 (2019) 337–343. doi:10.1016/j.jmat.2019.03.002.

[28] Y. Qin, J.X. Liu, F. Li, X. Wei, H. Wu, G.J. Zhang, A high entropy silicide by reactive spark plasma sintering, J. Adv. Ceram. 8 (2019) 148–152. doi:10.1007/s40145-019-0319-3.

[29] Y. Qin, J.-C. Wang, J.-X. Liu, X.-F. Wei, F. Li, G.-J. Zhang, C. Jing, J. Zhao, H. Wu, High-entropy silicide ceramics developed from (TiZrNbMoW)Si2 formulation doped with aluminum, J. Eur. Ceram. Soc. (2020). doi:10.1016/j.jeurceramsoc.2020.02.059.

[30] N. Zhou, S. Jiang, T. Huang, M. Qin, T. Hu, J. Luo, Single-phase high-entropy intermetallic compounds (HEICs): bridging high-entropy alloys and ceramics, Sci. Bull. 64 (2019) 856–864. doi:10.1016/j.scib.2019.05.007.

[31] X. Chen, Y. Wu, High-entropy transparent fluoride laser ceramics, J. Am. Ceram. Soc. 103 (2019) 750–756. doi:10.1111/jace.16842.

[32] T. Wang, H. Chen, Z. Yang, J. Liang, S. Dai, High-entropy perovskite fluorides: A new platform for oxygen evolution catalysis, J. Am. Chem. Soc. (2020). doi:10.1021/jacs.9b12377.

[33] Z. Zhao, H. Chen, H. Xiang, F.Z. Dai, X. Wang, Z. Peng, Y. Zhou, (La0.2Ce0.2Nd0.2Sm0.2Eu0.2)PO4: A high-entropy rare-earth phosphate monazite ceramic with low thermal conductivity and good compatibility with Al2O3, J. Mater. Sci. Technol. 35 (2019) 2892–2896. doi:10.1016/j.jmst.2019.08.012.

[34] Z. Zhao, H. Xiang, F.Z. Dai, Z. Peng, Y. Zhou, (TiZrHf)P2O7: An equimolar multicomponent or high entropy ceramic with good thermal stability and low thermal conductivity, J. Mater. Sci. Technol. 35 (2019) 2227–2231. doi:10.1016/j.jmst.2019.05.030.

[35] N. Qiu, H. Chen, Z. Yang, S. Sun, Y. Wang, Y. Cui, A high entropy oxide (Mg0.2Co0.2Ni0.2Cu0.2Zn0.2O) with superior lithium storage performance, J. Alloys Compd. 777 (2019) 767–774. doi:10.1016/j.jallcom.2018.11.049.

[36] Q. Wang, A. Sarkar, Z. Li, Y. Lu, L. Velasco, S.S. Bhattacharya, T. Brezesinski, H. Hahn, B. Breitung, High entropy oxides as anode material for Li-ion battery applications: A practical approach, Electrochem. Commun. 100 (2019) 121–125. doi:10.1016/j.elecom.2019.02.001.

[37] A. Sarkar, L. Velasco, D. Wang, Q. Wang, G. Talasila, L. de Biasi, C. Kübel, T. Brezesinski, S.S. Bhattacharya, H. Hahn, B. Breitung, High entropy oxides for reversible energy storage, Nat. Commun. 9 (2018) 3400. doi:10.1038/s41467-018-05774-5.

[38] B. Breitung, Q. Wang, A. Schiele, Đ. Tripković, A. Sarkar, L. Velasco, D. Wang, S.S. Bhattacharya, H. Hahn, Breze, Gassing behavior of high-entropy oxide anode and oxyfluoride cathode probed using differential electrochemical mass spectrometry, Batter. Supercaps. (n.d.). doi:10.1002/batt.202000010.

[39] A.G. de la Obra, M.A. Avilés, Y. Torres, E. Chicardi, F.J. Gotor, A new family of cermets: Chemically complex but microstructurally simple, Int. J. Refract. Met. Hard Mater. 63 (2017) 17–25. doi:10.1016/j.ijrmhm.2016.04.011.

[40] J. Gild, A. Wright, K. Quiambao-tomko, M. Qin, A. John, S. Hoque, J.L. Braun, B. Bloomfield, D. Martinez, T. Harrington, K. Vecchio, P.E. Hopkins, J. Luo, Thermal conductivity and hardness of three single-phase high-entropy metal diborides fabricated by borocarbothermal reduction and spark plasma sintering, Ceram. Int. (2019). doi:10.1016/j.ceramint.2019.11.186.

[41] H. Zhang, D. Hedman, P. Feng, G. Han, F. Akhtar, A high-entropy B4(HfMo2TaTi)C and SiC ceramic composite, Dalt. Trans. 48 (2019) 5161–5167. doi:10.1039/c8dt04555k.

[42] P. Sarker, T. Harrington, C. Toher, C. Oses, M. Samiee, J.P. Maria, D.W. Brenner, K.S. Vecchio, S. Curtarolo, High-entropy high-hardness metal carbides discovered by entropy descriptors, Nat. Commun. 9 (2018) 1–10. doi:10.1038/s41467-018-07160-7.

[43] R. Liu, H. Chen, K. Zhao, Y. Qin, B. Jiang, T. Zhang, G. Sha, X. Shi, C. Uher, W. Zhang, L. Chen, Entropy as a gene-like performance indicator promoting thermoelectric materials, Adv. Mater. 29 (2017) 1702712. doi:10.1002/adma.201702712.

[44] K. Kaufmann, D. Maryanovsky, W.M. Mellor, C. Zhu, A.S. Rosengarten, T.J. Harrington, C. Oses, C. Toher, S. Curtarolo, K.S. Vecchio, Discovery of high-entropy ceramics via machine learning, Npj Comput. Mater. 6 (2020) 42. doi:10.1038/s41524-020-0317-6.

[45] A. Giri, J.L. Braun, P.E. Hopkins, Reduced dependence of thermal conductivity on temperature and pressure of multi-atom component crystalline solid solutions, J. Appl. Phys. 123 (2018) 015106. doi:10.1063/1.5010337.

[46] A. Giri, J.L. Braun, C.M. Rost, P.E. Hopkins, On the minimum limit to thermal conductivity of multi-atom component crystalline solid solutions based on impurity mass scattering, Scr. Mater. 138 (2017) 134–138. doi:10.1016/j.scriptamat.2017.05.045.

[47] K. Ren, Q. Wang, G. Shao, X. Zhao, Y. Wang, Multicomponent high-entropy zirconates with comprehensive properties for advanced thermal barrier coating, Scr. Mater. 178 (2020) 382–386. doi:10.1016/j.scriptamat.2019.12.006.

[48] A.J. Wright, Q. Wang, S.T. Ko, K.M. Chung, R. Chen, J. Luo, Size disorder as a descriptor for predicting reduced thermal conductivity in medium- and high-entropy pyrochlore oxides, Scr. Mater. 181 (2020) 76–81. doi:10.1016/j.scriptamat.2020.02.011.

[49] J.L. Braun, C.M. Rost, M. Lim, A. Giri, D.H. Olson, G.N. Kotsonis, G. Stan, D.W. Brenner, J.P. Maria, P.E. Hopkins, Charge-induced disorder controls the thermal conductivity of entropy-stabilized oxides, Adv. Mater. 30 (2018) 1805004. doi:10.1002/adma.201805004.

[50] H. Chen, Z. Zhao, H. Xiang, F.-Z. Dai, W. Xu, K. Sun, J. Liu, Y. Zhou, High entropy (Y0.2Yb0.2Lu0.2Eu0.2Er0.2)3Al5O12: a novel high temperature stable thermal barrier material, J. Mater. Sci. Technol. (2020). doi:10.1016/j.jmst.2020.01.056.

[51] Z. Zhao, H. Xiang, F.-Z. Dai, Z. Peng, Y. Zhou, (La0.2Ce0.2Nd0.2Sm0.2Eu0.2)2Zr2O7: A novel high-entropy ceramic with low thermal conductivity and sluggish grain growth rate, J. Mater. Sci. Technol. 35 (2019) 2647–2651. doi:10.1016/j.jmst.2019.05.054.

[52] J. Yang, X. Qian, W. Pan, R. Yang, Z. Li, Y. Han, M. Zhao, M. Huang, C. Wan, Diffused lattice vibration and ultralow thermal conductivity in the binary Ln–Nb–O oxide system, Adv. Mater. 31 (2019) 1808222. doi:10.1002/adma.201808222.

[53] ASTM International, C373-18 Standard Test Methods for Determination of Water Absorption and Associated Properties by Vacuum Method for Pressed Ceramic Tiles and Glass Tiles and Boil Method for Extruded Ceramic Tiles and Non-tile Fired Ceramic Whiteware Products, West Conshohocken, PA, 2018. doi:10.1520/C0373-16.2.

[54] I. Barin, Thermochemical Data of Pure Substances, VCH, Weinheim, 1995. doi:10.1016/s0165-2427(96)05632-2.

[55] E.A. Dean, J.A. Lopez, Empirical dependence of elastic moduli on porosity for ceramic materials, J. Am. Ceram. Soc. 66 (1983) 366–370. doi:10.1111/j.1151-2916.1983.tb10051.x.

[56] R.W. Rice, Porosity of Ceramics: Properties and Applications, CRC Press, 1998. doi:10.1017/CBO9781107415324.004.

[57] C.L. Farrow, P. Juhas, J.W. Liu, D. Bryndin, E.S. Boin, J. Bloch, T. Proffen, S.J.L. Billinge, PDFfit2 and PDFgui: Computer programs for studying nanostructure in crystals, J. Phys. Condens. Matter. 19 (2007) 335219. doi:10.1088/0953-8984/19/33/335219.

[58] K. Momma, F. Izumi, VESTA 3 for three-dimensional visualization of crystal, volumetric and morphology data, J. Appl. Crystallogr. 44 (2011) 1272–1276. doi:10.1107/S0021889811038970.

[59] M.G. Tucker, D.A. Keen, M.T. Dove, A.L. Goodwin, Q. Hui, RMCProfile: Reverse Monte Carlo for polycrystalline materials, J. Phys. Condens. Matter. 19 (2007) 335218. doi:10.1088/0953-8984/19/33/335218.

[60] G. King, C.M. Thompson, J.E. Greedan, A. Llobet, Local structure of the vacancy disordered fluorite Yb3TaO7 from neutron total scattering, J. Mater. Chem. A. 1 (2013) 10487–10494. doi:10.1039/c3ta12100c.

[61] B.H. Toby, R.B. Von Dreele, GSAS-II: The genesis of a modern open-source all purpose crystallography software package, J. Appl. Crystallogr. 46 (2013) 544–549. doi:10.1107/S0021889813003531.

[62] D.C. Palmer, Visualization and analysis of crystal structures using CrystalMaker software, Zeitschrift Fur Krist. - Cryst. Mater. 230 (2015) 559–572. doi:10.1515/zkri-2015-1869.

[63] R.D. Shannon, Revised effective ionic radii and systematic studies of interatomic distances in halides and chalcogenides, Acta Crystallogr. Sect. A. 32 (1976) 751–767. doi:10.1107/S0567739476001551.

[64] F. Wu, P. Wu, R. Zong, J. Feng, Investigation on thermo-physical and mechanical properties of Dy3(Ta1-xNbx)O7 ceramics with order-disorder transition, Ceram. Int. 45 (2019) 15705–15710. doi:10.1016/j.ceramint.2019.04.207.

[65] Y. Doi, Y. Harada, Y. Hinatsu, Crystal structures and magnetic properties of fluorite-related oxides Ln3NbO7 (Ln=lanthanides), J. Solid State Chem. 182 (2009) 709–715. doi:10.1016/j.jssc.2008.12.012.

[66] M. Wakeshima, H. Nishimine, Y. Hinatsu, Crystal structures and magnetic properties of rare earth tantalates RE3TaO7 (Re = rare earths), J. Phys. Condens. Matter. 16 (2004) 4103–4120. doi:10.1088/0953-8984/16/23/025.

[67] 琳陈, 晶冯, 稀土钽酸盐RE3TaO7和RETa3O9陶瓷 热-力学性质研究进展, J. Adv. Ceram. 40 (2019) 367–397.

[68] J. Zhu, X. Meng, J. Xu, P. Zhang, Z. Lou, M.J. Reece, F. Gao, Ultra-low thermal conductivity and enhanced mechanical properties of high-entropy rare earth niobates (Re3NbO7, Re=Dy, Y, Ho, Er, Yb), J. Eur. Ceram. Soc. (2020). doi:10.1016/j.psyneuen.2020.104810.

[69] L. Chen, P. Wu, J. Feng, Optimization thermophysical properties of TiO2 alloying Sm3TaO7 ceramics as promising thermal barrier coatings, Int. J. Appl. Ceram. Technol. 16 (2019) 230–242. doi:10.1111/ijac.13079.

[70] L. Chen, J. Guo, Y. Zhu, M. Hu, J. Feng, Features of crystal structures and thermo-mechanical properties of weberites RE3NbO7 (RE=La, Nd, Sm, Eu, Gd) ceramics, J. Am. Ceram. Soc. (2020). doi:10.1111/jace.17437.

[71] F. DeAngelis, M.G. Muraleedharan, J. Moon, H.R. Seyf, A.J. Minnich, A.J.H. McGaughey, A. Henry, Thermal transport in disordered materials, Nanoscale Microscale Thermophys. Eng. 23 (2019) 81–116. doi:10.1080/15567265.2018.1519004.

[72] P.B. Allen, J.L. Feldman, J. Fabian, F. Wooten, Diffusons, locons and propagons: Character of atomic vibrations in amorphous Si, Philos. Mag. B. 79 (1999) 1715–1731. doi:10.1080/13642819908223054.

[73] S. Shin, Q. Wang, J. Luo, R. Chen, Advanced materials for high-temperature thermal transport, Adv. Funct. Mater. (2019) 1904815. doi:10.1002/adfm.201904815.

[74] W. Zhou, Y. Cheng, K. Chen, G. Xie, T. Wang, G. Zhang, Thermal conductivity of amorphous materials, Adv. Funct. Mater. (2019) 1903829. doi:10.1002/adfm.201903829.

[75] D.G. Cahill, S.K. Watson, R.O. Pohl, Lower limit to the thermal conductivity of disordered crystals, Phys. Rev. B. 46 (1992) 6131–6140. doi:10.1103/PhysRevB.46.6131.

[76] Y. Luo, X. Yang, T. Feng, J. Wang, X. Ruan, Vibrational hierarchy leads to dual-phonon transport in low thermal conductivity crystals, Nat. Commun. 11 (2020) 2554. doi:10.1038/s41467-020-16371-w.

[77] M.T. Agne, R. Hanus, G.J. Snyder, Minimum thermal conductivity in the context of: Diffuson-mediated thermal transport, Energy Environ. Sci. 11 (2018) 609–616. doi:10.1039/c7ee03256k.

[78] A.R. Overy, A. Simonov, P.A. Chater, M.G. Tucker, A.L. Goodwin, Phonon broadening from supercell lattice dynamics: Random and correlated disorder, Phys. Status Solidi Basic Res. 254 (2017). doi:10.1002/pssb.201600586.

[79] A.R. Overy, A.B. Cairns, M.J. Cliffe, A. Simonov, M.G. Tucker, A.L. Goodwin, Design of crystal-like aperiodic solids with selective disorder-phonon coupling, Nat. Commun. 7 (2016) 1–8. doi:10.1038/ncomms10445.

[80] D.A. Keen, A.L. Goodwin, The crystallography of correlated disorder, Nature. 521 (2015) 303–309. doi:10.1038/nature14453.

[81] J.G. Allpress, H.J. Rossell, Fluorite-related phases Ln3MO7, Ln = rare earth, Y, or Sc, M = Nb, Sb, or Ta. I. Crystal chemistry, J. Solid State Chem. 27 (1979) 105–114. doi:10.1016/0022-4596(79)90149-X.

[82] E.C. O'Quinn, K.E. Sickafus, R.C. Ewing, G. Baldinozzi, J.C. Neuefeind, M.G. Tucker, A.F. Fuentes, D. Drey, M.K. Lang, Predicting short-range order and correlated phenomena in disordered crystalline materials, Sci. Adv. 6 (2020) eabc2758. doi:10.1126/sciadv.abc2758.

[83] D.L. Drey, E.C. O'Quinn, T. Subramani, K. Lilova, G. Baldinozzi, I.M. Gussev, A.F. Fuentes, J.C. Neuefeind, M. Everett, D. Sprouster, A. Navrotsky, R.C. Ewing, M. Lang, Disorder in Ho2Ti2−xZrxO7: pyrochlore to defect fluorite solid solution series, RSC Adv. 10 (2020) 34632–34650. doi:10.1039/D0RA07118H.

[84] A.F. Fuentes, S.M. Montemayor, M. Maczka, M. Lang, R.C. Ewing, U. Amador, A critical review of existing criteria for the prediction of pyrochlore formation and stability, Inorg. Chem. 57 (2018) 12093–12105. doi:10.1021/acs.inorgchem.8b01665.

[85] J. Shamblin, C.L. Tracy, R.I. Palomares, E.C. O'Quinn, R.C. Ewing, J. Neuefeind, M. Feygenson, J. Behrens, C. Trautmann, M. Lang, Similar local order in disordered fluorite and aperiodic pyrochlore structures, Acta Mater. 144 (2018) 60–67. doi:10.1016/j.actamat.2017.10.044.

[86] J. Shamblin, M. Feygenson, J. Neuefeind, C.L. Tracy, F. Zhang, S. Finkeldei, D. Bosbach, H. Zhou, R.C. Ewing, M. Lang, Probing disorder in isometric pyrochlore and related complex oxides, Nat. Mater. 15 (2016) 507–511. doi:10.1038/nmat4581.

[87] S.J. McCormack, A. Navrotsky, Thermodynamics of high entropy ceramics, Acta Mater. (2020). doi:10.1201/9780367374426-11.

4. SIZE DISORDER AS A DESCRIPTOR FOR PREDICTING REDUCED THERMAL CONDUCTIVITY IN MEDIUM- AND HIGH-ENTROPY PYROCHLORE OXIDES

4.1 INTRODUCTION

High-entropy ceramics (HECs), including rocksalt [1], perovskite [2], fluorite [3], and pyrochlore [4,5] oxides, borides [6], carbides [7–10], silicides [11,12] and silicates [13,14] have been reported in the last four years and attracted great research interests. In addition, single-phase high-entropy aluminides (intermetallic compounds), which bridge the well-studied high-entropy alloys (HEAs) [15–17] with new families of HECs, have been made [18]. Some unusual properties of HECs, such as colossal dielectric constants [19], super ionic conductivity [20], and increased hardness [7], have been reported.

One exciting and widely-observed property of HECs is represented by the reduced thermal conductivity [3,10,11,21–24]. While reduced thermal conductivity is generally expected from strong phonon scattering in HECs, only a few studies have investigated the underlying mechanisms or key controlling factor(s) in depth. Recently, Braun et al. [23] attributed the reduction in thermal conductivity in six-component rocksalt oxides to disorder in the force constants arising from charge variations. Yang et al. [25] also attributed the low thermal conductivity in Ln_3NbO_7 (albeit not an HEC) to the force-constant disorder, suggested to be a result of both increased size disorder and charge variation. Furthermore, both reports [23,25] noted high Young's modulus to thermal conductivity (E/k) ratios, indicative of a large phonon scattering rate. However, a descriptor to predict the reduced thermal conductivity is still lacking.

To unveil the key parameter controlling the reduced thermal conductivity in HECs, we have fabricated and investigated a series of 22 single-phase pyrochlores, including 18 medium- and high-entropy pyrochlores (referred to as "M/HEPs") and four additional low-entropy

benchmark compositions. We recognize there are many definitions/criteria of HEAs [17]. Our group has recently attempted to streamline this by broadening HECs to compositionally-complex ceramics (CCCs) or multi-principal cation ceramics (MPCCs) [26]. Here we loosely use "high entropy" to refer to ceramics with five or more cations of high (typically 5%-35%) concentrations (or ideal mixing entropy $\Delta S_X^{mix,ideal}$ >1.5R per mol of cations, where R is the gas constant) on at least one sublattice (if there are multiple ordered cation sublattices), while "medium entropy" refers to cases with three or four cations of high concentrations (or R < $\Delta S_X^{mix,ideal}$ < 1.5R) on at least one sublattice. As we will show later, the thermal conductivity is better correlated with size disorder, but not the entropy itself, so that we are not limited to HECs for searching new low-k materials. Thus, we propose to extend HECs to "compositionally-complex ceramics (CCCs)" to include both medium-entropy and high-entropy compositions. With this definition, this study examined 15 MEPs and 3 HEPs, which represent perhaps the largest set of CCCs made and investigated in a single study.

Pyrochlores of $A_2B_2O_7$ structure can be considered as ordered fluorites with two cation sublattices, which represent a potential alternative to yttria-stabilized zirconia (YSZ) as thermal barrier coatings (TBCs) [27]. Cubic pyrochlores have moderately high Young's moduli (E ~ 250 GPa) [28–30] and low thermal conductivities (k ~ 2 W m^{-1} K^{-1}) [31–34]. Further efforts to reduce the thermal conductivity include introducing another rare earth element on the A-site [35–42] or B-site [41,42]. Recently, a couple of studies reported the fabrication single-phase high-entropy zirconate-based pyrochlores with low thermal conductivities (albeit possibly some porosity and microstructure effects) [4,5]. Herein, we fabricated >20 dense M/HEPs, where we systematically varied mass and size disorder on both cation sublattices. Subsequently, we identify a useful descriptor for predicting reduced thermal conductivity.

4.2 EXPERIMENTAL PROCEDURE

In this work, we adopt the mass disorder (g) and size disorder (δ) parameters that are used in thermal transport [43,44] and HEAs [45,46] fields, which are defined as:

$$g = \sum_{i=0}^{n} x_i \left(1 - {m_i}/{\overline{m}}\right)^2 \quad (1)$$

$$\delta = \sqrt{\sum_{i=0}^{n} x_i \left(1 - {r_i}/{\bar{r}}\right)^2}, \quad (2)$$

where x_i is the atomic fraction, m_i and r_i are the mass and radius of the i^{th} component, and $\overline{m}$ and $\bar{r}$ are the overall weighted average of mass and ionic radius. Here, we used the Shannon effective ionic radius [47]. Eqs. (1) and (2) assume all cations share the same lattice site; however, the pyrochlore structure has two cation sublattices. Thus, we propose to modify the mass disorder and size disorder parameters as:

$$g^* = \sqrt{g_A^2 + g_B^2} \quad (3)$$

$$\delta_{size}^* = \sqrt{\delta_A^2 + \delta_B^2} \quad (4)$$

Here, subscripts "A" and "B" refer to the application of Eqs. (1) and (2) on the A-site and B-site sublattices of $A_2B_2O_7$ pyrochlores (and similar definitions can be extended to other HECs or CCCs with multiple cation sublattices).

All starting constituents were binary oxides purchased from US Research Nanomaterials (~5 μm initial particle sizes). As-received powders were weighed in appropriate amounts, ~2 wt. % stearic acid was added, and the powders were then placed inside a poly(methyl methacrylate) tube with tungsten carbide inserts on both ends along with one Ø5/16" tungsten carbide ball. The powder mixture was dry milled for six hours utilizing a high energy ball mill (SPEX 8000D,

SPEX SamplePrep, USA). The milling was interrupted every 30 min to allow for 10 min of cooling to prevent overheating. The milled powders were uniaxially pressed under 100 MPa to form green compacts. The pellets were then placed on a Pt foil inside a calcia-stabilized zirconia crucible within a box furnace and sintered at 1600°C for 24 h.

The densities (ρ) were measured following the ASTM C373-18 Standard [48]. The relative densities were calculated from the theoretical densities obtained by X-ray diffraction (XRD). The XRD (Miniflex II, Rigaku, Japan, operating at 30 kV and 15 mA) data were collected at 0.01° 2θ steps. The thermal diffusivity (α) was measured by laser flash analysis (LFA 467 HT HyperFlash, NETZSCH, Germany). The specific heat capacity (c_p) was estimated by Neumann-Kopp rule using tabulated values of the constituent oxides [49]. The thermal conductivity (k) was then calculated by the product of α, ρ, and c_p (Suppl. Table S4.1). A pulse-echo sonic resonance measurement (TDS 420A, Tektronix, USA) was used to determine the transverse (u_T) and longitudinal (u_L) waves speeds. From these, Poisson's ratio (ν) and Young's modulus (E) were determined by following the ASTM C1198-09 Standard [50].

The relative densities of our sintered specimens were 94-100%. We further corrected the effects of porosity to obtain the intrinsic conductivity and modulus based on [51,52]: $k = k_{measured}/(1-P)^{3/2}$ and $E = E_{measured}/(1-2.9P)$, where P is the fraction of pores, and k and E are the corrected intrinsic thermal conductivity and Young's modulus, respectively, of 100% dense specimens that are reported in Table 4.1 and all figures.

4.3 RESULTS AND DISCUSSION

XRD examined the phase formation and crystal structures of all the specimens. Fig. 4.1 shows XRD pattern, which confirms the formation of the desired pyrochlore phase ($Fd\bar{3}m$, space

group #227) without debatable secondary phases, except for Composition P2 and P3 with secondary phases (which were excluded from further measurements).

The measured thermal conductivities and Young's moduli of the referencing $La_2Zr_2O_7$ and $Sm_2Zr_2O_7$ specimens made in this study (Table 4.1) agree well with prior reports [28,30,38,53]. As shown in Table 4.1, most M/HEPs exhibited reduced thermal conductivities in comparison with the benchmark $La_2Zr_2O_7$ and $Sm_2Zr_2O_7$ specimens, with up to 35% reductions. We should note that composition P1 ($La_2(Hf_{1/2}Zr_{1/2})_2O_7$) shows a higher conductivity than $La_2Zr_2O_7$, which is in direct contrast to the well-established point defect scattering theory. We examined the specimen by SEM-EDS (Suppl. Fig. S4.1), and it was revealed that small inclusions (~ 5 μm) of monoclinic ZrO_2 (k ~ 6 W m^{-1} K^{-1}) were present [33]. However, this amount was too small to be detected by XRD. Another group has investigated the thermal conductivity of $La_2Zr_2O_7$ and $La_2(Hf_{1/2}Zr_{1/2})_2O_7$, where they found them to be 2.2 and 1.9 W m^{-1} K^{-1}, respectively [54]. Moreover, the reduced thermal conductivity was achieved with retained moduli (most in the range of ~230 – 260 GPa, with exception of P20-2, P20-3, P20-4, and P23, as shown in Table 4.1), thereby attaining insulative yet stiff properties (or high E/k ratios). This is an interesting and useful phenomenon for HECs, including high-entropy rocksalts reported earlier [23], as the reduction of thermal conductivity typically occurs along with decreased modulus.

The correlations between three descriptors (δ^*_{size}, g^*, ρ) and the measured k and E of 22 specimens were examined. Mass disorder g^* and size disorder δ^*_{size} are both pertinent in point defect scattering theory [54,55] and density ρ is a relevant factor in determining k_{min} [56], thus all were examined. In each case, linear regressions were performed, and the degree of correlation was characterized by the Pearson correlation coefficient (PCC) and r^2.

Fig. 4.2 shows that thermal conductivity k and the E/k ratio have the best correlations with the size disorder δ^*_{size}. The size disorder δ^*_{size} displays a negative correlation (PCC = -0.86, r^2 = 0.73) with measured k. Furthermore, the thermal conductivity k correlates better with the δ^*_{size}, defined in Eq. (4) above, than the individual δ_A or δ_B for each sublattice (Suppl. Fig. S4.2) and the overall δ assuming random mixing (Suppl Fig. S4.3). A careful examination further found that the size disorder on the B-site (δ_B) is larger than that on the A-site (δ_A), thereby being more effective in reducing k (Suppl. Fig. S4.2), being consistent with prior modeling studies [57,58].

A positive correlation was also found between the E/k ratio and δ^*_{size} (PCC = 0.91, r^2 = 0.83). We should emphasize that we do not expect a perfect linear relation ($r^2 \sim 1$) of thermal conductivity k with any single descriptor, since many other factors can influence k (as a complex material property).

Virtually no correlation between δ^*_{size} and E (PCC = 0.13, r^2 = 0.02) was found (Suppl. Fig. S4.4), implying the high modulus is retained after introducing size disorder in M/HEPs.

The mass disorder g^* was also considered, and its correlations with k and E/k are shown in Suppl. Fig. S4.5. The mass disorder g^* appears to be a less effective descriptor in comparison with the size disorder δ^*_{size}. Here, the main discrepancies stemmed from the Ti-containing compounds. The correlations of k and E/k with density ρ are weak (Suppl. Fig. S4.6).

Interestingly, mixing entropies only exhibit weaker correlations with thermal conductivities (Suppl. Table S4.3 and Fig. S4.7, although there should be a correlation between size disorder and mixing entropy, particularly those on the B site). This study showed the size disorder is a stronger descriptor for designing low-k CCCs than the mixing entropy itself.

Additionally, all the compositions containing Ti had δ^*_{size} > 6% and low k (Fig. 4.2). As a result, the E/k was significantly higher. Ti is smaller and lighter than other metal elements selected in this study (Suppl. Table S4.2). In addition to increasing the size disorder, it can act as a "rattler" on the B-site to reduce k [35]. This effect further shows that ionic radius can be a more significant factor in controlling k than the atomic mass. Consequently, the Ti-containing families exhibit high E/k ratios, achieving 155.6 ± 5.9 GPa·m·K·W^{-1} for Composition P20 $(Sm_{1/3}Eu_{1/3}Gd_{1/3})_2(Ti_{1/4}Sn_{1/4}Hf_{1/4}Zr_{1/4})_2O_7$.

To further explore the Ti effects, the fraction of Ti was systematically varied in $(Sm_{1/3}Eu_{1/3}Gd_{1/3})_2(Ti_xSn_{(1-x)/3}Hf_{(1-x)/3}Zr_{(1-x)/3})_2O_7$. The measured k, E, and E/k ratio vs. the Ti fraction on the B site (x) curves are shown in Fig. 4.3. It was found that the thermal conductivity k reaches a minimum around x = 0.25. The modulus E increases with increasing Ti concentration overall, with a jump when Ti occupies ~50% of the B-site. Consequently, the E/k ratio reaches a maximum of 163.9 ± 6.1 GPa·m·K·W^{-1} for P20-2 $(Sm_{1/3}Eu_{1/3}Gd_{1/3})_2(Ti_{1/2}Sn_{1/6}Hf_{1/6}Zr_{1/6})_2O_7$, where Ti may fit more tightly in the B-site to raise E.

The rattler effect has been demonstrated in pyrochlores previously [35,41]. Since Yb is small and can behave as a rattler on the A site, a $(Sm_{1/4}Eu_{1/4}Gd_{1/4}Yb_{1/4})_2(Ti_{1/4}Sn_{1/4}Hf_{1/4}Zr_{1/4})_2O_7$ P20 + Yb specimen was synthesized to further verify the rattler effect. The addition of Yb led to a ~13% reduction in k with near negligible loss in E (~4%), thereby resulting in a high E/k ratio of 172.3 ± 5.9 GPa·m·K·W^{-1}.

We note that Composition P21 is a material that was recently reported in the literature to have an unusually low RT thermal conductivity of 0.76 W·m^{-1}·K^{-1} [4]. However, we measured a much higher RT thermal conductivity of 2.06 W·m^{-1}·K^{-1}. Our value appears to be robust since several other HEPs of similar compositions that have similar k values (Table 4.1). Furthermore,

we verified the k values of the two benchmark $La_2Zr_2O_7$ and $Sm_2Zr_2O_7$ specimens widely reported in the literature. In the only other report of HEPs [5], the specimens exhibit similar low k values, but those can be well attributed to the reported low relative densities of ~75%. Thus, the lower k reported in Ref. [4] might also be due to an unknown microstructure effect. Our specimens have high relative densities of 94-100%, and we have corrected the porosity effects to report intrinsic k values in all cases.

In the underlying mechanisms, size disorder can result in both distorted sublattices and oversized cages for the rattler effect, both of which can severely suppress heat conduction [23,25]. Furthermore, unique to the pyrochlore structure, the 8*a*-site oxygen ion can relax into the oxygen vacancy site, which likely results in a strained anion sublattice [35,41]. Here, the size disorder can be increased in a four-component composition with the largest and smallest elements on each sublattice. To test this effect, Compositions P20-5 and P20-6 were synthesized. On the one hand, P20-6 $(Sm_{3/4}Yb_{1/4})_2(Ti_{1/2}Zr_{1/2})_2O_7$ represents the four-component system with nearly maximized size disorder of 9.50, which exhibits a low k of 1.40 ± 0.04 $W{\cdot}m^{-1}{\cdot}K^{-1}$ and a high E/k ratio of 163.1 ± 5.5 $GPa{\cdot}m{\cdot}K{\cdot}W^{-1}$. On the other hand, P20-5 $(Sm_{1/4}Eu_{1/4}Gd_{1/4}Yb_{1/4})_2(Ti_{1/2}Hf_{1/4}Zr_{1/4})_2O_7$, of a slightly lower size disorder of 9.04, shows more attractive properties with the lowest k of 1.36 ± 0.04 $W{\cdot}m^{-1}{\cdot}K^{-1}$ and the highest E/k ratio of 175.2 ± 5.7 $GPa{\cdot}m{\cdot}K{\cdot}W^{-1}$ among all 22 specimens examined in this study.

4.4 CONCLUSION

In summary, 22 dense, single-phase cubic pyrochlores, including 18 M/HEPs have been made and measured in this study, representing the largest set of data collected in a single family of HECs and CCCs. Overall, M/HEPs exhibit reduced conductivities (up to ~35%) while retaining similar stiffness (~ 230 – 260 GPa excluding a few exceptions mentioned earlier),

thereby achieving high E/k ratios, in comparison with simpler pyrochlores such as $La_2Zr_2O_7$, $Sm_2Zr_2O_7$ and $La_2(Hf_{1/2}Zr_{1/2})_2O_7$.

Notably, we find a simple descriptor, size disorder δ^*_{size} (with a modified definition proposed in this study) to predict reduced thermal conductivities in M/HEPs and potentially other HECs and CCCs. This size disorder parameter δ^*_{size} is a more effective descriptor to forecast reduce thermal conductivity than the ideal mixing entropy itself. In fact, our three HEPs (P21, P22, and P23) all have relatively higher *k* values (~2 $W \cdot m^{-1} \cdot K^{-1}$) in comparison with of our best MEPs, *e.g.*, P20 + Yb $(Sm_{1/4}Eu_{1/4}Gd_{1/4}Yb_{1/4})_2(Ti_{1/4}Sn_{1/4}Hf_{1/4}Zr_{1/4})_2O_7$ (~1.39 $W \cdot m^{-1} \cdot K^{-1}$) and P6 $(Sm_{1/2}Gd_{1/2})_2(Ti_{1/3}Hf_{1/3}Zr_{1/3})_2O_7$ (~1.47 $W \cdot m^{-1} \cdot K^{-1}$). The analysis was all conducted on RT measurements, and the temperature dependence analysis and trends will be included in a separate publication. This study also supports our proposal to extend HECs to compositionally-complex ceramics or CCCs to include both medium-entropy and high-entropy compositions to search for better properties.

Chapter 4, in full, is a reprint of the material as it appears in Scripta Materialia 2020. A.J. Wright, Q.Y. Wang, S.T. Ko, K.M. Chung, R.K. Chen, J. Luo, Size disorder as a descriptor for predicting reduced thermal conductivity in medium- and high-entropy pyrochlore oxides. *Scripta Mater.*, 2020, 181. The dissertation author was the primary investigator and author of this paper.

Table 4.1. Summary of the results of all synthesized single-phase pyrochlore oxides.

Identifier	Composition	g^* (%)	δ^*_{Size} (%)	r_A^{3+}/r_B^{4+}	Relative Density	$k\left(\frac{W}{m\cdot K}\right)$	$E\ (GPa)$	$\frac{E/k}{\left(\frac{GPa\cdot m\cdot K}{W}\right)}$
--	$La_2Zr_2O_7$	0.00	0.00	1.61	95.5 ± 0.6%	2.14 ± 0.06	236.2 ± 6.7	110.5 ± 4.6
--	$Sm_2Zr_2O_7$	0.00	0.00	1.50	100.0 ± 0.7%	2.04 ± 0.06	220.1 ± 3.0	107.9 ± 3.7
P1	$La_2(Hf_{1/2}Zr_{1/2})_2O_7$	10.47	0.70	1.62	98.1 ± 0.6%	2.29 ± 0.06	250.2 ± 4.2	109.4 ± 3.6
P4	$Sm_2(Sn_{1/4}Ti_{1/4}Hf_{1/4}Zr_{1/4})_2O_7$	18.86	6.65	1.58	97.7 ± 0.6%	1.73 ± 0.05	250.2 ± 4.7	144.3 ± 5.2
P5	$Gd_2(Sn_{1/4}Ti_{1/4}Hf_{1/4}Zr_{1/4})_2O_7$	18.86	6.65	1.55	96.2 ± 0.6%	1.58 ± 0.05	229.4 ± 4.4	145.6 ± 5.2
P6	$(Sm_{1/2}Gd_{1/2})_2(Ti_{1/3}Hf_{1/3}Zr_{1/3})_2O_7$	26.33	7.76	1.57	97.9 ± 0.6%	1.47 ± 0.04	242.0 ± 4.2	164.8 ± 5.8
P7	$(Eu_{1/2}Gd_{1/2})_2(Ti_{1/3}Hf_{1/3}Zr_{1/3})_2O_7$	26.33	7.69	1.56	97.5 ± 0.6%	1.52 ± 0.05	243.1 ± 4.0	160.3 ± 5.6
P8	$(La_{1/2}Pr_{1/2})_2(Sn_{1/3}Hf_{1/3}Zr_{1/3})_2O_7$	7.92	2.31	1.62	94.8 ± 0.6%	2.24 ± 0.07	275.5 ± 7.9	122.8 ± 5.1
P9	$(Eu_{1/2}Gd_{1/2})_2(Sn_{1/3}Hf_{1/3}Zr_{1/3})_2O_7$	7.92	1.87	1.50	93.5 ± 0.6%	2.24 ± 0.07	253.3 ± 4.3	113.0 ± 3.9
P10	$(La_{1/3}Pr_{1/3}Nd_{1/3})_2(Hf_{1/2}Zr_{1/2})_2O_7$	10.47	2.00	1.58	96.5 ± 0.6%	2.16 ± 0.06	240.0 ± 4.3	110.9 ± 3.6
P11	$(Sm_{1/3}Eu_{1/3}Gd_{1/3})_2(Hf_{1/2}Zr_{1/2})_2O_7$	10.47	1.22	1.49	97.9 ± 0.6%	1.97 ± 0.06	235.7 ± 3.8	119.8 ± 4.1
P20-1	$(Sm_{1/3}Eu_{1/3}Gd_{1/3})_2(Sn_{1/3}Hf_{1/3}Zr_{1/3})_2O_7$	7.92	2.03	1.51	93.8 ± 0.6%	2.21 ± 0.07	256.7 ± 4.1	116.0 ± 4.0
P20	$(Sm_{1/3}Eu_{1/3}Gd_{1/3})_2(Ti_{1/4}Sn_{1/4}Hf_{1/4}Zr_{1/4})_2O_7$	18.86	6.73	1.56	96.4 ± 0.6%	1.67 ± 0.05	260.4 ± 5.0	155.6 ± 5.9
P20 + Yb	$(Sm_{1/4}Eu_{1/4}Gd_{1/4}Yb_{1/4})_2(Ti_{1/4}Sn_{1/4}Hf_{1/4}Zr_{1/4})_2O_7$	18.87	7.50	1.54	98.1 ± 0.6%	1.45 ± 0.04	249.4 ± 4.0	172.3 ± 5.9
P20-2	$(Sm_{1/3}Eu_{1/3}Gd_{1/3})_2(Ti_{1/2}Sn_{1/6}Hf_{1/6}Zr_{1/6})_2O_7$	29.62	7.93	1.63	94.9 ± 0.6%	1.71 ± 0.05	280.1 ± 6.2	163.9 ± 6.1
P20-3	$(Sm_{1/3}Eu_{1/3}Gd_{1/3})_2(Ti_{3/4}Sn_{1/12}Hf_{1/12}Zr_{1/12})_2O_7$	33.91	7.12	1.69	94.6 ± 0.6%	1.90 ± 0.06	273.6 ± 5.3	144.2 ± 5.2
P20-4	$(Sm_{1/3}Eu_{1/3}Gd_{1/3})_2Ti_2O_7$	0.04	1.00	1.76	94.1 ± 0.6%	2.88 ± 0.09	281.3 ± 5.0	97.7 ± 3.4
P20-5	$(Sm_{1/4}Eu_{1/4}Gd_{1/4}Yb_{1/4})_2(Ti_{1/2}Hf_{1/4}Zr_{1/4})_2O_7$	34.07	9.04	1.58	97.8 ± 0.6%	1.36 ± 0.04	238.3 ± 2.5	175.2 ± 5.7
P20-6	$(Sm_{3/4}Yb_{1/4})_2(Ti_{1/2}Zr_{1/2})_2O_7$	9.72	9.50	1.59	98.8 ± 0.6%	1.40 ± 0.04	227.7 ± 2.5	163.1 ± 5.5
P21	$(La_{1/5}Ce_{1/5}Nd_{1/5}Sm_{1/5}Eu_{1/5})_2Zr_2O_7$	0.13	3.24	1.54	99.1 ± 0.7%	2.06 ± 0.06	230.6 ± 2.9	112.1 ± 3.7
P22	$(La_{1/7}Ce_{1/7}Pr_{1/7}Nd_{1/7}Sm_{1/7}Eu_{1/7}Gd_{1/7})_2(Hf_{1/2}Zr_{1/2})_2O_7$	10.47	3.46	1.55	98.6 ± 0.6%	1.97 ± 0.06	242.0 ± 3.5	123.0 ± 4.2
P23	$(La_{1/7}Ce_{1/7}Pr_{1/7}Nd_{1/7}Sm_{1/7}Eu_{1/7}Gd_{1/7})_2(Sn_{1/3}Hf_{1/3}Zr_{1/3})_2O_7$	7.92	3.82	1.56	98.7 ± 0.7%	2.02 ± 0.06	187.0 ± 5.0	92.4 ± 3.7

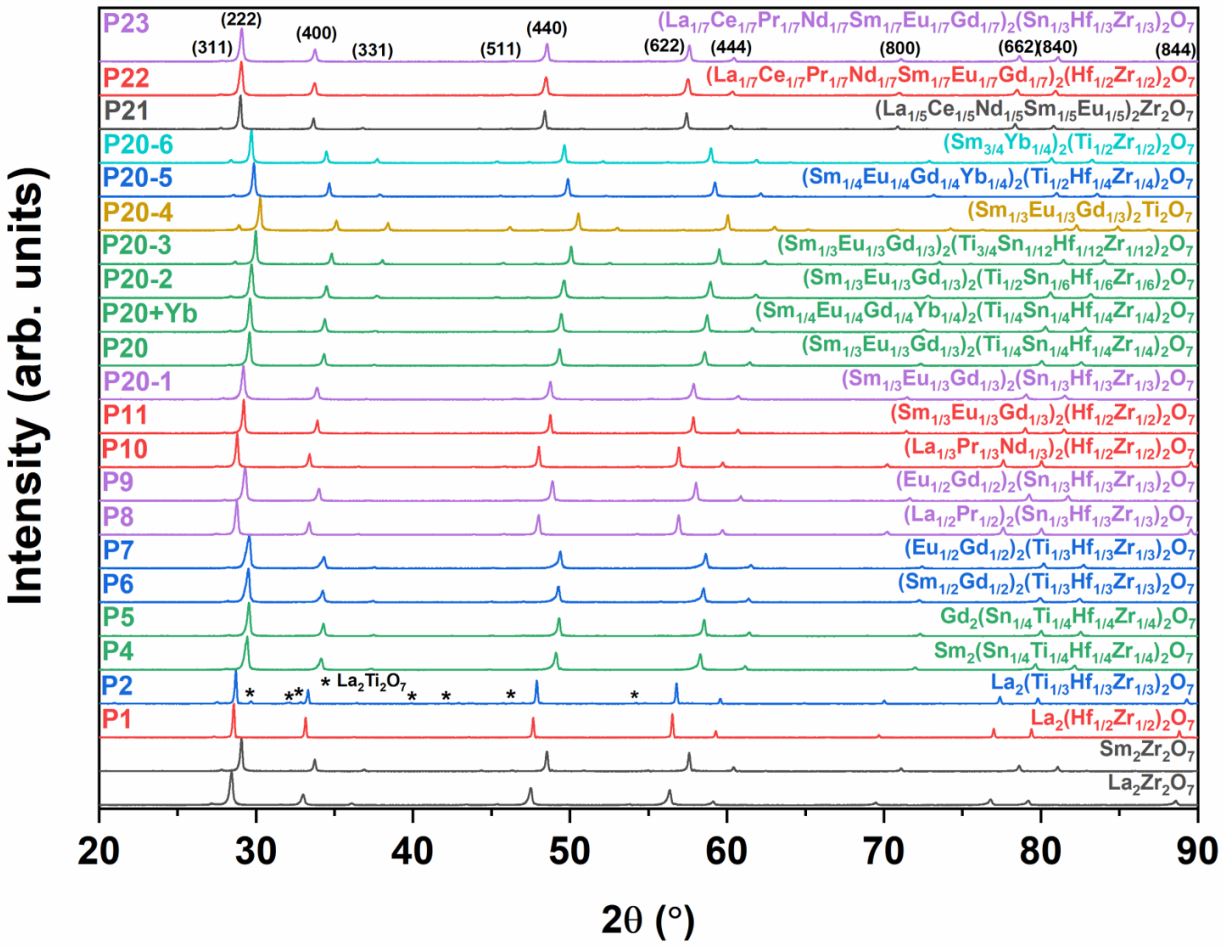

Figure 4.1. XRD pattern of various pyrochlore oxides synthesized in this study. Composition P2 exhibits secondary phases. The XRD of P3 ($La_2(Sn_{1/4}Ti_{1/4}Hf_{1/4}Zr_{1/4})_2O_7$) is not shown because it was not successfully consolidated into a pellet. The other 22 compositions all exhibit single pyrochlore phases.

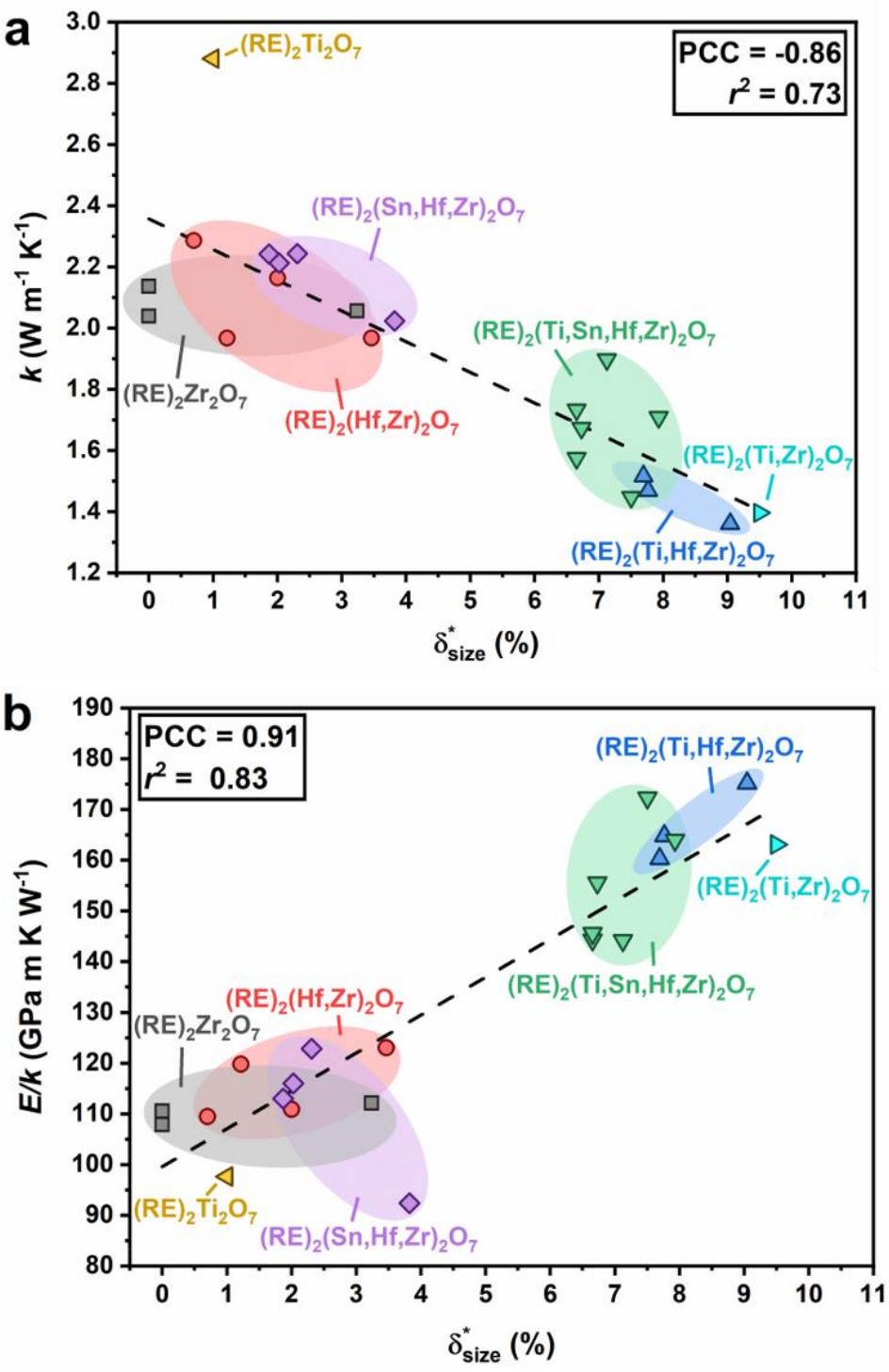

Figure 4.2. Correlation of (a) thermal conductivity (k) and (b) the E/k ratios of all 22 single-phase pyrochlores made in this study with the size disorder parameter, δ^*_{size}. The error bars are given in Table 1, which are not shown here for figure clarity. The best-fit line for (a) is $k = -0.10\delta^*_{size} + 2.36\frac{W}{m\cdot K}$. The best-fit line for (b) is $E/k = 7.5\delta^*_{size} + 99.6\frac{GPa\cdot m\cdot K}{W}$.

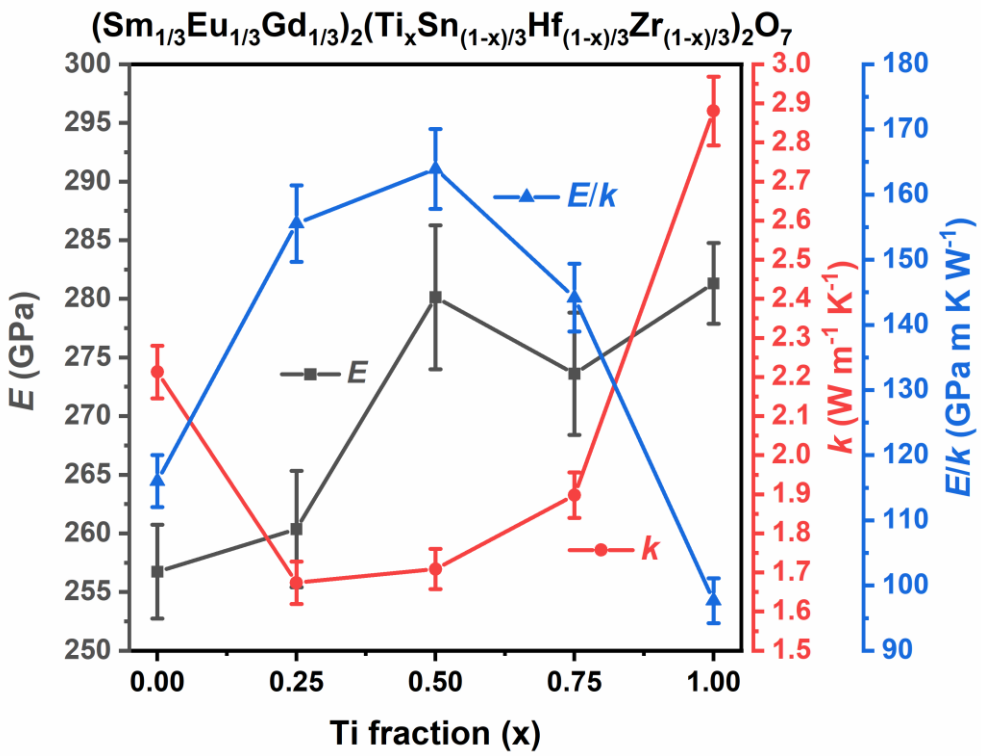

Figure 4.3. Variations in Young's modulus (E), thermal conductivity (k), and the E/k ratio as functions of Ti concentration in P20-n ($(Sm_{1/3}Eu_{1/3}Gd_{1/3})_2(Ti_xSn_{(1-x)/3}Hf_{(1-x)/3}Zr_{(1-x)/3})_2O_7$).

Table 4.2. Raw data of thermal diffusivity (α) measured by laser flash analysis at room temperature and calculated values of heat capacity (c_p) at 298 K following Neumann-Kopp law based on the values of constituent oxides in I. Barin, Thermochemical Data of Pure Substances, VCH, Weinheim, 1995.

Identifier	**Composition**	$\boldsymbol{\alpha}\left(\frac{\boldsymbol{mm^2}}{\boldsymbol{s}}\right)$	$\boldsymbol{c_p}\left(\frac{\boldsymbol{J}}{\boldsymbol{g \cdot K}}\right)$
--	$La_2Zr_2O_7$	0.900	0.386
--	$Sm_2Zr_2O_7$	0.803	0.383
P1	$La_2(Hf_{1/2}Zr_{1/2})_2O_7$	0.870	0.341
P4	$Sm_2(Sn_{1/4}Ti_{1/4}Hf_{1/4}Zr_{1/4})_2O_7$	0.653	0.361
P5	$Gd_2(Sn_{1/4}Ti_{1/4}Hf_{1/4}Zr_{1/4})_2O_7$	0.609	0.338
P6	$(Sm_{1/2}Gd_{1/2})_2(Ti_{1/3}Hf_{1/3}Zr_{1/3})_2O_7$	0.556	0.356
P7	$(Eu_{1/2}Gd_{1/2})_2(Ti_{1/3}Hf_{1/3}Zr_{1/3})_2O_7$	0.558	0.362
P8	$(La_{1/2}Pr_{1/2})_2(Sn_{1/3}Hf_{1/3}Zr_{1/3})_2O_7$	0.896	0.347
P9	$(Eu_{1/2}Gd_{1/2})_2(Sn_{1/3}Hf_{1/3}Zr_{1/3})_2O_7$	0.836	0.335
P10	$(La_{1/3}Pr_{1/3}Nd_{1/3})_2(Hf_{1/2}Zr_{1/2})_2O_7$	0.781	0.345
P11	$(Sm_{1/3}Eu_{1/3}Gd_{1/3})_2(Hf_{1/2}Zr_{1/2})_2O_7$	0.746	0.337
P20-1	$(Sm_{1/3}Eu_{1/3}Gd_{1/3})_2(Sn_{1/3}Hf_{1/3}Zr_{1/3})_2O_7$	0.834	0.336
P20	$(Sm_{1/3}Eu_{1/3}Gd_{1/3})_2(Ti_{1/4}Sn_{1/4}Hf_{1/4}Zr_{1/4})_2O_7$	0.621	0.357
P20 + Yb	$(Sm_{1/4}Eu_{1/4}Gd_{1/4}Yb_{1/4})_2(Ti_{1/4}Sn_{1/4}Hf_{1/4}Zr_{1/4})_2O_7$	0.536	0.352
P20-2	$(Sm_{1/3}Eu_{1/3}Gd_{1/3})_2(Ti_{1/2}Sn_{1/6}Hf_{1/6}Zr_{1/6})_2O_7$	0.614	0.381
P20-3	$(Sm_{1/3}Eu_{1/3}Gd_{1/3})_2(Ti_{3/4}Sn_{1/12}Hf_{1/12}Zr_{1/12})_2O_7$	0.671	0.407
P20-4	$(Sm_{1/3}Eu_{1/3}Gd_{1/3})_2Ti_2O_7$	0.992	0.439
P20-5	$(Sm_{1/4}Eu_{1/4}Gd_{1/4}Yb_{1/4})_2(Ti_{1/2}Hf_{1/4}Zr_{1/4})_2O_7$	0.489	0.374
P20-6	$(Sm_{3/4}Yb_{1/4})_2(Ti_{1/2}Zr_{1/2})_2O_7$	0.514	0.403
P21	$(La_{1/5}Ce_{1/5}Nd_{1/5}Sm_{1/5}Eu_{1/5})_2Zr_2O_7$	0.813	0.389
P22	$(La_{1/7}Ce_{1/7}Pr_{1/7}Nd_{1/7}Sm_{1/7}Eu_{1/7}Gd_{1/7})_2(Hf_{1/2}Zr_{1/2})_2O_7$	0.763	0.343
P23	$(La_{1/7}Ce_{1/7}Pr_{1/7}Nd_{1/7}Sm_{1/7}Eu_{1/7}Gd_{1/7})_2(Sn_{1/3}Hf_{1/3}Zr_{1/3})_2O_7$	0.793	0.343

Table 4.3. Candidate metal elements for making medium- and high-entropy pyrochlore oxides with their corresponding atomic mass, ionic radius (CN^{3+} = 8, CN^{4+} = 6), and the assumed nominal valency state.

Cation	Atomic Mass (amu)	Ionic Radius (Å)	Valency
Ti^{4+}	47.87	0.605	4
Zr^{4+}	91.224	0.72	4
Sn^{4+}	118.71	0.69	4
La^{3+}	138.91	1.16	3
Ce^{3+}	140.12	1.143	3
Pr^{3+}	140.91	1.126	3
Nd^{3+}	144.24	1.109	3
Sm^{3+}	150.36	1.079	3
Eu^{3+}	151.96	1.066	3
Gd^{3+}	157.25	1.053	3
Yb^{3+}	173.04	0.985	3
Hf^{4+}	178.49	0.71	4

Table 4.4. Summary of calculated mixing entropies on the A and B sublattices and the average (measured in R per mol. of metal cations, where R is gas constant), along with measured thermal conductivities.

Identifier	Composition	$\Delta S_A^{mix,ideal}$ (R/mol)	$\Delta S_B^{mix,ideal}$ (R/mol)	$\overline{S}_{all\ cations}^{mix,ideal}$ (R/mol)	$k\left(\frac{W}{m \cdot K}\right)$
--	$La_2Zr_2O_7$	0	0	0	2.14 ± 0.06
--	$Sm_2Zr_2O_7$	0	0	0	2.04 ± 0.06
P1	$La_2(Hf_{1/2}Zr_{1/2})_2O_7$	0	0.69	0.35	2.29 ± 0.06
P4	$Sm_2(Sn_{1/4}Ti_{1/4}Hf_{1/4}Zr_{1/4})_2O_7$	0	1.39	0.69	1.73 ± 0.05
P5	$Gd_2(Sn_{1/4}Ti_{1/4}Hf_{1/4}Zr_{1/4})_2O_7$	0	1.39	0.69	1.58 ± 0.05
P6	$(Sm_{1/2}Gd_{1/2})_2(Ti_{1/3}Hf_{1/3}Zr_{1/3})_2O_7$	0.69	1.10	0.90	1.47 ± 0.04
P7	$(Eu_{1/2}Gd_{1/2})_2(Ti_{1/3}Hf_{1/3}Zr_{1/3})_2O_7$	0.69	1.10	0.90	1.52 ± 0.05
P8	$(La_{1/2}Pr_{1/2})_2(Sn_{1/3}Hf_{1/3}Zr_{1/3})_2O_7$	0.69	1.10	0.90	2.24 ± 0.07
P9	$(Eu_{1/2}Gd_{1/2})_2(Sn_{1/3}Hf_{1/3}Zr_{1/3})_2O_7$	0.69	1.10	0.90	2.24 ± 0.07
P10	$(La_{1/3}Pr_{1/3}Nd_{1/3})_2(Hf_{1/2}Zr_{1/2})_2O_7$	1.10	0.69	0.90	2.16 ± 0.06
P11	$(Sm_{1/3}Eu_{1/3}Gd_{1/3})_2(Hf_{1/2}Zr_{1/2})_2O_7$	1.10	0.69	0.90	1.97 ± 0.06
P20-1	$(Sm_{1/3}Eu_{1/3}Gd_{1/3})_2(Sn_{1/3}Hf_{1/3}Zr_{1/3})_2O_7$	1.10	1.10	1.10	2.21 ± 0.07
P20	$(Sm_{1/3}Eu_{1/3}Gd_{1/3})_2(Ti_{1/4}Sn_{1/4}Hf_{1/4}Zr_{1/4})_2O_7$	1.10	1.39	1.24	1.67 ± 0.05
P20 + Yb	$(Sm_{1/4}Eu_{1/4}Gd_{1/4}Yb_{1/4})_2(Ti_{1/4}Sn_{1/4}Hf_{1/4}Zr_{1/4})_2O_7$	1.39	1.39	1.39	1.45 ± 0.04
P20-2	$(Sm_{1/3}Eu_{1/3}Gd_{1/3})_2(Ti_{1/2}Sn_{1/6}Hf_{1/6}Zr_{1/6})_2O_7$	1.10	1.24	1.17	1.71 ± 0.05
P20-3	$(Sm_{1/3}Eu_{1/3}Gd_{1/3})_2(Ti_{3/4}Sn_{1/12}Hf_{1/12}Zr_{1/12})_2O_7$	1.10	0.84	0.97	1.90 ± 0.06
P20-4	$(Sm_{1/3}Eu_{1/3}Gd_{1/3})_2Ti_2O_7$	1.10	0	0.55	2.88 ± 0.09
P20-5	$(Sm_{1/4}Eu_{1/4}Gd_{1/4}Yb_{1/4})_2(Ti_{1/2}Hf_{1/4}Zr_{1/4})_2O_7$	1.39	1.04	1.21	1.36 ± 0.04
P20-6	$(Sm_{3/4}Yb_{1/4})_2(Ti_{1/2}Zr_{1/2})_2O_7$	0.56	0.69	0.63	1.40 ± 0.04
P21	$(La_{1/5}Ce_{1/5}Nd_{1/5}Sm_{1/5}Eu_{1/5})_2Zr_2O_7$	1.61	0	0.80	2.06 ± 0.06
P22	$(La_{1/7}Ce_{1/7}Pr_{1/7}Nd_{1/7}Sm_{1/7}Eu_{1/7}Gd_{1/7})_2(Hf_{1/2}Zr_{1/2})_2O_7$	1.95	0.69	1.32	1.97 ± 0.06
P23	$(La_{1/7}Ce_{1/7}Pr_{1/7}Nd_{1/7}Sm_{1/7}Eu_{1/7}Gd_{1/7})_2(Sn_{1/3}Hf_{1/3}Zr_{1/3})_2O_7$	1.95	1.10	1.52	2.02 ± 0.06

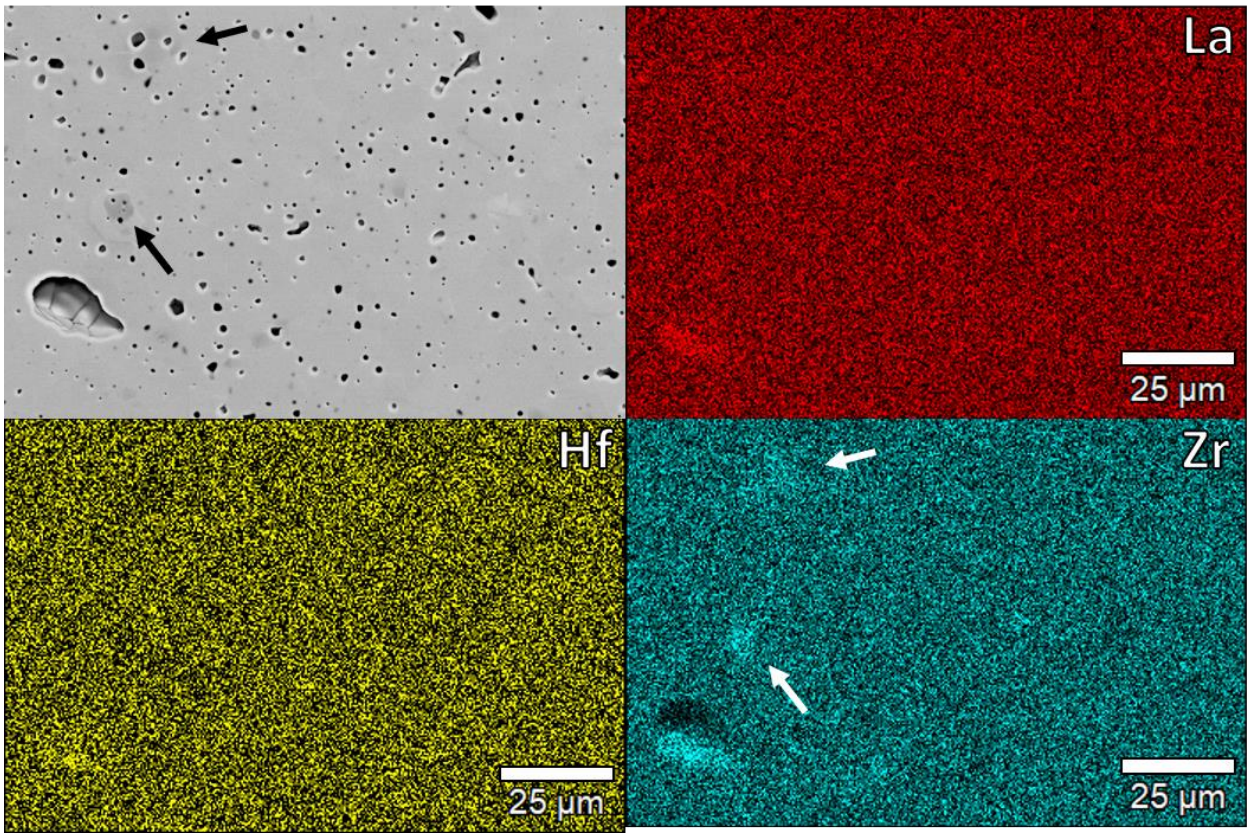

Figure 4.4. Small ZrO_2 inclusions (~ 5 µm) were found in composition P1 ($La_2(Hf_{1/2}Zr_{1/2})_2O_7$) resulting in a larger thermal conductivity than expected. Arrows point to the distinct ZrO_2 phase.

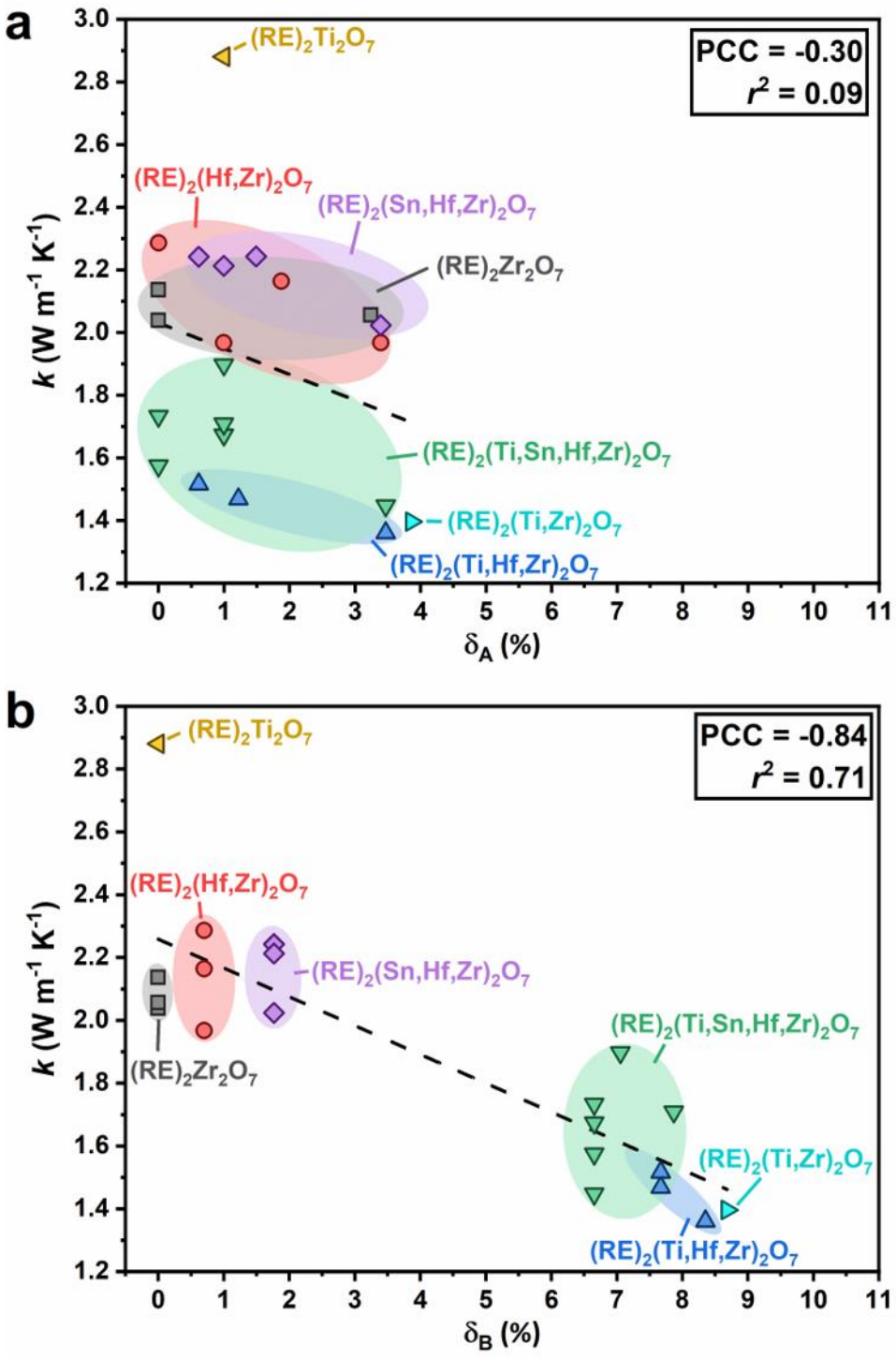

Figure 4.5. Separate correlations of thermal conductivity with the size disorder parameter on the (a) A-site and (b) B-site, respectively. The best-fit line for (a) is $k = -0.08\delta_A + 2.03\frac{W}{m\cdot K}$. The best-fit line for (b) is $k = -0.09\delta_B + 2.26\frac{W}{m\cdot K}$.

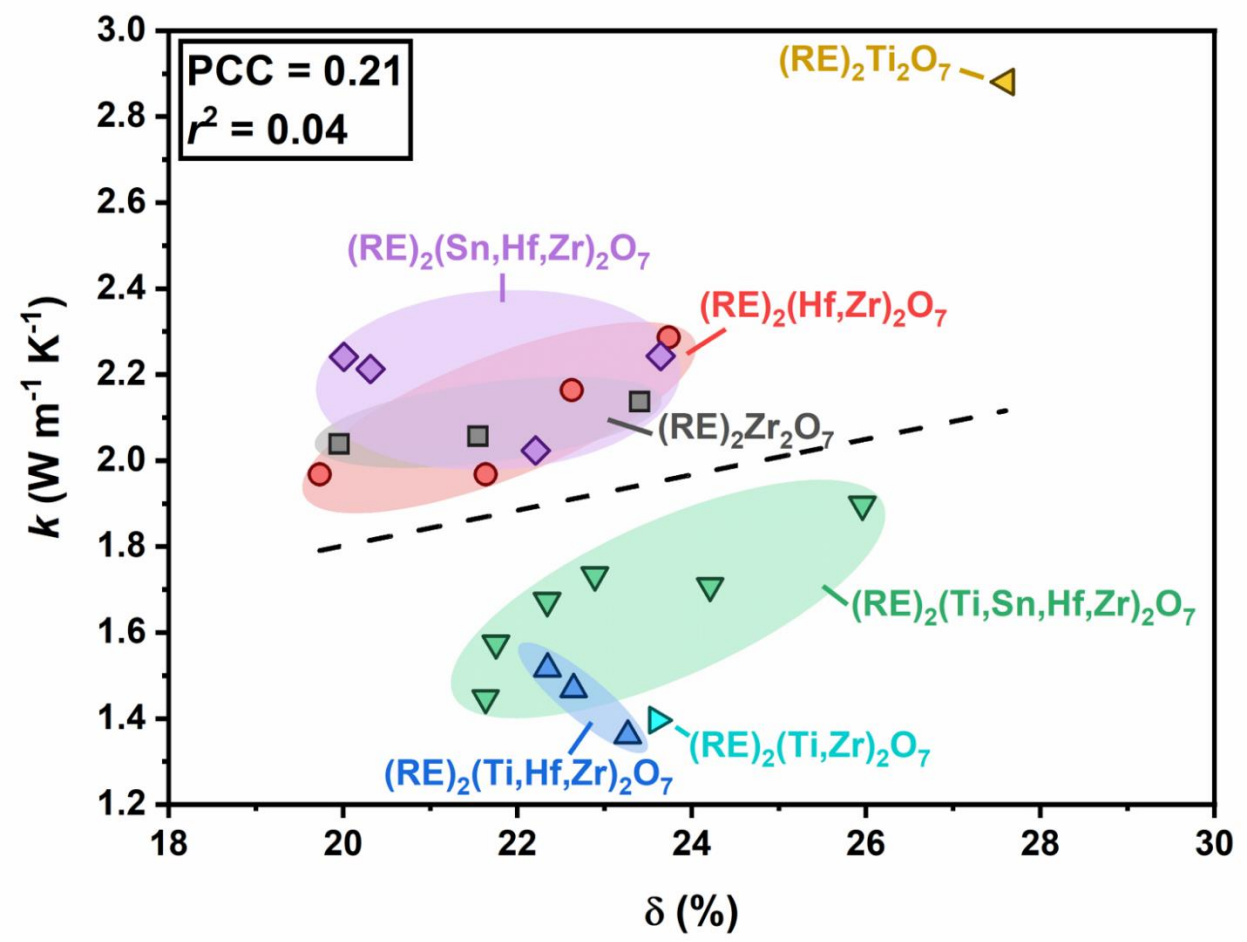

Figure 4.6. Correlation of thermal conductivity (k) with the size disorder parameter assuming a random (disordered) cation distribution in A-sites and B-sites. The best-fit line is $k = 0.04\delta + 0.98\frac{W}{m \cdot K}$.

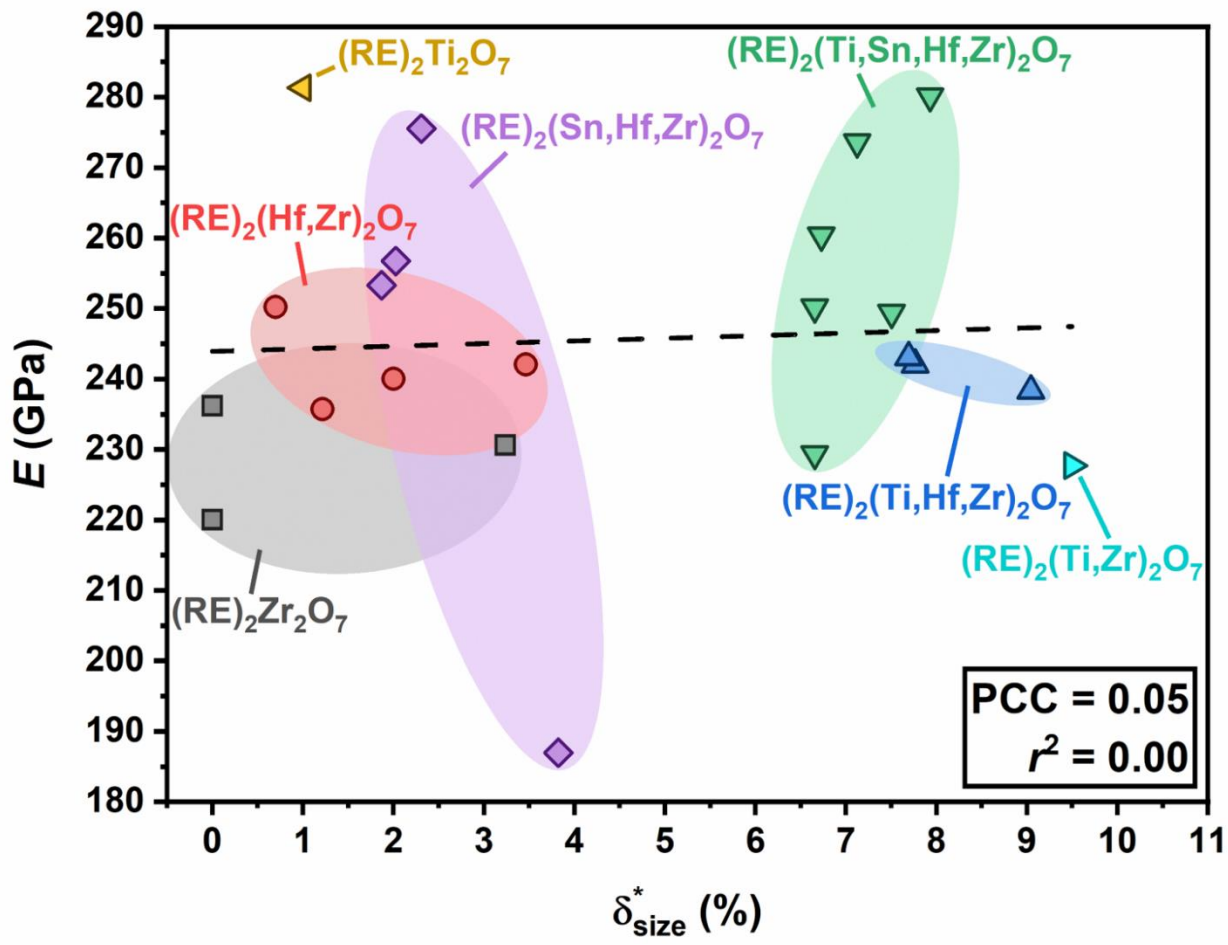

Figure 4.7. Correlation of Young's modulus (E) with the size disorder. The best-fit line is $E = 0.4\delta^*_{size} + 243.9\ GPa$.

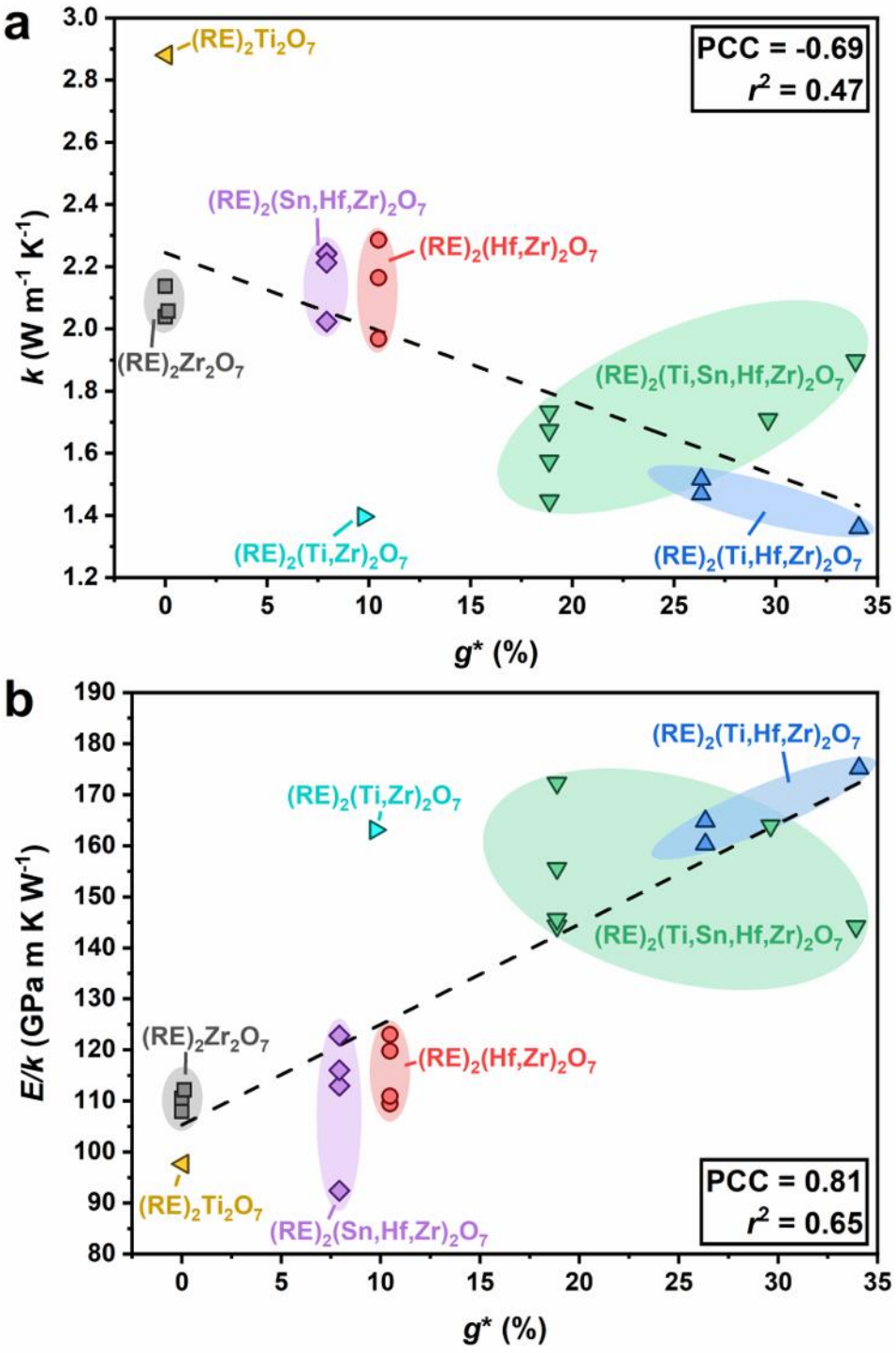

Figure 4.8. Correlations of (a) thermal conductivity (k) and (b) E/k with the calculated mass disorder parameter g^*. The best-fit line for (a) is $k = -0.02g^* + 2.24 \frac{W}{m \cdot K}$. The best-fit line for (b) is $^{E}/_{k} = 2.0g^* + 105.3 \frac{GPa \cdot m \cdot K}{W}$.

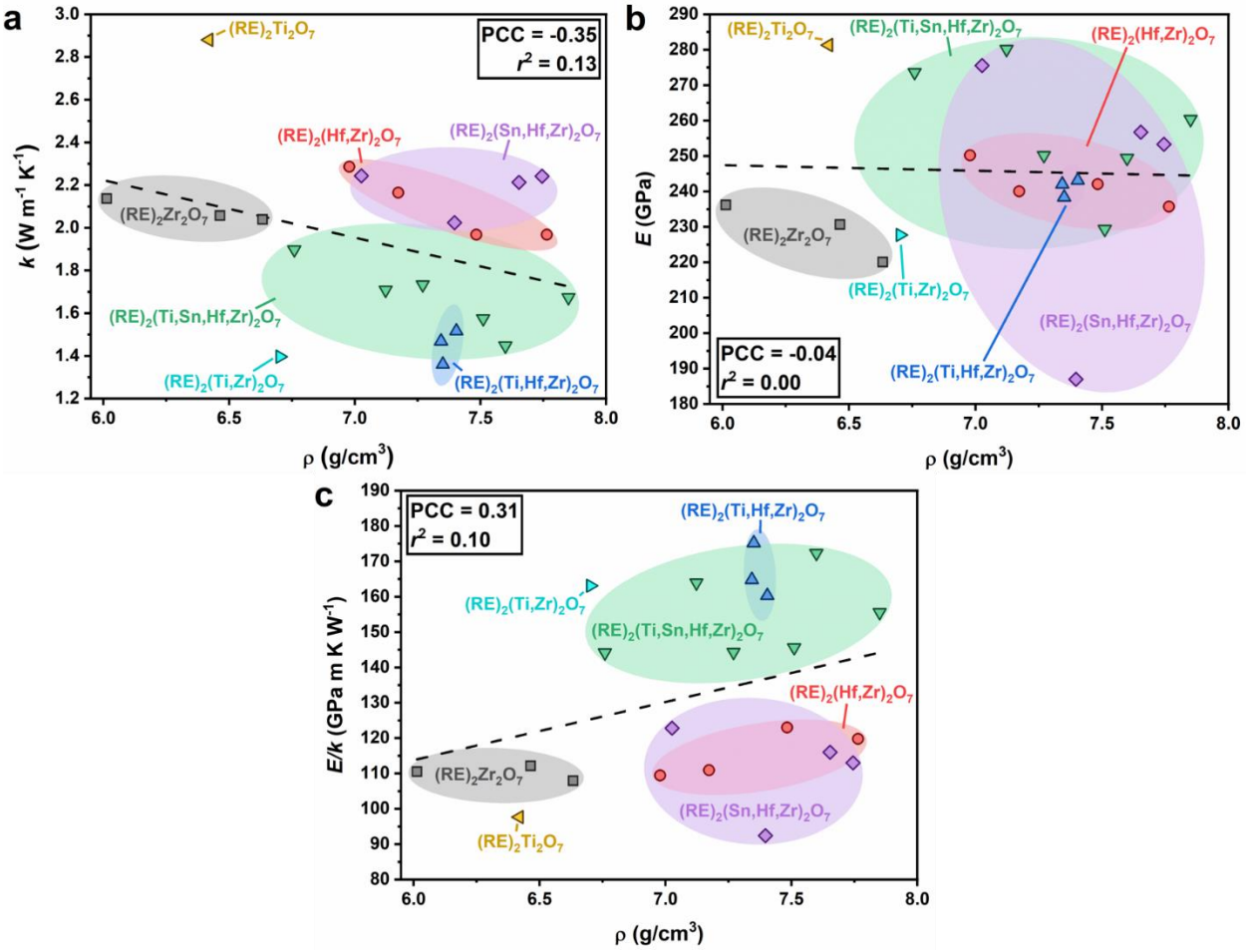

Figure 4.9. Correlations of (a) thermal conductivity (k), (b) Young's Modulus (E), and (c) E/k of with the density ρ. The best-fit line for (a) is $k = -0.27\rho + 3.84 \frac{W}{m \cdot K}$. The best-fit line for (b) is $E = -1.6\rho + 256.9\ GPa$. The best-fit line for (c) is ${}^{E}/_{k} = 16.4\rho + 15.2 \frac{GPa \cdot m \cdot K}{W}$.

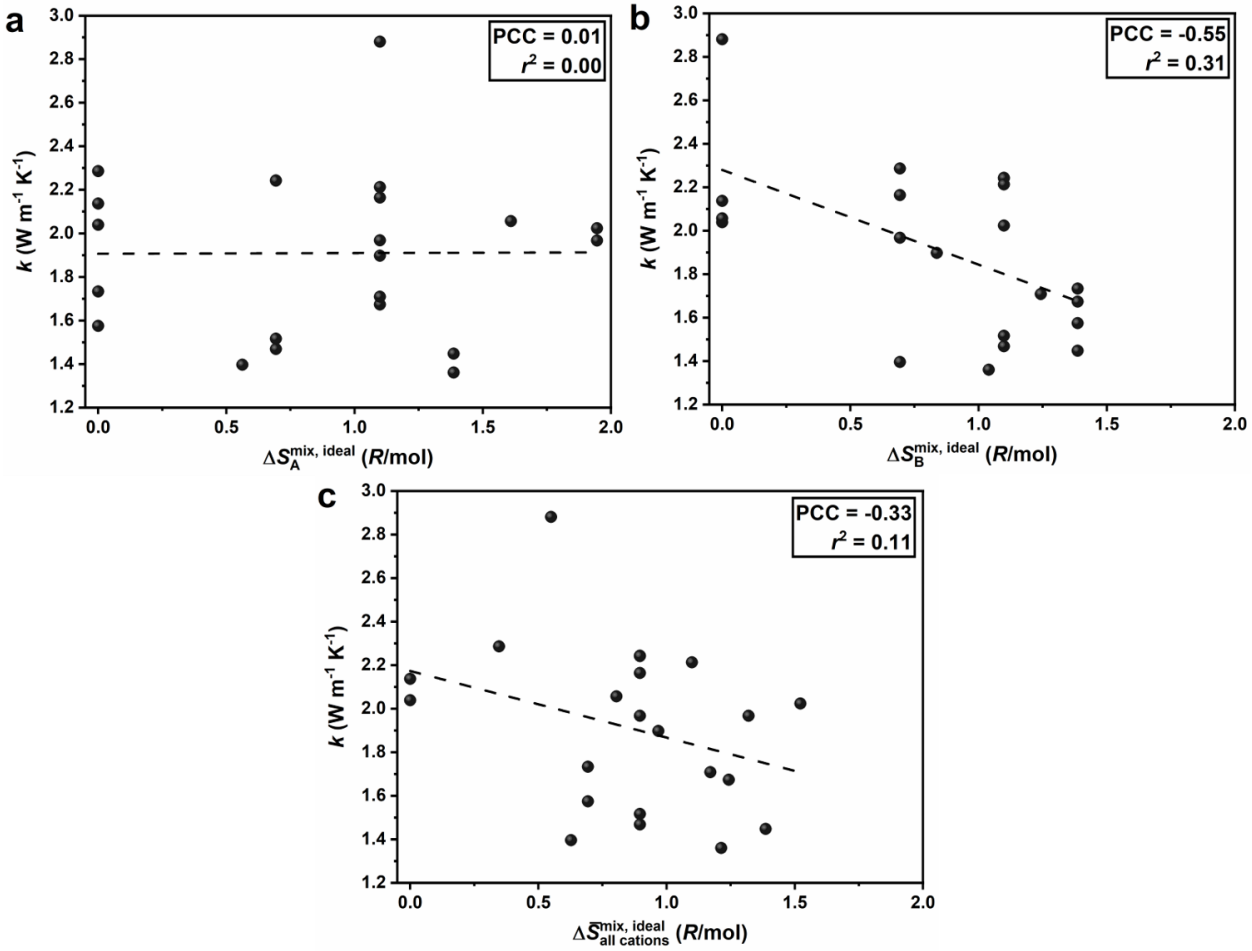

Figure 4.10. Correlations of thermal conductivity (k) with mixing entropies on (a) the A sublattice, $\Delta S_A^{mix,ideal}$, (b) the B sublattice, $\Delta S_B^{mix,ideal}$, and (c) the averaged value, $\bar{S}_{all\ cations}^{mix,ideal}$, all measured in R per mol. of metal cations. The best-fit line for (a) is $k = 1.91 \frac{W}{m \cdot K}$. The best-fit line for (b) is $k = -0.44 \Delta S_B^{mix,ideal} + 2.28 \frac{W}{m \cdot K}$. The best-fit line for (c) is $k = -0.31 \bar{S}_{all\ cations}^{mix,ideal} + 2.17 \frac{W}{m \cdot K}$.

4.5 REFERENCES

[1] C.M. Rost, E. Sachet, T. Borman, A. Moballegh, E.C. Dickey, D. Hou, J.L. Jones, S. Curtarolo, J.P. Maria, Entropy-stabilized oxides, Nat. Commun. 6 (2015) 1–8. doi:10.1038/ncomms9485.

[2] S. Jiang, T. Hu, J. Gild, N. Zhou, J. Nie, M. Qin, T. Harrington, K. Vecchio, J. Luo, A new class of high-entropy perovskite oxides, Scr. Mater. 142 (2018) 116–120. doi:10.1016/j.scriptamat.2017.08.040.

[3] J. Gild, M. Samiee, J.L. Braun, T. Harrington, H. Vega, P.E. Hopkins, K. Vecchio, J. Luo, High-entropy fluorite oxides, J. Eur. Ceram. Soc. 38 (2018) 3578–3584. doi:10.1016/j.jeurceramsoc.2018.04.010.

[4] Z. Zhao, H. Xiang, F.-Z. Dai, Z. Peng, Y. Zhou, (La0.2Ce0.2Nd0.2Sm0.2Eu0.2)2Zr2O7: A novel high-entropy ceramic with low thermal conductivity and sluggish grain growth rate, J. Mater. Sci. Technol. 35 (2019) 2647–2651. doi:10.1016/j.jmst.2019.05.054.

[5] F. Li, L. Zhou, J.-X. Liu, Y. Liang, G.-J. Zhang, High-entropy pyrochlores with low thermal conductivity for thermal barrier coating materials, J. Adv. Ceram. 8 (2019) 576–582. doi:10.1007/s40145-019-0342-4.

[6] J. Gild, Y. Zhang, T. Harrington, S. Jiang, T. Hu, M.C. Quinn, W.M. Mellor, N. Zhou, K. Vecchio, J. Luo, High-entropy metal diborides: A new class of high-entropy materials and a new type of ultrahigh temperature ceramics, Sci. Rep. 6 (2016) 37946. doi:10.1038/srep37946.

[7] E. Castle, T. Csanádi, S. Grasso, J. Dusza, M. Reece, Processing and properties of high-entropy ultra-high temperature carbides, Sci. Rep. 8 (2018) 8609. doi:10.1038/s41598-018-26827-1.

[8] P. Sarker, T. Harrington, C. Toher, C. Oses, M. Samiee, J.P. Maria, D.W. Brenner, K.S. Vecchio, S. Curtarolo, High-entropy high-hardness metal carbides discovered by entropy descriptors, Nat. Commun. 9 (2018) 1–10. doi:10.1038/s41467-018-07160-7.

[9] T.J. Harrington, J. Gild, P. Sarker, C. Toher, C.M. Rost, O.F. Dippo, C. McElfresh, K. Kaufmann, E. Marin, L. Borowski, P.E. Hopkins, J. Luo, S. Curtarolo, D.W. Brenner, K.S. Vecchio, Phase stability and mechanical properties of novel high entropy transition metal carbides, Acta Mater. 166 (2019) 271–280. doi:10.1016/j.actamat.2018.12.054.

[10] X. Yan, L. Constantin, Y. Lu, J.F. Silvain, M. Nastasi, B. Cui, (Hf 0.2 Zr 0.2 Ta 0.2 Nb 0.2 Ti 0.2)C high-entropy ceramics with low thermal conductivity, J. Am. Ceram. Soc. 101 (2018) 4486–4491. doi:10.1111/jace.15779.

[11] J. Gild, J. Braun, K. Kaufmann, E. Marin, T. Harrington, P. Hopkins, K. Vecchio, J. Luo, A high-entropy silicide: (Mo0.2Nb0.2Ta0.2Ti0.2W0.2)Si2, J. Mater. 5 (2019) 337–343. doi:10.1016/j.jmat.2019.03.002.

[12] Y. Qin, J.X. Liu, F. Li, X. Wei, H. Wu, G.J. Zhang, A high entropy silicide by reactive spark plasma sintering, J. Adv. Ceram. 8 (2019) 148–152. doi:10.1007/s40145-019-0319-3.

[13] X. Ren, Z. Tian, J. Zhang, J. Wang, Equiatomic quaternary (Y1/4Ho1/4Er1/4Yb1/4)2SiO5 silicate: A perspective multifunctional thermal and environmental barrier coating material, Scr. Mater. 168 (2019) 47–50. doi:10.1016/j.scriptamat.2019.04.018.

[14] Y. Dong, K. Ren, Y. Lu, Q. Wang, J. Liu, Y. Wang, High-entropy environmental barrier coating for the ceramic matrix composites, J. Eur. Ceram. Soc. 39 (2019) 2574–2579. doi:10.1016/j.jeurceramsoc.2019.02.022.

[15] J.W. Yeh, S.K. Chen, S.J. Lin, J.Y. Gan, T.S. Chin, T.T. Shun, C.H. Tsau, S.Y. Chang, Nanostructured high-entropy alloys with multiple principal elements: novel alloy design concepts and outcomes, Adv. Eng. Mater. 6 (2004) 299–303. doi:10.1002/adem.200300567.

[16] B. Cantor, I.T.H. Chang, P. Knight, A.J.B. Vincent, Microstructural development in equiatomic multicomponent alloys, Mater. Sci. Eng. A. 375 (2004) 213–218. doi:10.1016/j.msea.2003.10.257.

[17] D.B. Miracle, O.N. Senkov, A critical review of high entropy alloys and related concepts, Acta Mater. 122 (2017) 448–511. doi:10.1016/j.actamat.2016.08.081.

[18] N. Zhou, S. Jiang, T. Huang, M. Qin, T. Hu, J. Luo, Single-phase high-entropy intermetallic compounds (HEICs): bridging high-entropy alloys and ceramics, Sci. Bull. 64 (2019) 856–864. doi:10.1016/j.scib.2019.05.007.

[19] D. Bérardan, S. Franger, D. Dragoe, A.K. Meena, N. Dragoe, Colossal dielectric constant in high entropy oxides, Phys. Status Solidi - Rapid Res. Lett. 10 (2016) 328–333. doi:10.1002/pssr.201600043.

[20] D. Bérardan, S. Franger, A.K. Meena, N. Dragoe, Room temperature lithium superionic conductivity in high entropy oxides, J. Mater. Chem. A. 4 (2016) 9536–9541. doi:10.1039/c6ta03249d.

[21] Z. Fan, H. Wang, Y. Wu, X.J. Liu, Z.P. Lu, Thermoelectric high-entropy alloys with low lattice thermal conductivity, RSC Adv. 6 (2016) 52164–52170. doi:10.1039/c5ra28088e.

[22] A. Giri, J.L. Braun, P.E. Hopkins, Reduced dependence of thermal conductivity on temperature and pressure of multi-atom component crystalline solid solutions, J. Appl. Phys. 123 (2018) 015106. doi:10.1063/1.5010337.

[23] J.L. Braun, C.M. Rost, M. Lim, A. Giri, D.H. Olson, G.N. Kotsonis, G. Stan, D.W. Brenner, J.P. Maria, P.E. Hopkins, Charge-induced disorder controls the thermal conductivity of entropy-stabilized oxides, Adv. Mater. 30 (2018) 1805004. doi:10.1002/adma.201805004.

[24] R. Liu, H. Chen, K. Zhao, Y. Qin, B. Jiang, T. Zhang, G. Sha, X. Shi, C. Uher, W. Zhang, L. Chen, Entropy as a gene-like performance indicator promoting thermoelectric materials, Adv. Mater. 29 (2017) 1702712. doi:10.1002/adma.201702712.

[25] J. Yang, X. Qian, W. Pan, R. Yang, Z. Li, Y. Han, M. Zhao, M. Huang, C. Wan, Diffused lattice vibration and ultralow thermal conductivity in the binary Ln–Nb–O oxide system, Adv. Mater. 31 (2019) 1808222. doi:10.1002/adma.201808222.

[26] A.J. Wright, Q. Wang, C. Huang, A. Nieto, R. Chen, J. Luo, From high-entropy ceramics to compositionally-complex ceramics: A case study of fluorite oxides, J. Eur. Ceram. Soc. 40 (2020) 2120–2129. doi:10.1016/j.jeurceramsoc.2020.01.015.

[27] J. Wu, X. Wei, N.P. Padture, P.G. Klemens, M. Gell, E. García, P. Miranzo, M.I. Osendi, Low-thermal-conductivity rare-earth zirconates for potential thermal-barrier-coating applications, J. Am. Ceram. Soc. 85 (2004) 3031–3035. doi:10.1111/j.1151-2916.2002.tb00574.x.

[28] B. Liu, J.Y. Wang, F.Z. Li, Y.C. Zhou, Theoretical elastic stiffness, structural stability and thermal conductivity of La2T2O7 (T = Ge, Ti, Sn, Zr, Hf) pyrochlore, Acta Mater. 58 (2010) 4369–4377. doi:10.1016/j.actamat.2010.04.031.

[29] J.M. Pruneda, E. Artacho, First-principles study of structural, elastic, and bonding properties of pyrochlores, Phys. Rev. B. 72 (2005) 085107. doi:10.1103/PhysRevB.72.085107.

[30] J. Yang, M. Shahid, M. Zhao, J. Feng, C. Wan, W. Pan, Physical properties of La2B2O7(B=Zr, Sn, Hf and Ge) pyrochlore: First-principles calculations, J. Alloys Compd. 663 (2016) 834–841. doi:10.1016/j.jallcom.2015.12.189.

[31] W. Pan, S.R. Phillpot, C. Wan, A. Chernatynskiy, Z. Qu, Low thermal conductivity oxides, MRS Bull. 37 (2012) 917–922. doi:10.1557/mrs.2012.234.

[32] D.R. Clarke, S.R. Phillpot, Thermal barrier coating materials, Mater. Today. 8 (2005) 22–29. doi:10.1016/S1369-7021(05)70934-2.

[33] M.R. Winter, D.R. Clarke, Oxide materials with low thermal conductivity, J. Am. Ceram. Soc. 90 (2007) 533–540. doi:10.1111/j.1551-2916.2006.01410.x.

[34] R. Vassen, X. Cao, F. Tietz, D. Basu, D. Stöver, Zirconates as New Materials for Thermal Barrier Coatings, J. Am. Ceram. Soc. 83 (2004) 2023–2028. doi:10.1111/j.1151-2916.2000.tb01506.x.

[35] C. Wan, W. Zhang, Y. Wang, Z. Qu, A. Du, R. Wu, W. Pan, Glass-like thermal conductivity in ytterbium-doped lanthanum zirconate pyrochlore, Acta Mater. 58 (2010) 6166–6172. doi:10.1016/j.actamat.2010.07.035.

[36] Z.G. Liu, J.H. Ouyang, Y. Zhou, Structural evolution and thermophysical properties of (SmxGd1-x)2Zr2O7 ($0 \leq x \leq 1.0$) ceramics, J. Alloys Compd. 472 (2009) 319–324. doi:10.1016/j.jallcom.2008.04.042.

[37] Z. Qu, C. Wan, W. Pan, Thermal expansion and defect chemistry of MgO-doped Sm2Zr2O7, Chem. Mater. 19 (2007) 4913–4918. doi:10.1021/cm071615z.

[38] H. Zhang, K. Sun, Q. Xu, F. Wang, L. Liu, Thermal conductivity of (Sm1-xLax)2Zr2O7 (x=0, 0.25, 0.5, 0.75 and 1) oxides for advanced thermal barrier coatings, J. Rare Earths. 27 (2009) 222–226. doi:10.1016/S1002-0721(08)60223-9.

[39] C. Wan, Z. Qu, A. Du, W. Pan, Order-disorder transition and unconventional thermal conductivities of the (Sm1-xYbx)2Zr2O7 series, J. Am. Ceram. Soc. 94 (2011) 592–596. doi:10.1111/j.1551-2916.2010.04113.x.

[40] W. Pan, C.L. Wan, Q. Xu, J.D. Wang, Z.X. Qu, Thermal diffusivity of samarium-gadolinium zirconate solid solutions, Thermochim. Acta. 455 (2007) 16–20. doi:10.1016/j.tca.2006.12.001.

[41] Y. Wang, F. Yang, P. Xiao, Rattlers or oxygen vacancies: Determinant of high temperature plateau thermal conductivity in doped pyrochlores, Appl. Phys. Lett. 102 (2013) 141902. doi:10.1063/1.4801319.

[42] C. Wan, Z. Qu, A. Du, W. Pan, Influence of B site substituent Ti on the structure and thermophysical properties of A2B2O7-type pyrochlore Gd2Zr2O7, Acta Mater. 57 (2009) 4782–4789. doi:10.1016/j.actamat.2009.06.040.

[43] J. Garg, N. Bonini, B. Kozinsky, N. Marzari, Role of disorder and anharmonicity in the thermal conductivity of silicon-germanium alloys: A first-principles study, Phys. Rev. Lett. 106 (2011) 045901. doi:10.1103/PhysRevLett.106.045901.

[44] J. Garg, G. Chen, Minimum thermal conductivity in superlattices: A first-principles formalism, Phys. Rev. B. 87 (2013) 140302. doi:10.1103/PhysRevB.87.140302.

[45] Y. Zhang, Y.J. Zhou, J.P. Lin, G.L. Chen, P.K. Liaw, Solid-solution phase formation rules for multi-component alloys, Adv. Eng. Mater. 10 (2008) 534–538. doi:10.1002/adem.200700240.

[46] C.S. Wu, P.H. Tsai, C.M. Kuo, C.W. Tsai, Effect of atomic size difference on the microstructure and mechanical properties of high-entropy alloys, Entropy. 20 (2018) 967. doi:10.3390/e20120967.

[47] R.D. Shannon, Revised Effective Ionic Radii and Systematic Studies of Interatomie Distances in Halides and Chaleogenides bond strength-bond length relationships , and plots of (1) radii vs volume , (2) radii vs coordination partial occupancy of cation sites , coval, Acta Crystallogr. A32 (1976) 751.

[48] ASTM International, C373-18 Standard Test Methods for Determination of Water Absorption and Associated Properties by Vacuum Method for Pressed Ceramic Tiles and Glass Tiles and Boil Method for Extruded Ceramic Tiles and Non-tile Fired Ceramic Whiteware Products, West Conshohocken, PA, 2018. doi:10.1520/C0373-16.2.

[49] I. Barin, Thermochemical Data of Pure Substances, VCH, Weinheim, 1995. doi:10.1016/s0165-2427(96)05632-2.

[50] ASTM International, ASTM C1198-09: Standard test method for dynamic Young's modulus, shear modulus, and Poisson's ratio for advanced ceramics by sonic resonance, Annu. B. ASTM Stand. 09 (2013) 1–11. doi:10.1520/C1198-09R13.2.

[51] R.W. Rice, Porosity of Ceramics: Properties and Applications, CRC Press, 1998. doi:10.1017/CBO9781107415324.004.

[52] E.A. Dean, J.A. Lopez, Empirical dependence of elastic moduli on porosity for ceramic materials, J. Am. Ceram. Soc. 66 (1983) 366–370. doi:10.1111/j.1151-2916.1983.tb10051.x.

[53] Y. Zhang, M. Xie, F. Zhou, X. Cui, X. Lei, X. Song, S. An, Low thermal conductivity in La2Zr2O7 pyrochlore with A-site partially substituted with equimolar Yb2O3 and Er2O3, Ceram. Int. 40 (2014) 9151–9157. doi:10.1016/j.ceramint.2014.01.130.

[54] Y. Wang, F. Yang, P. Xiao, Role and determining factor of substitutional defects on thermal conductivity: A study of La2(Zr1-xB x)2O7 (B = Hf, Ce, $0 \leq x \leq 0.5$) pyrochlore solid solutions, Acta Mater. 68 (2014) 106–115. doi:10.1016/j.actamat.2014.01.011.

[55] M.C. Roufosse, P.G. Klemens, Thermal conductivity of complex dielectric solids, Phys. Rev. B. 7 (1973) 5379. doi:10.1007/978-1-4899-3751-3_30.

[56] D.R. Clarke, Materials selections guidelines for low thermal conductivity thermal barrier coatings, Surf. Coatings Technol. 163–164 (2003) 67–74. doi:10.1016/S0257-8972(02)00593-5.

[57] P.K. Schelling, S.R. Phillpot, R.W. Grimes, Optimum pyrochlore compositions for low thermal conductivity, Philos. Mag. Lett. 84 (2004) 127–137. doi:10.1080/09500830310001646699.

[58] L. Minervini, R.W. Grimes, K.E. Sickafus, Disorder in pyrochlore oxides, J. Am. Ceram. Soc. 83 (2004) 1873–1878. doi:10.1111/j.1151-2916.2000.tb01484.x.

5. SINGLE-PHASE DUODENARY HIGH-ENTROPY FLUORITE/PYROCHLORE OXIDES WITH AN ORDER-DISORDER TRANSITION

5.1 INTRODUCTION

High-entropy ceramics (HECs), including rocksalt [1], perovskite [2], fluorite [3], and pyrochlore [4,5] oxides, borides [6,7], carbides [8–11], and silicides [12,13] have attracted great research interests. Recently, it is further proposed to broaden HECs to compositionally-complex ceramics (CCCs) [14–16]. The majority of the past studies focused on HECs with about five (sometimes four, and, in a few cases, six) cations. Here, the only few exceptions are represented by high-entropy ABO_3 perovskite $(Gd_{1/5}La_{1/5}Nd_{1/5}Sm_{1/5}Y_{1/5})(Co_{1/5}Cr_{1/5}Fe_{1/5}Mn_{1/5}Ni_{1/5})O_3$ [17] and high-entropy $A_2B_2O_7$ pyrochlore $(La_{1/7}Ce_{1/7}Pr_{1/7}Nd_{1/7}Sm_{1/7}Eu_{1/7}Gd_{1/7})_2(Sn_{1/3}Hf_{1/3}Zr_{1/3})_2O_7$ [18], where 10 metal cations are distributed over two cation sublattices. However, each of these two studies only included one 10-cation composition, and both cases are ordered phases only (so there are 3-7 cations in each sublattices). Notably, no systematic study has been reported to investigate how the change in composition affects the phase stability (particularly cation order and disorder) and subsequently the properties of such many-cation HECs.

One distinct property of HECs and CCCs is represented by their reduced thermal conductivities that have been observed across nearly all systems examined [3–5,12,15,16,19–31]. This is presumably due to the increased disorder in mass, size, and valency in solid solutions with five or more different cations [16,27,32–35]. From the materials science point of view, reduced thermal conductivities typically come at the expense of Young's modulus [14,27]. For HECs, the modulus appears to be retained while the thermal conductivity is remarkably reduced [12,15,16,22,27,28], thereby being scientifically interesting and technologically useful.

Fluorite and pyrochlore oxides demonstrate the lowest potential thermal conductivities

(k's) with values approaching 1 $W \cdot m^{-1} \cdot K^{-1}$ [16,36–38]. With their Young's moduli (E) of 200-250 GPa, these oxides exhibit the highest E/k ratios so far [15,16,36]. Various traditional (typically ternary) fluorite or pyrochlore oxides have widely been used or examined as thermal barrier coatings (TBCs) [39–45]. The pyrochlore and fluorite crystal structures have a direct connection to each other through an order-disorder transition (ODT) of the cations and anions [46–51]. Previous studies have examined this ODT through diffraction techniques and the measurement of ionic and thermal conductivities [44,52–58]. However, all these prior studies were conducted on simpler ternary (and occasionally quaternary) oxides. The ODT in HECs, which has the potential for opening a new window to tailor thermomechanical properties, has not been examined.

In this study, we first synthesized a series of duodenary (11 metals + oxygen) oxides by mixing a five-cation disordered fluorite niobate and a seven-cation ordered pyrochlore oxide (both containing Yb) with negligible lattice constant and density mismatch. Here, we use "duodenary oxides" to refer to oxides with 11 unique metal cations (12 elements including oxygen), similar to the terminology in literature: "binary (or ternary) oxides," referring to oxides with one (or two) metal cation(s) plus oxygen. The focus and novelty of this study lies in the first investigation of an ODT in HECs with changing composition and its influence on thermomechanical properties, along with the first investigation of a series of duodenary HECs with systematic compositional variation. An abnormal increase in Young's modulus above the rule of mixture (RoM) is observed, and it abruptly occurs at low doping levels. Consequently, the E/k ratio also increases above the RoM of the two endmembers.

5.2 PYROCHLORE VS. FLUORITE AND ORDER-DISORDER TRANSITION (ODT)

Figure 5.1 highlights the differences between the pyrochlore and fluorite phases and three

conventional routes to induce the ODT. The ideal pyrochlore (space group 227, $Fd\bar{3}m$) is an ordered (cations and anions) $2 \times 2 \times 2$ variant of the disordered fluorite unit cell. This ordered $A_2B_2O_7$ pyrochlore structure, where the AO_8 polyhedral is a distorted scalenohedron and the BO_6 polyhedral is a perfect octahedron, is signified by the 48*f* oxygen positional parameter $x = 0.3125$. Disordering initiates as the 48*f* site migrates towards $x = 0.375$ (or 3/8, the ideal oxygen position in a disordered fluorite phase [48]). It is energetically unfavorable for the 48f oxygen in the pyrochlore phase to have x≳0.36 due to an increasing O-O repulsive force. Instead, the 48*f* oxygen begin to populate the 8*a* vacancy sites, thus initiating the disordering process [53]. In the disordered fluorite structure, the AO_8 polyhedral become a perfect cube while the BO_6 polyhedral becomes a distorted octahedron. However, this is never reached as the cations disorder form one average polyhedral of $(A, B)O_7$.

The three most common routes to induce the ODT are via increasing temperature, the difference in the cation radii, and nonstoichiometry [59]. First, most rare earth zirconate and hafnate pyrochlores undergo temperature-induced disordering transition at ≥1600℃ [60]. Second, the ordered pyrochlore structure is preferred if the size difference between the A- and B-site cations is significant, while the disordered fluorite structure is preferred if the cations are of similar radii. Here, the critical radius ratio for the ODT is approximately 1.46 (disordering if $r_A^{VIII}/\, r_B^{VI} <$ ~1.46), where the radii of the A- and B-site are assumed to be eight- and six-coordinated [50,59]. Third, non-stoichiometry arising from an imbalance in the concentration of A- and B-site cations, of the form $A_{2\pm y}B_{2\pm y}O_{7\pm\delta}$, can induce an ODT. For rare earth zirconates and hafnates, the ODT (disordering) occurs when $y > \ 0.1 - 0.2$ [60].

5.3 EXPERIMENTAL PROCEDURES

5.3.1 DESIGN OF COMPOSITIONS

On one side, we selected $[(Sm_{0.25}Eu_{0.25}Gd_{0.25}Yb_{0.25})_2(Ti_{0.5}Hf_{0.25}Zr_{0.25})_2O_7]_{1-x}$ (denoted as P1) and its two variations (with different atomic fractions on the B site, denoted as P1' and P1") in the ordered pyrochlore structure that we have investigated recently [16] as one (ordered pyrochlore) endmember. They are the high-entropy version of the rare earth (RE)-stabilized zirconia $(RE^{3+})_2(Zr^{4+})_2O_7$ or hafnia $(RE^{3+})_2(Hf^{4+})_2O_7$ that are commonly used in TBCs.

On the other side, we made fluorite-structured $[(Sc_{0.266}Dy_{0.248}Tm_{0.246}Yb_{0.240})_3NbO_7]_x$ (N1) $[(Sc_{0.333}Dy_{0.226}Tm_{0.224}Yb_{0.218})_3NbO_7]_{0.5}$ (N1'), and $[(Y_{0.266}Dy_{0.248}Tm_{0.246}Yb_{0.240})_3NbO_7]_{0.5}$ (N2) as the other (disordered fluorite) endmember. They are the high-entropy version of rare earth niobates $(RE^{3+})_3(Nb^{5+})O_7$ in disordered fluorite structure (space group 225, $Fm\bar{3}m$), where both the cations and 1/8 oxygen vacancies per unit cell are disordered. These rare earth niobates have ultralow thermal conductivities [36–38]. Noting that the specific compositions were designed so there are matches in both lattice parameters and densities of the two endmembers.

We then fabricated duodenary high-entropy oxides by mixing three pairs of endmembers. In the P1N1 series, we mixed P1: $[(Sm_{0.25}Eu_{0.25}Gd_{0.25}Yb_{0.25})_2(Ti_{0.5}Hf_{0.25}Zr_{0.25})_2O_7]_{1-x}$ and N1: $[(Sc_{0.266}Dy_{0.248}Tm_{0.246}Yb_{0.240})_3NbO_7]_x$ in the volumetric ratios of 100:0, 98:2, 90:10, 75:25, 50:50, 25:75, 10:90, 2:98, and 0:100, respectively. Here, for example, P1N1 50:50 refers the composition mixed $(P1)_{50}(N1)_{50}$ (but it is a single-phase pyrochlore after the mixing). We also made two extra compositions, P1'N1' 50:50 [= $(P1')_{50}(N1')_{50}$] and P1"N2 50:50 [= $(P1")_{50}(N2)_{50}$], where P1', P1" and N1' are derivative compositions of P1 and N1 with varying atomic ratios, and N2 is another high-entropy niobate of different cation combination (with Y to replace Sc in N1/N1'). The compositions and nomenclatures of all specimens studied is in Table 5.1. It is

important to emphasize that all nine mixed compositions are single-phase (either fluorite- or pyrochlore-structured) high-entropy solid solutions after mixing.

5.3.2 MATERIALS AND SYNTHESIS

The specimens were consolidated by first synthesizing the pure phase of the high-entropy pyrochlore (P1, P1', and P1") and high-entropy niobate (N1, N1' and N2) endmembers in parallel. For each endmember, stoichiometric amounts of the constituent binary oxides with particle sizes of ~5 μm (purchased from US Research Nanomaterials) were weighed with 0.01 mg precision (Secura125-1S, Sartorius, Germany). A total of 15 g was weighed for the desired composition and placed in a 100 ml Y-stabilized ZrO_2 (YSZ) planetary mill jar. YSZ grinding media was added to the jar in a ball-to-powder mass ratio of 10:1. Ten milliliters of ethanol was also added to the jar. The jar was planetary milled at 300 RPM for 24 h (PQN04, Across International, United States). The contents were transferred to a 1 L glass beaker and dried at 85°C overnight. The dried powder was collected, pressed in a 1” stainless steel die, and calcined at 1600°C for 12 h. These specimens of endmembers were then coarsely ground back into a powder with an agate mortar and pestle.

The coarse single-phase powders of two endmembers were then mixed in the desired volume ratios for a total weight of 2 g. The mixed powders were placed in a poly(methyl methacrylate) high-energy ball mill (HEBM) vial with tungsten carbide (WC) inserts and one Ø5/16” WC ball. Additionally, 2 wt% stearic acid was added to the vial to serve as a lubricant and binder. The vials were dry-milled for 100 minutes (SPEX 8000D, SPEX SamplePrep, USA). Following milling, the powders were uniaxially pressed in a Ø13 mm stainless steel die and placed on Pt foil in an Al_2O_3 crucible to undergo sintering in air at 1600°C for 24 h. Lastly, the sintered pellets were ground with a 30 μm diamond disc before characterization.

5.3.3 CHARACTERIZATION

5.3.3.1 X-RAY DIFFRACTION (XRD) AND DENSITY (ρ)

A Miniflex II XRD (Rigaku, Japan) operating at 30 kV and 15 mA was used to collect data on specimens at 0.02° 2θ steps for 2θ of 20 – 90° with a 2 s dwell time per step. Rietveld refinements through GSAS-II [61] were used to obtain the lattice constant and theoretical density.

The bulk density (ρ) of each specimen was determined through the boiling method abiding by the ASTM Standard C373-18 [62]. The relative density was computed by dividing the measured bulk density by the theoretical density. All specimens were found to have relative densities within 96-99 %, except for P1"N2 50-50 with a lower relative density of 91.3 %.

5.3.3.2 SCANNING ELECTRON MICROSCOPY (SEM)

Specimens were hot-mounted in acrylic and polished to 40 nm colloidal silica. A scanning electron microscope (SEM, FEI Apreo, OR, USA) operating at 20 kV was used to examine the microstructure. Elemental maps were generated through energy dispersive spectroscopy (EDS, Oxford N-Max^{N}) to probe the compositional homogeneity.

5.3.3.3 SCANNING TRANSMISSION ELECTRON MICROSCOPY (STEM)

Scanning transmission electron microscopy (STEM) were prepared by a dual-beam focused ion beam (FIB, FEI Scios DualBeam, OR, USA). A 300 kV, double aberration-corrected STEM (JEOL JEM-ARM300CF, Japan) scope was used to generate atomic resolution images with a high-angle annular dark-field (HAADF) detector of an inner collection angle ~ 80 mrad. Atomic resolution EDS elemental maps were collected over five minutes with a probe current of ~ 300 pA. The STEM-HAADF image was passed through the default bandpass filter available through Gatan Microscopy Suite 3.3 (GMS 3.3, Gatan, CA, USA). A radial Wiener filter was

used to reduce the noise of the EDS elemental maps. The GMS 3.3 plug-in was available in a free software package offered by HREM Research Inc.

5.3.3.4 YOUNG'S MODULUS (E)

The Young's modulus of the specimens was determined through a pulse-echo sonic resonance setup following the ASTM Standard C1198-20 [63]. The longitudinal (u_L) and transverse (u_T) wave speeds were determined for each of the specimens. Poisson's ratio (ν) and Young's modulus were determined from Eqs. (1) and (2) below:

$$\nu = \frac{u_L^2 - 2u_T^2}{2(u_L^2 - u_T^2)} \tag{1}$$

$$E_{measured} = 2u_T^2\rho(1+\nu) \tag{2}$$

The modulus was corrected for porosity [64] through Eq. (3):

$$E = \frac{E_{measured}}{1 - 2.9P} \tag{3}$$

Here, P is the fraction of pores.

5.3.3.5 THERMAL CONDUCTIVITY (k)

The thermal diffusivity (α) was measured at 25°C and then from 200°C – 1000°C in 200°C steps through laser flash analysis (LFA 467 HT HyperFlash, NETZSCH, Germany). Before measurement, the specimens had a carbon coating sprayed onto the top and bottom surfaces to maximize laser absorption and infrared emission. The values obtained from T>200°C were corrected for external radiation. However, internal radiation is still present as it is inherent to the specimen [65]. The Neumann-Kopp rule was used to estimate the specific heat capacity (c_p) using tabulated values of the constituent binary oxides [66]. The thermal conductivity (k) was determined through the product of thermal diffusivity, density, and specific heat capacity, as shown in Eq. (4).

$$k_{measured} = \alpha \rho c_p \quad (4)$$

Similarly to the modulus, the thermal conductivity was corrected for porosity [67] by Eq. (5).

$$k = \frac{k_{measured}}{(1-P)^{3/2}} \quad (5)$$

5.4 RESULTS AND DISCUSSION

5.4.1 FORMATION OF SINGLE HIGH-ENTROPY PHASES AND ODT

The pyrochlore endmember P1 (P1N1 100-0) came from a prior publication from our group, $(Sm_{1/4}Eu_{1/4}Gd_{1/4}Yb_{1/4})_2(Ti_{1/2}Hf_{1/4}Zr_{1/4})_2O_7$, which displayed an attractive E/k ratio ($175.2\ \frac{GPa \cdot m \cdot K}{W}$) [16]. The N1 (P1N1 0-100) high-entropy niobate, $(Sc_{0.266}Dy_{0.248}Tm_{0.246}Yb_{0.240})_3NbO_7$, was designed so that the lattice parameter was half that of the pyrochlore ($a_{N1} = \frac{1}{2}a_{P1} = 5.163$ Å) and the densities were identical ($\rho_{P1} = \rho_{N1} = 7.37\ g/cm^3$). This was designed to remove any potential effects from lattice and density mismatch. A calibration curve (Figure S5.1 in Suppl. Data) was used to determine the elements and exact molar amounts to obtain desired lattice parameters and densities. The pyrochlore calibration curve was generated by data from a prior publication from our group [16] while the niobate calibration curve is unpublished.

The XRD patterns of the P1N1 series are shown in Figure 5.2(a). Figure 5.2(b) shows the logarithmic intensity of the peak evolution of the (331) superstructure peak for the ordered pyrochlore phase. All specimens exhibit a single high-entropy solid solution phases (of either pyrochlore or fluorite structure). No visible secondary phase peak was present in any XRD patterns. It is evident that the lattice parameter variation is negligible in this series with changing *x* in the mixed $P1_{1-x}N1_x$ compositions.

The formation of single high-entropy phase is further supported by the compositional and microstructural homogeneity. For example, Figure 5.3 shows the microstructure of the polished cross-section along with the elemental maps for all the cations for P1N1 50:50. The backscattered electron image shows no distinct contrast from different mass (Z) beyond slight grain contrast. The grain size is ~10-20 μm. The EDS elemental maps suggest the material is homogenous, albeit slight Zr agglomeration. The overall metal cation composition was quantified and compared to theoretical values calculated through the stoichiometry. Both values are in excellent agreement, and differences are within the EDS errors. Additional EDS elemental maps are shown in Suppl. Figs. 5.2 and 5.3, which all suggest homogenous compositions (that agreed with theoretical/nominal values) supporting the formation of single high-entropy phases.

Notably, the pyrochlore structure vanishes (*i.e.*, with an ODT) slightly above x = 75 % (*i.e.*, the (331) superstructure peak is barely observed in P1N1 75:25 but disappears in P1N1 90:10). EDS elemental mapping confirmed that the compositions are homogenous in both the pyrochlore (Suppl. Fig. S5.2 for P1N1 25-75) and fluorite (Suppl. Fig. S5.3 for P1N1 10-90) phases just before and after the occurrence of the ODT.

5.4.2 ATOMIC-RESOLUTION STRUCTURE AND COMPOSITION

To further characterize the atomic resolution structure and composition, particularly the distribution of cations like Sc in A vs. B sublattice in the ordered $A_2B_2O_7$ pyrochlore phase, a TEM lamella of the specimen P1N1 50-50 was prepared by FIB-SEM lift-out. In the STEM, the specimen was tilted to the [110] zone axis because it is the lowest index where A- and B-sites can be separated. The low magnification STEM-HAADF image in Figure 5.4(a) shows structural homogeneity with no observable nanodomains and clustering.

The higher magnification image in Figure 5.4(b) reveals the different Z contrast from

different sites in the pyrochlore structure due to larger, higher Z (brighter) atoms on the A-site and smaller, lower Z elements on the B-site. A simulated STEM image was generated from a 10×10×10 supercell and compared to the raw STEM-HAADF image, which shows a good match of the intensity modulations from the alternating A-site and mixed-site rows.

A schematic Figure 5.4(c) and (d) further show the EDS collection area and the bandpass filtered STEM-HAADF image, which makes the site contrast clearer along with the filtered elemental maps for Yb and Sc as an example for an A- and B-site cation. The elemental maps suggest that Yb atoms are on A-site and Sc are on the B-site, respectively. Note that Sc is the only element with some ambiguity on which site to occupy sole based on the atomic radius. Here the atomic resolution element map directly confirm that Sc atoms sit on B-site.

In summary, the STEM-HAADF-EDS, in conjunction with the SEM-EDS and XRD, unequivocally showed the formation of an ordered single high-entropy pyrochlore phase in P1N1 50:50, with compositional homogeneity at both micrometer and atomic scale, and it further clarified that Sc occupies the B-site the ordered $A_2B_2O_7$ pyrochlore.

5.4.3 SC INFLUENCE ON ORDER VS. DISORDER

Upon adding the high-entropy niobate endmember into the high-entropy pyrochlore, it is well expected that the large 3+ rare earth *f*-elements, such as Dy, Tm, and Yb, prefer the A-site of the pyrochlore structure where Sm, Eu, Gd, and Yb already reside. Niobium ($r_{Nb}^{VI} = 0.64$ Å) can then be assumed to go to the B-site where Ti ($r_{Ti}^{VI} = 0.605$ Å), Zr ($r_{Zr}^{VI} = 0.72$ Å), and Hf ($r_{Hf}^{VI} = 0.71$ Å) [68] are since these cations are relatively small. The preferred site of Sc is the only one in question. The Sc cation has a 3+ valency that is suited for the A-site, but it is also small enough to fit on the B-site ($r_{Sc}^{VI} = 0.745$ Å). Prior studies (albeit not on high-entropy compositions) by Allpress and Rossell concluded that Sc has little tendency to enter the A-site in

the pyrochlore structure [69]. When excess Sc was added to the pyrochlore structure, Sc precipitated out in a second phase before any amount significantly entered the A-site. Our atomic resolution STEM-EDS analysis directly confirmed that Sc atoms sit on the B-site.

In addition to its small size, the occupation of Sc on B-site also helps to keep stoichiometric A/B ratio and the mixing of Sc^{3+} and Nb^{5+} cations on the B-site also supplies a charge balance (to the average of 4+ in normal pyrochlore); both will be ideally maintained if Sc^{3+} and Nb^{5+} atomic fractions are 1/4 in the high-entropy niobate endmember. However, there is less Sc^{3+} cations in the N1 endmember. This implies that other, larger, rare earth elements have to fill some of the B-site in the P1N1 series, which will destabilize the pyrochlore structure and promote disorder.

To test this hypothesis, two additional fluorite-structured high-entropy niobate endmembers (N1' and N2) were designed and synthesized. The first one modified P1N1 0-100 by increasing the concentration of Sc to 25% of the total cations in the high-entropy niobate endmember N1': $(Sc_{0.333}Dy_{0.226}Tm_{0.224}Yb_{0.218})_3NbO_7$ to enable equiatomic Sc^{3+} and Nb^{5+} cations on the B-site as well as the ideal 1:1 A/B stoichiometric ratio. In the second case, we replaced the Sc with Y to make a Sc-free high-entropy niobate endmember N2: $(Sc_{0.266}Dy_{0.248}Tm_{0.246}Yb_{0.240})_3NbO_7$. Subsequently, both N1' and N2 were mixed in a 50:50 vol. % ratio with designed P1' and P2" (variations of P1 with different cation ratios to ensure negligible lattice and density mismatch).

The XRD results of these two duodenary oxides are shown in Figure 5.5. As expected, the P1'N1' 50-50 that enables the ideal 1:1 A/B stoichiometric ratio with an equal amount of Sc and Nb in B-site possessed the ordered pyrochlore phase. On the other hand, the Sc-free P1"N2 50-50 become disordered fluorite structure (because larger rare earth elements would have to occupy at least 25% B-site to destabilize the ordered $A_2B_2O_7$ structure if it were pyrochlore).

5.4.4 PYROCHLORE STABILITY RULES

We may further explore how the ODT rules obtained from simpler ternary and quaternary oxides transform to many-component (such as duodenary) high-entropy oxides. As we have discussed in §2 and schematically shown in Figure 5.1, the three common routes to induce a pyrochlore to fluorite transformation or ODT are through increasing temperature, size ratio (r_A/r_B), and nonstoichiometry (A/B).

The temperature effect was not investigated in this study as all of our specimens are sintered at 1600°C. Prior studies showed the lowest ODT temperature is ~1575°C in $Gd_2Zr_2O_7$ [70], and the ODT temperatures are > 1600°C for all other stoichiometric ternary pyrochlores [60].

The r_A/r_B ratios for specimens are shown in Figure 5.6(a). Prior studies, based mostly on stoichiometric ternary oxides, suggested that the ordered pyrochlore structure should form when $r_A/r_B > 1.46$ with an estimated error of $\pm\, 0.003$ [71]. Our results of duodenary oxides showed an ODT (or disordering) occurred at higher threshold of $r_A/r_B \sim 1.48$ in the P1N1 series. The observed higher tendency to disorder can be well explained from two facts. First, high-entropy solid solutions with severe lattice distortion promotes disordering. Second, the prior threshold of ~1.46 was proposed based on stoichiometric ternary oxides. In the P1N1 series, there is Sc deficiency, so that some other larger rare earth elements have to fill a small fraction (<5%) of the B-site, which will also promote disordering. This second proposed cause is further supported by the disordering of Sc-free of P1"N2 50:50 with r_A/r_B of ~1.49, since more larger rare earth elements have to fill (25% of) the B-site, which strongly promotes disordering.

Similarly, the A/B ratios for specimens are shown in Figure 5.6(b). Here, we estimate the critical A/B ratio from the mean of all available ODTs in relevant ternary oxides, *e.g.*, $Sm_2Ti_2O_7$,

$Sm_2Hf_2O_7$, $Sm_2Zr_2O_7$, $Eu_2Ti_2O_7$, at 1600℃ (but excluding $Gd_2Zr_2O_7$, $Yb_2Hf_2O_7$, and $Yb_2Zr_2O_7$, which do not possess a pyrochlore phase at 1600℃). This estimation based on ternary oxides suggests that the disordered fluorite structure should form when the A/B ratio is > 1.16 ± 0.04 (for B-site deficient, with estimated 3% errors). Here, our results of duodenary oxides show that an ODT (or disordering) occurred at a critical A/B ratio of 1.16-1.20 in the P1N1 series. Again, high-entropy solid solutions with severe lattice distortion promotes disordering and shift the threshold of the A/B ratio a bit higher. The two additional specimens have much larger (P1"N2) and smaller (P1'N1') A/B ratios, which are consistently disordered and ordered, respectively.

5.4.5 ROOM TEMPERATURE THERMOMECHANICAL PROPERTIES

Figure 5.7(a) displays the measured room temperature Young's modulus of all the duodenary oxides. Young's modulus has a noticeable increase in all mixed compositions of P1N1 above the rule of mixtures (RoM). More interestingly, sharp increases occur at low concentrations of mixing at both sides. Such the sharp increases may be resulted from a strongly negative excess volume of mixing or a negative enthalpy of mixing [72]. The negative excess volume of mixing is unlikely in this case because the measured lattice parameters do not deviate significantly from Vegard's law, as shown in Figure 5.7(b). A recent study suggested that a negative enthalpy of mixing in pyrochlore-fluorite $Ho_2Ti_{2-x}Zr_xO_7$ resulted in short-range ordering [73]. We hypothesize that similar short-range chemical or structural orders, which are almost inevitable for such complex high-entropy oxides according to a recent thermodynamic analysis [74], can explain our observation of increased stiffness in this duodenary P1N1 series. Moreover, a softening in modulus is also seen after the ODT, which is expected as the pyrochlore is generally stiffer than the fluorite [75]. At intermediate doping levels, the trend is nearly linear.

The measured thermal conductivity (k), as shown in Figure 5.7(c), also sharply changes at

low concentrations of mixing on both ends, in comparison with the RoM values. However, the change is negative (with more reduced *k* from RoM) at the P1 side, but positive at the N1 side. A more considerable drop in thermal conductivity is seen after the ODT, which may be related to lattice softening. Similar to prior discussion, possible formation of short-range chemical or structural orders may help explain the sharp decrease in thermal conductivity [76,77], at least in the P1 end. Reductions in thermal conductivity may also be due to locon effects where certain atoms may profoundly distort the local field that allows for localized, non-propagating phonons [78–81]. The increase in thermal conductivity at the N1 end may simply be due to the increased modulus.

Notably, the *E/k* ratios in Figure 5.7(d) are enhanced above the RoM values consequently, compared to the two endmembers (P1 and N1, which have similar *E/k* ratios of ~175 $GPa{\cdot}m{\cdot}K{\cdot}W^{-1}$). This effect is more pronounced on the P1-rich side. At intermediate concentrations, the changes are typically linear. In all cases, the measured properties tend to deviate significantly from the RoM. The ability to increase the *E/k* ratio is scientifically interesting, as reduction of thermal conductivity typically accompanies with decreasing modulus. In addition to potential "high-entropy" effects (including severe lattice distortion and short-range orders), potential benefits may also result with the new ability to include "non-traditional" elements (i.e., elements that are not stable on their own in the phase, such as $Dy_2Zr_2O_7$ in the pyrochlore phase) in many-component solid solutions. Some of such "non-traditional" elements include Sm, Ti, Zr, and Hf in the niobate matrix and Nb in the pyrochlore matrix. Further investigation is underway to examine the influence of these "non-traditional" elements and the short-range ordering.

5.4.6 TEMPERATURE-DEPENDENT THERMAL CONDUCTIVITY

Figure 5.8 shows the temperature-dependent thermal conductivity of all the specimens from room temperature to 1000°C. Nearly all compositions have ultralow thermal conductivity and primarily shows diffuson-like trends (with the thermal conductivity primarily rising due to heat capacity contributions). This diffuson-like behavior at high temperature (T>600°C) is similar to that of $La_2Zr_2O_7$ pyrochlore at high temperature [82]. However, at room temperature, these duodenary high-entropy oxides have much lower thermal conductivity than that of $La_2Zr_2O_7$, presumably due to the severe lattice distortion that scatters the propagating vibrational modes (propagons). It should also be noted that significant internal radiation contributions likely exist at high temperatures (T>600°C), leading to a small but non-negligible photon thermal conductivity that is also increasing with temperature [65]. Qualitatively, the temperature dependence of the P1N1 series in Figure 5.8(a) has the same trend as the two endmembers. Quantitatively, the relative values of temperature-dependent thermal conductivity follow similar trends as the room-temperature thermal conductivity shown in Figure 5.7(c). However, P1N1 50-50 exhibits the lowest thermal conductivity at 1000°C, lower than the endmember N1 that has the lowest thermal conductivity at room temperature.

The temperature-dependent thermal conductivity of P1'N1' 50-50 and P1"N2 50-50 shown in Figure 5.8(b) has similar trends to the P1N1 series. The fluorite-structured P1"N2 50-50 has a near temperature-independent and lower thermal conductivity compared to the pyrochlore-structured P1'N1' 50-50, and it has the lowest measured thermal conductivity of <1.4 $W \cdot m^{-1} \cdot K^{-1}$ at 1000°C.

The temperature-dependent phonon and diffuson limit was computed for P1N1 50-50 and P1"N2 50-50 (the two compositions that exhibited the lowest k at high temperatures) and plotted

in Figure 5.8(a) and 5.8(b). The phonon limit is based on Cahill, Watson, and Pohl's seminal work in 1992 [83]:

$$k_P \approx \left(\frac{\pi}{6}\right)^{\frac{1}{3}} k_B n^{\frac{2}{3}} \sum_i \nu_i \left(\frac{T}{\theta_i}\right)^2 \int_0^{\frac{\theta_i}{T}} \frac{x^3 e^x}{(e^x - 1)^2} dx \quad (6)$$

The diffuson limit is based on Allen and Feldman's work on amorphous Si [80,84,85]:

$$k_D \approx \frac{n^{-\frac{2}{3}} k_B}{2\pi^3 \nu_s^3} \left(\frac{k_B T}{\hbar}\right)^4 \int_0^{0.95\frac{\theta_D}{T}} \frac{x^5 e^x}{(e^x - 1)^2} dx \quad (7)$$

Here, n is the number density of atoms per unit cell, ν is the speed of sound, and θ is the Debye temperature. Equation (6) sums the contributions over the longitudinal and both transverse sound modes in the material while equation (7) averages these by using:

$$\nu_s = \left(\frac{1}{3}\left(\frac{1}{\nu_L} + \frac{2}{\nu_T}\right)\right)^{-1} \quad (8)$$

The lattice parameter, density, and longitudinal and transverse wave speeds used were determined at room temperature and were not corrected for reductions at increasing temperatures. For both specimens in which the limits were calculated for in Figure 5.8, the experimentally determined thermal conductivity approaches the phonon limit and lies within the uncertainties of the model and experiment ($\pm$ 3 %).This indicates significant contributions from diffusons, although still far from their limit. In broader perspective, the glass-like thermal conductivity of this niobate-tantalate fluorite oxides has recently attracted significant research interests due to their attractive thermal properties and high temperature capabilities [25,36–38,86].

While noting the ultralow thermal conductivity and attributing the thermal conductivity primarily to diffuson contributions, the potential reasons for the amorphous-like conductivity remain elusive. A few crystallography papers dating back to the 1960s and 1970s have reported

nanodomains or short-range ordering in niobate and tantalate fluorites evident by diffuse scattering in electron diffraction patterns [87,88]. The nanodomain is of the weberite structure, which has an orthorhombic cell (space group 20, *$C222_1$*). The weberite structure has a close relationship to the fluorite structure (and thus pyrochlore) in that it is a ~ $\sqrt{2}a_F \times \sqrt{2}a_F \times 2a_F$ derivative of the fluorite cell [89,90]. Similar to 3+/4+ fluorites (such as zirconates) that transform to the ordered pyrochlore structure when $\frac{r_A^{VIII}}{r_B^{VI}} > 1.46$, 3+/5+ fluorites (such as niobates) transform to the partially ordered weberite structure when $\frac{r_{3+}^{VII}}{r_{5+}^{VII}} > \sim 1.40$ [91–93]. The ODT temperatures in these niobates and tantalates (e.g., Y_3TaO_7 and Ho_3TaO_7 is ~ 1500°C [88]) are lower than the pyrochlore (typically >1600°C). Thus, as our duodenary oxides were cooled after sintering at 1600°C, the precipitation of nanoscale weberite domains (a.k.a. short-range structural ordering) is possible. Due to the strong effect of dispersed nanodomains on reducing thermal conductivity [77,94], this can be a possible cause of the ultralow, diffuson-like thermal conductivity observed. Further (non-trivial) experiments and characterization are needed to verify or clarify the exact underlying mechanism.

5.5 CONCLUSIONS

A five-cation fluorite-structured high-entropy niobate and a seven-cation high-entropy pyrochlore were mixed in different fractions and consolidated to make a series of duodenary oxides. All seven (plus two additional) compositions made are single phase high-entropy solid solutions, where an order-disorder transition (ODT) is evident with changing composition. The critical ODT composition in these duodenary oxides is shifted with respect to that predicted based on two criteria proposed based on ternary oxides. These duodenary oxides are more prone to disorder, which are attributed to a high-entropy effect and Sc deficiency on the B-site.

Increases in measured Young's modulus above the rule of mixture (RoM) are observed, with abrupt enhancements at low mixing compositions near the two endmembers. Consequently, the E/k ratios of the duodenary oxides are higher than those of both the endmembers. Nearly all of the compositions show glass-like temperature-dependent thermal conductivity. Possible existence and effects of short-range ordering (forming nanodomains) in these complex duodenary oxides are discussed.

This study represents the first report of a series of duodenary HECs and the first investigation an ODT in HECs with changing composition and its influence on thermomechanical properties. It further suggests a new route to tailor the properties of HECs via controlling the order and disorder.

Chapter 5, in full, is currently being prepared for submission. A.J. Wright, Q. Wang, C. Hu, Y.T. Yeh, R. Chen, J. Luo, Single-phase duodenary high-entropy fluorite/pyrochlore oxides with an order-disorder transition. The dissertation author was the primary investigator and author of this paper.

Table 5.1. Compositions examined in this study. All specimens are made by mixing different fractions of the pyrochlore (P1, P1' and P1") and niobate (N1, N1' and N2) endmembers of nominally 0% mismatches in both lattice and density. Here, P1', P1" and N1' are derivative compositions of P1 and N1 with varying atomic ratios, and "x" denotes the fraction of the fluorite phase before the mixing (for the P1N1 series). For example, "P1N1 10-90" (i.e., x = 0.9 in the P1N1 series in this table) in text represents the composition starting from mixing 10 % of the P1 pyrochlore and 90 % of the N1 niobate (albeit it exhibits a single-phase fluorite structure after mixing). In fact, all nine mixed compositions are single-phase (either fluorite or pyrochlore) high-entropy solid solutions after mixing.

		Compositions (x = 0, 0.02, 0.1, 0.25, 0.5, 0.75, 0.9, 0.98, 1)
P1N1 Series	P1	$[(Sm_{0.25}Eu_{0.25}Gd_{0.25}Yb_{0.25})_2(Ti_{0.5}Hf_{0.25}Zr_{0.25})_2O_7]_{1-x}$
	N1	$[(Sc_{0.266}Dy_{0.248}Tm_{0.246}Yb_{0.240})_3NbO_7]_x$
P1'N1' 50-50	P1'	$[(Sm_{0.25}Eu_{0.25}Gd_{0.25}Yb_{0.25})_2(Ti_{0.611}Hf_{0.166}Zr_{0.223})_2O_7]_{0.5}$
	N1'	$[(Sc_{0.333}Dy_{0.226}Tm_{0.224}Yb_{0.218})_3NbO_7]_{0.5}$
P1"N2 50-50	P1"	$[(Sm_{0.25}Eu_{0.25}Gd_{0.25}Yb_{0.25})_2(Ti_{0.065}Hf_{0.234}Zr_{0.701})_2O_7]_{0.5}$
	N2	$[(Y_{0.266}Dy_{0.248}Tm_{0.246}Yb_{0.240})_3NbO_7]_{0.5}$

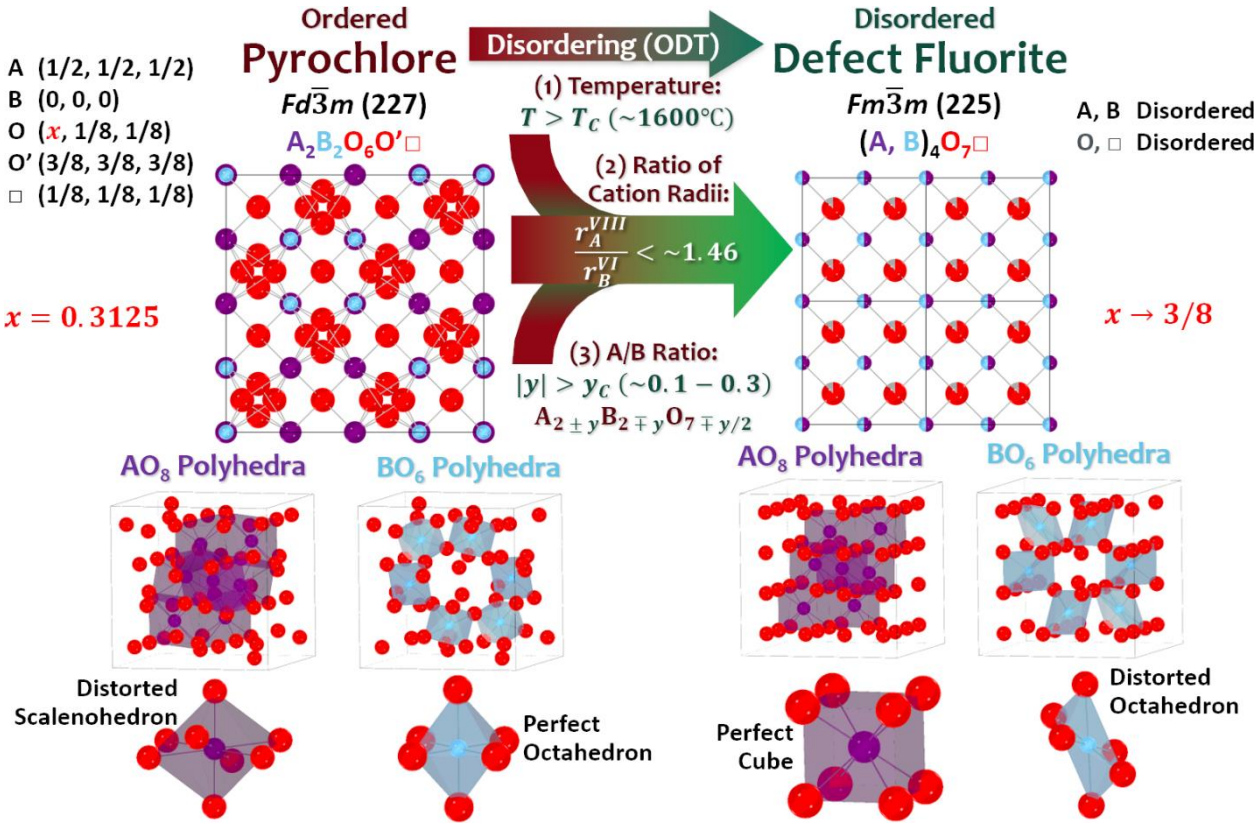

Figure 5.1. Schematic illustration of the ordered pyrochlore and disordered defect fluorite structures and the associated order-disorder transition (ODT). In simple ternary $A_2B_2O_7$ pyrochlore oxides, three criteria to induce an ODT are through (1) increasing temperature ($T > T_c$), (2) reducing the ratio of cation radii (r_A^{VIII}/r_B^{VI} > ~1.46, where r_A^{VIII} is the average radius of the A-site cation with a coordination number of eight and r_B^{VI} is the average radius of the B-site cations with a coordination number of six), and (3) increasing the non-stoichiometry ($|y| > y_c$, i.e., deviating from the ideal 1:1 A/B ratio). In the ideal ordered $A_2B_2O_7$ (or $A_2B_2O_6O'□$) pyrochlore structure, there are 1/8 ordered oxygen vacancies (represented by □), and six oxygen atoms are displaced to (x, 1/8, 1/8), where x = 0.3125. Upon an ODT, oxygen atoms are at the ideal (3/8, 1/8, 1/8) or x = 3/8 in the fluorite structure, accompanying with disordering on both cation (A and B) and anion (oxygen ions and vacancies) sublattices. Note that both the AO_8 and BO_6 polyhedra does not exist in the fluorite structure as each cation is randomly distributed on the same site and have an average coordination number of VII representative of $(A, B)O_7$ polyhedra instead. The AO_8 and BO_6 polyhedra are merely shown to represent the transformation.

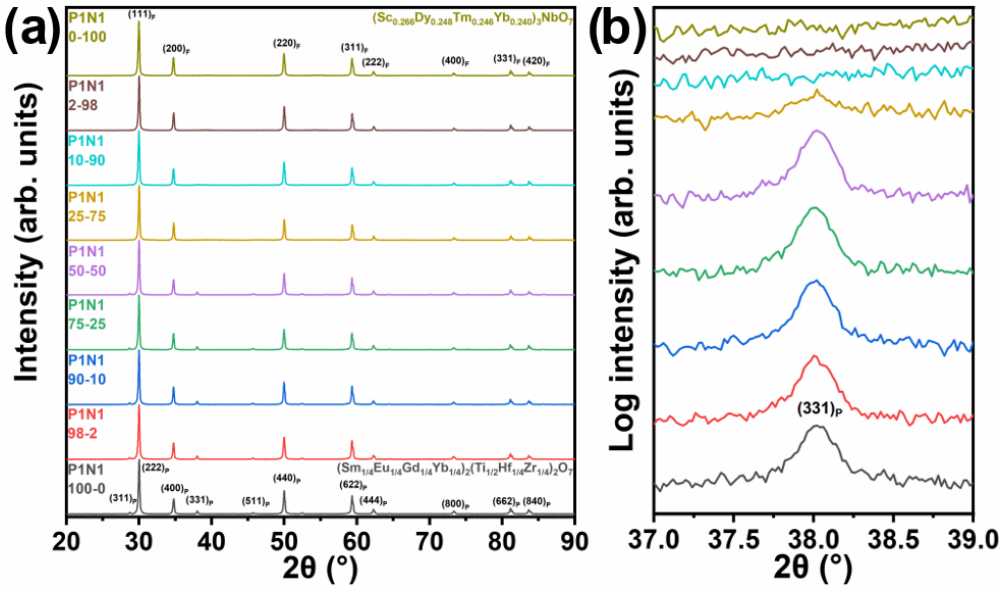

Figure 5.2. (**a**) XRD spectra of P1N1 series and (**b**) the evolution of (331) pyrochlore superstructure peak. The evolution of the pyrochlore superstructure peak is plotted on a logarithmic intensity scale.

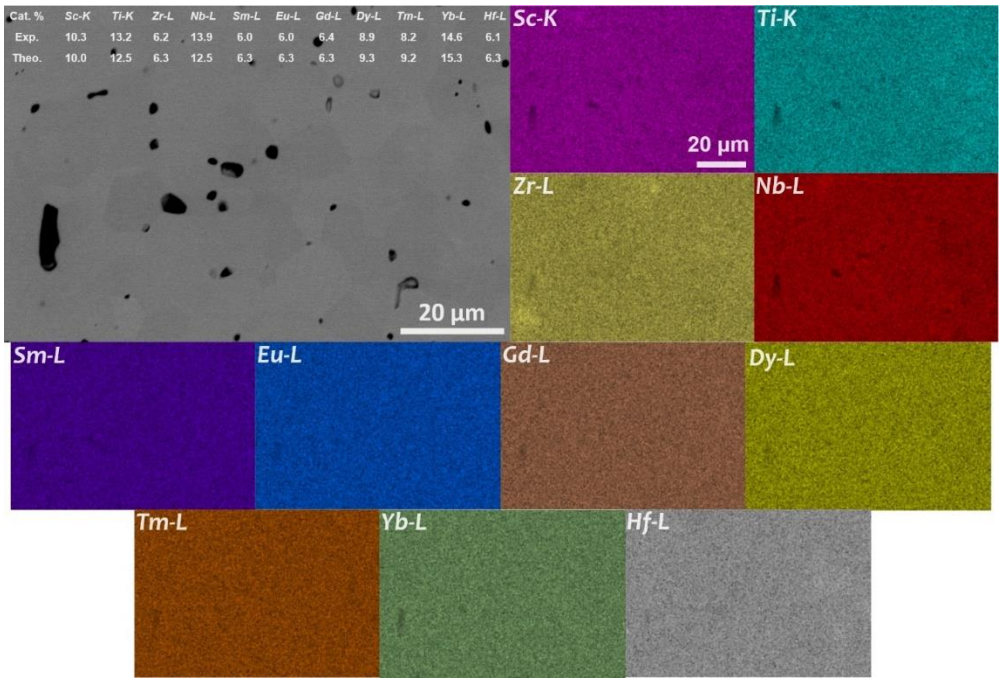

Figure 5.3. Backscattered electron SEM microstructure and EDS elemental maps of P1N1 50-50. The composition is predominantly homogeneous, albeit slight Zr agglomeration. The grain size is about 10 – 20 µm. The nominal (theoretical) and measured metal cation percentages are listed in the SEM micrograph, which agree well with each other within the experimental errors. Additional EDS elemental maps are documented in Suppl. Figs. S2 and S3, showing homogeneous compositions before and after the ODT.

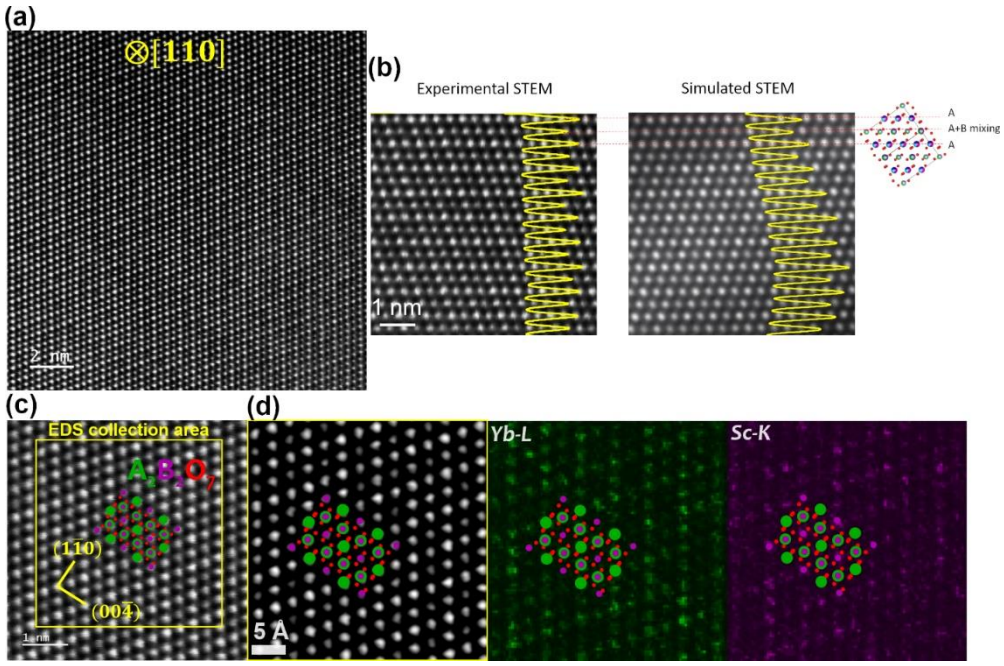

Figure 5.4. Raw (unfiltered) STEM-HAADF images of P1N1 50-50 at (**a**) low and (**b**) high magnification viewed along the [110] zone axis, showing intensity modulations due to the cation ordering. (**c**) Atomic resolution STEM was performed on a small area. (**d**) Bandpass filtered STEM-HAADF image and radial Wiener filtered EDS elemental maps of Yb (on the A site) and Sc (on the B site).

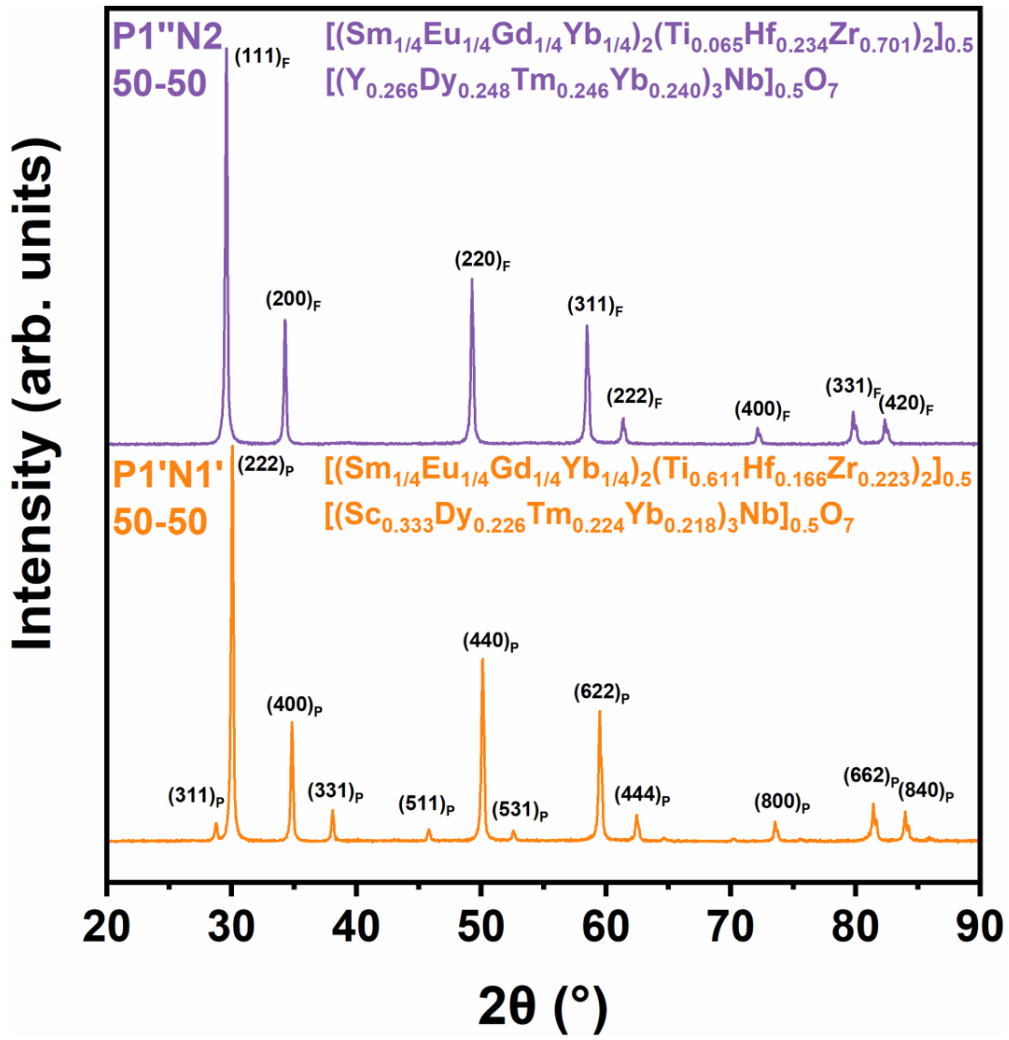

Figure 5.5. XRD spectra of the pyrochlore-structured P1'N1' 50-50 (containing Sc) and the fluorite-structured P1"N2 50-50 (without Sc).

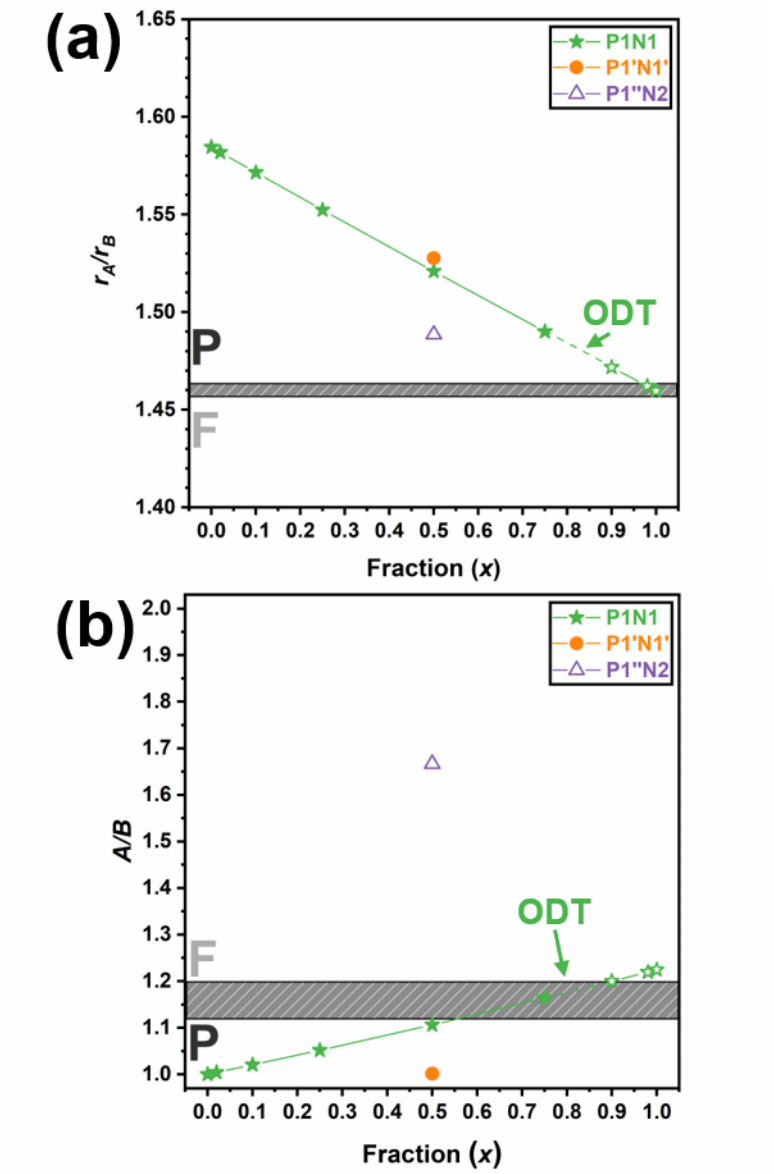

Figure 5.6. Key factors controlling the relative stabilities of the disordered fluorite (F) vs. ordered pyrochlore (P). The estimated (**a**) ratio of cation radii (r_A/r_B) and (**b**) stoichiometric ratio of A/B cations. The striped region marks the expected pyrochlore-to-fluorite transition from ternary oxides (with the thickness representing errors); see text for further explanation. Filled and open data points represent the high-entropy pyrochlore and fluorite phases, respectively, from this study, which do not exactly follow the empirical laws primarily obtained from ternary oxides.

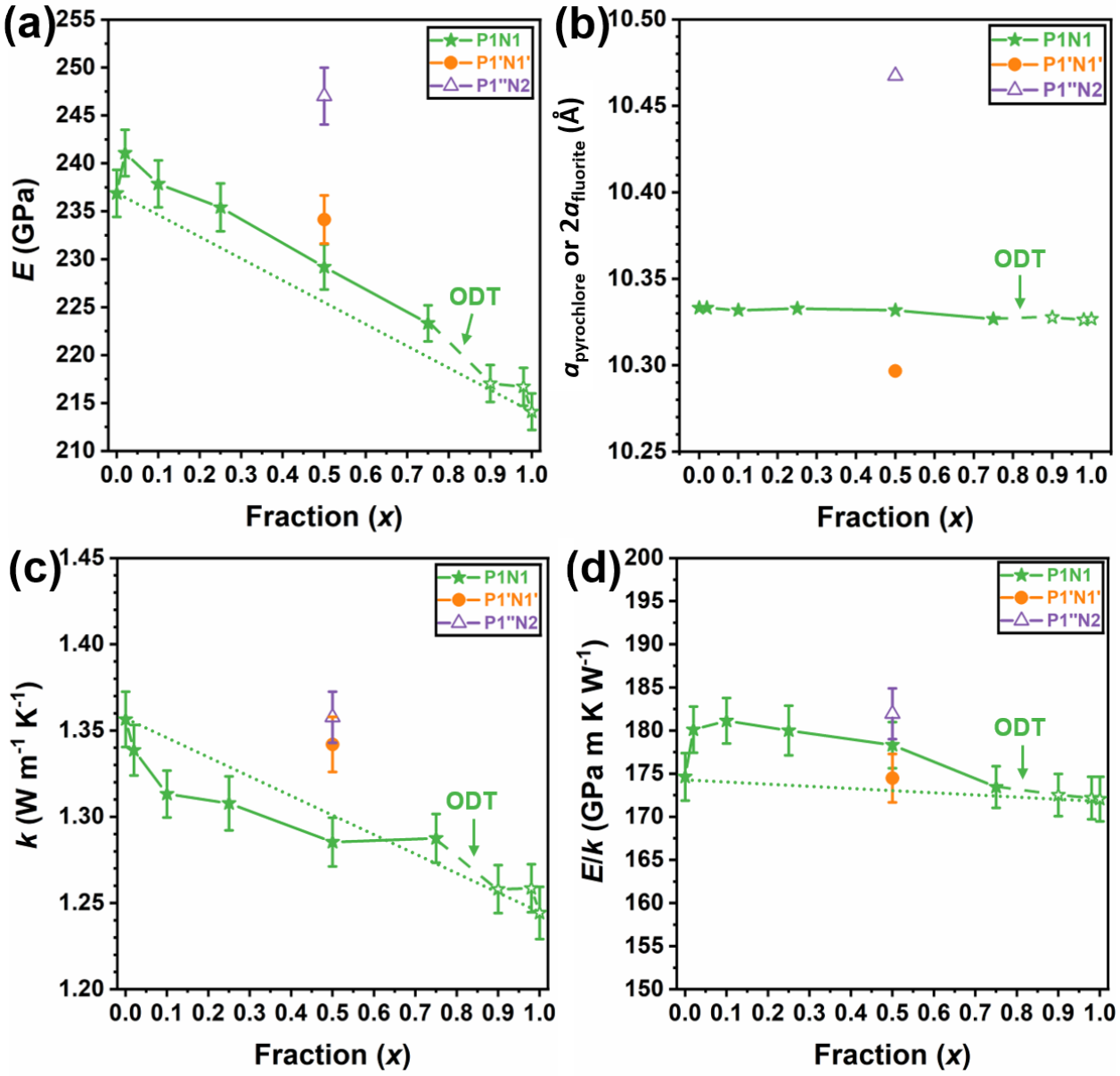

Figure 5.7. Room-temperature (**a**) Young's modulus (E), (**b**) lattice parameter, (**c**) thermal conductivity (k), and (**d**) E/k measured for the P1N1 series and two single specimens, P1'N1' 50-50 and P1"N2 50-50. Arrows and dashed lines are used to denote the order-to-disorder (pyrochlore-to-fluorite) transition (ODT). Filled and open data points represent the pyrochlore and fluorite phases, respectively. The dotted lines represent the rule-of-mixture averages from two endmembers for the P1N1 series.

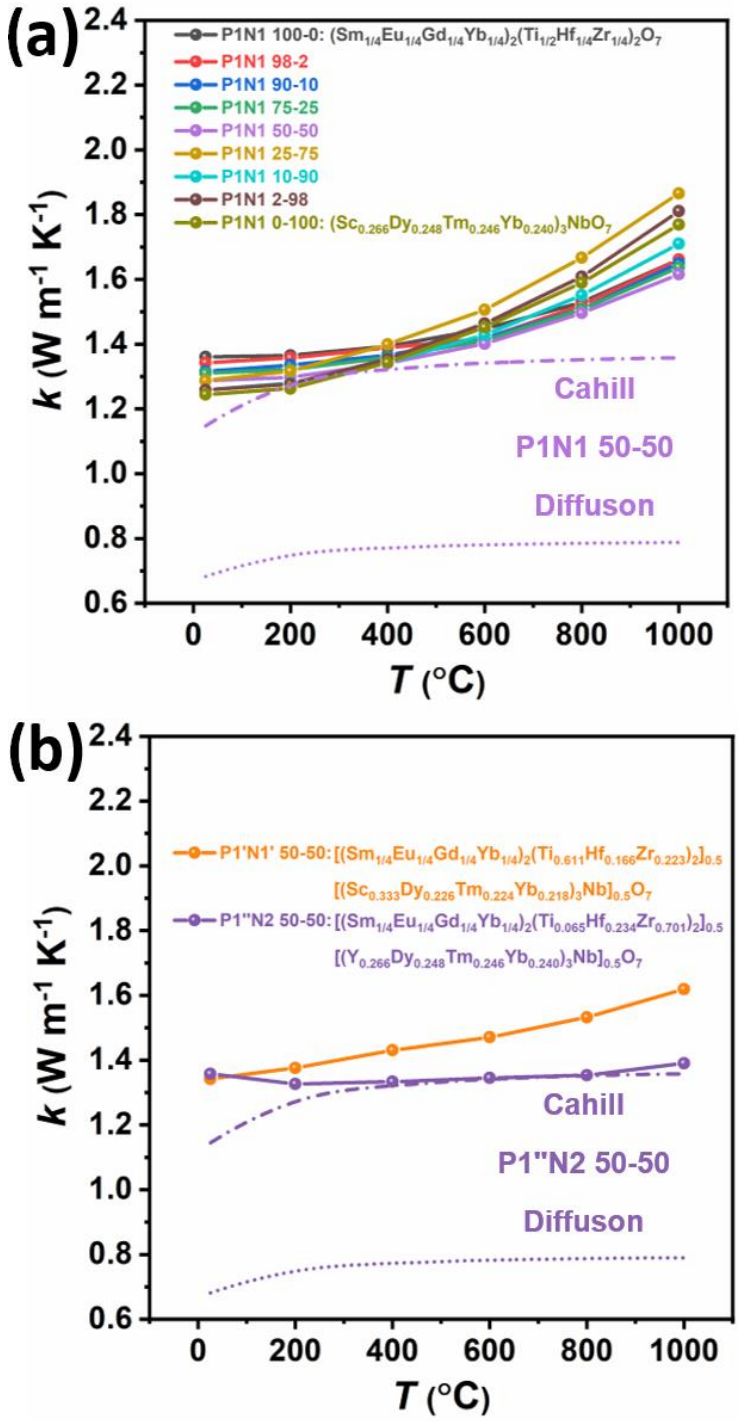

Figure 5.8. Temperature-dependent thermal conductivity of (**a**) P1N1 and (**b**) P1'N1' 50-50 and P1"N2 50-50. Cahill and diffuson model limits are shown for P1N1 50-50 and P1"N2 50-50, respectively (representing the compositions with the lowest k at high *T* in each panel).

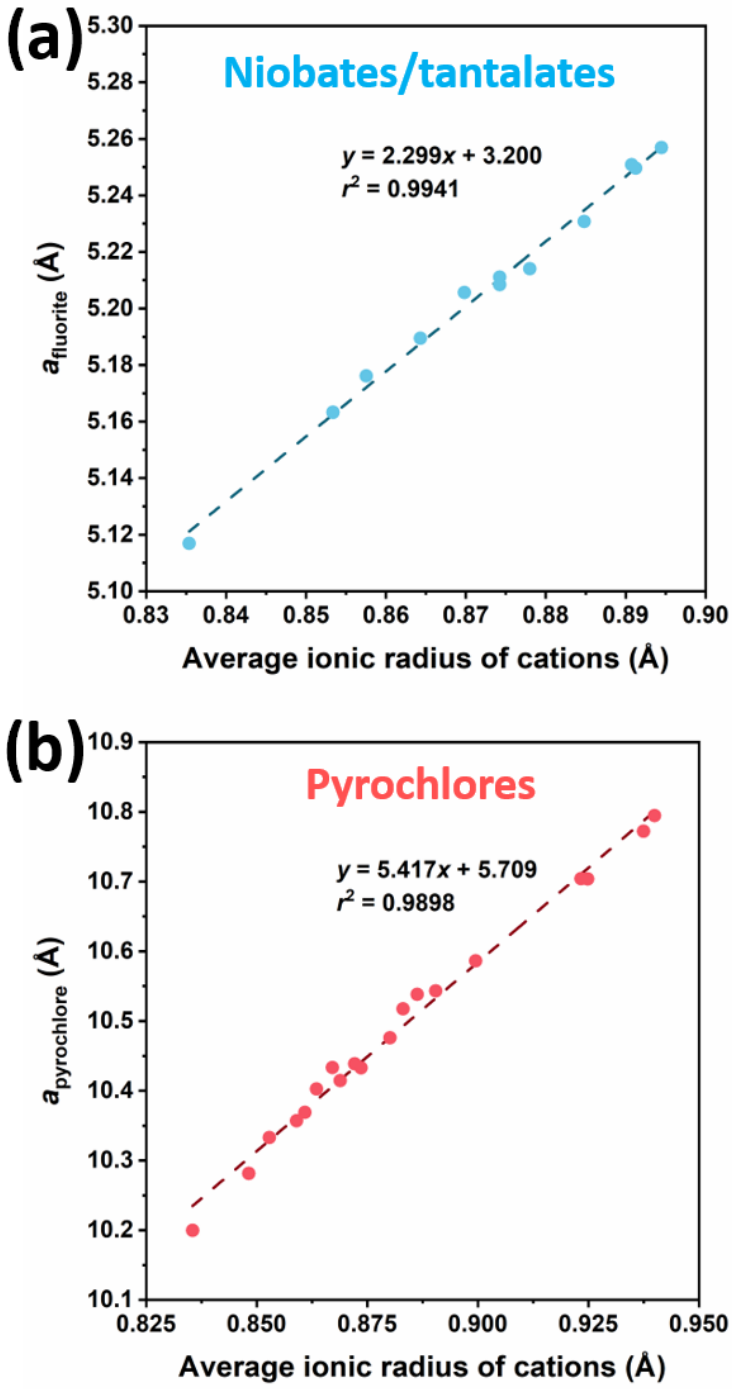

Figure 5.9. Calibration curves for (**a**) niobates/tantalates and (**b**) pyrochlores used to determine lattice matching. The data for the niobates/tantalates are from high-entropy niobates/tantalates synthesized by our group (unpublished). The data for the pyrochlores are from a previous publication from our group, Wright et al., Scr. Mater. 181 (2020).

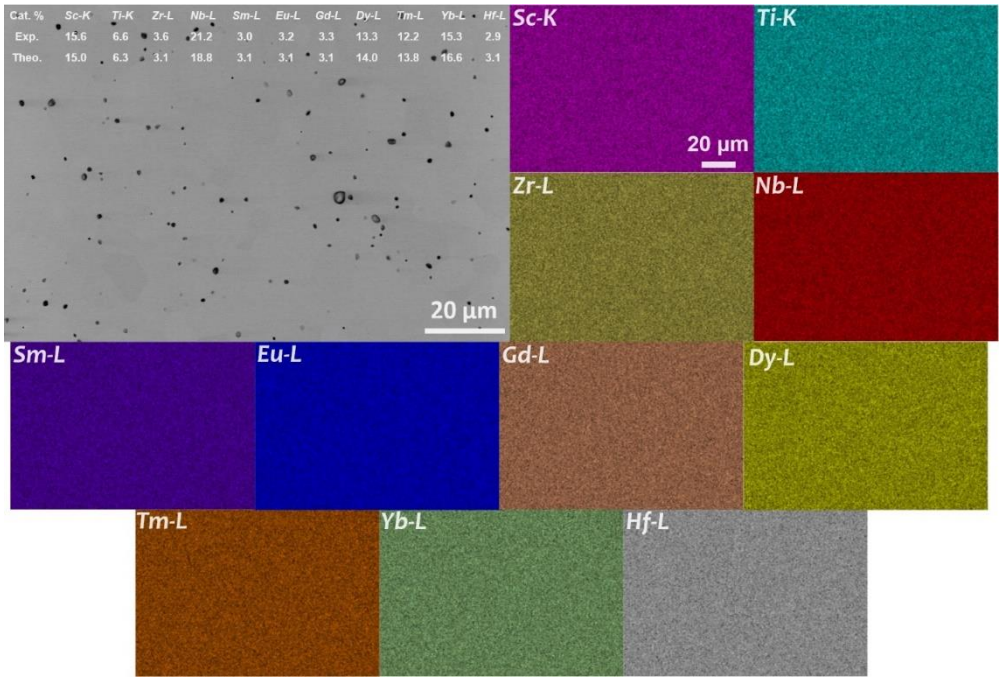

Figure 5.10. Backscattered electron SEM microstructure and EDS elemental maps of pyrochlore-structured P1N1 25-75 (the composition before the ODT). The composition is homogeneous with no evidence of elemental clustering. The grain size is about 10 – 20 µm. The nominal and measured metal cation percentages are listed in the SEM micrograph, which agree well with each other within the experimental errors.

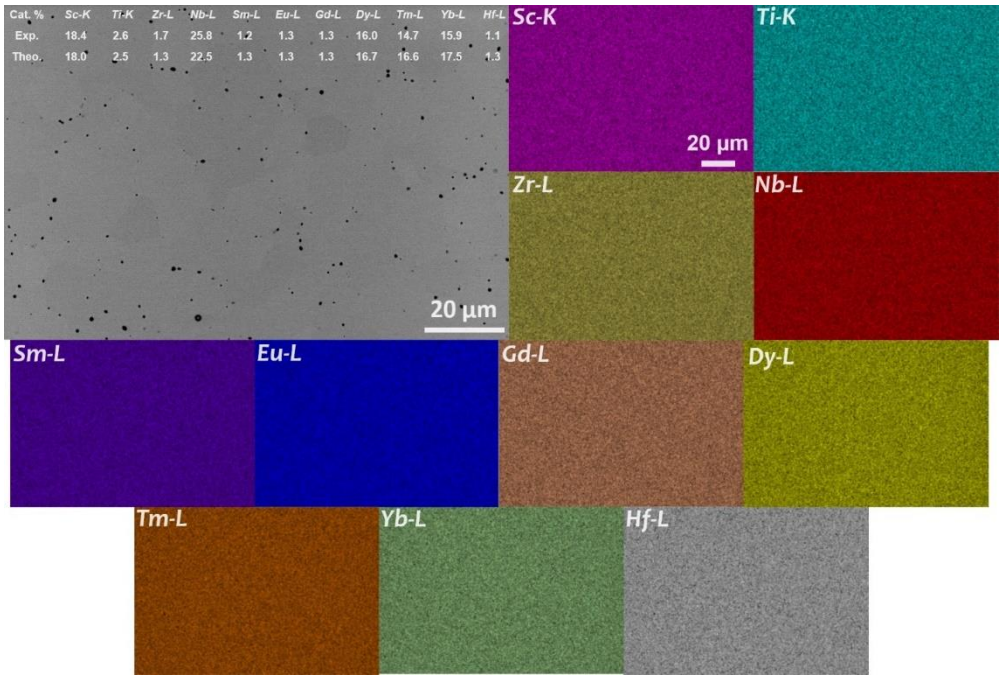

Figure 5.11. Backscattered electron SEM microstructure and EDS elemental maps of the fluorite-structured P1N1 10-90 (the composition after the ODT). The composition is homogeneous with no evidence of elemental clustering. The grain size is 10 – 20 μm. The nominal and measured metal cation percentages are listed in the SEM micrograph, which agree well with each other within the experimental errors.

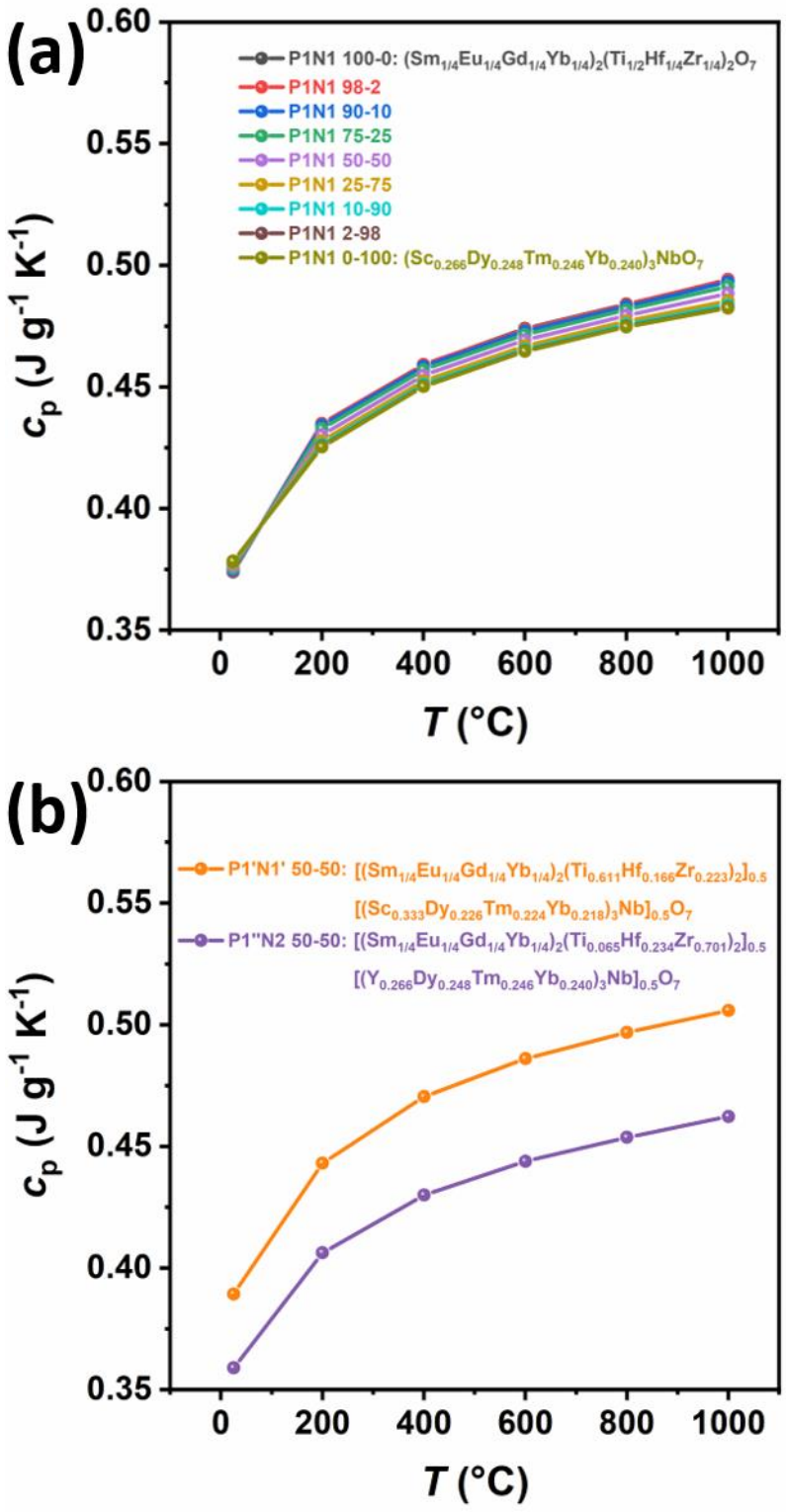

Figure 5.12. Heat capacity of (**a**) P1N1 and (**b**) P1'N1' 50-50 and P1''N2 50-50. Data were calculated through the Neumann-Kopp law using the heat capacities of the constituent oxides from I. Barin, Thermochemical Data of Pure Substances, VCH, Weinheim, 1995.

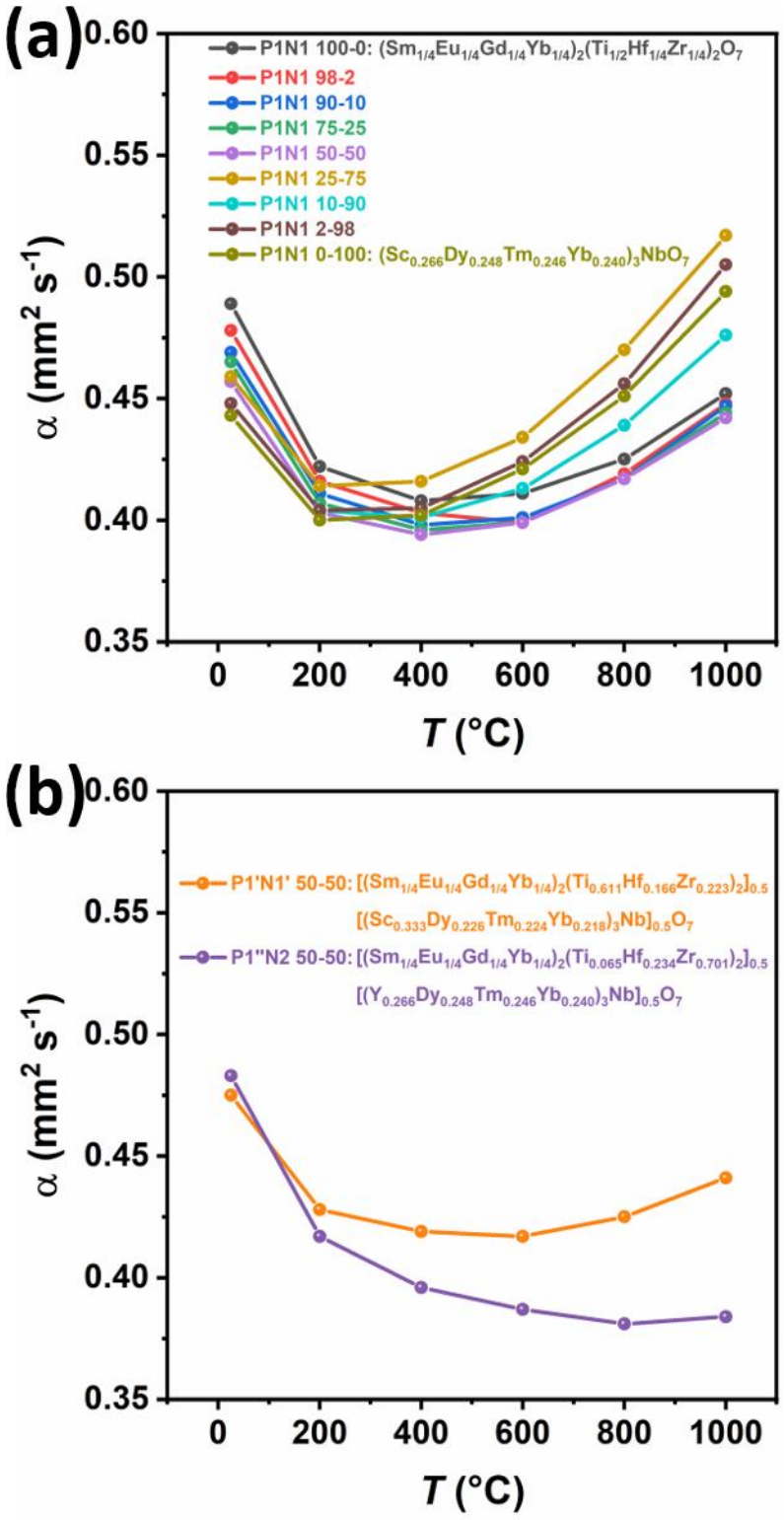

Figure 5.13. Measured thermal diffusivity of **(a)** P1N1 and **(b)** P1'N1' 50-50 and P1''N2 50-50.

5.6 REFERENCES

[1] C.M. Rost, E. Sachet, T. Borman, A. Moballegh, E.C. Dickey, D. Hou, J.L. Jones, S. Curtarolo, J.P. Maria, Entropy-stabilized oxides, Nat. Commun. 6 (2015) 8485. doi:10.1038/ncomms9485.

[2] S. Jiang, T. Hu, J. Gild, N. Zhou, J. Nie, M. Qin, T. Harrington, K. Vecchio, J. Luo, A new class of high-entropy perovskite oxides, Scr. Mater. 142 (2018) 116–120. doi:10.1016/j.scriptamat.2017.08.040.

[3] J. Gild, M. Samiee, J.L. Braun, T. Harrington, H. Vega, P.E. Hopkins, K. Vecchio, J. Luo, High-entropy fluorite oxides, J. Eur. Ceram. Soc. 38 (2018) 3578–3584. doi:10.1016/j.jeurceramsoc.2018.04.010.

[4] Z. Zhao, H. Xiang, F.-Z. Dai, Z. Peng, Y. Zhou, (La0.2Ce0.2Nd0.2Sm0.2Eu0.2)2Zr2O7: A novel high-entropy ceramic with low thermal conductivity and sluggish grain growth rate, J. Mater. Sci. Technol. (2019). doi:10.1016/j.jmst.2019.05.054.

[5] F. Li, L. Zhou, J.-X. Liu, Y. Liang, G.-J. Zhang, High-entropy pyrochlores with low thermal conductivity for thermal barrier coating materials, J. Adv. Ceram. (2019) 1–7. doi:10.1007/s40145-019-0342-4.

[6] J. Gild, Y. Zhang, T. Harrington, S. Jiang, T. Hu, M.C. Quinn, W.M. Mellor, N. Zhou, K. Vecchio, J. Luo, High-entropy metal diborides: A new class of high-entropy materials and a new type of ultrahigh temperature ceramics, Sci. Rep. 6 (2016) 37946. doi:10.1038/srep37946.

[7] P. Zhao, J. Zhu, Y. Zhang, G. Shao, H. Wang, M. Li, W. Liu, B. Fan, H. Xu, H. Lu, Y. Zhou, R. Zhang, A novel high-entropy monoboride (Mo0.2Ta0.2Ni0.2Cr0.2W0.2)B with superhardness and low thermal conductivity, Ceram. Int. 46 (2020) 26626–26631. doi:10.1016/j.ceramint.2020.07.131.

[8] E. Castle, T. Csanádi, S. Grasso, J. Dusza, M. Reece, Processing and properties of high-entropy ultra-high temperature carbides, Sci. Rep. 8 (2018) 8609. doi:10.1038/s41598-018-26827-1.

[9] P. Sarker, T. Harrington, C. Toher, C. Oses, M. Samiee, J.P. Maria, D.W. Brenner, K.S. Vecchio, S. Curtarolo, High-entropy high-hardness metal carbides discovered by entropy descriptors, Nat. Commun. 9 (2018) 1–10. doi:10.1038/s41467-018-07160-7.

[10] T.J. Harrington, J. Gild, P. Sarker, C. Toher, C.M. Rost, O.F. Dippo, C. McElfresh, K. Kaufmann, E. Marin, L. Borowski, P.E. Hopkins, J. Luo, S. Curtarolo, D.W. Brenner, K.S. Vecchio, Phase stability and mechanical properties of novel high entropy transition metal carbides, Acta Mater. 166 (2019) 271–280. doi:10.1016/j.actamat.2018.12.054.

[11] X. Yan, L. Constantin, Y. Lu, J.F. Silvain, M. Nastasi, B. Cui, (Hf 0.2 Zr 0.2 Ta 0.2 Nb 0.2 Ti 0.2)C high-entropy ceramics with low thermal conductivity, J. Am. Ceram. Soc. 101 (2018) 4486–4491. doi:10.1111/jace.15779.

[12] J. Gild, J. Braun, K. Kaufmann, E. Marin, T. Harrington, P. Hopkins, K. Vecchio, J. Luo, A high-entropy silicide: (Mo0.2Nb0.2Ta0.2Ti0.2W0.2)Si2, J. Mater. (2019). doi:10.1016/j.jmat.2019.03.002.

[13] Y. Qin, J.X. Liu, F. Li, X. Wei, H. Wu, G.J. Zhang, A high entropy silicide by reactive spark plasma sintering, J. Adv. Ceram. 8 (2019) 148–152. doi:10.1007/s40145-019-0319-3.

[14] A.J. Wright, J. Luo, A step forward from high-entropy ceramics to compositionally complex ceramics: a new perspective, J. Mater. Sci. (n.d.). doi:10.1007/s10853-020-04583-w.

[15] A.J. Wright, Q. Wang, C. Huang, A. Nieto, R. Chen, J. Luo, From high-entropy ceramics to compositionally-complex ceramics: A case study of fluorite oxides, J. Eur. Ceram. Soc. (2020). doi:10.1016/j.jeurceramsoc.2020.01.015.

[16] A.J. Wright, Q. Wang, S.-T. Ko, K.M. Chung, R. Chen, J. Luo, Size disorder as a descriptor for predicting reduced thermal conductivity in medium- and high-entropy pyrochlores, Scr. Mater. (2020). doi:10.1016/j.scriptamat.2020.02.011.

[17] A. Sarkar, R. Djenadic, D. Wang, C. Hein, R. Kautenburger, O. Clemens, H. Hahn, Rare earth and transition metal based entropy stabilised perovskite type oxides, J. Eur. Ceram. Soc. 38 (2018) 2318–2327. doi:10.1016/j.jeurceramsoc.2017.12.058.

[18] A.J. Wright, Q. Wang, S.T. Ko, K.M. Chung, R. Chen, J. Luo, Size disorder as a descriptor for predicting reduced thermal conductivity in medium- and high-entropy pyrochlore oxides, Scr. Mater. 181 (2020) 76–81. doi:10.1016/j.scriptamat.2020.02.011.

[19] K. Chen, X. Pei, L. Tang, H. Cheng, Z. Li, C. Li, X. Zhang, L. An, A five-component entropy-stabilized fluorite oxide, J. Eur. Ceram. Soc. 38 (2018) 4161–4164. doi:10.1016/j.jeurceramsoc.2018.04.063.

[20] R.-Z. Zhang, F. Gucci, H. Zhu, K. Chen, M.J. Reece, Data-driven design of ecofriendly thermoelectric high-entropy sulfides, Inorg. Chem. 57 (2018) 13027–13033. doi:10.1021/acs.inorgchem.8b02379.

[21] H. Chen, H. Xiang, F.Z. Dai, J. Liu, Y. Lei, J. Zhang, Y. Zhou, High porosity and low thermal conductivity high entropy (Zr0.2Hf0.2Ti0.2Nb0.2Ta0.2)C, J. Mater. Sci. Technol. 35 (2019) 1700–1705. doi:10.1016/j.jmst.2019.04.006.

[22] J. Gild, A. Wright, K. Quiambao-tomko, M. Qin, A. John, S. Hoque, J.L. Braun, B. Bloomfield, D. Martinez, T. Harrington, K. Vecchio, P.E. Hopkins, J. Luo, Thermal conductivity and hardness of three single-phase high-entropy metal diborides fabricated by borocarbothermal reduction and spark plasma sintering, Ceram. Int. (2019). doi:10.1016/j.ceramint.2019.11.186.

[23] Z. Zhao, H. Xiang, F.Z. Dai, Z. Peng, Y. Zhou, (TiZrHf)P2O7: An equimolar multicomponent or high entropy ceramic with good thermal stability and low thermal conductivity, J. Mater. Sci. Technol. 35 (2019) 2227–2231. doi:10.1016/j.jmst.2019.05.030.

[24] H. Chen, Z. Zhao, H. Xiang, F.-Z. Dai, W. Xu, K. Sun, J. Liu, Y. Zhou, High entropy (Y0.2Yb0.2Lu0.2Eu0.2Er0.2)3Al5O12: a novel high temperature stable thermal barrier material, J. Mater. Sci. Technol. (2020). doi:10.1016/j.jmst.2020.01.056.

[25] Z. Zhao, H. Chen, H. Xiang, F.Z. Dai, X. Wang, W. Xu, K. Sun, Z. Peng, Y. Zhou, High entropy defective fluorite structured rare-earth niobates and tantalates for thermal barrier applications, J. Adv. Ceram. 9 (2020) 303–311. doi:10.1007/s40145-020-0368-7.

[26] M. Ridley, J. Gaskins, P.E. Hopkins, E. Opila, Tailoring thermal properties of multi-component rare earth monosilicates, Acta Mater. (2020). doi:10.2139/ssrn.3525134.

[27] J.L. Braun, C.M. Rost, M. Lim, A. Giri, D.H. Olson, G.N. Kotsonis, G. Stan, D.W. Brenner, J.P. Maria, P.E. Hopkins, Charge-induced disorder controls the thermal conductivity of entropy-stabilized oxides, Adv. Mater. 30 (2018) 1805004. doi:10.1002/adma.201805004.

[28] X. Ren, Z. Tian, J. Zhang, J. Wang, Equiatomic quaternary (Y1/4Ho1/4Er1/4Yb1/4)2SiO5 silicate: A perspective multifunctional thermal and environmental barrier coating material, Scr. Mater. 168 (2019) 47–50. doi:10.1016/j.scriptamat.2019.04.018.

[29] Z. Fan, H. Wang, Y. Wu, X.J. Liu, Z.P. Lu, Thermoelectric high-entropy alloys with low lattice thermal conductivity, RSC Adv. 6 (2016) 52164–52170. doi:10.1039/c5ra28088e.

[30] R. Liu, H. Chen, K. Zhao, Y. Qin, B. Jiang, T. Zhang, G. Sha, X. Shi, C. Uher, W. Zhang, L. Chen, Entropy as a gene-like performance indicator promoting thermoelectric materials, Adv. Mater. 29 (2017) 1702712. doi:10.1002/adma.201702712.

[31] X. Yan, L. Constantin, Y. Lu, J.F. Silvain, M. Nastasi, B. Cui, (Hf0.2Zr0.2Ta0.2Nb0.2Ti0.2)C high-entropy ceramics with low thermal conductivity, J. Am. Ceram. Soc. 101 (2018) 4486–4491. doi:10.1111/jace.15779.

[32] C. Oses, C. Toher, S. Curtarolo, High-entropy ceramics, Nat. Rev. Mater. (2020) 1–15. doi:10.1038/s41578-019-0170-8.

[33] M. Lim, Z. Rak, J.L. Braun, C.M. Rost, G.N. Kotsonis, P.E. Hopkins, J.P. Maria, D.W. Brenner, Influence of mass and charge disorder on the phonon thermal conductivity of entropy stabilized oxides determined by molecular dynamics simulations, J. Appl. Phys. 125 (2019) 055105. doi:10.1063/1.5080419.

[34] A. Giri, J.L. Braun, P.E. Hopkins, Reduced dependence of thermal conductivity on temperature and pressure of multi-atom component crystalline solid solutions, J. Appl. Phys. 123 (2018) 015106. doi:10.1063/1.5010337.

[35] A. Giri, J.L. Braun, C.M. Rost, P.E. Hopkins, On the minimum limit to thermal conductivity of multi-atom component crystalline solid solutions based on impurity mass scattering, Scr. Mater. 138 (2017) 134–138. doi:10.1016/j.scriptamat.2017.05.045.

[36] J. Yang, X. Qian, W. Pan, R. Yang, Z. Li, Y. Han, M. Zhao, M. Huang, C. Wan, Diffused Lattice Vibration and Ultralow Thermal Conductivity in the Binary Ln–Nb–O Oxide System, Adv. Mater. 31 (2019) 1808222. doi:10.1002/adma.201808222.

[37] L. Chen, M. Hu, F. Wu, P. Song, J. Feng, Thermo-mechanical properties of fluorite Yb3TaO7 and Yb3NbO7 ceramics with glass-like thermal conductivity, J. Alloys Compd. 788 (2019) 1231–1239. doi:10.1016/j.jallcom.2019.02.317.

[38] P. Wu, M. Hu, F. Wu, X. Chong, J. Feng, The rattler effect of phonon propagation in defect-fluorite Dy3(Nb1-xTix)O7-x/2, Ceram. Int. 44 (2018) 21998–22002. doi:10.1016/j.ceramint.2018.08.070.

[39] D.R. Clarke, S.R. Phillpot, Thermal barrier coating materials, Mater. Today. 8 (2005) 22–29. doi:10.1016/S1369-7021(05)70934-2.

[40] V. Ponnilavan, A. Aravind, M. Ezhilan, S. Kannan, Titanium substitution in Gd2Zr2O7 for thermal barrier coating applications, Ceram. Int. 45 (2019) 16450–16457. doi:10.1016/j.ceramint.2019.05.176.

[41] K.H. Kwak, B.C. Shim, S.M. Lee, Y.S. Oh, H.T. Kim, B.K. Jang, S. Kim, Formation and thermal properties of fluorite-pyrochlore composite structure in La2(ZrxCe1-X)2O7 oxide system, Mater. Lett. 65 (2011) 2937–2940. doi:10.1016/j.matlet.2011.06.043.

[42] S. Krämer, J. Yang, C.G. Levi, Infiltration-inhibiting reaction of gadolinium zirconate thermal barrier coatings with CMAS melts, J. Am. Ceram. Soc. 91 (2008) 576–583. doi:10.1111/j.1551-2916.2007.02175.x.

[43] D.L. Poerschke, C.G. Levi, Effects of cation substitution and temperature on the interaction between thermal barrier oxides and molten CMAS, J. Eur. Ceram. Soc. 35 (2015) 681–691. doi:10.1016/j.jeurceramsoc.2014.09.006.

[44] C. Wan, W. Zhang, Y. Wang, Z. Qu, A. Du, R. Wu, W. Pan, Glass-like thermal conductivity in ytterbium-doped lanthanum zirconate pyrochlore, Acta Mater. 58 (2010) 6166–6172. doi:10.1016/j.actamat.2010.07.035.

[45] W. Pan, S.R. Phillpot, C. Wan, A. Chernatynskiy, Z. Qu, Low thermal conductivity oxides, MRS Bull. 37 (2012) 917–922. doi:10.1557/mrs.2012.234.

[46] Z. Song, Q. Liu, Tolerance Factor, phase stability and order-disorder of the pyrochlore structure, Inorg. Chem. Front. (2020). doi:10.1039/D0QI00016G.

[47] B.P. Mandal, A. Banerji, V. Sathe, S.K. Deb, A.K. Tyagi, Order-disorder transition in Nd2-yGdyZr2O7 pyrochlore solid solution: An X-ray diffraction and Raman spectroscopic study, J. Solid State Chem. 180 (2007) 2643–2648. doi:10.1016/j.jssc.2007.07.007.

[48] M.A. Subramanian, G. Aravamudan, G. V. Subba Rao, Oxide pyrochlores - A review, Prog. Solid State Chem. 15 (1983) 55–143. doi:10.1016/0079-6786(83)90001-8.

[49] D. Simeone, G.J. Thorogood, D. Huo, L. Luneville, G. Baldinozzi, V. Petricek, F. Porcher, J. Ribis, L. Mazerolles, L. Largeau, J.F. Berar, S. Surble, Intricate disorder in defect fluorite/pyrochlore: A concord of chemistry and crystallography, Sci. Rep. 7 (2017) 1–7. doi:10.1038/s41598-017-02787-w.

[50] A.F. Fuentes, S.M. Montemayor, M. Maczka, M. Lang, R.C. Ewing, U. Amador, A critical review of existing criteria for the prediction of pyrochlore formation and stability, Inorg. Chem. 57 (2018) 12093–12105. doi:10.1021/acs.inorgchem.8b01665.

[51] B.J. Wuensch, K.W. Eberman, Order-disorder phenomena in A2B2O7 pyrochlore oxides, JOM. 52 (2000) 19–21. doi:10.1007/s11837-000-0155-4.

[52] Y. Wang, F. Yang, P. Xiao, Glass-like thermal conductivities in (La1-x1Yx1)2(Zr1-x2Yx2)2O7-x2 (x = x1 + x2, 0≤ x ≤ 1.0) solid solutions, Acta Mater. 60 (2012) 7024–7033. doi:10.1016/j.actamat.2012.08.063.

[53] C. Heremans, B.J. Wuensch, J.K. Stalick, E. Prince, Fast-ion conducting Y2(ZryTi1-y)2O7 pyrochlores: Neutron Rietveld analysis of disorder induced by Zr substitution, J. Solid State Chem. 117 (1995) 108–121. doi:10.1006/jssc.1995.1253.

[54] C. Wan, Z. Qu, A. Du, W. Pan, Order-disorder transition and unconventional thermal conductivities of the (Sm1-xYbx)2Zr2O7 series, J. Am. Ceram. Soc. 94 (2011) 592–596. doi:10.1111/j.1551-2916.2010.04113.x.

[55] T. van Dijk, K.J. de Vries, A.J. Burggraaf, Electrical conductivity of fluorite and pyrochlore LnxZr1–xO2–x/2 (Ln = Gd, Nd) Solid Solutions, Phys. Status Solidi. 58 (1980) 115–125. doi:10.1002/pssa.2210580114.

[56] Y. Liu, R.L. Withers, L. Norén, The pyrochlore to “defect fluorite” transition in the Y2(ZryTi1-y)2O7 system and its underlying crystal chemistry, J. Solid State Chem. 177 (2004) 4404–4412. doi:10.1016/j.jssc.2004.09.014.

[57] D.L. Drey, E.C. O’Quinn, T. Subramani, K. Lilova, G. Baldinozzi, I.M. Gussev, A.F. Fuentes, J.C. Neuefeind, M. Everett, D. Sprouster, A. Navrotsky, R.C. Ewing, M. Lang, Disorder in Ho2Ti2−xZrxO7: pyrochlore to defect fluorite solid solution series, RSC Adv. 10 (2020) 34632–34650. doi:10.1039/D0RA07118H.

[58] E.C. O'Quinn, K.E. Sickafus, R.C. Ewing, G. Baldinozzi, J.C. Neuefeind, M.G. Tucker, A.F. Fuentes, D. Drey, M.K. Lang, Predicting short-range order and correlated phenomena in disordered crystalline materials, Sci. Adv. 6 (2020) eabc2758. doi:10.1126/sciadv.abc2758.

[59] L. Martel, M. Naji, K. Popa, J.F. Vigier, J. Somers, Fingerprint of local disorder in long range ordered isometric pyrochlores, Sci. Rep. 7 (2017) 1–8. doi:10.1038/s41598-017-12544-8.

[60] E.R. Andrievskaya, Phase equilibria in the refractory oxide systems of zirconia, hafnia and yttria with rare-earth oxides, J. Eur. Ceram. Soc. 28 (2008) 2363–2388. doi:10.1016/j.jeurceramsoc.2008.01.009.

[61] B.H. Toby, R.B. Von Dreele, GSAS-II: The genesis of a modern open-source all purpose crystallography software package, J. Appl. Crystallogr. 46 (2013) 544–549. doi:10.1107/S0021889813003531.

[62] ASTM International, ASTM C373-18: Standard test methods for determination of water absorption and associated properties by vacuum method for pressed ceramic tiles and glass tiles and boil method for extruded ceramic tiles and non-tile fired ceramic whiteware products, Annu. B. ASTM Stand. (2018) 7. doi:10.1520/C0373-16.2.

[63] ASTM International, C1198-20 Standard Test Method for Dynamic Young's Modulus, Shear Modulus, and Poisson's Ratio for Advanced Ceramics by Sonic Resonance, West Conshohocken, PA, 2020. doi:10.1520/C1198-20.

[64] E.A. Dean, J.A. Lopez, Empirical dependence of elastic moduli on porosity for ceramic materials, J. Am. Ceram. Soc. 66 (1983) 366–370. doi:10.1111/j.1151-2916.1983.tb10051.x.

[65] Q. Flamant, D.R. Clarke, Opportunities for minimizing radiative heat transfer in future thermal and environmental barrier coatings, Scr. Mater. 173 (2019) 26–31. doi:10.1016/j.scriptamat.2019.07.041.

[66] I. Barin, Thermochemical data of pure substances, VCH, Weinheim, 1995. doi:10.1016/s0165-2427(96)05632-2.

[67] R.W. Rice, Porosity of ceramics: Properties and applications, CRC Press, 1998. doi:10.1017/CBO9781107415324.004.

[68] R.D. Shannon, Revised effective ionic radii and systematic studies of interatomic distances in halides and chalcogenides, Acta Crystallogr. Sect. A. 32 (1976) 751–767. doi:10.1107/S0567739476001551.

[69] J.G. Allpress, H.J. Rossell, Fluorite-related phases Ln3MO7, Ln = rare earth, Y, or Sc, M = Nb, Sb, or Ta. I. Crystal chemistry, J. Solid State Chem. 27 (1979) 105–114. doi:10.1016/0022-4596(79)90149-X.

[70] J. Wu, X. Wei, N.P. Padture, P.G. Klemens, M. Gell, E. García, P. Miranzo, M.I. Osendi, Low-thermal-conductivity rare-earth zirconates for potential thermal-barrier-coating applications, J. Am. Ceram. Soc. 85 (2004) 3031–3035. doi:10.1111/j.1151-2916.2002.tb00574.x.

[71] A.F. Fuentes, S.M. Montemayor, M. Maczka, M. Lang, R.C. Ewing, U. Amador, A critical review of existing criteria for the prediction of pyrochlore formation and stability, Inorg. Chem. 57 (2018) 12093–12105. doi:10.1021/acs.inorgchem.8b01665.

[72] B. Roos, H. Richter, J. Wollweber, Composition dependence of hardness and elastic modulus in Si-Ge measured by nanoindentation - Possible consequences for elasto-plastic relaxation and diffusion, Solid State Phenom. 47–48 (1996) 509–516. doi:10.4028/www.scientific.net/ssp.47-48.509.

[73] D.L. Drey, E.C. O'Quinn, T. Subramani, K. Lilova, G. Baldinozzi, I.M. Gussev, A.F. Fuentes, J.C. Neuefeind, M. Everett, D. Sprouster, A. Navrotsky, R.C. Ewing, M. Lang, Disorder in Ho2Ti2−xZrxO7: pyrochlore to defect fluorite solid solution series, RSC Adv. 10 (2020) 34632–34650. doi:10.1039/D0RA07118H.

[74] S.J. McCormack, A. Navrotsky, Thermodynamics of high entropy ceramics, Acta Mater. (2020). doi:10.1201/9780367374426-11.

[75] K. Shimamura, T. Arima, K. Idemitsu, Y. Inagaki, Thermophysical properties of rare-earth-stabilized zirconia and zirconate pyrochlores as surrogates for actinide-doped zirconia, Int. J. Thermophys. 28 (2007) 1074–1084. doi:10.1007/s10765-007-0232-9.

[76] P.Y. Deng, K.K. Wang, J.Y. Du, H.J. Wu, From dislocation to nano-precipitation: Evolution to low thermal conductivity and high thermoelectric performance in n-type PbTe, Adv. Funct. Mater. (2020). doi:10.1002/adfm.202005479.

[77] S. Il Kim, K.H. Lee, H.A. Mun, H.S. Kim, S.W. Hwang, J.W. Roh, D.J. Yang, W.H. Shin, X.S. Li, Y.H. Lee, G.J. Snyder, S.W. Kim, Dense dislocation arrays embedded in grain boundaries for high-performance bulk thermoelectrics, Science (80-.). 348 (2015) 109–114. doi:10.1126/science.aaa4166.

[78] F. DeAngelis, M.G. Muraleedharan, J. Moon, H.R. Seyf, A.J. Minnich, A.J.H. McGaughey, A. Henry, Thermal transport in disordered materials, Nanoscale Microscale Thermophys. Eng. 23 (2019) 81–116. doi:10.1080/15567265.2018.1519004.

[79] W. Lv, A. Henry, Non-negligible contributions to thermal conductivity from localized modes in amorphous silicon dioxide, Sci. Rep. 6 (2016) 1–8. doi:10.1038/srep35720.

[80] P.B. Allen, J.L. Feldman, J. Fabian, F. Wooten, Diffusons, locons and propagons: Character of atomic vibrations in amorphous Si, Philos. Mag. B. 79 (1999) 1715–1731. doi:10.1080/13642819908223054.

[81] V.P. Carey, G. Chen, C. Grigoropoulos, M. Kaviany, A. Majumdar, A review of heat transfer physics, Nanoscale Microscale Thermophys. Eng. 12 (2008) 1–60. doi:10.1080/15567260801917520.

[82] Y. Luo, X. Yang, T. Feng, J. Wang, X. Ruan, Vibrational hierarchy leads to dual-phonon transport in low thermal conductivity crystals, Nat. Commun. 11 (2020) 2554. doi:10.1038/s41467-020-16371-w.

[83] D.G. Cahill, S.K. Watson, R.O. Pohl, Lower limit to the thermal conductivity of disordered crystals, Phys. Rev. B. 46 (1992) 6131–6140. doi:10.1103/PhysRevB.46.6131.

[84] P.B. Allen, J.L. Feldman, Thermal conductivity of glasses: Theory and application to amorphous Si, Phys. Rev. Lett. 62 (1989) 645–648. doi:10.1103/PhysRevLett.62.645.

[85] M.T. Agne, R. Hanus, G.J. Snyder, Minimum thermal conductivity in the context of: Diffuson-mediated thermal transport, Energy Environ. Sci. 11 (2018) 609–616. doi:10.1039/c7ee03256k.

[86] Y. Wang, L. Chen, J. Feng, Impact of ZrO2 alloying on thermo-mechanical properties of Gd3NbO7, Ceram. Int. (2019). doi:10.1016/j.ceramint.2019.11.084.

[87] H.P. Rooksby, E.A.D. White, Rare-earth niobates and tantalates of defect fluorite- and weberite-type structures, J. Am. Ceram. Soc. 47 (1964) 94–96. doi:10.1111/j.1151-2916.1964.tb15663.x.

[88] J.G. Allpress, H.J. Rossell, Fluorite-related phases Ln3MO7, Ln = rare earth, Y, or Sc, M = Nb, Sb, or Ta. I. Crystal chemistry, J. Solid State Chem. 27 (1979) 105–114. doi:10.1016/0022-4596(79)90149-X.

[89] J. Shamblin, M. Feygenson, J. Neuefeind, C.L. Tracy, F. Zhang, S. Finkeldei, D. Bosbach, H. Zhou, R.C. Ewing, M. Lang, Probing disorder in isometric pyrochlore and related complex oxides, Nat. Mater. 15 (2016) 507–511. doi:10.1038/nmat4581.

[90] J. Shamblin, C.L. Tracy, R.I. Palomares, E.C. O'Quinn, R.C. Ewing, J. Neuefeind, M. Feygenson, J. Behrens, C. Trautmann, M. Lang, Similar local order in disordered fluorite and aperiodic pyrochlore structures, Acta Mater. 144 (2018) 60–67. doi:10.1016/j.actamat.2017.10.044.

[91] L. Lõpez-Conesa, J.M. Rebled, M.H. Chambrier, K. Boulahya, J.M. González-Calbet, M.D. Braida, G. Dezanneau, S. Estradé, F. Peirõ, Local structure of rare earth niobates (RE3NbO7, RE = Y, Er, Yb, Lu) for proton conduction applications, Fuel Cells. 13 (2013) 29–33. doi:10.1002/fuce.201200136.

[92] M. Wakeshima, H. Nishimine, Y. Hinatsu, Crystal structures and magnetic properties of rare earth tantalates RE3TaO7 (Re = rare earths), J. Phys. Condens. Matter. 16 (2004) 4103–4120. doi:10.1088/0953-8984/16/23/025.

[93] G. King, C.M. Thompson, J.E. Greedan, A. Llobet, Local structure of the vacancy disordered fluorite Yb3TaO 7 from neutron total scattering, J. Mater. Chem. A. 1 (2013) 10487–10494. doi:10.1039/c3ta12100c.

[94] P.G. Klemens, The scattering of low-frequency lattice waves by static imperfections, Proc. Phys. Soc. Sect. A. 68 (1955) 1113–1128. doi:10.1088/0370-1298/68/12/303.

6. SAND CORROSION, THERMAL EXPANSION, AND ABLATION PROPERTIES OF MEDIUM- AND HIGH-ENTROPY COMPOSITIONALLY-COMPLEX FLUORITE OXIDES

6.1 INTRODUCTION

Thermal barrier coatings (TBCs) have provided a safe mechanism for increasing the operating temperature of gas-turbine engines since the 1970s.[1] With the ever-increasing efficiency and higher power demand for gas-turbine engines, the need for materials that exhibit thermal stability, excellent adhesion to substrates, and good chemical stability are increasing. The current industry standard, 7 wt. % (~ 4 mol. %) yttria-stabilized zirconia (YSZ), has been used for a few decades to satisfy the above requirements.[2, 3] However, the use of YSZ is limited to approximately 1200°C – 1300°C primarily due to an undesirable phase transformation,[4] and its poor sintering and corrosion resistance.[5] As a result, a massive influx of efforts has focused on synthesizing new materials capable of minimizing these undesirable properties. Enhanced tetragonal stability or fully stabilized cubic zirconia have been proposed as next-generation TBCs to combat the phase transformation issue.[6, 7] However, these still have corrosion and sintering resistance issues.

In addition to the thermal protection, another significant problem is the degradation due to chemical attack from molten calcia-magnesia-alumina-silicates (CMAS). Molten CMAS proves to be a significant factor in the failure of gas turbine engines when machinery is operating in sand, dust or volcanic ash laden environments.[8-10] YSZ is also known to provide inadequate protection against molten sand since the CMAS will easily penetrate YSZ through grain boundaries (GBs) and dissolve the YSZ grains.[11-13] Recently, significant efforts have focused on providing materials with enhanced CMAS resistance. Various efforts have suggested that rare earth elements may provide more chemical stability in molten sand environments due to

crystallization of the melt, which halts further penetration.[7, 14-17] Further analysis has suggested that substituting ions with a large radius into the coating material creates a stronger tendency for crystallization.[18]

High-entropy alloys (HEAs) emerged in 2004 in the metallurgy community.[19, 20] Only in the last a few years, the ceramic community has fabricated their ceramic counterparts in the bulk form, including high-entropy oxides,[21-25] borides,[26] carbides,[27, 28] and nitrides.[29] High-entropy alloys and ceramics have improved not only mechanical properties compared to their constituents, but also reduced thermal conductivities due to their disordered structures.[25, 27, 30, 31] In particular, high-entropy fluorite oxides with rare-earth stabilizers, which have recently been synthesized by Gild et al.[25] and Wright et al.[32] appears to be a promising choice to begin the search for novel TBC materials due to their low thermal conductivity, higher resistance to sintering, and compositional and structural similarities compared to traditional YSZ.

Initial studies of high-entropy ceramics (HECs) have focused on equimolar, five-component compositions, similar to the earlier studies of metallic HEAs. In the broader context, HEAs are a subset of multi-principal element alloys (MPEAs), also known as complex-concentrated or compositionally-complex alloys (CCAs), which include non-equimolar and/or medium entropy compositions.[20, 33] In general, it is not necessary that the equimolar HEAs and HECs with maximal mixing configurational entropy should have the most desirable properties overall.

Similar to their metallic counterparts,[34-37] Wright et al. recently proposed to broaden the HECs to compositionally-complex ceramics (CCCs) to include non-equimolar compositions.[32, 38, 39] It has been demonstrated that these medium-entropy compositions can often outperform their high-entropy counterparts regarding thermal conductivity and mechanical properties.[32, 38, 39]

While several studies have investigated thermally insulative HECs and CCCs,[31, 32, 38, 40-43] only a couple of reports investigated TBC related properties,[30, 44] such as mitigating water vapor induced corrosion. While this new class of HECs and CCCs exhibit attractive reduced thermal conductivities,[31, 32, 39, 43] an analysis of their interaction to molten silicates and high-temperature flame ablation, which are essential to qualify them as potential TBCs, is limited in the literature.

In this paper, we examine three compositionally-complex fluorite oxides (CCFOs) of the general formula of $[Hf_{(1-2x)/3}Zr_{(1-2x)/3}Ce_{(1-2x)/3}Y_xYb_x]O_{2-\delta}$, including a high-entropy equimolar composition ($x = 0.2$) and two additional non-equimolar compositions that resemble 8 mol. % YSZ or 8YSZ ($x = 0.074$) and 3 mol. % or 3YSZ ($x = 0.029$) in term of the total molar percentages of the stabilizers (Y and Yb). These compositions were selected in continuation of a previous study that investigated the thermal conductivity and mechanical properties of similar CCFOs as potential TBCs.[32] However, this study focuses on the stability against molten CMAS and flame resistance, as well as thermal expansion (compatibility with substrates), to investigate their potential application as a TBC material. The primary focus of this paper is to benchmark medium- and high-entropy CCFOs to CMAS resistance as these materials have demonstrated their attractive thermomechanical properties on numerous occasions already. These CCFOs were compared to 8YSZ as a benchmark as they are mostly cubic (instead of benchmarking with the most commonly used TBC material 7 wt. % or ~4 mol. % YSZ that is primarily tetragonal, so it is not a direct comparison). These materials are subject to sand laden environments from 1200°C – 1500°C to investigate the stability and kinetics of the CMAS infiltration. The reaction products formed are determined. It is found that all the specimens, including 8YSZ, show a preference for GB infiltration except the equimolar high-entropy $(Hf_{0.2}Zr_{0.2}Ce_{0.2}Y_{0.2}Yb_{0.2})O_{2-\delta}$, which preferably rapidly reacts with CMAS to form an apatite phase. Furthermore, the CCFOs experience reduced

penetration at 1300°C or lower temperatures compared to YSZ. The thermal expansion coefficients (CTEs) of the CCFOs are all larger and more compatible than YSZ, which is beneficial for the stability and compatibility on a Ni-superalloy substrate. Lastly, ablation testing was conducted to investigate their resistance in extreme environments and applicability on supersonic/hypersonic vehicles. The CCFOs show undesirable deformation at ultra-high temperatures (> 1900°C) compared to YSZ but exhibit lower emissivities. Overall, the CCFOs appear to outperform cubic YSZ at intermediate temperatures (≤ 1300°C); however, the benefits are marginal. We aim to provide data that will serve as a stepping stone and lead to more exceptional improvements against standard materials by providing a multi-component platform that allows for limitless tuning.

6.2 MATERIALS AND METHODS

6.2.1 MATERIALS AND SYNTHESIS

Commercial nanopowders of HfO_2 (61 – 80 nm, US Research Nanomaterials), ZrO_2 (15 – 25 nm, Alfa Aesar), CeO_2 (15 – 30 nm, Alfa Aesar), Y_2O_3 (25 – 50 nm, Alfa Aesar), and Yb_2O_3 (< 50 nm, MTI Corporation) were purchased and weighed in stoichiometric amounts to reflect the CCFOs of the general formula of $[Hf_{(1-2x)/3}Zr_{(1-2x)/3}Ce_{(1-2x)/3}Y_xYb_x]O_{2-\delta}$ (x = 0.2, 0.074, and 0.029), i.e., 4H – $(Hf_{0.2}Zr_{0.2}Ce_{0.2}Y_{0.2}Yb_{0.2})O_{2-\delta}$, 4M – $(Hf_{0.284}Zr_{0.284}Ce_{0.284}Y_{0.074}Yb_{0.074})O_{2-\delta}$, and 4L – $(Hf_{0.314}Zr_{0.314}Ce_{0.314}Y_{0.029}Yb_{0.029})O_{2-\delta}$.

The equimolar composition 4H was reported in a prior publication of high-entropy fluorite oxides (as the Composition #4),[25, 32] with 40 cat. % total stabilizers. The stabilizer concentrations were then modified to create 8YSZ-equivalent (14.8 cat. %) and 3YSZ-equivalent (5.8 cat. %) variants. Here, the “H”, “M”, and “L” labels denote high, medium, and low stabilizer concentrations, respectively. However, it should be noted that all the compositions are solid

solutions with varying cubic stabilizer concentrations, as no compositions were found to have any elemental clustering through X-ray diffraction and element dispersive spectroscopy methods.

The powders were then planetary milled in ethanol using a YSZ jar and media (ball-to-powder mass ratio ≈ 10:1) for 24 h. A rotary evaporator was used to dry the powder. The raw powder was then pressed under 100 MPa in a 1" stainless-steel die and sintered in a box furnace at 1600°C for 24 h in air and subsequently cooled in the furnace (after shutting the power) naturally. The density of the consolidated pellets was calculated based on the measured mass and geometrical parameters.

Commercial 8YSZ nanopowder (Tosoh, TZ-8Y, 8 mol. %) was used to make the benchmark specimens. YSZ was conventionally sintered at 1500°C for 2 h. For the thermal expansion measurement, YSZ was sintered at 1600°C for 24 h.

6.2.2 CHARACTERIZATION OF THE MICROSTRUCTURE, PHASE, AND COMPOSITION

Scanning electron microscopy (SEM, FEI Apreo, USA), in conjunction with electron backscatter diffraction (EBSD, Oxford Symmetry) and energy dispersive spectroscopy (EDS, Oxford N-Max^{N}), was used to examine the top surface of all samples. Each sample was mounted and polished to a fineness of 40 nm before examination. EBSD was used to determine the grain size of the pristine materials and the crystallographic phase of the precipitates/reaction products. Point EDS was used simultaneously with EBSD to determine the composition.

X-ray diffraction (XRD) was used to investigate the phase formation and crystallinity of the CCFOs and the CCFO-CMAS reaction products. The XRD spectra were generated from an XRD (Rigaku Miniflex II, Japan, 30 kV, 15 mA) operating from 20° - 80° 2θ with a 0.01° step and 1 s collection time per step.

6.2.3 SAND INFILTRATION AND REACTION

Sand infiltration experiments were conducted on Ø 20 mm and 1.5 mm thick, dense specimens with a 325-grit diamond disc ground surface. Commercial, synthetic sand (AFRL-02, Powder Technology Inc.) was used as received; 0.25 g of the sand was uniaxially pressed under 350 MPa inside a 0.5" (12.7 mm) stainless-steel die to form a "green" pellet. The green pellet was then placed on top of the sintered 8YSZ or CCFO pellet. The CMAS loading was ~ 200 mg/cm^2. The structure was then placed on an Al_2O_3 crucible inside a furnace and annealed at 1200°C – 1500°C for 24 h in air and naturally cooled in the furnace. At these temperatures, the viscosity of the molten sand was high enough to flow off the top surface of some of the pellets; however, only the top surface (original CCFO-CMAS interface) was examined. After annealing, the CMAS loading was reduced to ~ 55 mg/cm^2 due to the volatilization of various hydroxides and carbonates and the spreading of the CMAS over the 20 mm specimen. The CMAS volatilization was measured by considering the change in mass of the specimen and CMAS pellets following annealing. We chose an immense loading amount compared to literature[16, 18] so that the 24 hour reaction would not be limited nor reach a steady state. Additionally, a larger loading amount and longer annealing time allows for more noticeable differences between specimens to be realized, although the nominal values may not be realistic. After annealing, the specimens were then cut, mounted, and polished to examine the infiltration depth by SEM. The average depth originated from approximately 200 line-measurements made through the ImageJ software. CMAS volume percentages were calculated though thresholding techniques.

XRD analysis of the CCFO-CMAS mixed specimens allowed for additional insight into the reaction products. 8YSZ and CCFO specimens were crushed into a powder by mortar and pestle and then mixed with a synthetic, CMAS-forming sand (AFRL-02) in a 90CCFO:10CMAS

wt. % ratio (~ 75:25 vol. % ratio) in a vortex mixer for a few minutes. This ratio was chosen because it reflected the approximate ratio of the reaction layer in our CMAS experiments with the pellets described earlier. The mixed powder was then pressed at 350 MPa and annealed at 1300°C for 24 hours. The annealed samples were then crushed back into a powder to be examined by powder XRD using the conditions described above. AFRL-02 primarily contains CaO, MgO, Al_2O_3, and SiO_2 forming compounds, but there is also Na_2O, K_2O, and Fe_2O_3 forming compounds as well, which likely measurably affect the corrosion. However, this CMAS precursor was chosen because it is purchasable from Powder Technology Inc. and represents a way toward standardized testing.

6.2.4 THERMAL EXPANSION

High-temperature thermal expansion measurements were performed on 5 x 5 x 25 mm bars with a push-rod dilatometer (NETZSCH DIL 402 PC, Germany) from 25 – 1600°C operating under ambient air. Each sample was heated and cooled at 3°C/min for one cycle. The curves were corrected by subtracting data from a blank measurement to obtain the sample response. Linear CTEs were calculated from 100°C – 1500°C. Instantaneous CTEs were calculated using a 0.1 min (0.3°C) time step. The resulting data were then smoothed using a LOESS function with a span of 0.5. The instantaneous CTE data was fit to a linear line to extract the intrinsic and temperature-dependent CTE from 700°C – 1000°C.

6.2.5 ABLATION TESTING

Ablation testing was conducted by subjecting the dense specimens to an oxy-propane torch positioned approximately 19 mm from the sample for 5 minutes. Gas flow rates were optimized to obtain a neutral flame. Surface temperatures and emissivities were recorded by

dual-wavelength (λ = 1.1 & 1.2 μm) pyrometer (Williamson, MA, USA) with a 0.1 s collection time.

6.3 RESULTS AND DISCUSSION

6.3.1 DENSITY AND GRAIN SIZE

After sintering, all samples were nearly fully dense (i.e., >95 % relative density, thereby with negligible open porosity), which is necessary to minimize porosity effects in CMAS infiltration and investigate the chemical and microstructural stability. Table 6.1 shows the density of each material. The distributions of grain sizes after annealing at 1600°C for 24 h are shown in Figure 6.1. The mean grain size of 4H remains below 5 μm, and 4M and 4L have relatively large grain sizes (~ 25 μm). Noting that 8YSZ (with the same stabilizer fraction as 4M) can experience exaggerated grain growth at elevated temperatures.[45] Our 8YSZ sample was sintered at 1500°C for two hours; the sintering temperature and duration were also chosen to produce a more standard specimen with a small grain size for a better benchmark. The grain sizes were all within an order of magnitude, albeit they cannot be made exactly the same, which allows valid comparisons in the behaviors of the CMAS infiltration. It should be noted, though, that these varying grain sizes may cause differences in gathered results. A smaller grain size specimen should correlate to a larger surface energy, and this will tend to increase the corrosion rate provided that the grain boundaries are the preferred method of infiltration/reaction. Therefore, the grain size differences may induce some atypical (deeper) infiltration. Particularly in 8YSZ, since the grain boundary infiltration is not the dominant reaction mechanism in CCFO 4H.

6.3.2 SAND INFILTRATION AT 1300℃

6.3.2.1 8YSZ: $(Zr_{0.852}Y_{0.148})O_{2-\delta}$

The CCFOs 4H, 4M, and 4L were selected because they have a low thermal conductivity of 2.23, 1.74, and 1.78 W m^{-1} K^{-1}, respectively, from a previous publication from our group.[32] Here, we benchmark their CMAS resistance against the standard YSZ by subjecting the materials to a CMAS laden environment. However, the YSZ used here is 8 mol. %, as opposed to the commonly used 7 wt. %, to minimize any differences arising from phase (tetragonal vs. cubic). We have provided the CMAS corrosion of 7 wt. (4 mol.) % YSZ at 1300°C for 24 h in the Supplementary Information (SI).

The measured infiltration depths and microstructures of the CCFO-CMAS interactions (from the top surface) after 24 h at 1300°C are shown in Figure 6.2. The microstructure of 8YSZ (Figure 6.2a) shows two distinct regions that have been labeled as the infiltration and secondary layers. This "secondary mixed layer" has also been referred to as the "reprecipitation layer" in literature,[9, 13, 46, 47] and consists of monoclinic zirconia after yttria is leached into CMAS (albeit it may not actually be precipitated). We will refer to them as "secondary mixed layer" in this paper. The secondary mixed layer exhibits a structure with reprecipitated or fall-off ("dissolved") grains of irregular size and shape. The residual CMAS is homogenous and free of defects or crystalline phases. The total infiltration depth, accounting for both the infiltrated and secondary layer, was approximately 60 μm.

Agreeing with prior reports,[13, 47] the molten CMAS likely first penetrated the YSZ through the GBs, where then, the YSZ grains started to dissolve into the molten CMAS. Since Y^{3+} has a higher solubility than Zr^{4+} in molten CMAS, Y^{3+} ions are selectively dissolved, leading

to the fall-off of Zr-rich grains.[9, 46] In other words, YSZ becomes destabilized and transforms into monoclinic ZrO_2. The process continued with further GB infiltration.

6.3.2.2 4L: $(Hf_{0.314}Zr_{0.314}Ce_{0.314}Y_{0.029}Yb_{0.029})O_{2-\delta}$

A similar microstructure is evident in CCFO 4L. In Figure 6.2b, two distinct layers are also seen with the same secondary mixed layer and GB infiltration layer. The transition region from the infiltration to the secondary layer is slightly wider than the 8YSZ case. The total infiltration depth (64.5 ± 3.3 μm) is similar to 8YSZ. However, there are a couple of differences from 8YSZ. A feathery-like structure appears in a few locations at the CMAS-secondary layer boundary. Large cracks are also visible on the microscale. The cracking is likely due to the reaction phase transformations and associated volume changes at the interfaces.

Since the microstructure is similar to YSZ, it is believed that the mechanism of infiltration is also similar. Most likely, the CMAS penetrated through the GBs where it then began to dissolve the CCFO grains and leach out the cubic stabilizers (Y and Yb) to form stabilizer-deficient $(Hf_{1/3}Zr_{1/3}Ce_{1/3})O_2$ grains. However, a couple of other phases also formed when the CMAS interacted with 4L. For example, the precipitation of the feathery-like phase and a zircon/hafnon phase, which are discussed later.

6.3.2.3 4M: $(Hf_{0.284}Zr_{0.284}Ce_{0.284})(Y_{0.074}Yb_{0.074})O_{2-\delta}$

Figure 6.2c shows that the CMAS-affected microstructure of 4M is significantly different from that 8YSZ although the total stabilizer fractions are identical. In this specimen, there is a GB infiltration layer, but the secondary layer thickness is negligible at this temperature. These results suggest that this composition is more resistant to dissolution in the melt. Consequently, the total interaction depth (~ 50 μm) is shorter compared to the previous two cases. Like 8YSZ, no reaction products were seen at this temperature.

6.3.2.4 4H: $(Hf_{0.2}Zr_{0.2}Ce_{0.2})(Y_{0.2}Yb_{0.2})O_{2-\delta}$

The equimolar 4H specimen shows the most significant reduction in infiltration depth at this temperature (albeit with extra precipitation inside the CMAS). Examining the SEM image in Figure 6.2d, the residual CMAS exhibits elongated hexagonal needles of precipitates along with nearly circular grains. The needles have been identified as the apatite phase of the following composition: $Ca_2(RE)_8(SiO_4)_6O_2$, where RE denotes rare earth elements (Ce, Y, and Yb). This phase is known to form by a reactive crystallization process when the matrix has a sufficient concentration of rare earth elements.[15, 18, 47-51]

Notably, there is no GB infiltration layer in the equimolar high-entropy composition 4H, which was seen in all other samples. Figure 6.3 reveals the 4H-CMAS boundary at high magnification to highlight the absence of GB penetration. The total infiltration depth was measured from the top of the circular grains to the reaction boundary to be approximately 37 μm. Although the infiltration depth measured is less than the previous cases, it is important to note that the numerous apatite needles in the residual CMAS also represent additional reaction products.

A reaction with negligible GB infiltration differentiates the observations of this composition in the presence of molten CMAS from other cases discussed. The proposed mechanism in this sample is to be identical to the earlier cases in that the RE elements are leached from the grains, and the less soluble transition metal oxides (ZrO_2 and HfO_2) fall-off and form the secondary mixed layer. However, the difference in this composition is that the high RE concentration provides high reactivity rates with the CaO and SiO_2 constituents to form that apatite phase that leads to no observable infiltration. This finding is in agreement with previous

studies.[9, 52] The high concentration of rare earth elements is beneficial in arresting GB infiltration by reactive crystallization.

6.3.3 CCFO-CMAS REACTION PRODUCTS

6.3.3.1 SEM-EDS-EBSD CHARACTERIZATION

EDS and EBSD were used in conjunction with SEM to confirm the presence of the precipitates and reaction products seen after the 1300°C anneal. Figure 6.4 (a, b) shows the SEM micrograph and the corresponding phase analysis based on EBSD for the equimolar high-entropy composition 4H. EBSD confirms the hexagonal needles are the apatite phase, and they extend down to the CCFO-CMAS interface where they originate. Also, the grains in the mixed secondary layer exhibit the fluorite structure indicating that a significant amount excess RE elements was left over from the apatite reaction to maintain stabilization of the cubic ZrO_2 and HfO_2 phases.

The microstructure and corresponding phase fraction analysis for the reaction interface between 8YSZ and CMAS is shown in Figure 6.4 (c, d). Here, the bulk matrix was determined to be cubic, while those in the secondary mixed layer was of monoclinic structure. This agrees with the speculation that Y^{3+} selectively dissolves into the silicate melt, and ZrO_2 becomes destabilized to the monoclinic structure.

The feathery structure found in 4L was subject to the same SEM-EDS-EBSD procedure. Upon closer examination by SEM, a brighter phase was found embedded within the darker feathery structure shown in Figure 6.5 (a). Point EDS and EBSD were conducted simultaneously for both phases, and it was determined that the brighter phase was a perovskite phase, $CeAlO_3$, and the feathery structure was a cyclosilicate, $Ca_2Zr(Si_4O_{12})$. The corresponding electron backscatter pattern and fit, and the EDS spectrum for $CeAlO_3$ and $Ca_2Zr(Si_4O_{12})$ are displayed in

Figure 6.5 (b-d) and Figure 6.5 (e-g), respectively. Both of these are common reaction products found in TBCs.[47, 53] No reaction products were seen in 4M, so this sample was not analyzed.

6.3.3.2 XRD

CCFO powder and CMAS were mixed and annealed at 1300°C for 24 h to investigate the observed reaction products further. The 90CCFO:10CMAS wt. % ratio (~ 75:25 vol. %) was used, which was approximately the same as that found in the secondary mixed layer used in our sand penetration experiments (with sintered dense specimens). The CCFO powders were synthesized at 1600°C for 24 h, and the XRD spectra are shown in Figure 6.6a. All samples exhibit a cubic fluorite structure except 4L, which possesses a body-centered tetragonal phase. This is the same structure as tetragonal YSZ (~ 4 mol. %) as noted by a prior report.[32]

After mixing the CCFO powder with CMAS and annealing, all the samples show reaction products. 8YSZ and 4L show a minimal presence of a zircon/hafnon phase. This phase was seen in the SEM images of 4L (left side of Figure 6.2b), but not in 8YSZ. 4H shows a strong presence of the apatite phase, which was also observed in SEM of the specimens from the sand penetration experiments. 4M shows a mixture of both phases; however, neither of these phases were seen in SEM of the specimens from the sand penetration experiments. The discrepancies between XRD of powder mixtures and SEM of sand penetration specimens may be due to the kinetic effects (better mixing in powder specimens). Moreover, the formation of a small amount of the phase at interfaces might not be found in the cross-sectional SEM. Lastly, the local composition has a strong effect on the corrosion and reaction products, and the differing nature of these experiments compared with the cross-sectional experiments likely produced differences in phase evolution following reaction. However, this mixing experiment complements the SEM-

EDS-EBSD data and provides valuable insight into the sensitivity of the local composition and the various products that can occur.

6.3.4 TEMPERATURE DEPENDENCE

Similar experimentation and analysis were also conducted at 1200°C, 1400°C, and 1500°C to investigate the temperature-dependent kinetics of the reaction and infiltration. As an example, the microstructure of equimolar 4H $(Hf_{0.2}Zr_{0.2}Ce_{0.2}Y_{0.2}Yb_{0.2})O_{2-\delta}$ at each temperature is shown in Figure 6.7. In general, the interaction zone exhibited similar characters, while the length scale of the interaction increased. No new products or different mechanisms were found. At 1200°C, the reaction is nearly negligible as the kinetics are relatively slow. The CMAS is only partially molten at this temperature, and there are some crystalline products in the residual CMAS. The microstructures at 1400°C are very similar to those observed at 1300°C; however, the length scale of the interaction zone increased substantially. At 1500°C, the reaction is prominent. No residual CMAS was found at this temperature suggesting all the CMAS reacted or evaporated. There are also large voids present near to the top surface, presumably due to off-gassing of various CMAS constituents.

SEM micrographs for the other CCFOs and 8YSZ from 1200°C - 1500°C at low, medium, and high magnification are shown in the SI. Similar characteristics have been observed generally for the low- and medium-entropy specimens; however, no reaction appeared to occur for 8YSZ at all investigated temperatures.

A plot of the measured interaction lengths at the respective temperatures is shown for all samples in Figure 6.8. It was found that the CCFOs exhibited smaller infiltration depths at 1200°C and 1300°C, but the trend flipped at $T \geq 1400$°C, where 8YSZ now showed significantly less penetration and interaction compared to the CCFOs. At these higher temperatures, all the

CCFOs began to show significant dissolution and reaction with the melt. Moreover, the penetration depth for the CCFOs exhibited an exponential trend versus temperature, while that for 8YSZ was almost linear. This likely resulted from the higher reactivity of CCFOs with CMAS at high temperatures, in comparison with YSZ.

The enhanced reactivity between CMAS and equimolar 4H $(Hf_{0.2}Zr_{0.2}Ce_{0.2}Y_{0.2}Yb_{0.2})O_{2-\delta}$ form an apatite phase. The benefits of reactive crystallization are often the most sought after mechanism in designing a CMAS-resistant TBC and has been successfully demonstrated multiple times.[14, 18, 47, 50] For TBCs, which are traditionally ~ 20 vol. % porous, a highly reactive material (such as $Gd_2Zr_2O_7$) can react with CMAS to form a reaction product that subsequently seals the pores and drastically reduces any further CMAS penetration. However, for EBCs, which are typically < 10 vol. % porosity, the objective is to achieve a material that is inert to CMAS to minimize recession and loss of the material.[49]

Although the primary difference between 8YSZ and the CCFOs investigated here is configurational entropy, we believe the differences seen here are not led by entropy differences, and instead by the concentration rare-earth elements. Performance tends to degrade with increasing entropy, but the cubic stabilizer concentration simultaneously increases as well. To this effect, we looked at the optical basicity of the specimens, which is a common descriptor for measuring reactivity in glasses and oxides. Studies have attributed the tendency of glasses/oxides to react with another compound with the difference in optical basicity (OB, Λ) of both materials.[7, 47-49, 54] The concept of OB is an extension of the Lewis theory of acid-base reactions and expresses the tendency of the material to donate electrons based on the electron density carried by oxygen.[55, 56]

The OB of CMAS is approximately 0.64 (see the calculation in Ref. [49]). A large OB difference tends to result in high reaction rates, while a small difference results in negligible reaction/interaction. The OB of 8YSZ with 4L, 4M, and 4H are 0.87, 0.88, 0.89, and 0.91, respectively. Thus, the $\Delta\Lambda$ suggests higher reaction rates as the stabilizer concentration increases, which is in agreement with our experimental observations at high temperatures ($T \sim 1500$℃). This trend is not fully realized at lower temperatures ($T < 1400$℃) that may be due to kinetic limitations and the absence of reaction products in the reported infiltration depths.

The OB values of the specimens in this study are similar to other candidate thermal/environmental barrier coating materials such as $Yb_2Zr_2O_7$ (0.89) and $Y_2Si_2O_7$ (0.70).[49] Wiesner et al. looked at the CMAS resistance of $Y_2Si_2O_7$ at 1200°C, 1300°C, 1400°C, and 1500°C after 20 h of annealing, which had infiltration depths of 12.7, 80.9, 215.8, and 217.6 μm, respectively.[16] The CCFOs in this study perform better temperatures below 1500°C; however, at 1500°C, the performance of $Y_2Si_2O_7$ is similar to our 8YSZ. Recently, Sun et al. studied the CMAS resistance of a high entropy disilicate, $(Er_{0.25}Tm_{0.25}Yb_{0.25}Lu_{0.25})_2Si_2O_7$.[57] The OB is approximately 0.70, and they report significant stability of the material and grain boundaries at 1500°C in contact with molten CMAS compared to the constituents. The authors attributed this enhanced performance to entropy stabilization. We did not find effects suggesting this in our (Zr, Hf, Ce)-based fluorites and instead found worsened stability with increasing entropy; however, this also comes with increased *f*-element concentration. Furthermore, the direct high-entropy effects on reactivity may be limited because $T\Delta S$ is generally smaller than ΔH in most reactions.

A higher stabilizer concentration of a simpler defect-fluorite, $Zr_{0.53}Y_{0.47}O_{2-\delta}$, has been reported in literature as have a reaction layer thickness of 468 μm after 5 h at 1310°C,[7] however, the relative density is ~ 90% making comparison difficult. When comparing our 8YSZ to CCFO

4M (same stabilizer concentration but higher configurational entropy in CCFO 4M), we do not see enhanced stability. Although, it should also be noted that Sun et al. compared the performance of their high entropy material to the constituents found in literature as opposed to measuring it themselves. Lastly, we used a synthetic sand (AFRL-02),[9, 50] which has minor impurities of Fe_2O_3, Na_2O, and K_2O. These impurities can have a strong influence on the corrosive nature because of the shifting chemical equilibrium. All of this together leaves the possibility of varying experimental conditions affecting results and difficulty in making direct comparisons to other work high.

Equimolar 4H $(Hf_{0.2}Zr_{0.2}Ce_{0.2}Y_{0.2}Yb_{0.2})O_{2-\delta}$ would likely perform successfully as a TBC with ~ 20 vol. % porosity. However, as an EBC, it would perform poorly, as evident in this study, particularly at high temperatures. Overall, the 3YSZ-like medium-entropy 4L would function better than the equimolar 4H as a TBC material in terms of the interaction with CMAS. However, the absence of GB penetration in equimolar 4H $(Hf_{0.2}Zr_{0.2}Ce_{0.2}Y_{0.2}Yb_{0.2})O_{2-\delta}$ (Figure 6.3) could potentially be useful as TBC if the extent of the reaction could be minimized. A further potential advantage of the high entropy system with rare earth elements is that the compositions can be tuned with more favorable elements with lower OB values while keeping the desired phase and other various properties because of the chemical similarity between the rare earth elements.

6.3.5 THERMAL EXPANSION

6.3.5.1 MEAN LINEAR CTE

High-temperature thermal expansion heating and cooling curves for all samples are shown in Figure 6.9. Since 4L exhibited a mix of tetragonal and cubic phase after sintering at 1600°C for 24 h, it was annealed at 1200°C for 24 h to produce a fully tetragonal specimen prior

to thermal expansion measurements. All samples show a parabolic nature over the broad temperature range, which is common to ceramic materials. The maximum expansion approaches nearly 2 % at 1600°C for 4L and 4M, expanding a bit more than 8YSZ.

The mean linear CTE was calculated for each sample from 100°C – 1500°C to obtain an overall value, which is shown in Table 6.1. The CTE for 4L was only calculated with data up to 1200°C due to its phase transition. The heating and cooling curves are in close agreement, so the average linear CTE was only calculated from the heating curve. A CTE of $11.4 \pm 0.5 \times 10^{-6}$ K^{-1} for 8YSZ is in excellent agreement with those reported in literature.[58] CTEs for 4L and 4H ($11.4 \pm 0.5 \times 10^{-6}$ K^{-1} and $11.6 \pm 0.4 \times 10^{-6}$ K^{-1}) are very similar to 8YSZ over the entire temperature range. The CTE for 4M ($12.2 \pm 0.5 \times 10^{-6}$ K^{-1}) is ~ 7 % higher than the other CCFOs and YSZ. The CTE appears to reach a maximum near a stabilizer concentration of ~ 15 % ($x = 0.074$) in 4M in this $[Hf_{(1-2x)/3}Zr_{(1-2x)/3}Ce_{(1-2x)/3}Y_xYb_x]O_{2-\delta}$ series of CCFOs.

The defective fluorite structure is known to have clustering/ordering of the oxygen vacancies when the oxygen percentage increases above approximately 5 %.[59-62] The introduction of oxygen vacancies will increase the disorder and anisotropy within the system up to this threshold of anion clustering transition, where the anisotropy starts to decrease and leads to a decreasing CTE. The oxygen vacancy percentages in 4L, 4M, and 4H are 1.5 %, 3.7 %, and 10 %, respectively. This helps explain why 4M has a higher CTE than both 4L and 4H. It is worth noting that a similar trend was observed in thermal conductivity for this series of CCFOs.[32] Although 4M has the same nominal oxygen vacancy concentration as 8YSZ, the disorder and anisotropy on the cation sublattice in 4M is significantly greater due to the presence of multiple cations. High CTEs that are closer to that of Ni-superalloy blade materials (CTE = $\sim 16 \times 10^{-6}$ K^{-1})[63, 64] are desired for TBCs to minimize the expansion mismatch between the coating and

substrate to reduce thermal stress. In this regard, a fluorite specimen with a similar oxygen vacancy concentration to 4M is a potential advantage. Our prior study also showed that this composition has reduced (the lowest) thermal conductivity and increased (the highest) modulus to thermal conductivity ratio for this series of CCFOs,[32] all of which are also advantageous properties for potential TBC applications.

6.3.5.2 INSTANTANEOUS CTE

The derivatives (at a 0.1-min time step) of the thermal expansion curves were used to calculate the instantaneous CTEs (α_T) as functions of temperature, as shown in Figure 6.10. The values increase with increasing temperature, thereby showing parabolic effects of thermal expansion.

Moreover, 4L and 4M show two distinct slopes. The change in slope for 4L (shown in Figure 6.10b) around 1300°C is due to the phase transition from body-centered tetragonal to fluorite cubic. There is a slight volume contraction (~ 0.7 vol. %) associated with this phase transition,[32] and the cubic phase has a moderately different CTE. Figure 6.10c also shows a moderate slope change in 4M around 1000°C, which may be due to an internal rearrangement of the ions in the structure. However, this transition is more gradual than that observed in 4L, and no phase transition was evident to occur in this sample by XRD.

These CTE curves from T = 700°C – 1000°C were fitted to extract the intrinsic CTE and the temperature-dependent coefficients, α_0 and α_1, respectively, using the following equation,

$$\alpha = \alpha_0 + \alpha_1 T. \quad (1)$$

Table 6.1 lists all CTEs. All CCFOs all have higher intrinsic CTEs (than that of the 8YSZ reference) and smaller dependences on the temperature within this temperature range. The larger intrinsic CTE (more compatible with Ni-superalloys) is desirable, and the smaller temperature-

dependence will allow for less stress during ramping and cooling, both of which are beneficial for TBC applications.

6.3.6 ABLATION

Ablation testing was conducted to test the feasibility of CCFOs as protective coatings on supersonic/hypersonic vehicles in areas away from the leading edge (where borides and carbides are preferred) and provide a preliminary benchmark for future candidate materials.[65] A neutral oxy-propane flame was positioned approximately 19 mm away from the sample surface and held for 5 min. The surface temperature and emissivity profile for each material was generated by a dual-wavelength pyrometer with a 0.1 s collection time. The results are shown in Figure 6.11. The average surface temperatures were in the range of 1800°C – 2100°C. All CCFOs experienced higher surface temperatures than YSZ. The experiments were conducted in a constant energy flux setup, so any differences are likely due to the emissivity (ε) and thermal conductivity of the samples. Thus, these results suggested that the CCFOs all show lower emissivities and thermal conductivities compared to 8YSZ at these high temperatures, with a trend of decreasing emissivity with an increasing fraction of stabilizers. The sudden change in the testing of 4L was due to an experimental artifact (pyrometer position correction). The correct measurement is represented by the latter half of the measurement, and the first half can be ignored. The lower thermal conductivity has been confirmed from our previous study.[32] The low ε suggests that the CCFOs emit (and likely absorb) less infrared energy, which will result in additional cooling requirements. Although a higher ε is more desirable in cooling needs, it is undesirable in stealth applications. Here, low emissivities of the CCFOs will reduce the heat signature and detection, which represents a potential merit.

A couple of the samples (8YSZ and 4M) fractured into several pieces upon cooling after removal of the oxy-propane flame shown in Fig. S6.14 in Suppl. Data. They also exhibited an inhomogeneous color change. Nearly all the CCFOs had a random distribution of dark green-black spots. Upon SEM examination, no noticeable difference in the microstructure or chemical inhomogeneity was seen on the spots. It is believed that the dark spots are due to changes in the oxidation states of Ce at high temperatures.

On the pieces examined by SEM, the CCFOs showed more signs of deformation than 8YSZ. No significant changes were seen in 8YSZ following testing. The non-equimolar medium-entropy $(Hf_{0.314}Zr_{0.314}Ce_{0.314}Y_{0.029}Yb_{0.029})O_{2-\delta}$ (4L) showed the most extreme microstructural changes by having nearly all the grains in specific regions, exhibiting an unusual step formation, as shown in Figure 6.12. The other CCFOs experienced this deformation but not to the same severity. These are likely due to either brittle fracture or plastic deformation (FCC (111) is prone to slip) along specific plane orientations. It is unknown currently if this deformation is beneficial or not.

Overall, the CCFOs did not exhibit any signs of melting at these temperatures, thus displaying their temperature stability up to 2000°C.

6.4 CONCLUSIONS

We have established the CCFOs as a benchmark coating material by measuring their interaction/reaction with molten CMAS at 1200 – 1500 °C and high-temperature flame ablation at 1800-2100 °C, as well as their CTEs.

The single-phase CCFOs exhibit improved resistance to sand (CMAS) infiltration at intermediate temperatures (1200 – 1300°C) in comparison with cubic 8YSZ. At 1300°C, the widths of interaction zones for three CCFOs, 4L, 4M, and 4H, were measured to be 64.5 ± 3.3

μm, 52.6 ± 8.6 μm, and 37.3 ± 2.0 μm, respectively, in comparison with 62.3 ± 7.4 μm for 8YSZ, after for 24 h. However, they undergo significant degradation at higher temperatures (1400-1500°C) due to increased reactivity. At relatively low stabilizer concentrations (< 15 cat. %), the molten CMAS penetrates the CCFOs through GBs. The CCFO grains dislocate into the CMAS melt, where the rare earth elements (Ce, Y, and Yb) leach out and remain solubilized in the melt. At higher concentrations (~ 40 cat. %), no GB penetration is observed and instead, the CMAS selectively leaches the RE elements out of the CCFO grains and reacts with the rare earth elements, and apatite crystals precipitated out in the CMAS matrix. The change in material performance is likely due to the cubic stabilizer concentration and not configurational entropy (although in this case, they are directly related). Additionally, the direct "high-entropy" effects on reactivity may be limited because $T\Delta S$ is still smaller than ΔH of most reactions.

All three CCFOs (4L, 4M, 4H) exhibit higher intrinsic CTEs ($11.4 \pm 0.5 \times 10^{-6}$ K^{-1}, $12.2 \pm 0.5 \times 10^{-6}$ K^{-1}, $11.6 \pm 0.4 \times 10^{-6}$ K^{-1}) than 8YSZ ($11.4 \pm 0.5 \times 10^{-6}$ K^{-1}), and they show a reduced temperature dependence, both of which are beneficial for a protective coating on Ni-based superalloys with a high CTE. Lastly, the CCFOs undergo severe microstructural changes at extreme temperatures (~ 2000°C) in ablation testing; however, no sign of melting was observed.

In summary, these CCFOs have some potential to be used as TBCs, because of their improved resistance to molten CMAS at intermediate temperatures (1200-1300°C) and larger CTEs that are more compatibility to nickel superalloy substrates, in addition to the reduced thermal conductivity and improved modulus to thermal conductivity ratios reported previously.[32] However, the improvements reported in this study are marginal compared to the performance of

8YSZ, although 4 mol. % YSZ is the industrial standard. Instead, we wish to provide a starting point and baseline for future T/EBC-related materials.

An interesting phenomenon is the formation of faceted microstructures in ablation testing for non-equimolar medium-entropy $(Hf_{0.314}Zr_{0.314}Ce_{0.314}Y_{0.029}Yb_{0.029})O_{2-\delta}$ (4L) and needs further investigation. In addition to the lowest thermal conductivity reported in the prior study,[32] the 8YSZ-like 4M, $(Hf_{0.284}Zr_{0.284}Ce_{0.284}Y_{0.074}Yb_{0.074})O_{2-\delta}$ exhibits the highest CTE in this series of CCFOs with different stabilizer fractions, due to oxygen clustering effects, which are also advantageous properties for potential TBC applications. We do note, however, that further testing is needed on coatings applied by physical vapor deposition methods (typically plasma spray or electron beam deposition) to investigate the role of processing on the microstructure and performance. Our hope is that this study can serve as a step toward further testing and understanding of CCFOs in TBC applications.

Chapter 6, in full, is a reprint of the material as it appears in Journal of the American Ceramic Society 2020. A.J. Wright, C. Huang, M.J. Walock, A. Ghoshal, M. Murugan, J. Luo, Sand corrosion, thermal expansion, and ablation of medium- and high-entropy compositionally-complex fluorite oxides. *J. Am. Ceram. Soc*., 2020.The dissertation author was the primary investigator and author of this paper.

Table 6.1. Measured density and CTE for all samples sintered at 1600°C for 24 h. The thermal expansion coefficients (CTEs) evaluated from 100°C – 1500°C are also included. Here, α_L is mean linear CTE, and the temperature-dependent CTE is also fitted into a linear equation $\alpha = \alpha_0 + \alpha_1 T$, where α_0 is intrinsic CTE and α_1 is a temperature-dependent coefficient.

	8YSZ	**4L**	**4M**	**4H**
Theoretical Density (g/cm^3)	5.97	7.85	7.83	7.59
Relative Density (%)	96.6 ± 2.9	95.4 ± 4.7	96.7 ± 2.7	96.4 ± 3.2
α_L (10^{-6} K^{-1}) (100°C – 1500°C)	11.4 ± 0.5	11.4 ± 0.5*	12.2 ± 0.5	11.6 ± 0.4
α_0 (10^{-6} K^{-1}) (700°C – 1000°C)	7.5	9.5	8.0	9.1
α_1 (10^{-9} K^{-2}) (700°C – 1000°C)	4.6	2.6	4.5	2.9

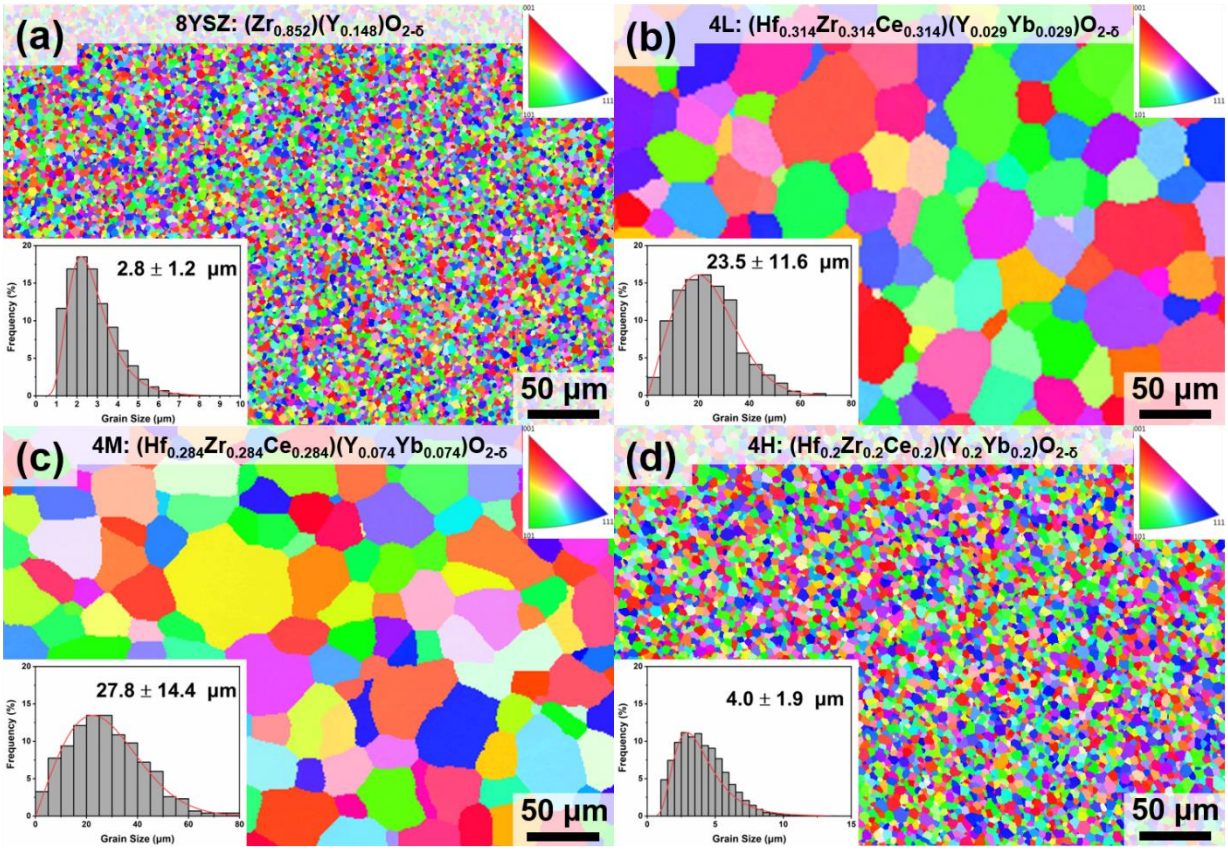

Figure 6.1. Electron backscatter diffraction (EBSD) grain size analysis of (a) 8YSZ and (b) 4L, (c) 4M, and (d) 4H CCFOs. Insets show the inverse pole figures and grain size distribution curves. The grain size distributions of 8YSZ and 4H were fit with lognormal distributions while those of 4L and 4M were fit with Weibull distributions.

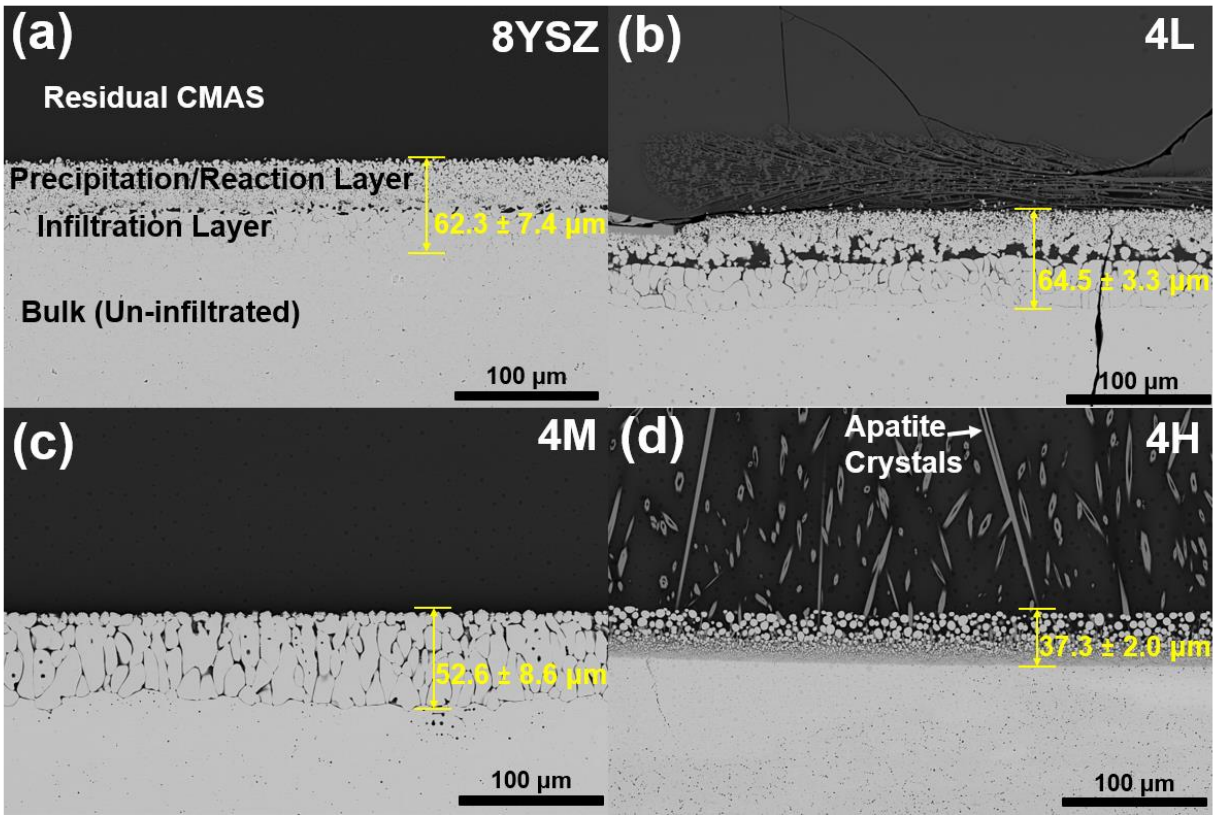

Figure 6.2. Polished cross-sectional SEM images of (a) 8YSZ and (b) 4L, (c) 4M, and (d) 4H CCFOs after contact with molten CMAS at 1300°C for 24 h. Similar to 8YSZ, a secondary mixed layer and a GB infiltration layer of similar thicknesses are visible in 4L. In contrast, 4M only shows a GB infiltration. In 4H, a reaction led to the formation of an apatite phase as needle-like precipitates (in the cross-section) in the molten sand.

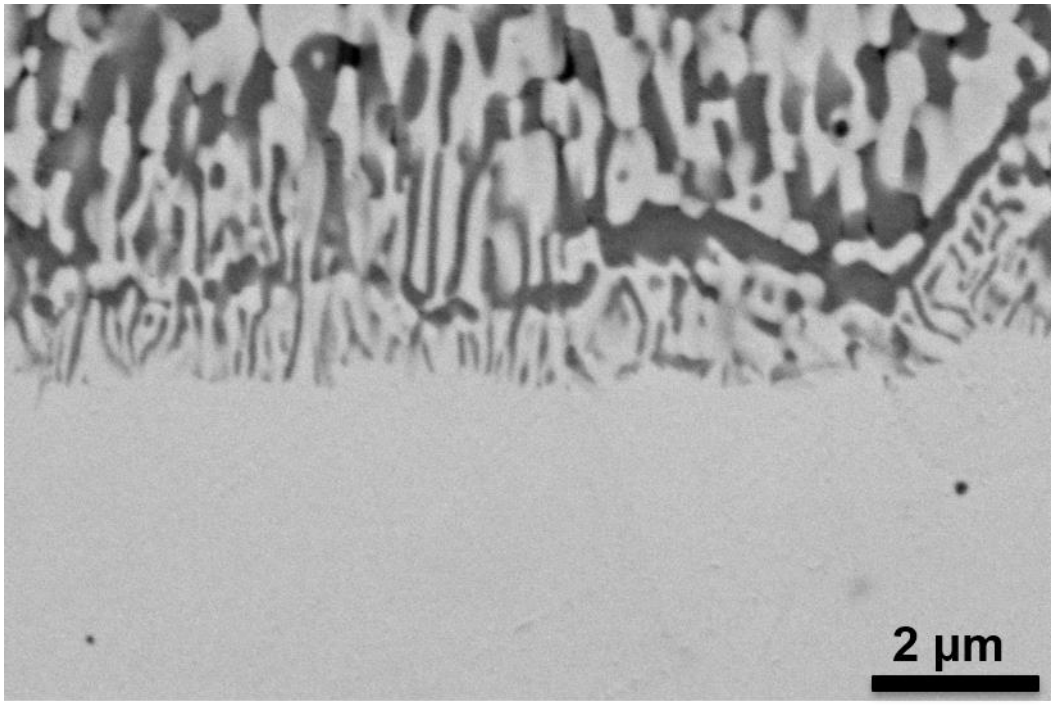

Figure 6.3. SEM micrograph of 4H high-entropy $(Hf_{0.2}Zr_{0.2}Ce_{0.2})(Y_{0.2}Yb_{0.2})O_{2-\delta}$ at higher magnification showing reaction occurring uniformly after annealing in contact with CMAS at 1300°C for 24 h. In this composition, there is no preferred GB infiltration, although reaction, as seen in all specimens of other compositions. Noting that the average grain size of the 4H specimen is ~ 4 μm.

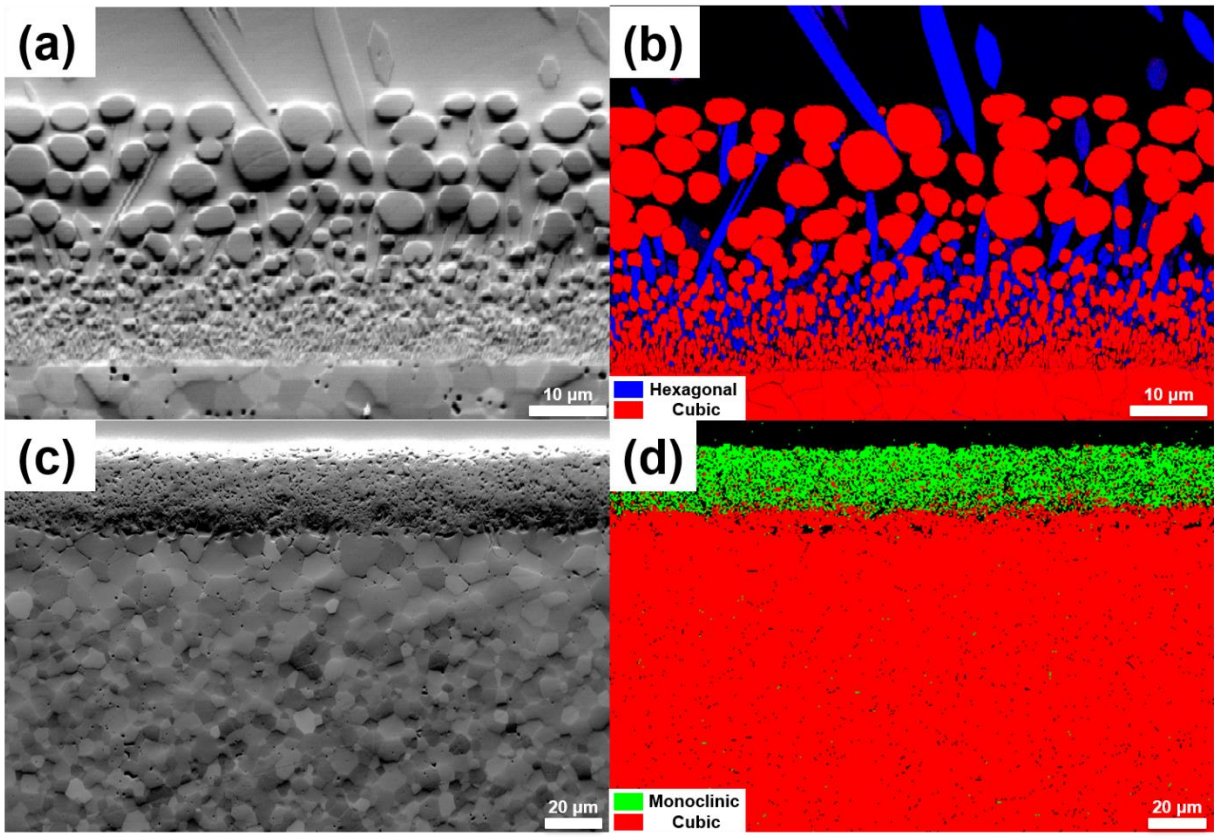

Figure 6.4. SEM images of the reaction and infiltration zone of (a) 4H and (c) 8YSZ after annealing at 1300°C in contact with molten CMAS. Electron backscatter diffraction (EBSD) phase analysis of (b) 4H and (d) 8YSZ reveal reactions and phase transformations after the interaction. Red, blue, and green denote cubic, hexagonal, and monoclinic crystals, respectively. The hexagonal phase corresponds to the apatite phase, and the green phase corresponds to monoclinic ZrO_2. The cubic structure is the disordered fluorite phase.

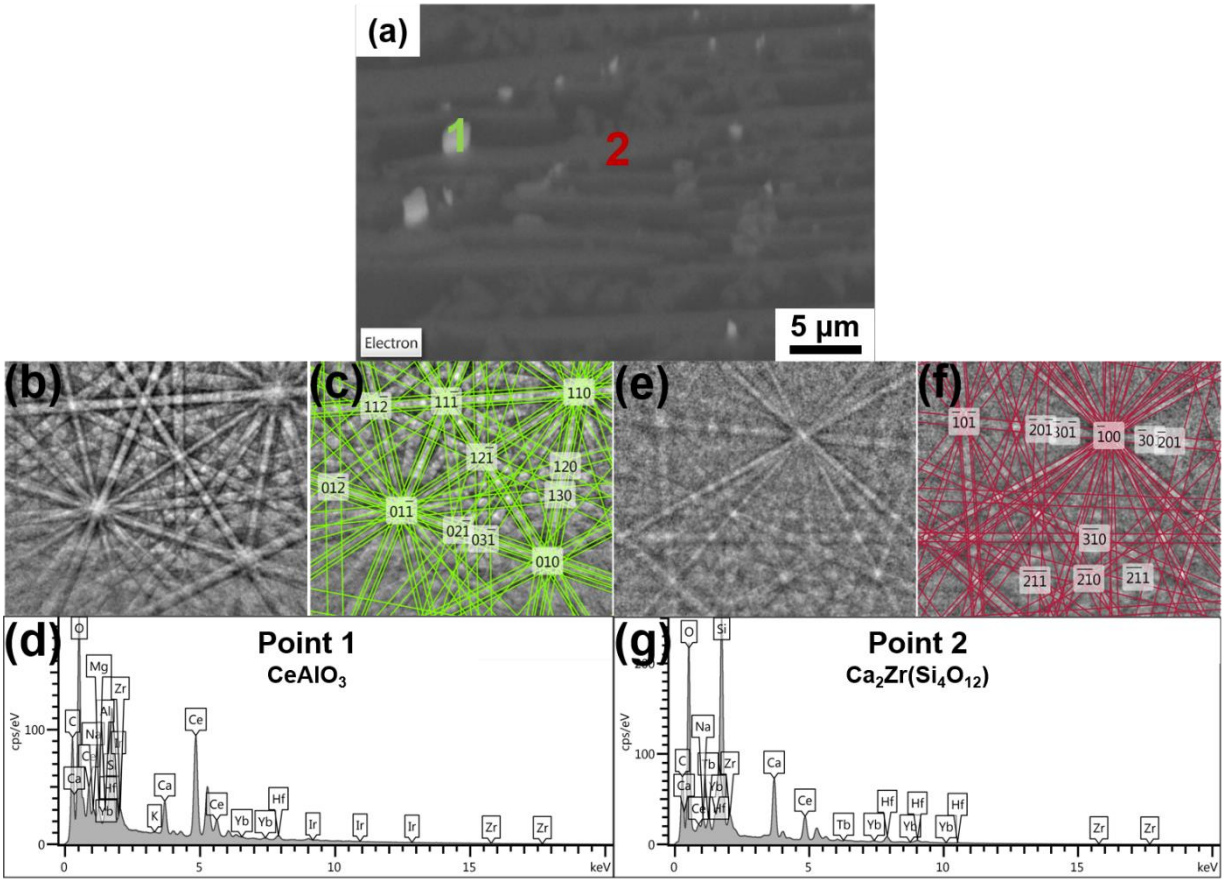

Figure 6.5. (a) SEM micrograph of feathery-like structure seen in 4L after 1300°C anneal with molten CMAS at high magnification. Electron backscatter diffraction (EBSD) patterns and their corresponding fits are shown for (b, c) Point 1 and (e, f) Point 2. EDS spectra were collected to measure the compositions for (d) Point 1 and (g) Point 2, which were determined to be $CeAlO_3$ and $Ca_2Zr(Si_4O_{12})$, respectively.

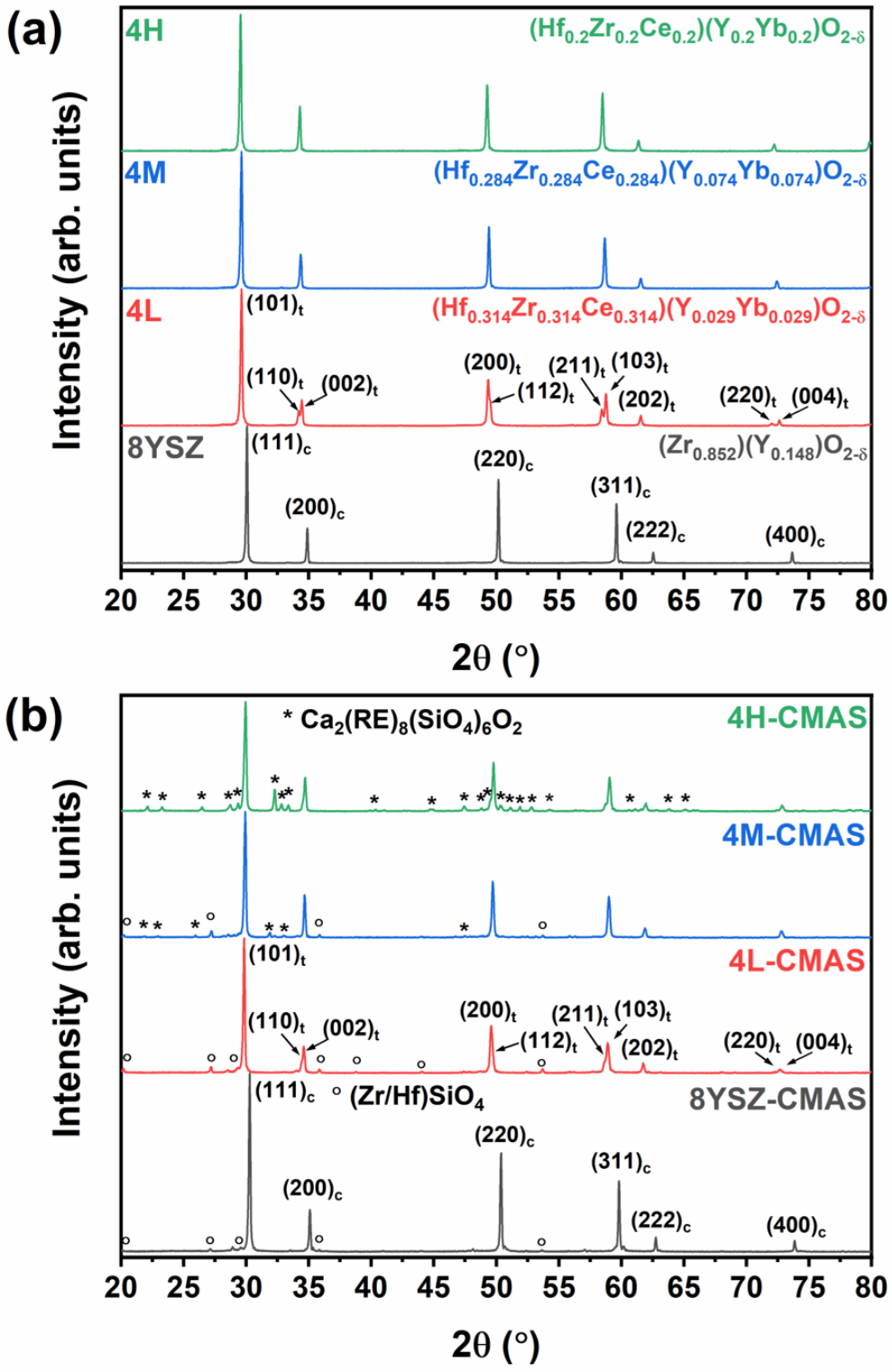

Figure 6.6. Powder XRD spectra of the 8YSZ and three CCFOs (a) before and (b) after annealing with 10 wt. % CMAS at 1300°C for 24 h.

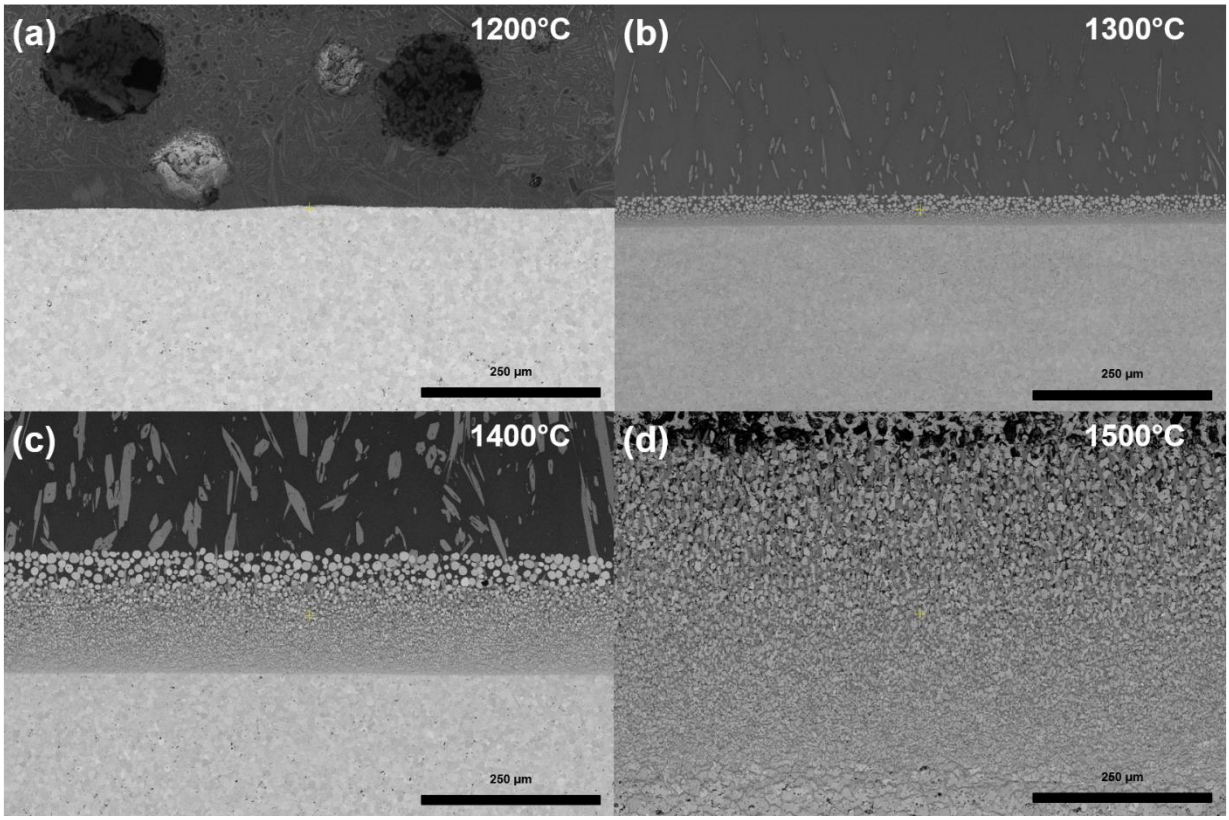

Figure 6.7. Cross-sectional SEM images of the high-entropy 4H $(Hf_{0.2}Zr_{0.2}Ce_{0.2})(Y_{0.2}Yb_{0.2})O_{2-\delta}$ in contact with molten CMAS at (a) 1200°C, (b) 1300°C, (c) 1400°C, and (d) 1500°C for 24 hours. Similar features are observed while the length scale of reaction increases.

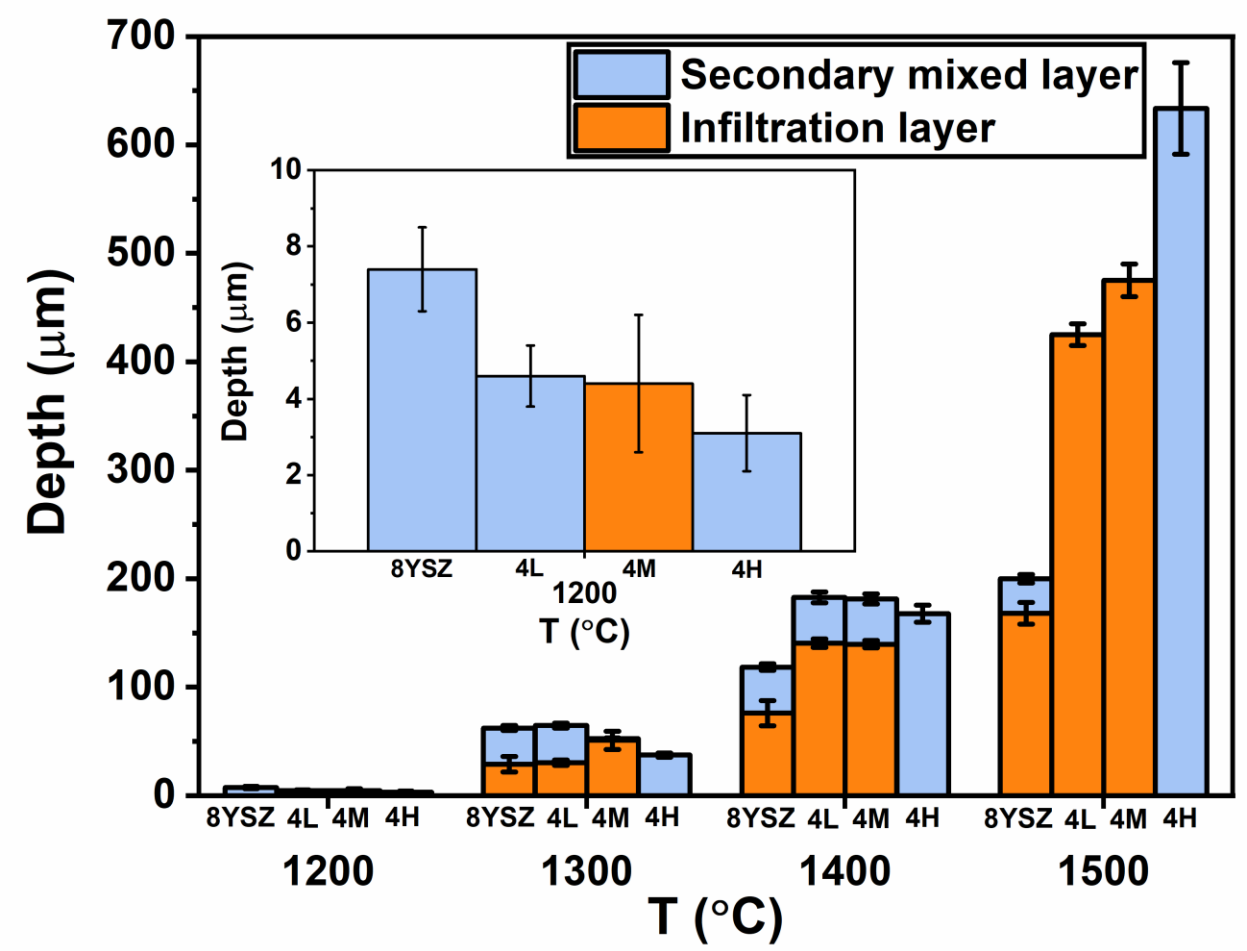

Figure 6.8. Total infiltration depths (including both secondary mixed and GB infiltration layers) for all samples annealed at 1200 to 1500°C in contact with molten sand. The inset shows the expanded view of the infiltration depths at 1200°C. In comparison with 8YSZ, CCFOs offer some improved chemical and microstructural stability at 1300°C but show high reactivity at higher temperatures.

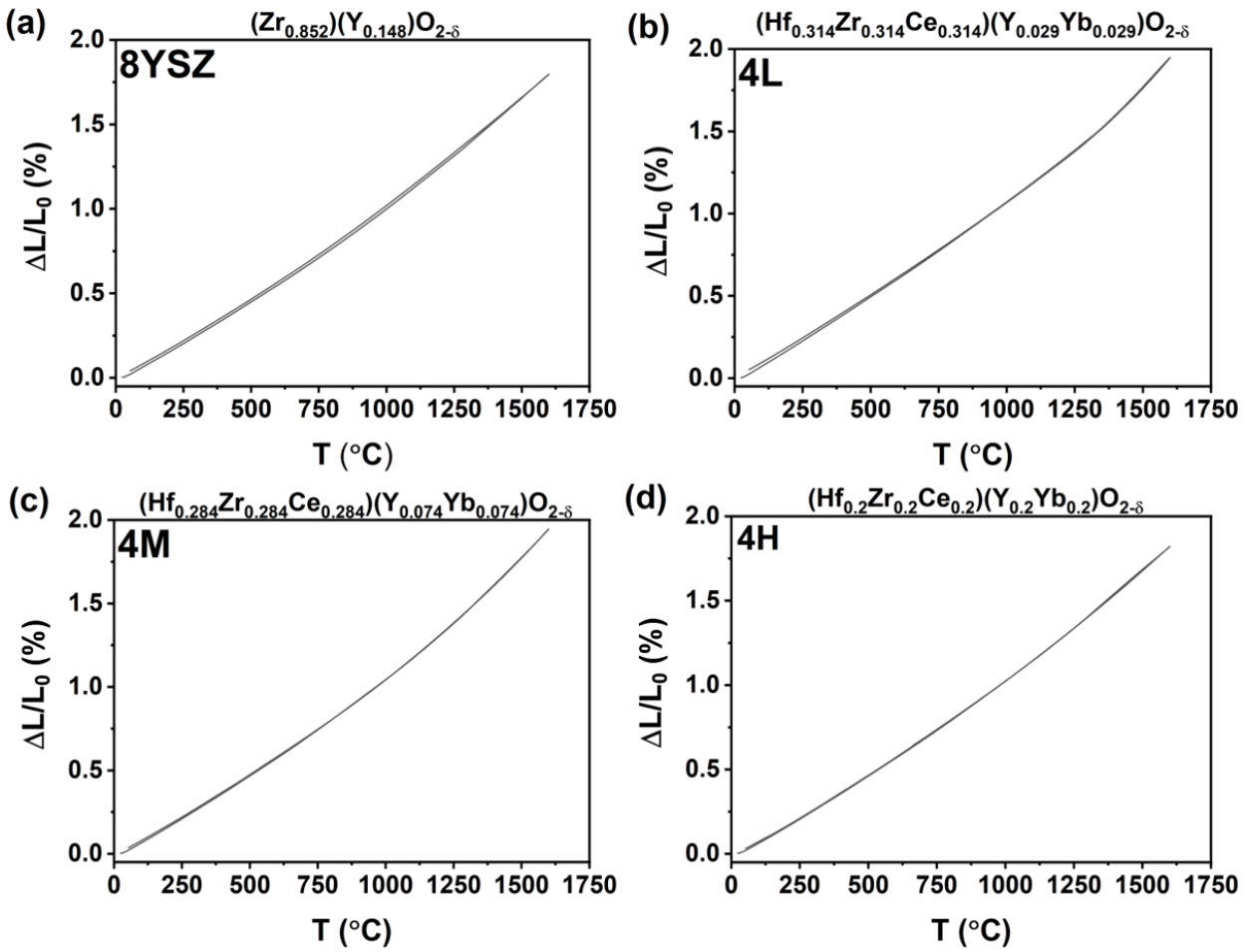

Figure 6.9. Thermal expansion curves for (a) 8YSZ and (b) 4L, (c) 4M, and (d) 4H CCFOs from 25°C to 1600°C during both heating and cooling. A phase transition occurs in 4L around 1250°C, resulting in a slight change in the slope.

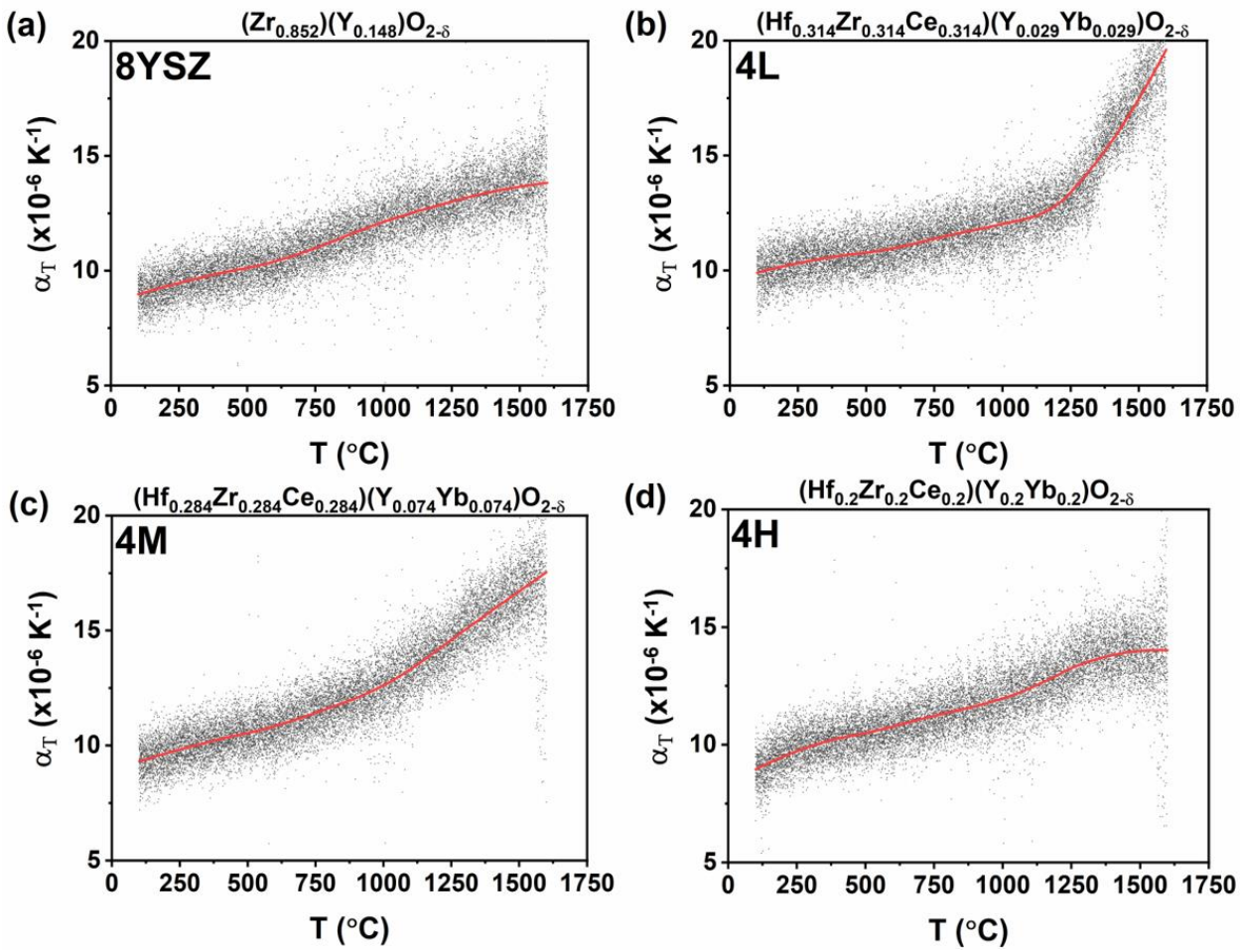

Figure 6.10. Scatter plots of instantaneous thermal expansion coefficients from 100°C to 1600°C of (a) 8YSZ and (b) 4L, (c) 4M, and (d) 4H CCFOs, which were generated with a 0.1 min time step. A tetragonal-to-cubic phase transition in 4L occurs around 1250°C, which causes a change in the thermal expansion coefficients. Red lines are smoothed curves generated using a LOESS function with a span of 0.5.

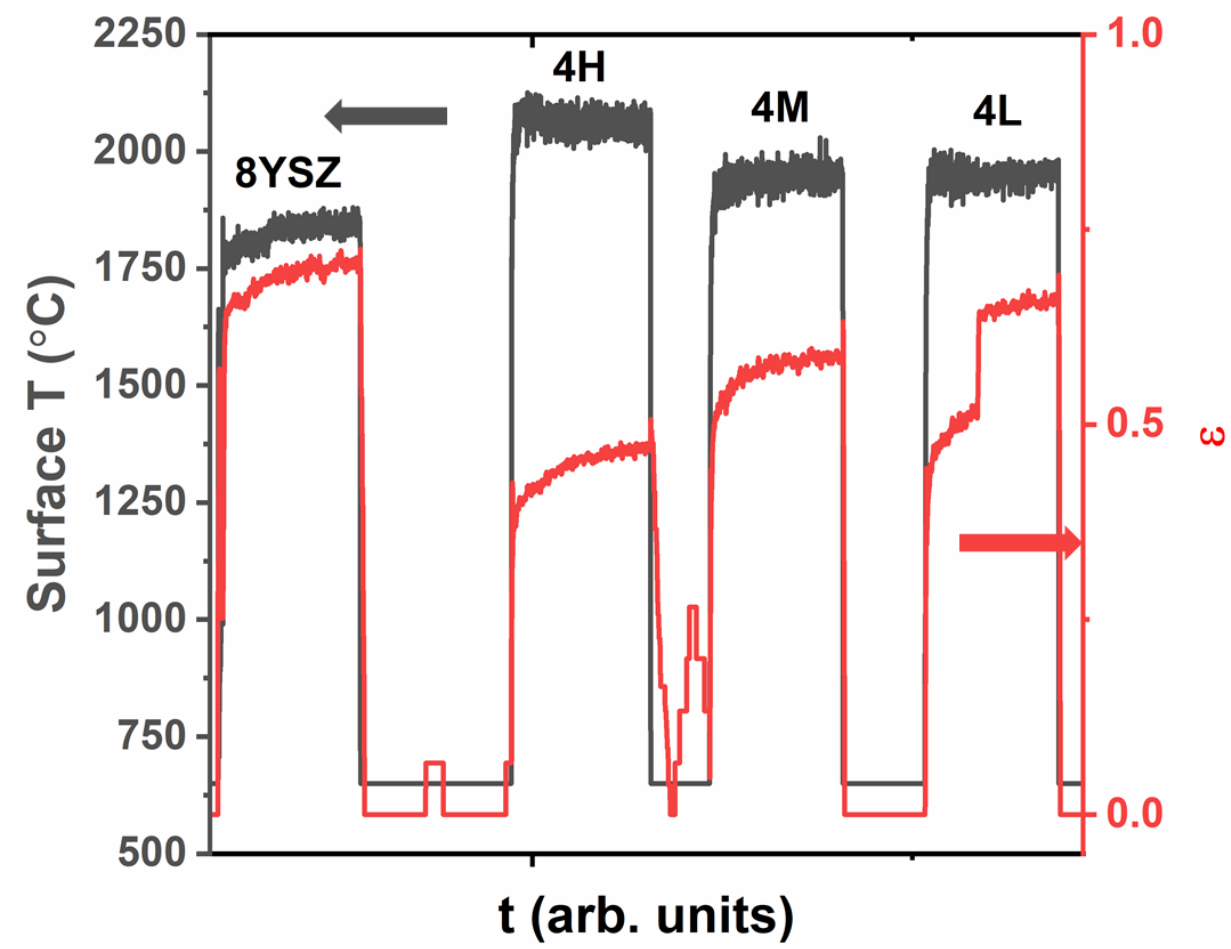

Figure 6.11. Surface temperature and emissivity of all samples during ablation tests generated by a dual-wavelength pyrometer. Each sample was held under an oxy-propane flame for five minutes. The spontaneous jump seen in 4L is due to an artifact due to an equipment adjustment.

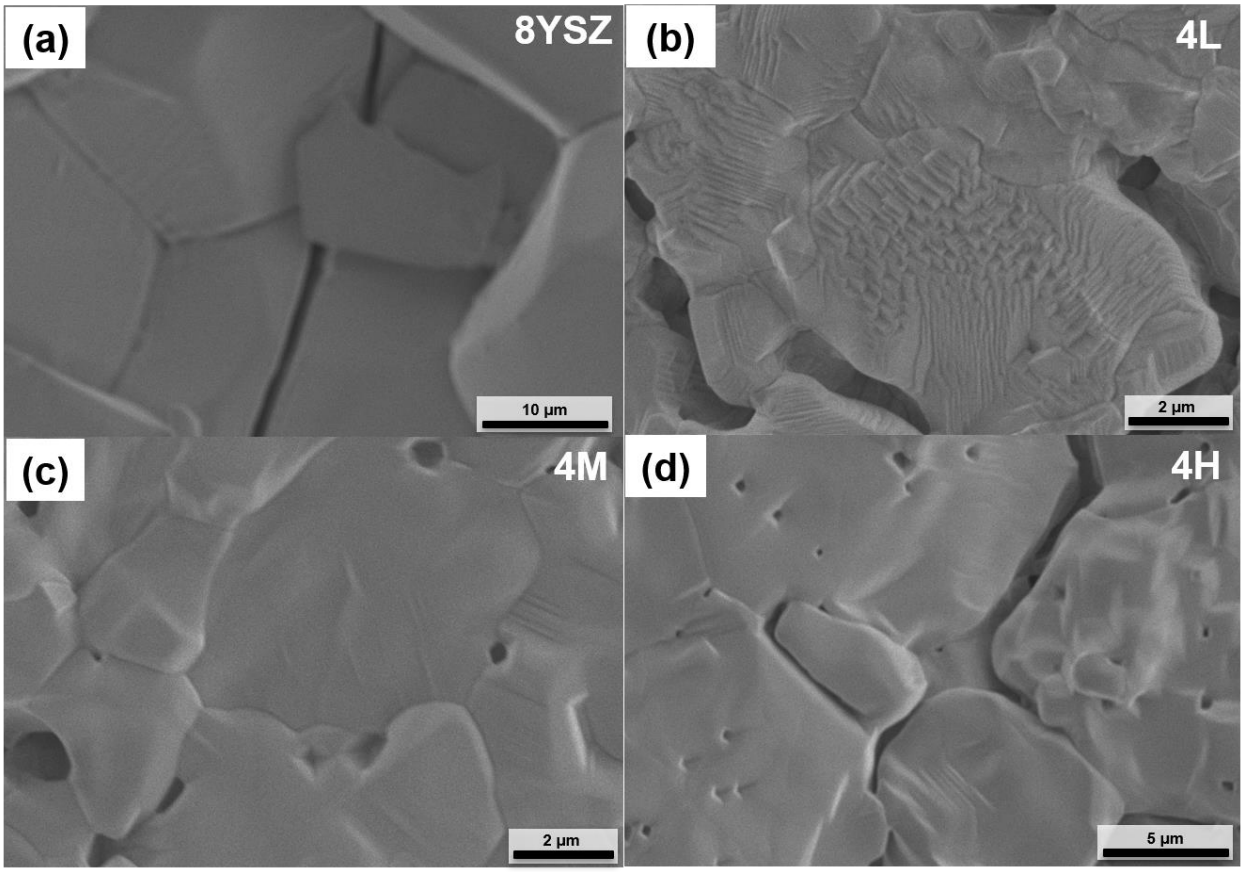

Figure 6.12. Post-ablation SEM images of (a) 8YSZ and CCFOs (b) 4L, (c) 4M, and (d) 4H. Steps and terraces are significantly present in CCFO 4L and sparsely present in other CCFOs; none observed in 8YSZ. The faceted structures (at a length scale of ~ 100 nm) revealed at increased magnification. Note varying magnification size to account for varying grain sizes (and thus grain size features) between specimens.

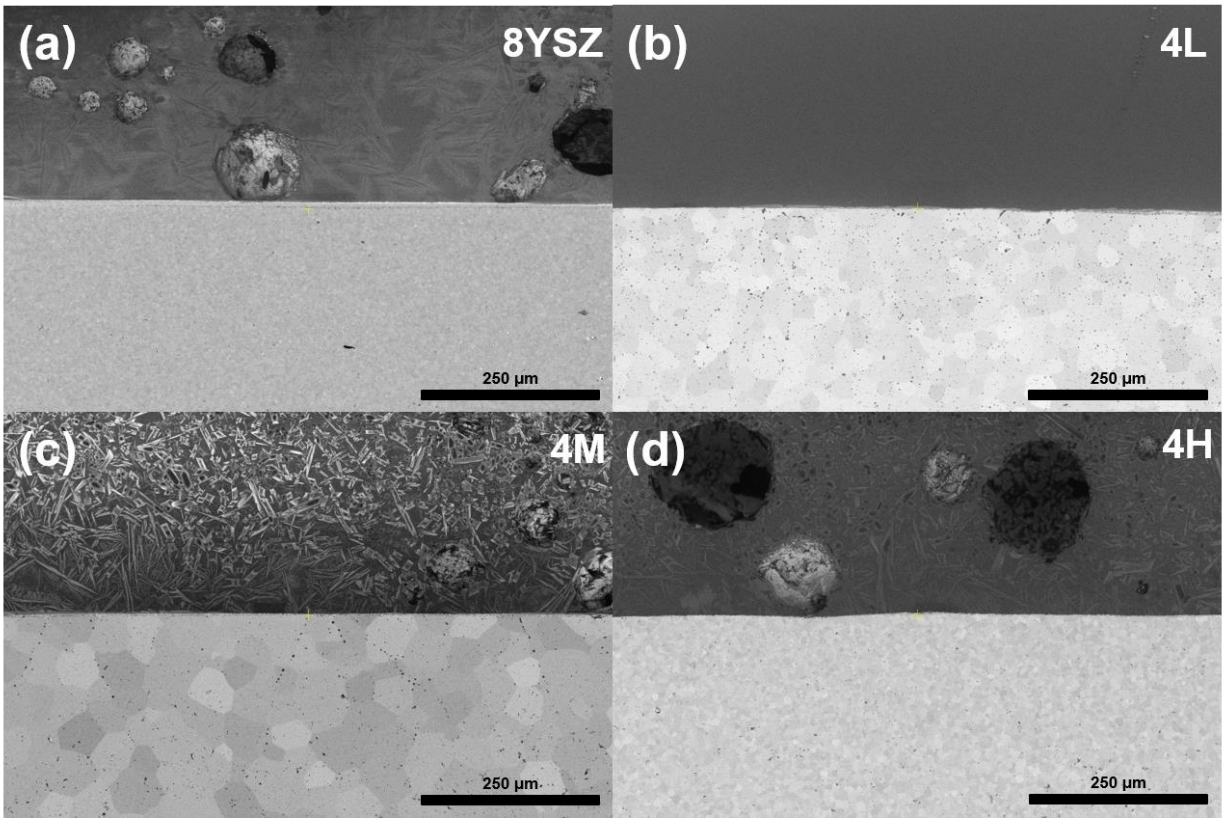

Figure 6.13. SEM images of (a) 8YSZ and (b) 4L, (c) 4M, and (d) 4H CCFOs annealed in contact with molten CMAS at 1200°C for 24 hours at a low magnification.

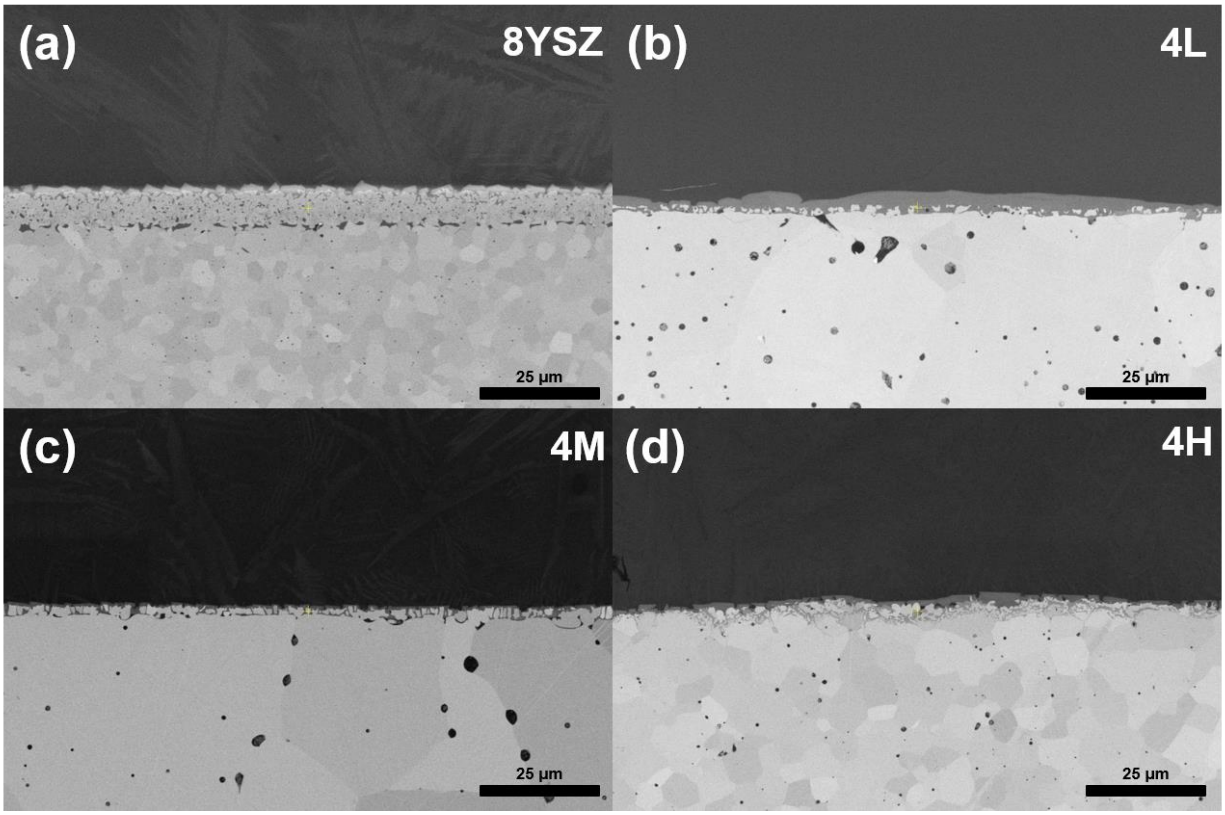

Figure 6.14. SEM images of (a) 8YSZ and (b) 4L, (c) 4M, and (d) 4H CCFOs annealed in contact with molten CMAS at 1200°C for 24 hours at a medium magnification.

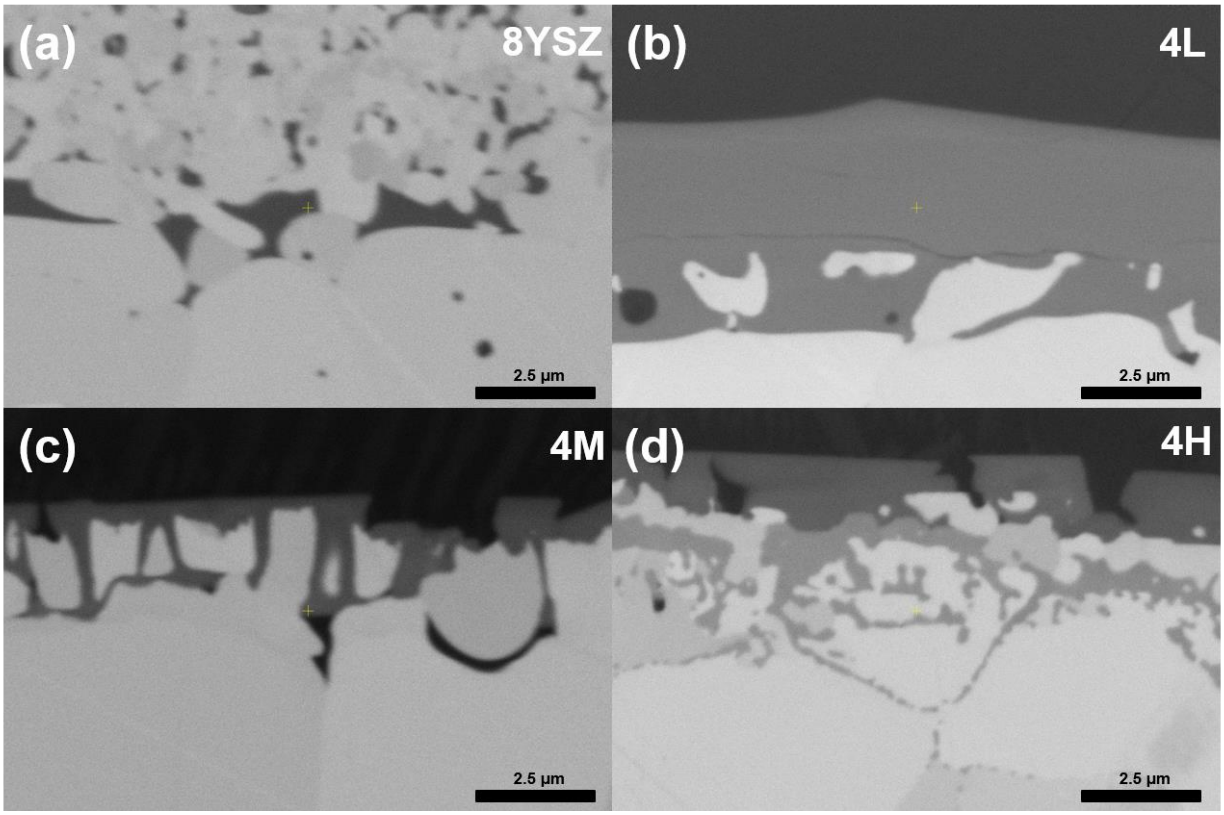

Figure 6.15. SEM images of (a) 8YSZ and (b) 4L, (c) 4M, and (d) 4H CCFOs annealed in contact with molten CMAS at 1200°C for 24 hours at a high magnification.

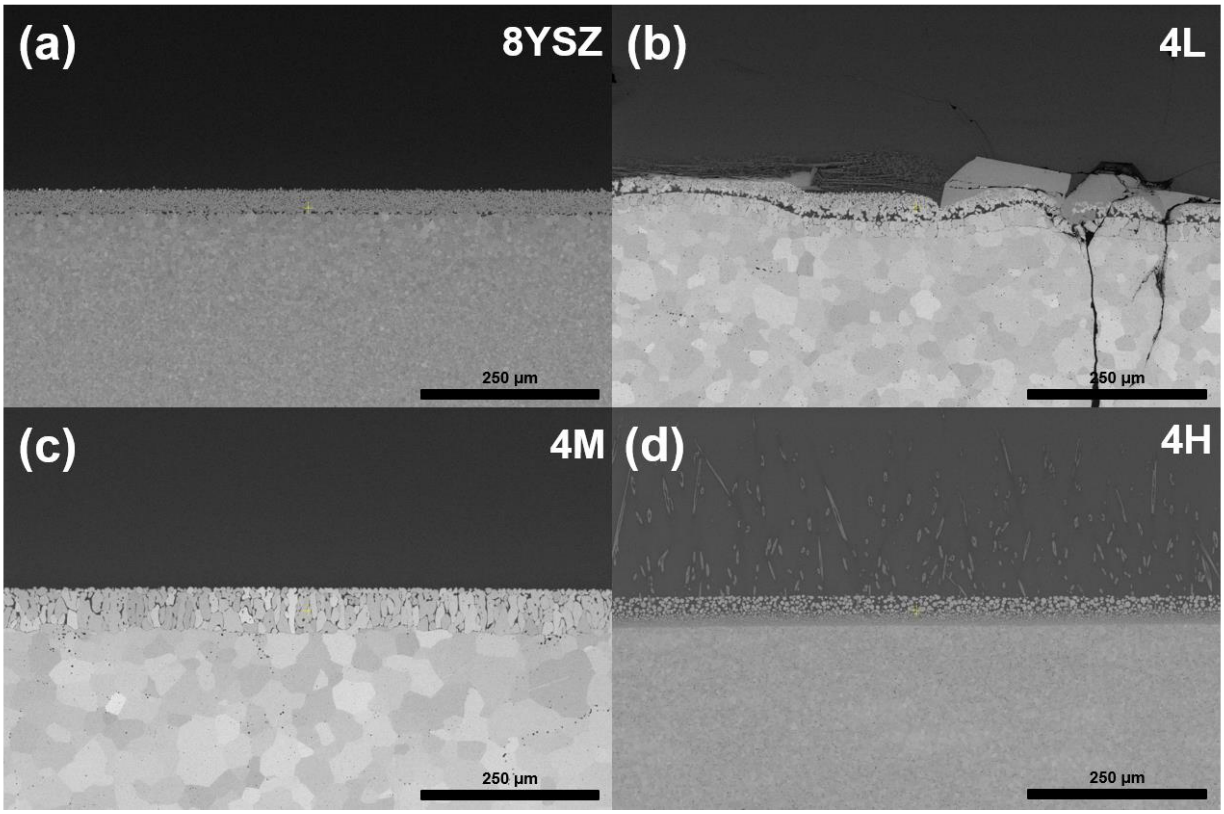

Figure 6.16. SEM images of (a) 8YSZ and (b) 4L, (c) 4M, and (d) 4H CCFOs annealed in contact with molten CMAS at 1300°C for 24 hours at a low magnification.

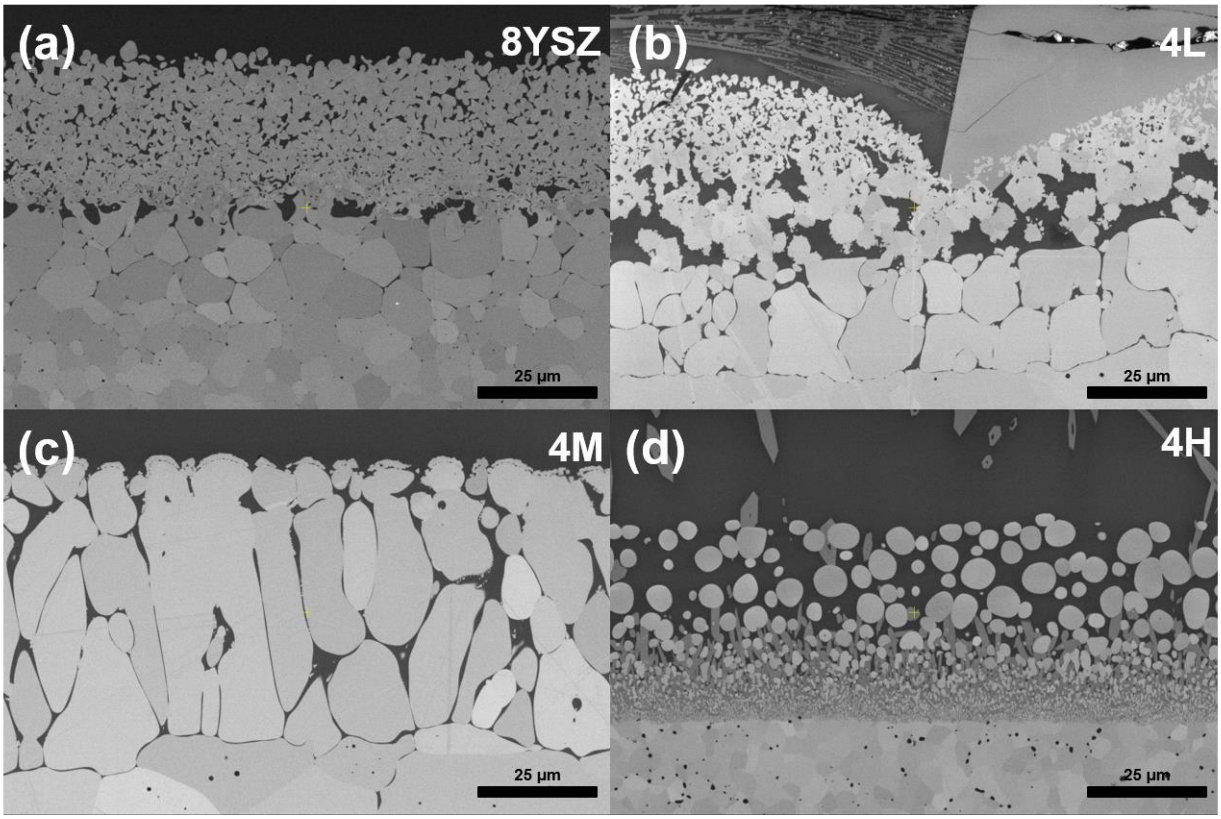

Figure 6.17. SEM images of (a) 8YSZ and (b) 4L, (c) 4M, and (d) 4H CCFOs annealed in contact with molten CMAS at 1300°C for 24 hours at a medium magnification.

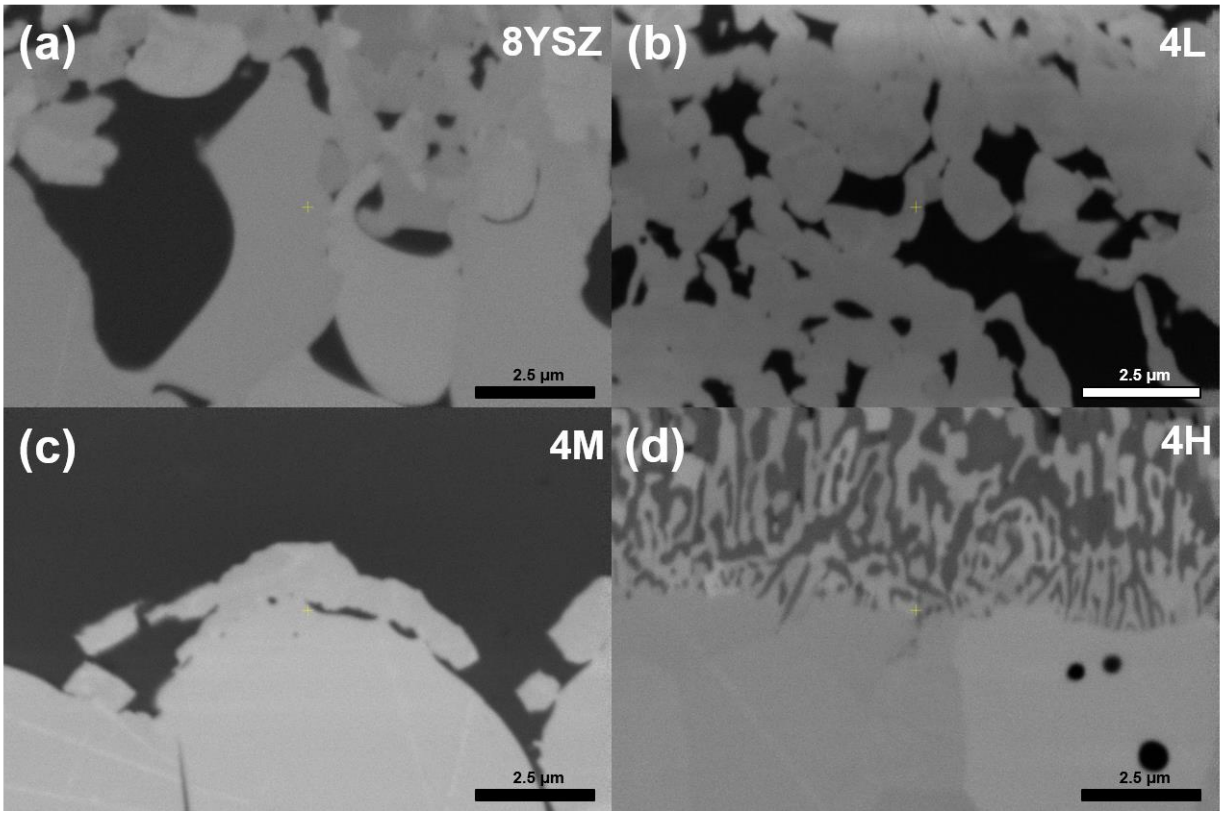

Figure 6.18. SEM images of (a) 8YSZ and (b) 4L, (c) 4M, and (d) 4H CCFOs annealed in contact with molten CMAS at 1300°C for 24 hours at a high magnification.

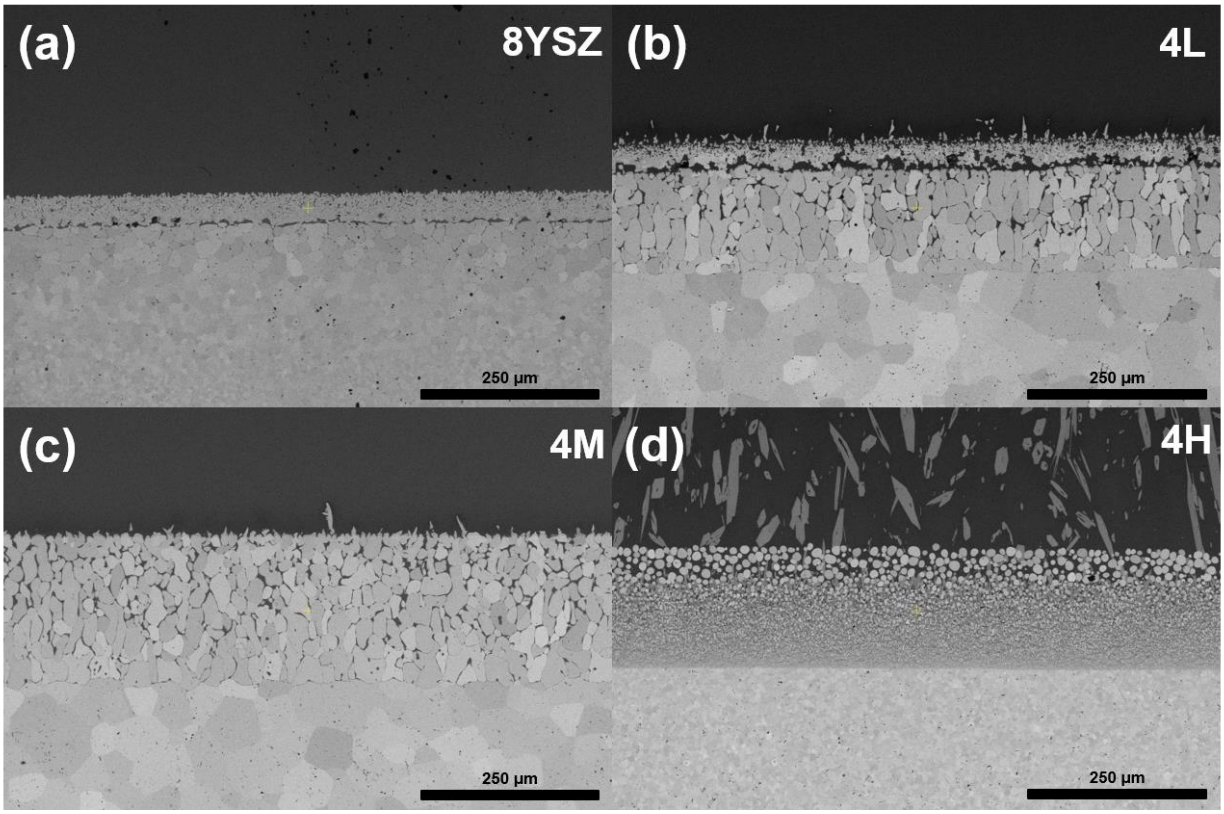

Figure 6.19. SEM images of (a) 8YSZ and (b) 4L, (c) 4M, and (d) 4H CCFOs annealed in contact with molten CMAS at 1400°C for 24 hours at a low magnification.

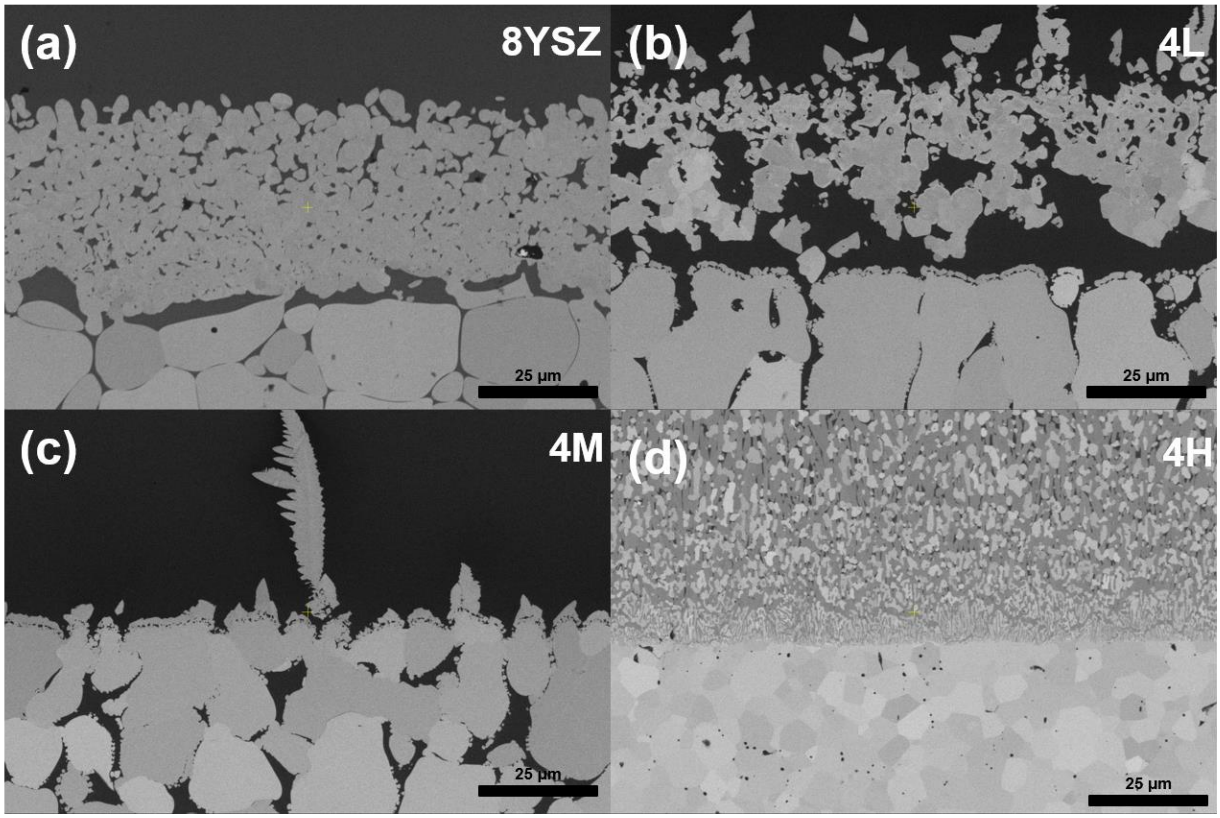

Figure 6.20. SEM images of (a) 8YSZ and (b) 4L, (c) 4M, and (d) 4H CCFOs annealed in contact with molten CMAS at 1400°C for 24 hours at a medium magnification.

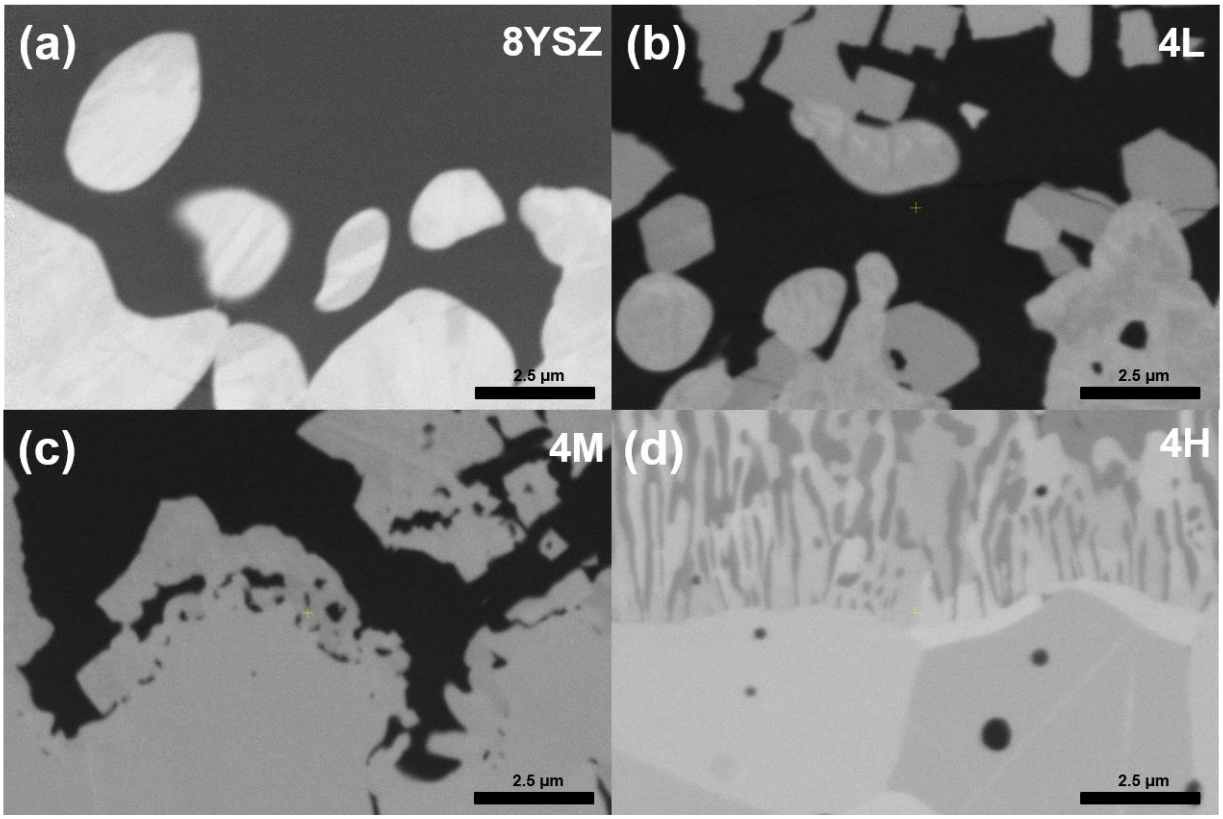

Figure 6.21. SEM images of (a) 8YSZ and (b) 4L, (c) 4M, and (d) 4H CCFOs annealed in contact with molten CMAS at 1400°C for 24 hours at a high magnification.

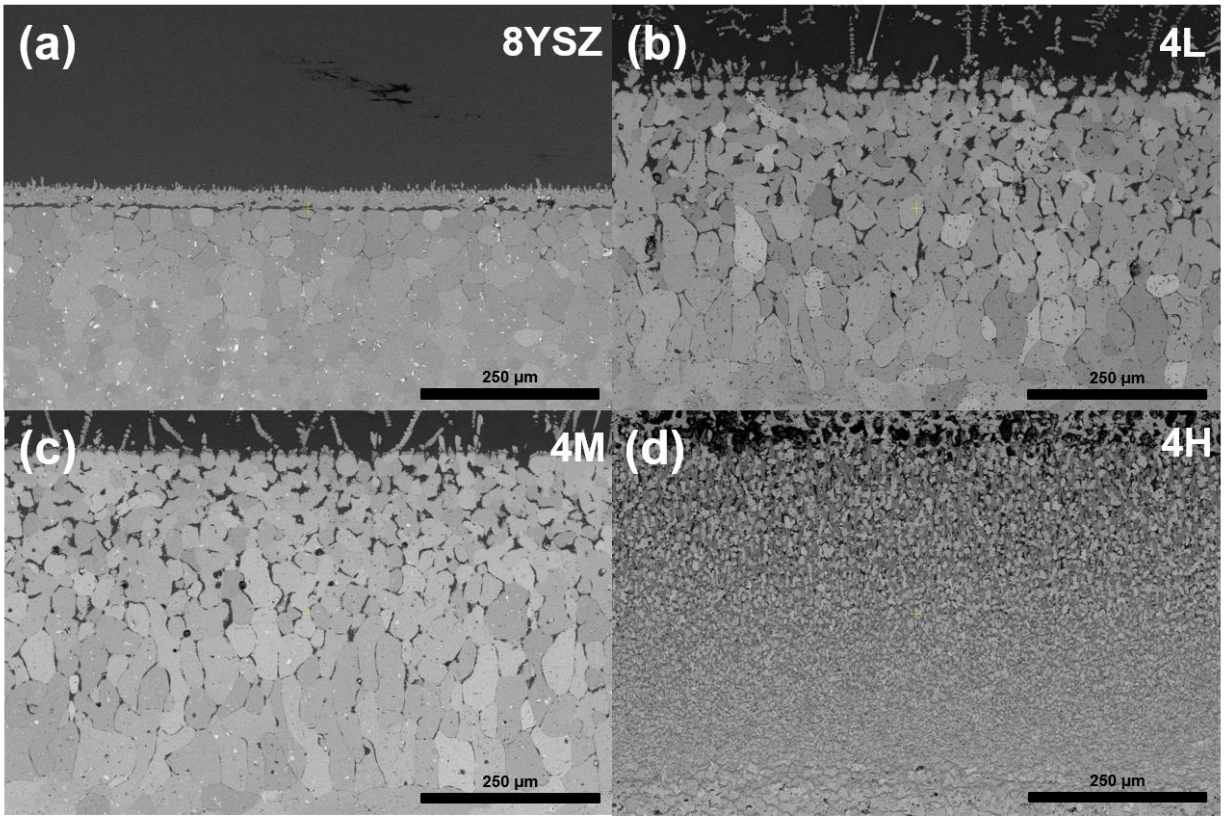

Figure 6.22. SEM images of (a) 8YSZ and (b) 4L, (c) 4M, and (d) 4H CCFOs annealed in contact with molten CMAS at 1500°C for 24 hours at a low magnification.

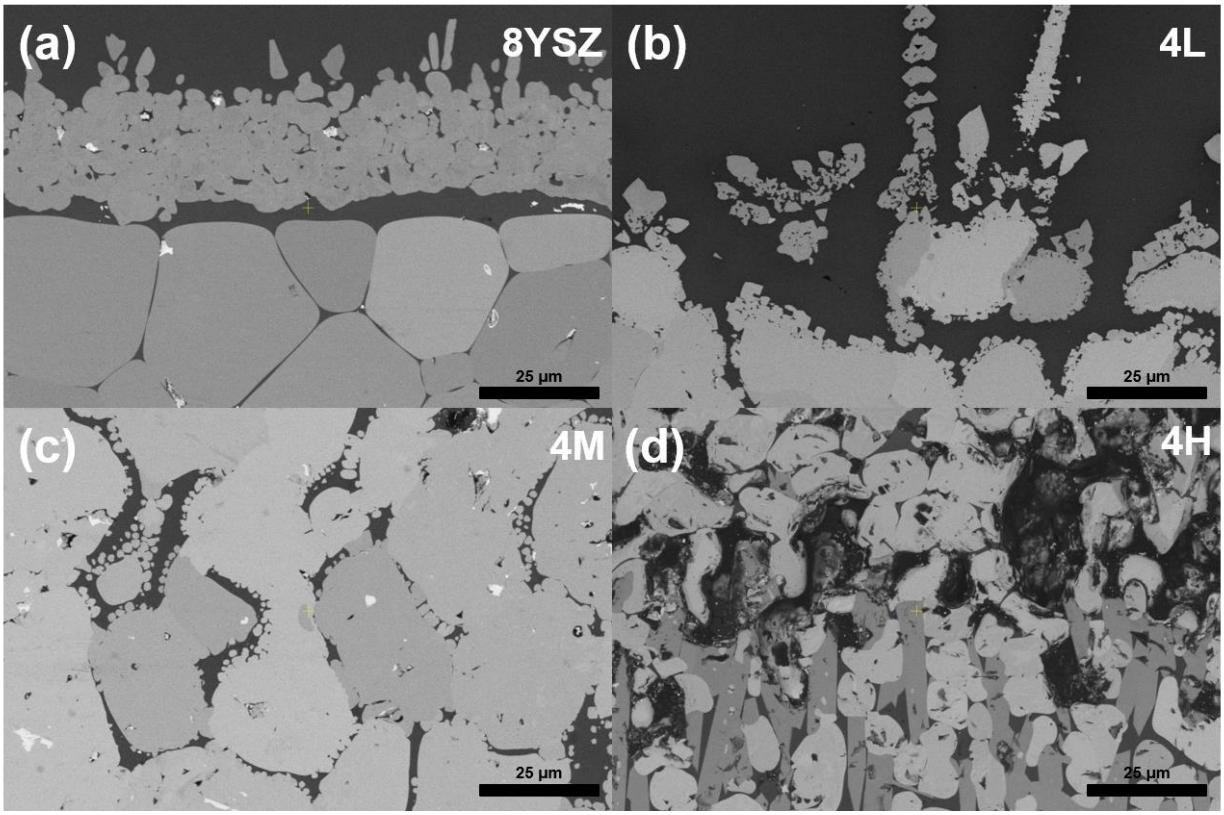

Figure 6.23. SEM images of (a) 8YSZ and (b) 4L, (c) 4M, and (d) 4H CCFOs annealed in contact with molten CMAS at 1500°C for 24 hours at a medium magnification.

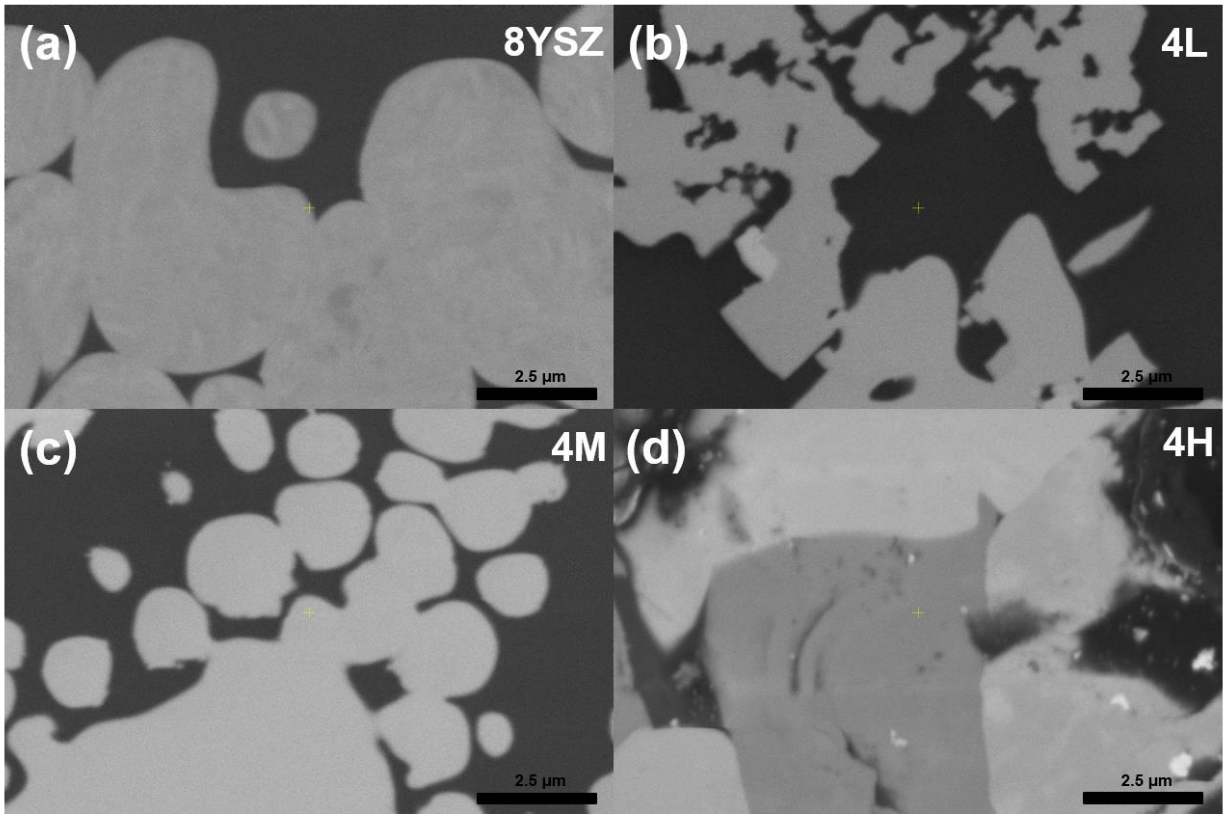

Figure 6.24. SEM images of (a) 8YSZ and (b) 4L, (c) 4M, and (d) 4H CCFOs annealed in contact with molten CMAS at 1500°C for 24 hours at a high magnification.

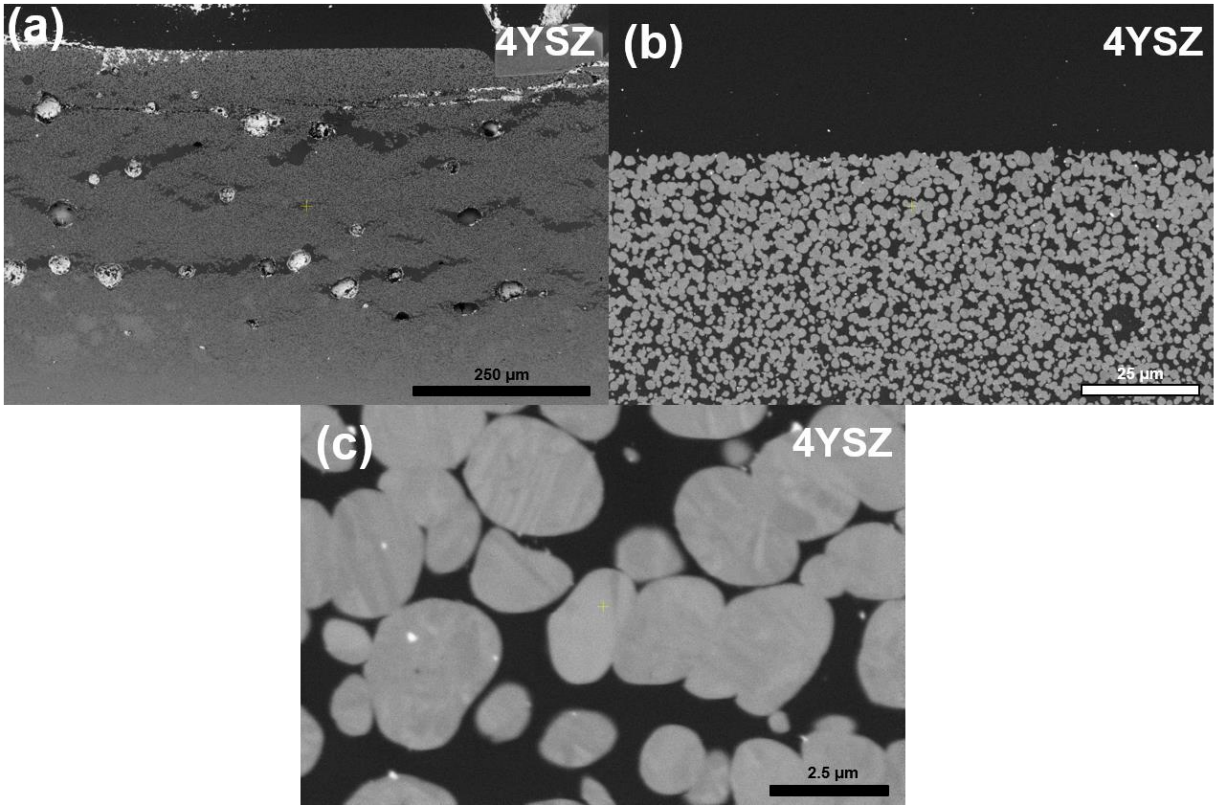

Figure 6.25. SEM images at (a) low, (b) medium, and (c) high magnifications of 4 mol. (7 wt.) % YSZ annealed in contact with molten CMAS at 1300°C for 24 hours.

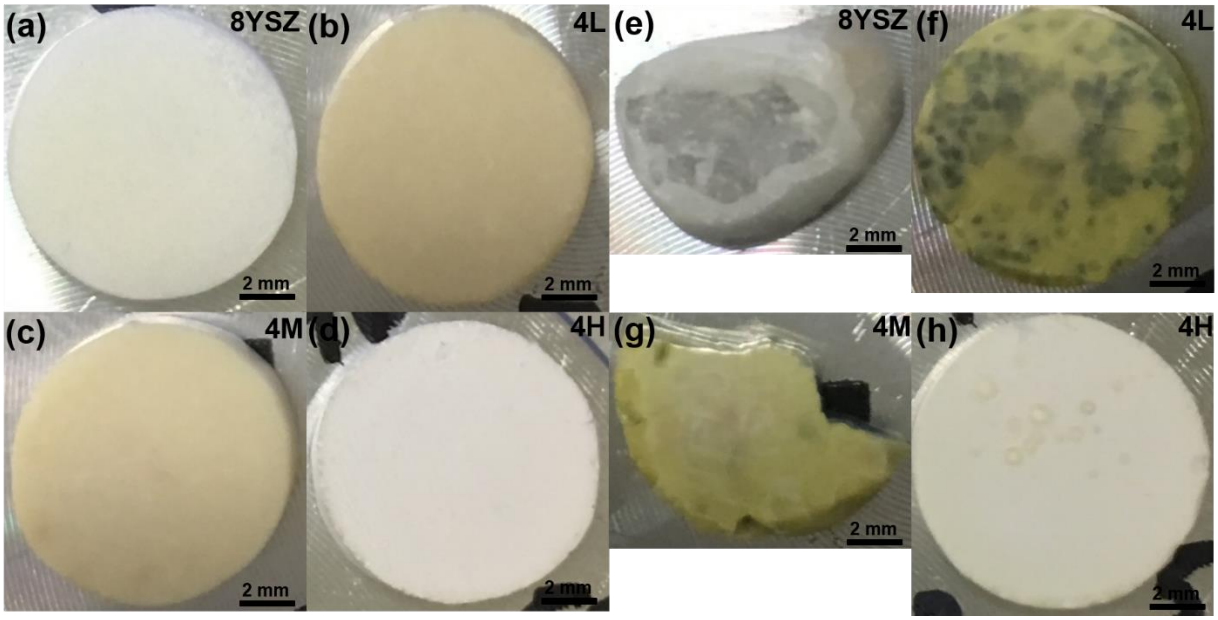

Figure 6.26. Digital images of all specimens (a-d) Pre-ablation and (e-h) post-ablation experiments. 8YSZ and CCFO 4M cracked upon cooling. Black and yellow color changes in CCFOs 4L and 4M are suggested to be due to Ce oxidation state changes.

6.5 REFERENCES

[1] C.H. Liebert, R.E. Jacobs, S. Stecura, C.R. Morse, Durability of zirconia thermal-barrier ceramic coatings on air-cooled turbine blades in cyclic jet engine operation, n.d.

[2] R.A. Miller, Current status of thermal barrier coatings — An overview, Surf. Coatings Technol. 30 (1987) 1–11. doi:10.1016/0257-8972(87)90003-X.

[3] M.J. Stiger, N.M. Yanar, M.G. Topping, F.S. Pettit, G.H. Meier, Thermal barrier coatings for the 21st century, Zeitschrift Fur Met. 90 (1999) 1069–1078. doi:10.1192/bjp.112.483.211-a.

[4] V. Lughi, D.R. Clarke, High temperature aging of YSZ coatings and subsequent transformation at low temperature, Surf. Coatings Technol. 200 (2005) 1287–1291. doi:10.1016/j.surfcoat.2005.07.089.

[5] V. Lughi, V.K. Tolpygo, D.R. Clarke, Microstructural aspects of the sintering of thermal barrier coatings, Mater. Sci. Eng. A. 368 (2004) 212–221. doi:10.1016/j.msea.2003.11.018.

[6] R.L. Jones, D. Mess, Improved tetragonal phase stability at 1400°C with scandia, yttria-stabilized zirconia, Surf. Coatings Technol. 86 (1996) 94–101. doi:10.1016/S0257-8972(96)03006-X.

[7] G.C.C. Costa, D. Zhu, M.J. Kulis, W.A. Acosta, A. Ghoshal, Reactivity between rare-earth oxides based thermal barrier coatings and a silicate melt, J. Am. Ceram. Soc. 101 (2018) 3674–3693. doi:10.1111/jace.15516.

[8] M.G. Dunn, A.J. Baran, J. Miatech, Operation of gas turbine engines in volcanic ash clouds, J. Eng. Gas Turbines Power. 118 (1996) 724–731. doi:10.1115/1.2816987.

[9] C.G. Levi, J.W. Hutchinson, M.H. Vidal-Sétif, C.A. Johnson, Environmental degradation of thermal-barrier coatings by molten deposits, MRS Bull. 37 (2012) 932–941. doi:10.1557/mrs.2012.230.

[10] A. Ghoshal, M. Murugan, M.J. Walock, A. Nieto, B.D. Barnett, M.S. Pepi, J.J. Swab, D. Zhu, K.A. Kerner, C.R. Rowe, C.Y. Shiao, D.A. Hopkins, G.A. Gazonas, Molten particulate impact on tailored thermal barrier coatings for gas turbine engine, J. Eng. Gas Turbines Power. 140 (2018) 022601. doi:10.1115/1.4037599.

[11] L. Li, N. Hitchman, J. Knapp, Failure of thermal barrier coatings subjected to CMAS attack, J. Therm. Spray Technol. 19 (2010) 148–155. doi:10.1007/s11666-009-9356-8.

[12] J. Wu, H. Guo, Y. Gao, S. Gong, Microstructure and thermo-physical properties of yttria stabilized zirconia coatings with CMAS deposits, J. Eur. Ceram. Soc. 31 (2011) 1881–1888. doi:10.1016/j.jeurceramsoc.2011.04.006.

[13] G. Pujol, F. Ansart, J.P. Bonino, A. Malié, S. Hamadi, Step-by-step investigation of degradation mechanisms induced by CMAS attack on YSZ materials for TBC applications, Surf. Coatings Technol. 237 (2013) 71–78. doi:10.1016/j.surfcoat.2013.08.055.

[14] S. Krämer, J. Yang, C.G. Levi, Infiltration-inhibiting reaction of gadolinium zirconate thermal barrier coatings with CMAS melts, J. Am. Ceram. Soc. 91 (2008) 576–583. doi:10.1111/j.1551-2916.2007.02175.x.

[15] U. Schulz, W. Braue, Degradation of La2Zr2O7 and other novel EB-PVD thermal barrier coatings by CMAS (CaO-MgO-Al2O3-SiO2) and volcanic ash deposits, Surf. Coatings Technol. 235 (2013) 165–173. doi:10.1016/j.surfcoat.2013.07.029.

[16] V.L. Wiesner, B.J. Harder, N.P. Bansal, High-temperature interactions of desert sand CMAS glass with yttrium disilicate environmental barrier coating material, Ceram. Int. 44 (2018) 22738–22743. doi:10.1016/j.ceramint.2018.09.058.

[17] A. Nieto, M. Walock, A. Ghoshal, D. Zhu, W. Gamble, B. Barnett, M. Murugan, M. Pepi, C. Rowe, R. Pegg, Layered, composite, and doped thermal barrier coatings exposed to sand laden flows within a gas turbine engine: Microstructural evolution, mechanical properties, and CMAS deposition, Surf. Coatings Technol. 349 (2018) 1107–1116. doi:10.1016/j.surfcoat.2018.05.089.

[18] D.L. Poerschke, C.G. Levi, Effects of cation substitution and temperature on the interaction between thermal barrier oxides and molten CMAS, J. Eur. Ceram. Soc. 35 (2015) 681–691. doi:10.1016/j.jeurceramsoc.2014.09.006.

[19] J.W. Yeh, S.K. Chen, S.J. Lin, J.Y. Gan, T.S. Chin, T.T. Shun, C.H. Tsau, S.Y. Chang, Nanostructured high-entropy alloys with multiple principal elements: novel alloy design concepts and outcomes, Adv. Eng. Mater. 6 (2004) 299–303. doi:10.1002/adem.200300567.

[20] B. Cantor, I.T.H. Chang, P. Knight, A.J.B. Vincent, Microstructural development in equiatomic multicomponent alloys, Mater. Sci. Eng. A. 375 (2004) 213–218. doi:10.1016/j.msea.2003.10.257.

[21] C.M. Rost, E. Sachet, T. Borman, A. Moballegh, E.C. Dickey, D. Hou, J.L. Jones, S. Curtarolo, J.P. Maria, Entropy-stabilized oxides, Nat. Commun. 6 (2015) 1–8. doi:10.1038/ncomms9485.

[22] R. Djenadic, A. Sarkar, O. Clemens, C. Loho, M. Botros, V.S.K. Chakravadhanula, C. Kübel, S.S. Bhattacharya, A.S. Gandhi, H. Hahn, Multicomponent equiatomic rare earth oxides, Mater. Res. Lett. 5 (2017) 102–109. doi:10.1080/21663831.2016.1220433.

[23] S. Jiang, T. Hu, J. Gild, N. Zhou, J. Nie, M. Qin, T. Harrington, K. Vecchio, J. Luo, A new class of high-entropy perovskite oxides, Scr. Mater. 142 (2018) 116–120. doi:10.1016/j.scriptamat.2017.08.040.

[24] M.R. Chellali, A. Sarkar, S.H. Nandam, S.S. Bhattacharya, B. Breitung, H. Hahn, L. Velasco, On the homogeneity of high entropy oxides: An investigation at the atomic scale, Scr. Mater. 166 (2019) 58–63. doi:10.1016/j.scriptamat.2019.02.039.

[25] J. Gild, M. Samiee, J.L. Braun, T. Harrington, H. Vega, P.E. Hopkins, K. Vecchio, J. Luo, High-entropy fluorite oxides, J. Eur. Ceram. Soc. 38 (2018) 3578–3584. doi:10.1016/j.jeurceramsoc.2018.04.010.

[26] J. Gild, Y. Zhang, T. Harrington, S. Jiang, T. Hu, M.C. Quinn, W.M. Mellor, N. Zhou, K. Vecchio, J. Luo, High-entropy metal diborides: A new class of high-entropy materials and a new type of ultrahigh temperature ceramics, Sci. Rep. 6 (2016) 37946. doi:10.1038/srep37946.

[27] P. Sarker, T. Harrington, C. Toher, C. Oses, M. Samiee, J.P. Maria, D.W. Brenner, K.S. Vecchio, S. Curtarolo, High-entropy high-hardness metal carbides discovered by entropy descriptors, Nat. Commun. 9 (2018) 1–10. doi:10.1038/s41467-018-07160-7.

[28] T.J. Harrington, J. Gild, P. Sarker, C. Toher, C.M. Rost, O.F. Dippo, C. McElfresh, K. Kaufmann, E. Marin, L. Borowski, P.E. Hopkins, J. Luo, S. Curtarolo, D.W. Brenner, K.S. Vecchio, Phase stability and mechanical properties of novel high entropy transition metal carbides, Acta Mater. 166 (2019) 271–280. doi:10.1016/j.actamat.2018.12.054.

[29] T.K. Chen, M.S. Wong, T.T. Shun, J.W. Yeh, Nanostructured nitride films of multi-element high-entropy alloys by reactive DC sputtering, Surf. Coatings Technol. 200 (2005) 1361–1365. doi:10.1016/j.surfcoat.2005.08.081.

[30] Y. Dong, K. Ren, Y. Lu, Q. Wang, J. Liu, Y. Wang, High-entropy environmental barrier coating for the ceramic matrix composites, J. Eur. Ceram. Soc. 39 (2019) 2574–2579. doi:10.1016/j.jeurceramsoc.2019.02.022.

[31] J.L. Braun, C.M. Rost, M. Lim, A. Giri, D.H. Olson, G.N. Kotsonis, G. Stan, D.W. Brenner, J.P. Maria, P.E. Hopkins, Charge-induced disorder controls the thermal conductivity of entropy-stabilized oxides, Adv. Mater. 30 (2018) 1805004. doi:10.1002/adma.201805004.

[32] A.J. Wright, Q. Wang, C. Huang, A. Nieto, R. Chen, J. Luo, From high-entropy ceramics to compositionally-complex ceramics: A case study of fluorite oxides, J. Eur. Ceram. Soc. 40 (2020) 2120–2129. doi:10.1016/j.jeurceramsoc.2020.01.015.

[33] D.B. Miracle, O.N. Senkov, A critical review of high entropy alloys and related concepts, Acta Mater. 122 (2017) 448–511. doi:10.1016/j.actamat.2016.08.081.

[34] A.J. Wright, Q. Wang, S.T. Ko, K.M. Chung, R. Chen, J. Luo, Size disorder as a descriptor for predicting reduced thermal conductivity in medium- and high-entropy pyrochlore oxides, Scr. Mater. 181 (2020) 76–81. doi:10.1016/j.scriptamat.2020.02.011.

[35] A.J. Wright, J. Luo, A step forward from high-entropy ceramics to compositionally complex ceramics: a new perspective, J. Mater. Sci. (2020) 1–16. doi:10.1007/s10853-020-04583-w.

[36] Z. Li, D. Raabe, Strong and ductile non-equiatomic high-entropy alloys: Design, processing, microstructure, and mechanical properties, Jom. 69 (2017) 2099–2106. doi:10.1007/s11837-017-2540-2.

[37] Z. Li, K.G. Pradeep, Y. Deng, D. Raabe, C.C. Tasan, Metastable high-entropy dual-phase alloys overcome the strength-ductility trade-off, Nature. 534 (2016) 227–230. doi:10.1038/nature17981.

[38] B. Gludovatz, A. Hohenwarter, K.V.S. Thurston, H. Bei, Z. Wu, E.P. George, R.O. Ritchie, Exceptional damage-tolerance of a medium-entropy alloy CrCoNi at cryogenic temperatures, Nat. Commun. 7 (2016) 1–8. doi:10.1038/ncomms10602.

[39] A. Gali, E.P. George, Tensile properties of high- and medium-entropy alloys, Intermetallics. 39 (2013) 74–78. doi:10.1016/j.intermet.2013.03.018.

[40] F. Li, L. Zhou, J.-X. Liu, Y. Liang, G.-J. Zhang, High-entropy pyrochlores with low thermal conductivity for thermal barrier coating materials, J. Adv. Ceram. 8 (2019) 576–582. doi:10.1007/s40145-019-0342-4.

[41] Z. Zhao, H. Xiang, F.-Z. Dai, Z. Peng, Y. Zhou, (La0.2Ce0.2Nd0.2Sm0.2Eu0.2)2Zr2O7: A novel high-entropy ceramic with low thermal conductivity and sluggish grain growth rate, J. Mater. Sci. Technol. 35 (2019) 2647–2651. doi:10.1016/j.jmst.2019.05.054.

[42] K. Ren, Q. Wang, G. Shao, X. Zhao, Y. Wang, Multicomponent high-entropy zirconates with comprehensive properties for advanced thermal barrier coating, Scr. Mater. 178 (2020) 382–386. doi:10.1016/j.scriptamat.2019.12.006.

[43] X. Yan, L. Constantin, Y. Lu, J.F. Silvain, M. Nastasi, B. Cui, (Hf0.2Zr0.2Ta0.2Nb0.2Ti0.2)C high-entropy ceramics with low thermal conductivity, J. Am. Ceram. Soc. 101 (2018) 4486–4491. doi:10.1111/jace.15779.

[44] X. Ren, Z. Tian, J. Zhang, J. Wang, Equiatomic quaternary (Y1/4Ho1/4Er1/4Yb1/4)2SiO5 silicate: A perspective multifunctional thermal and environmental barrier coating material, Scr. Mater. 168 (2019) 47–50. doi:10.1016/j.scriptamat.2019.04.018.

[45] K. Matsui, H. Yoshida, Y. Ikuhara, Review: Microstructure-development mechanism during sintering in polycrystalline zirconia, Int. Mater. Rev. 63 (2018) 375–406. doi:10.1080/09506608.2017.1402424.

[46] S. Krämer, J. Yang, C.G. Levi, C.A. Johnson, Thermochemical interaction of thermal barrier coatings with molten CaO-MgO-Al2O3-SiO2 (CMAS) deposits, J. Am. Ceram. Soc. 89 (2006) 3167–3175. doi:10.1111/j.1551-2916.2006.01209.x.

[47] D.L. Poerschke, R.W. Jackson, C.G. Levi, Silicate deposit degradation of engineered coatings in gas turbines: Progress toward models and materials solutions, Annu. Rev. Mater. Res. 47 (2017) 297–330. doi:10.1146/annurev-matsci-010917-105000.

[48] Z. Tian, J. Zhang, L. Zheng, W. Hu, X. Ren, Y. Lei, J. Wang, General trend on the phase stability and corrosion resistance of rare earth monosilicates to molten calcium–magnesium–aluminosilicate at 1300°C, Corros. Sci. 148 (2019) 281–292. doi:10.1016/j.corsci.2018.12.032.

[49] A.R. Krause, B.S. Senturk, H.F. Garces, G. Dwivedi, A.L. Ortiz, S. Sampath, N.P. Padture, 2ZrO2·Y2O3 thermal barrier coatings resistant to degradation by molten CMAS: Part I, Optical basicity considerations and processing, J. Am. Ceram. Soc. 97 (2014) 3943–3949. doi:10.1111/jace.13210.

[50] D.L. Poerschke, T.L. Barth, C.G. Levi, Equilibrium relationships between thermal barrier oxides and silicate melts, Acta Mater. 120 (2016) 302–314. doi:10.1016/j.actamat.2016.08.077.

[51] H. Zhao, C.G. Levi, H.N.G. Wadley, Molten silicate interactions with thermal barrier coatings, Surf. Coatings Technol. 251 (2014) 74–86. doi:10.1016/j.surfcoat.2014.04.007.

[52] Y. Zhang, H. Ni, Y. Chen, Diffusion data in silicate melts, Rev. Mineral. Geochemistry. 72 (2010) 311–408. doi:10.2138/rmg.2010.72.8.

[53] K. Fritscher, Life and FCT failure of yttria- and ceria-stabilized EBPVD TBC systems on Ni-base substrates, Oxid. Met. 91 (2019) 131–157. doi:10.1007/s11085-018-9870-5.

[54] N.P. Padture, Environmental degradation of high-temperature protective coatings for ceramic-matrix composites in gas-turbine engines, Npj Mater. Degrad. 3 (2019). doi:10.1038/s41529-019-0075-4.

[55] J.A. Duffy, M.D. Ingram, Establishment of an optical scale for lewis basicity in inorganic oxyacids, molten salts, and glasses, J. Am. Chem. Soc. 93 (1971) 6448–6454. doi:10.1021/ja00753a019.

[56] R.R. Reddy, Y. Nazeer Ahammed, K. Rama Gopal, P. Abdul Azeem, T.V.R. Rao, Correlation between optical basicity, electronegativity and electronic polarizability for some oxides and oxysalts, Opt. Mater. (Amst). 12 (1999) 425–428. doi:10.1016/S0925-3467(98)00083-4.

[57] L. Sun, Y. Luo, Z. Tian, T. Du, X. Ren, J. Li, W. Hu, J. Zhang, J. Wang, High temperature corrosion of (Er0.25Tm0.25Yb0.25Lu0.25)2Si2O7 environmental barrier coating material subjected to water vapor and molten calcium–magnesium–aluminosilicate (CMAS), Corros. Sci. (2020) 108881. doi:10.1016/j.corsci.2020.108881.

[58] H. Hayashi, T. Saitou, N. Maruyama, H. Inaba, K. Kawamura, M. Mori, Thermal expansion coefficient of yttria stabilized zirconia for various yttria contents, Solid State Ionics. 176 (2005) 613–619. doi:10.1016/j.ssi.2004.08.021.

[59] J.T.S. Irvine, A.J. Feighery, D.P. Fagg, S. García-Martín, Structural studies on the optimization of fast oxide ion transport, Solid State Ionics. 136 (2000) 879–885. doi:10.1016/S0167-2738(00)00568-3.

[60] K.N. Clausen, W. Hayes, Defect structure of yttria-stabilized zirconia and its influence on the ionic conductivity at elevated temperatures, Phys. Rev. B. 59 (1999) 14202–14219. doi:10.1103/PhysRevB.59.14202.

[61] A. Bogicevic, C. Wolverton, G.M. Crosbie, E.B. Stechel, Defect ordering in aliovalently doped cubic zirconia from first principles, Phys. Rev. B - Condens. Matter Mater. Phys. 64 (2001) 014106. doi:10.1103/PhysRevB.64.014106.

[62] E.D. Wachsman, Effect of oxygen sublattice order on conductivity in highly defective fluorite oxides, J. Eur. Ceram. Soc. 24 (2004) 1281–1285. doi:10.1016/S0955-2219(03)00509-0.

[63] R.J. Thompson, K.J. Hemker, Thermal expansion measurements on coating materials by digital image correlation, in: Proc. SEM Conf. Springfield, Massachusetts, 2007.

[64] J.A. Haynes, B.A. Pint, W.D. Porter, I.G. Wright, Comparison of thermal expansion and oxidation behavior of various high-temperature coating materials and superalloys, Mater. High Temp. 21 (2004) 87–94. doi:10.1179/mht.2004.012.

[65] N.P. Padture, Advanced structural ceramics in aerospace propulsion, Nat. Mater. 15 (2016) 804–809. doi:10.1038/nmat4687.

7. MOLTEN $KMgCl_3$ SALT CORROSION PERFORMANCE IN MEDIUM-/HIGH-ENTROPY OXIDES

7.1 INTRODUCTION

Refractory materials are in increasing demand as thermal systems around the world strive to increase temperature capabilities, and thus efficiencies [1]. Thermal barrier coatings (TBCs) are critical to the success of gas-turbine engines and their diminishing returns on improvement has their need stronger [2]. Yttria-stabilized zirconia provided sufficient protection for decades, but loses applicability at T>1300℃ due to a phase transformation and poor sintering resistance [3,4]. TBCs are also important in the emerging solar energy market as protective coatings inside molten salt thermal energy storage tanks so electricity can be provided continuously. Currently, success has been achieved in operating concentrated solar power plants at ~ 550℃ with nitrate salts [5,6]. However, there is further benefit for using chloride or carbonate salts at ~ 800℃ as these can provide higher efficiencies, more energy, and lower costs [7,8]. While many refractory oxide materials can provide sufficiently low thermal conductivities [9–11], their resistance to chemical attack is usually of upmost concern at these elevated temperatures.

Corrosion is an overly complex process that involves many variables. Consequently, this makes predicting corrosion performance and behavior challenging. The thermal energy storage tanks are typically made of austenitic steel (SS316), however, steel has poor corrosion resistance to nitrate salt at 600℃ [6]. As the demand for elevated temperatures increased, multiple structural alloys were proposed [12,13]. One alternative to steel proposed was a nickel superalloy (Haynes 230). This material is very tough and provides excellent temperature stability compared to stainless steel. Yet, Haynes 230 alloy has similar issues of corrosive protection issues with chloride salts at 750℃ with significant Cr loss [14]. Further efforts are underway to provide a

suitable TBC to protect the underlying alloy from corrosive effects. The challenge arises in deciding what are suitable candidates as there is little information on the corrosion of oxides in chloride salts and predictive methods are limited.

Recently, high-entropy alloys have demonstrated increased mechanical properties and stability in corrosive environments compared traditional alloys such as stainless steel [15–18]. High-entropy materials are interesting to investigate their corrosive resistance because on the one hand, an increase in configurational entropy should provide a more stable phase thermodynamically if the enthalpy of the solid solution is negative [18]. On the other hand, an increase in configurational entropy typically comes at the expense of additional elements, which increases the probability of undesirable corrosive effects. High-entropy ceramics (HECs) and oxides in particular would generally serve better as a coating material due to their extreme low thermal conductivities compared to a rule-of-mixtures analysis [19–23]. HECs such as high-entropy borides, carbides, and nitrides have demonstrated satisfactory resistance in oxidation environments compared to constituents [24–27]. Some preliminary work has been conducted on corrosion behavior in high-entropy oxides, but this has been limited to molten silicates and water vapor so far [28–30].

In this study, we establish for the first time a library of corrosion performance on numerous high-entropy oxides in pellet form across multiple different families, yet related, in a $KMgCl_3$ molten salt environment at 800°C. We also provide temperature-dependent thermal conductivity up to 1000°C and room temperature Young's modulus (each corrected for porosity) for all specimens. We fabricated 45 specimens across five similar families: compositionally-complex fluorite oxide (CCFOs, 11), high-entropy fluorites (HEFs, 7), high-entropy pyrochlores

(HEP, 6), high-entropy niobates/tantalates (HENTs, 7), and mixed high-entropy pyrochlore-niobates/tantalates (P-NT, 14).

A general screening was performed by subjecting all 45 materials to the molten chloride salt at 800℃ for 24 h and compared against a reference structural alloy (Haynes 230). In the process we also found a descriptive parameter, optical basicity, to be a reliable predictor of corrosion performance. We then narrowed our focus to three suitable candidates that appeared best in their class (plus Haynes 230) and conducted a kinetic study at 800℃ up to 1000 h. We found that while the oxides possessed relatively poor performance against Haynes 230 at short corrosion times (i.e., 24 h), they exhibited a parabolic rate constant due to the passivating layer that formed in contrast to the Haynes 230 alloy, which showed linear kinetics. Thus, the three high entropy oxides investigated in detail in this study provide greater corrosion protection in molten chloride salts at long corrosion times ($> 500\ h$) compared to Haynes 230, while also providing a low thermal conductivity ($k_{800℃} \approx 1.6\ W\ m^{-1}\ K^{-1}$) and structural rigidity due to the high Young's modulus ($E \sim 200 - 250\ GPa$). All of which are suitable for a TBC in a holding tank.

7.2 EXPERIMENTAL PROCEDURES

7.2.1 MATERIALS AND SYNTHESIS

Five different classes of high-entropy ceramic (HEC) materials were examined: compositionally-complex fluorite oxides (CCFOs), high-entropy fluorites (HEFs), high-entropy pyrochlores (HEPs), high-entropy niobate/tantalates (HENTs), and mixed high-entropy pyrochlore-niobates/tantalates (P-NT). Most of the specimens in this study were previously reported in earlier reports from our group [20,23]. A table in the Supplementary Information (Table S7.1) reports the compositions of all the materials studied.

Constituent oxides (~ 5 μm) were stoichiometrically weighed and placed in a poly(methyl methacrylate) high-energy ball mill (HEBM) vial with 2 wt. % stearic acid and one Ø5/16" WC grinding ball. The HEBM (SPEX 8000D, SPEX SamplePrep, USA) was operated for 100 minutes continuously. The milled powders were then placed in a 13 mm stainless steel die, uniaxially pressed under 100 MPa, and sintered at 1600°C for 24 h. Lastly, each surface was ground with a 30 μm diamond grinding disc to remove any surface contamination.

7.2.2 MOLTEN SALT CORROSION PROCEDURE

$KMgCl_3$ was used as the corrosive medium. The chloride salt was stored under Ar in a glovebox with less than 0.5 ppm of O_2 and H_2O. The HECs were dried at 75°C and allowed to cool before transferring to the glovebox. The HECs were placed in a 13 mm diameter quartz test tube with 4-6 g of salt. A Haynes 230 alloy (H230) was used as a control and followed the same procedure outlined for the HECs.

The quartz tubes were then removed one at a time to minimize O_2/H_2O contamination and quickly sealed with a torch to make a sealed capsule. These capsules were then annealed at 800°C for 24 h. A few promising specimens (low corrosion rate) were further pursued with a kinetic study so additional specimens were made and annealed at 48 h, 96 h, 500 h, and 1000 h.

Following annealing, the specimens were removed from the capsule, sonicated in deionized water for 15 minutes to remove any residual salt, and then allowed to remain in the water for an additional two hours. Finally, the pellets were dried at 75°C overnight. The mass and thickness (measured by a micrometer) of each specimen was recorded before and after the corrosion test.

7.2.3 CHARACTERIZATION

7.2.3.1 SCANNING ELECTRON MICROSCOPY-ENERGY DISPERSIVE SPECTROSCOPY (SEM-EDS)

An SEM (FEI Apreo, OR, USA) equipped with an EDS detector (EDS, Oxford N-MaxN) was operated at 20 kV and 13 nA to collect images and elemental data. The specimens were hot mounted in acrylic and polished with diamond discs and suspension. Final polishing was carried out with a 40 nm colloidal silica suspension. Lastly, the polished mounts were sonicated in isopropanol for 15 minutes and dried prior to SEM examination. The molten salt infiltration depth was calculated by measuring the length of approximately 40 lines across five images in different regions through ImageJ and computing the mean [31]. The standard deviation is given based off these ~ 200 measurements.

7.2.3.2 X-RAY DIFFRACTION (XRD) AND DENSITY (ρ)

A Rigaku Miniflex II (30 kV, 15 mA) collected structural information from 20-90° 2θ at 0.02° steps with a 2 s dwell per step. This data was fitted through GSAS-II [32] to extract the lattice parameter and theoretical density.

The bulk density was either calculated through an Archimedes method that involved boiling water (ASTM Standard C373-18) [33] or by thresholding techniques using SEM images and ImageJ [31]. Both methods were in good agreement.

7.2.3.3 YOUNG'S MODULUS (E)

The Young's modulus was determined by a sonic resonance method [34] using an oscilloscope in a pulse-echo setup where both the longitudinal and transverse wave speeds were collected. The modulus was calculated and corrected for porosity according to prior studies [20,23].

7.2.3.4 THERMAL CONDUCTIVITY (k)

The thermal diffusivity (α) of the materials was determined by laser flash analysis (LFA 467 HT HyperFlash, NETZSCH, Germany) at 25℃ and then from 200℃-1000℃ in 200℃ steps. The specific heat capacity (c_p) was estimated by the rule of mixtures based on the mass ratio of the constituent oxides (Neumann-Kopp rule) [35]. The thermal conductivity was calculated through the product of α, ρ, c_p.

7.2.4 MEASURES OF CORROSION PERFORMANCE

The two main measures of performance we focused on were total interaction depth (TID) and corrosion based on the mass loss (CR_{Mass}). We defined the TID as the infiltration depth (seen by SEM and measured through ImageJ) plus half the thickness loss (measured by a micrometer with a precision of 1 μm) as shown in Equation 1.

$$TID = ID + \Delta y/2 \tag{1}$$

Here, ID and Δy is the infiltration depth and thickness loss. In the scenario where a specimen increased in thickness following testing, Δy was taken to be null.

The corrosion rate was calculated by taking the mass loss (Δm) and normalizing it by the surface area (A), density (ρ), and corrosion time (t) as shown in Equation 2.

$$CR_{Mass} = \frac{\Delta m}{A\rho t} \tag{2}$$

Finally, we used optical basicity (Λ) as our independent parameter to distinguish each material. Optical basicity originates from the definition of Lewis acids and bases and is used to express the tendency of a material to donate electrons based on the electron density surrounding oxygen [36,37]. The change in optical basicity (ΔΛ) between two materials has been used successfully n predicting the severity of reactions in the thermal/environmental barrier coatings fields [11,38–41]. The calculation can be found in Ref. [40]. This expression was developed for

oxides and has limited uses with other anions (such as chlorides) so the nominal value of Λ was used instead of $\Delta\Lambda$.

7.3 RESULTS AND DISCUSSION

Our aim in this study was to be the first to elucidate the feasibility of novel high-entropy ceramics (oxides) providing corrosion protection (specifically from chloride salts) for structural alloys. We approached this by screening numerous (45) HECs against a Haynes 230 alloy reference in a simple $24\ h$ anneal at $800℃$ and monitoring the corrosion interaction depth and rate, while also taking into account attractive thermomechanical properties (low k and high E). On select promising specimens, we conducted a kinetic study to probe the long-term stability and found some a couple of the HECs possessed a parabolic rate constant in contrast to the reference metal, which displayed linear kinetics.

7.3.1 24 h SCREENING TEST

Five different classes of high-entropy oxides, although all related, along with a Haynes 230 alloy reference were all evaluated for their performance in a $KMgCl_3$ medium at 800°C for 24 h to screen out poor-performing specimens. Figure 7.1(a) shows the TID for all specimens after the 24 h anneal. In general, a trend can be seen where the lower Λ specimens (such as CCFOs) typically have lower interaction depths as opposed to the HENTs. However, this trend is not perfect as the HEPs (middle range Λ) perform the worse indicating that structure/composition also play a strong role. Moreover, this is evident by the relatively large spread of data within each family. A linear line was fit to all the data (although curved on a semi-log plot), which shows a positive relationship, albeit weak. Most of the specimens performed worse against the reference Haynes 230 alloy (H230); however, a few were comparable.

Figure 7.1(b) shows the corrosion rate of the same specimens versus Λ. Here, the trend is similar to panel (a), however, the trend is more realized. The CCFOs tend to have the least mass loss (as surface area and density are similar for all specimens) while the HENT tend to have more. This was found to be due to a reaction scale that develops in the HENTs that can spall off either during the reaction or sonication, which will be discussed more later. The H230 reference was found to have a low corrosion rate and only a few CCFOs were comparable.

This initial screening attempt shows that within this range of optical basicity values tested ($0.80 - 1.07$), lower values tend to have less microstructural changes (small TID) and less mass loss (low CR_{Mass}). Although we note the trend is not perfect due to all the factors involved and complexity within corrosion. To our knowledge, this is the first time this optical basicity concept has been applied to molten chloride salts where it seems serve as a reasonable estimate for performance and screening. However, we would also like to stress that it is unlikely that any one parameter is going to be able to predict the performance of corrosion resistance very accurately, which will be discussed later. All of the specimens used in this screening study and their $24\ h$ screening performance and relevant thermomechanical properties are available in Table 7.1.

7.3.2 48 h AND 96 h $KMgCl_3$ CORROSION TEST

Following the successful screening, we identified one CCFO, HEP, and HENT for further study. These materials are pointed out in Figure 7.1 by golden arrows. These materials were 4K ($Y_{0.15}Yb_{0.15}Zr_{0.35}Hf_{0.35}O_{2-\delta}$), NT21 ($(Sc_{0.266}Dy_{0.248}Tm_{0.246}Yb_{0.240})_3NbO_7$), and P20-5 ($(Sm_{0.25}Eu_{0.25}Gd_{0.25}Yb_{0.25})_2(Ti_{0.5}Hf_{0.25}Zr_{0.25})_2O_7$). These were selected to undergo the corrosion test at $48\ h$ and $96\ h$ to investigate the influence of time on the corrosion. Each of these were selected as a representative of each family so that we could still examine the differences among different structures and composition spaces.

Figure 7.2 shows the backscattered electron SEM images and microstructural evolution of H230 and all three specimens when anneal at $24\ h$, $48\ h$, and $96\ h$ in $KMgCl_3$. The interaction of the H230 reference with the chloride salt (panel (a)) did not produce a well-defined boundary, but the small voids and bright contrast at the grain boundaries were used. With increasing dwell times, the concentration of voids became more prevalent and the length scale increased, but the overall microstructure did not change.

In Fig. 7.2(b) CCFO 4K produced a needle-like interaction zone that was variable in depth across the cross-section. The variability in depth was very pronounced at $48\ h$ but not as much at $96\ h$. No change in the microstructure of the interaction zone was found and only the interaction length scale increased with increased annealing times.

HENT NT21 shown in Fig. 7.2(c) was found to develop a reaction scale that began to spall. A brighter needle-like phase exists amidst a darker phase with no distinct shape. At each annealing time, a void is present between the reaction zone and unreacted bulk. It is unknown whether this void form as a result of the reaction zone delaminating from the bulk or whether a fragile layer (or residual salt) existed there and broke apart during sonication/polishing. The length scale of the reaction zone increased above $24\ h$ annealing, however the interaction depth of the $48\ h$ and $96\ h$ specimens are very similar.

Figure 7.2(d) shows the molten chloride salt interaction with HEP P20-5, which was found to be the most complex (and intriguing). At $24\ h$, the infiltration depth is $\sim 30\ \mu m$ and has small a white phase interspersed within a dark matrix. On the top layer, long white crystal developed. When the annealing time was increased to $48\ h$, a distinct two-layered reaction zone structure appeared with a small void between the reaction layer and bulk. The bottom layer had a similar intensity to the bulk indicating no significant loss of constituents had occurred. The top

layer featured a dark phase with some light phase dispersed throughout. The $96\ h$ annealed specimen revealed a similar structure to the $48\ h$ with the exception that the length scale slightly increased ($TID \sim 60\ \mu m$) and certain regions had circular structures forming that appeared to be in the process of being cleaved off.

7.2.3 KINETIC STUDY

Notably, compared to the H230 reference, all the oxides developed some type of reaction layer. This can be beneficial in porous coatings as the reaction products can fill the pores and halt further reaction [42,43]. Moreover, this dense reaction layer further provides an increasing layer the infiltrant needs to diffuse across. This is recognized by parabolic kinetics, which are typically observed in oxidation of metals [44]. Specimens that do not have well-defined reaction layers characterized by distinct changes in microstructure are likely to proceed in a linear fashion; whereas the reaction kinetics are likely to proceed parabolically with time. This can be a drastic advantage as some materials may be overlooked for their poor performance at short times. While it was unreasonable to perform long-term annealing for all 45 specimens, we selected these three as they were the best performing in their class. We furthered the dwelling time to include 500 h and 800 h.

Figure 7.2(a) shows the total interaction depth up to $800\ h$. A two-phase model was fit to the data, $TID = k_{lin}t + k_{par}\sqrt{t}$, where k_{lin} and k_{par} are the linear and parabolic rate constants. The linear kinetics embodies the simple diffusion and reaction with negligible resistance. The parabolic rate constant should arise if the corroding medium (molten chloride salt) is impeded by a passivating layer. Consequently, this would increase the diffusion length of the molten salt and slow down corrosion. This is analogous to oxide corrosion in steels. Each high entropy ceramic shows a strong contribution of a parabolic rate constant whereas the H230 reference shows

primarily linear kinetics. A crossover occurs after $100\ h$ of annealing where the HECs begin to before better than the structural alloy. The values for the rate constants are shown in Table 7.1. The corrosion rate in shown in Figure 7.2(b) and shows a similar picture with the rate (fitted with an exponential decay) slowly declining with the HECs while the H230 alloy quickly reaches a constant value. However, regarding mass loss, Haynes 230 is superior as the bulk materials is stable.

7.3.4 CORROSION MECHANISM OF 96 H SPECIMENS

7.3.4.1 H230 ALLOY

Each specimen demonstrated noticeable interaction with the molten salt and the oxides all developed some distinct boundary. Some of the microstructures changed with increasing the annealing time from 24 h to 48 h. However, we each of these specimens did not show much change between the 48 h and 96 h tests. Consequently, we performed more in-depth analysis on the 96 h specimens in attempt to reveal the corrosion mechanism.

Figure 7.3(a) shows the microstructure of 96 h specimen and Fig. 7.3(b) shows the corresponding elemental maps obtained by EDS. Evidently, there is severe Cr loss within the interaction zone while the other elements are relatively stable. No significant presence of K, Mg, or Cl was found and thus was excluded. Figure 7.3(c) shows an elemental line profile across the interaction zone and found a decreasing slope in Cr concentration towards the surface. A Cr deficiency within the reaction zone for Haynes 230 alloy has also been reported by other researchers [14] (although at 750℃ for 300 h), which confirms the validity of our control sample.

In addition, to the elemental evolution during corrosion, we also investigated the structural evolution by XRD. Figure 7.4(a) compares the structure of the pure and 96 h-annealed

specimen. No new peaks were found, however, the broad peaks in the pristine sample noticeably sharpened and shifted toward higher 2θ. The sharpening likely originated from the prolonged annealing at high temperature causing crystallization and the peak shift presumably arises from the loss of the relatively large Cr atoms. Figure 7.4(b) shows the surface microstructure of the sample annealed for 96 h at low and high magnification. Small grain and pores exist presumably where the salt infiltrated and probably led to the dull appearance after testing. In agreement, with the cross sectional and XRD results, no new phases or structures were found on the surface.

A schematic of the proposed mechanism of corrosion of H230 is shown in Figure 7.5. The molten chloride salt is assumed to be dissociated and there is no oxygen or water present. Chromium cations are proposed to be leached out into melt and the excess electrons reduce the magnesium cation to metal. After removing the H230 specimens from the tube after tests. A metal layer would be found on top of the salt and inside of the quartz tube would be line with a metal. Since potassium is very unstable in air and would immediately oxidize and turn white, it is presumed Mg is the likely choice.

7.3.4.2 4K: $Y_{0.15}Yb_{0.15}Zr_{0.35}Hf_{0.35}O_{2-\delta}$

The SEM microstructure and elemental maps for CCFO 4K tested for 96 h are shown in Figure 7.6(a, b). The needle-like interaction zone is deficient in both Y and Yb. The specimen was not a single phase prior to the corrosion test and had Zr clusters dispersed throughout the sample. This appears to have persisted within the reaction zone as well suggesting Zr and Hf diffusion was minimal with during the test. The line profile across the interaction zone confirms these observations by showing a sharp decline to null in the concentration of the rare-earths (REs). This indicates that pure ZrO_2 and HfO_2 remains as the byproduct.

The XRD results in Figure 7.7(a) confirms this suspicion in showing that the fluorite phase transforms to a pure monoclinic $(Zr/Hf)O_2$ phase. No trace of the underlying fluorite phase was detected. The surface micrographs in Figure 7.7(b) reveal a similar structure to H230 in that there are small grains and pores where $KMgCl_3$ infiltrated. There does not appear to be any preference of infiltration through the grain boundaries.

The proposed corrosion mechanism for CCFO 4K is provided in Figure 7.8. The RE cations, Y and Yb, both leach out into the melt to form their respective chlorides. YCl_3 is liquid at 800°C, but $YbCl_3$ is a solid. No presence of this is seen however because nearly all chloride salts are readily soluble in water. The corresponding charge balanced oxygen is proposed to react with potassium ions to form potassium oxide (K_2O), which would be a liquid at 800°C. This material is unstable in air and water and would have been removed during specimen preparation. No XRD peaks corresponding to MgO were found and thus was excluded.

7.3.4.3 NT21: $(Sc_{0.266}Dy_{0.248}Tm_{0.246}Yb_{0.240})_3NbO_7$

Two distinct phases were found within the reaction zone of this NT21 specimen. Figure 7.9(a) shows the reaction zone after 96 h and the point EDS results for the two phases. Point 1, which has similar intensity to bulk phase, shows an approximately equal distribution of RE cations and a 1:1 atomic ratio of RE to Nb. The darker phase in point 2 reveals that most of the RE elements have been depleted by Sc still remains in a Sc:Nb atomic ratio of 2.6:1. The elemental maps in Figure 7.9(b) also allude to these results and show an enrichment of Nb within the reaction zone. Figure 7.9(c) shows the line profile EDS data and confirms the previous statements in that two phases coexist above the void.

The XRD results in Figure 7.10(a) reveal a strong presence of a $RENbO_4$ phase that is in agreement with the 1:1 atomic ratio of RE:Nb seen in point 1. The other predominant phase is

$Sc_{5.5}Nb_{1.5}O_{12}$, which agrees with the Sc-rich phase. The Sc:Nb ratio in this compound is 3.7:1, which is a bit higher than our point 2 ratio. We believe this is due to excess Nb_2O_5 neighboring these as we also identified this phase. The surface images in Figure 7.10(b) reveal the structure of these $RENbO_4$ (light) and $Sc_{5.5}Nb_{1.5}O_7$ (dark) phases. The $RENbO_4$ phase appears to have grown in platelet manner while the $Sc_{5.5}Nb_{1.5}O_7$ crystal grew in a perfect octahedron. A larger presence of the dark phase resides on the top surface that $Sc_{5.5}Nb_{1.5}O_7$ and Nb_2O_5 are the final products and $RENbO_4$ is an intermediate phase. The presence of the $RENbO_4$ phase is also significant because a high-entropy compound of this phase has yet to be reported in literature yet; however, here, it has been confirmed to be stable.

A schematic the proposed reaction mechanism is shown in Figure 7.11. Similar to CCFO 4K, we found all the RE cations quickly leach out into the melt where $DyCl_3$ is liquid, but $TmCl_3$ and $YbCl_3$ are solid. The corresponding O^{2-} anions are again suspected to reaction with K^+ to form K_2O since no presence of MgO was found. As the RE concentration steeply declines, the $Sc_{5.5}Nb_{1.5}O_{12}$ phase forms. Once the stoichiometry is reached, the excess Nb precipitates as Nb_2O_5.

7.3.4.4 P20-5: $(Sm_{1/4}Eu_{1/4}Gd_{1/4}Yb_{1/4})_2(Ti_{1/2}Hf_{1/4}Zr_{1/4})_2O_7$

The pyrochlore (P20-5) showed the most complex microstructure evolution (Figure 7.12(a)) of the samples investigated with a clear two zone region existing. The corresponding elemental maps are shown in Figure 7.12(b) and reveal that the zone above the bulk with similar intensity only shows a relative enrichment Yb and a decrease in the other RE elements. There is also some residual KCl that was unable to be removed from the sonicating and polishing procedure. The top layer showed no presence of RE cations, but a strong presence of Ti and Mg. Zr and Hf are also present in small clusters that correspond to the bright phase in the top layer.

The elemental line profile shows that in the bottom reaction layer, the composition is fairly similar to the bulk, however, there are a couple of important differences. First, the concentration of Sm, Eu, and Gd decrease steadily throughout this region, but the concentration of Yb is stable. Second, there is a noticeable concentration of Mg. In the top layer, the presence of all RE elements vanished and, Mg and Ti are present in equal proportions. This was also observed for Zr and Hf. Lastly, in the circular region at the top, the Mg concentration is negligible and is very strong in Ti.

This suggests that TiO_2 along with $(Zr/Hf)O_2$ are the final products in the bubble-like region which appears to being separated from the main structure. In the top layer, since Mg and Ti are present in equal proportions, it is likely that the phase is $MgTiO_3$ in addition to $(Zr/Hf)O_2$. In the bottom layer, we propose this $MgTiO_3$ persists since Mg is still significantly present in this region. This reduction in Ti available to the REs leaves a Ti-poor and Yb-rich phase. The abundance of Yb cations with Hf and Zr is likely to form a fluorite phase [45]. We are unable to identify if a pyrochlore phase still exists due to the small pyrochlore superstructure peaks and complex XRD pattern.

Figure 7.13(a) shows the phase evolution of the salt corrosion of P20-5 after $24\ h$ and $96\ h$ anneals. All of the previously proposed phases were identified. A small presence of the bulk phase was identifiable after $24\ h$, but not after $96\ h$. Additionally, the rutile TiO_2 phase was not detected after $24\ h$ suggesting that kinetics related to the formation of the TiO_2 are sluggish. The kinetics also appear to be slow in leaching out the RE elements compared to CCFO 4K for example. Figure 7.13(b, c) show the surface microstructure of P20-5 after annealing for $96\ h$ and $24\ h$. The structures are similar, but not identical because the reaction has not fully completed

after $24\ h$. In Figure 7.13b, the brighter $(Zr/Hf)O_2$ phase forms orthogonal needle-like structures while the darker, featureless TiO_2 is dispersed within.

The proposed corrosion mechanism is shown in Figure 7.14. The larger rare cations (Sm, Eu, and Gd) reduce quickly while concentration of Yb is maintained until the top layer. Each of these REs are expected to form their respective chlorides. $YbCl_3$ is a solid at $800℃$ while the rest are liquid. The TiO_2 is expected to react with Mg^{2+} and excess O^{2-} anions (from the REs leaching) to form $MgTiO_3$. The remaining cations are projected to remain in the pyrochlore or perhaps transform to the fluorite phase, which persists as an intermediate phase. As the reaction progresses, the REs are full leached out and $MgTiO_3$, $(Zr/Hf)O_2$, and TiO_2.

7.3.4.5 CORROSION SUMMARY

Each of the three specimens investigated all showed different interactions with the molten salt. One aspect captured in these experiments is the influence of entropy on corrosion resistance. On the hand, increased entropy theoretically should provide a more stable phase. While on the other hand, an increase in configurational entropy provide more elements and increases the chances of reaction. Overall, we did not see a clear relationship between configurational entropy and corrosion resistance. In fact, our best performing CCFO only has four components not in equimolar ratios. We do not dismiss the fact that entropy plays a role, but we believe it is eclipsed by the influence of structure and the specific elements present and their ratios. The specific elements and their ratios are directly related to the optical basicity, which we showed in the first section to be a reasonable predictor of corrosion performance in these high-entropy oxides. However, there are limitation within this statement as well because, for example, Yb leached out quickly in CCFO 4K ($\sim 5\ \mu m$) but was quite stable in P20-5 compared to the other RE elements. Additionally, the influence of structure is also important. While there was a fair

trend between the different families, we were able to find reasonably resistant compositions within each one as we have demonstrated in these longer dwell time experiments. Each of these compositions displayed a TID of $\sim 30\ \mu m$ after annealing for $24\ h$, which illustrates that optical basicity cannot perfectly predict the performance. Furthermore, the importance of annealing time is also important to see if the reaction has a linear or parabolic rate constant.

7.3.5 THERMAL CONDUCTIVITY

Figure 7.16 shows the temperature-dependent thermal conductivity for 4K, NT21, and P20-5. The directly measured thermal diffusivity and estimated specific heat capacity are shown in Supplementary Information. All specimens show attractive (insulative) properties with thermal conductivities below $2\ W\ m^{-1}K^{-1}$. CCFO 4K displays a $1/T$-like relationship characteristic of Umklapp scattering at high temperatures. Both NT21 and P20-5 show amorphous-like thermal conductivities representative of increasing conductivity with T corresponding to increases in c_p. The phonon limit was estimated for each specimen by Cahill, Watson, and Pohl's model [46]. CCFO 4K approaches this limit but remains 20 %-30 % above it. Both P20-5 and NT21 approach the limit at intermediate temperatures (200℃-400℃), however, they significantly deviate at higher temperatures. This is likely due to the significant contribution of internal radiation. Regardless, all three specimens (and many of the ones used in the screening) show insulative properties that tend to be much lower than yttria-stabilized zirconia [9,10,47,48].

7.4 CONCLUSIONS

Numerous (42) medium-/high-entropy oxide ceramics that all exhibit high Young's modulus-to-thermal conductivity ratios were screened for their compatibility in a molten $KMgCl_3$ environment at 800℃. We are the first to our knowledge to apply the concept of optical

basicity to molten chlorides salts and found that it can be used as a reasonable predictor for infiltration depth and mass loss. However, we stress that influence of structure, composition, and annealing are also all important. We conducted a more focused investigation on three specimens representing the best performance of their family during the $24\ h$ screening test. All three specimens show well-developed reaction layers that increase the diffusion length for the chloride salt to continue corroding. In-depth elemental analysis revealed all the rare-earth elements were leached into the melt. Hf, Zr, Sc, and Nb were found to be stable while Ti formed a stable compound with Mg, $MgTiO_3$. Corrosion tests carried out to $1000\ h$ reveal *** relationship. Lastly, all three of these specimens exhibit ultralow thermal conductivities that approach the diffuson limit. At 800℃, the conductivity for each is $\sim 1.6\ W\ m^{-1}\ K^{-1}$. This study introduces a new screening parameter to the field, but also stresses the importance of kinetic studies and of a reaction layer. The examined materials were found (in their pellet form) to perform worse in the short-term ($24\ h$) but significantly better in exposure times $> 500\ h$ due to the linear infiltration kinetics associated with the Haynes 230 metal and the parabolic reaction kinetics experienced with the medium-/high-entropy ceramics.

Chapter 7, in full, is currently being prepared for submission. A.J. Wright, K.M. Chung, Q. Wang, Y.T. Yeh, R. Chen, J. Luo, Molten $KMgCl_3$ salt corrosion in high entropy oxides. The dissertation author was the primary investigator and author of this paper.

Table 7.1. Relevant corrosion properties for specimens H230 (Ni-Cr-W-Mo alloy), CCFO 4K ($Y_{0.15}Yb_{0.15}Zr_{0.35}Hf_{0.35}O_{2-\delta}$), HENT NT21 ($(Sc_{0.266}Dy_{0.248}Tm_{0.246}Yb_{0.240})_3NbO_7$), and HEP P20-5 ($(Sm_{0.25}Eu_{0.25}Gd_{0.25}Yb_{0.25})_2(Ti_{0.5}Hf_{0.25}Zr_{0.25})_2O_7$).

		H230	4K	NT21	P20-5
	Λ	N/A	0.850	1.040	0.943
24 h	$TID\ (\mu m)$	9.8 ± 1.3	20.9 ± 7.0	23.5 ± 2.1	30.2 ± 3.6
	$CR_{Mass}\ (nm/h)$	96	252	628	899
48 h	$TID\ (\mu m)$	20.4 ± 4.1	68.3 ± 35.8	59.3 ± 3.7	45.5 ± 2.4
	$CR_{Mass}\ (nm/h)$	30	153	531	637
96 h	$TID\ (\mu m)$	51.8 ± 18.9	47.9 ± 18.2	50.6 ± 4.9	62.4 ± 2.4
	$CR_{Mass}\ (nm/h)$	27	167	263	380
500 h	$TID\ (\mu m)$	405.2 ± 47.0	177.9 ± 57.1	102.0 ± 7.2	126.3 ± 9.4
	$CR_{Mass}\ (nm/h)$	22	83	112	118
800 h	$TID\ (\mu m)$	313.2 ± 33.2	175.1 ± 90.4	89.0 ± 6.5	168.6 ± 5.6
	$CR_{Mass}\ (nm/h)$	81	48	42	98
$k_{lin}\ (\mu m/h)$		0.5 ± 0.1	0.1 ± 0.1	0.0 ± 0.1	0.0 ± 0.0
$k_{par}\ (\mu m/\sqrt{h})$		0.0 ± 0.8	3.9 ± 1.0	5.9 ± 2.6	6.5 ± 0.5

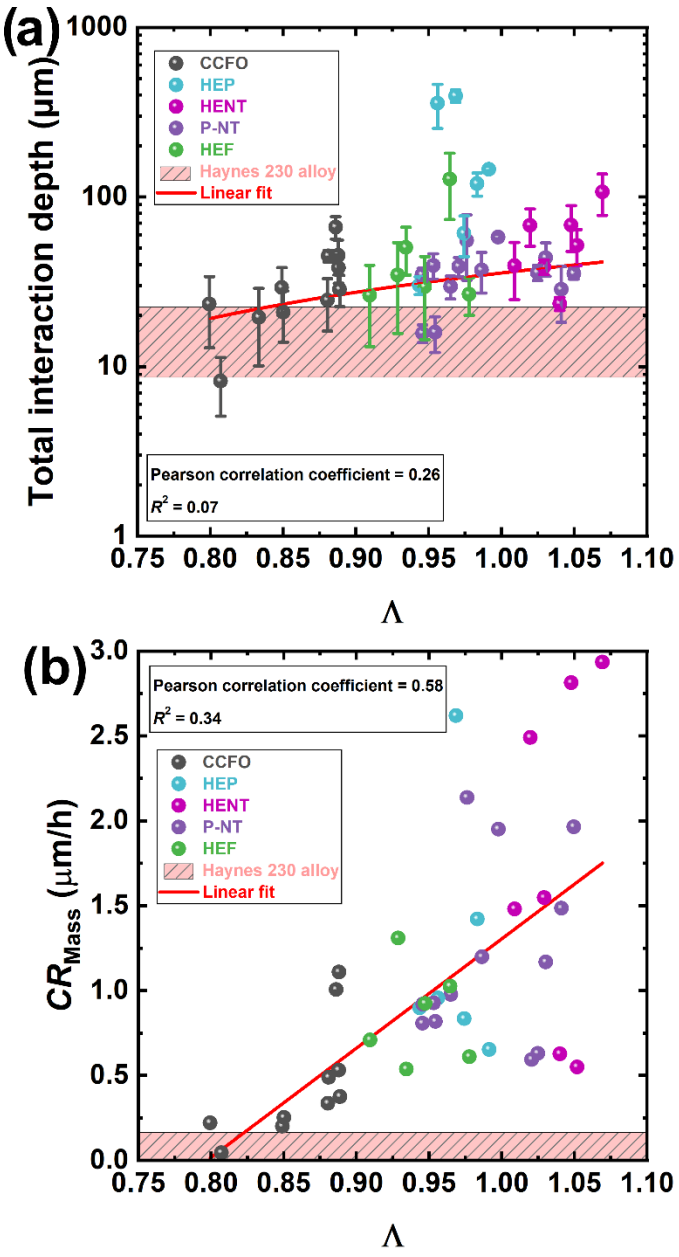

Figure 7.1. The **(a)** total interaction depth and **(b)** mass corrosion rate for all 45 screened materials. Five separate families were investigated a linear line was fit through all data (on a linear-linear plot). The striped pink region is the data for the reference Haynes 230 alloy with the thickness equal to the mean $\pm$ standard deviation. For the total infiltration depth and corrosion rate, the values are $9.8 \pm 1.3\ \mu m$ and $0.1 \pm 0.1\ \mu m/h$. CCFO: compositionally-complex fluorite oxide, HEP: high-entropy pyrochlore, HENT: high-entropy niobate/tantalate, P-NT: mixed pyrochlore-niobate/tantalate, HEF: high-entropy fluorite.

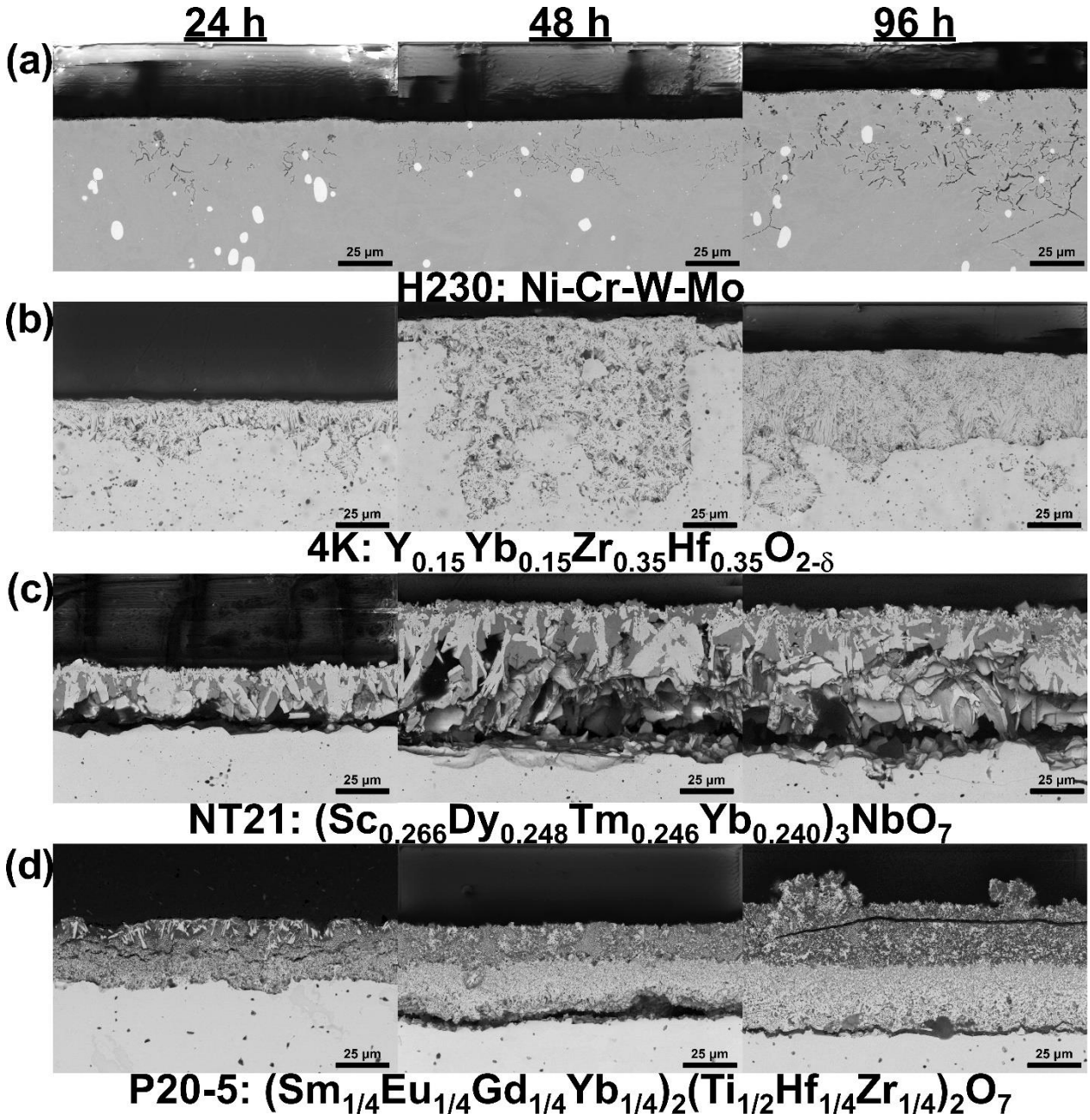

Figure 7.2. Cross-sectional micrographs of **(a)** Haynes 230 alloy, **(b)** CCFO 4K, **(c)** HENT NT21, and **(d)** HEP P20-5 after annealing in molten $KMgCl_3$ at 800℃ for 24 *h*, 48 *h*, and 96 *h*.

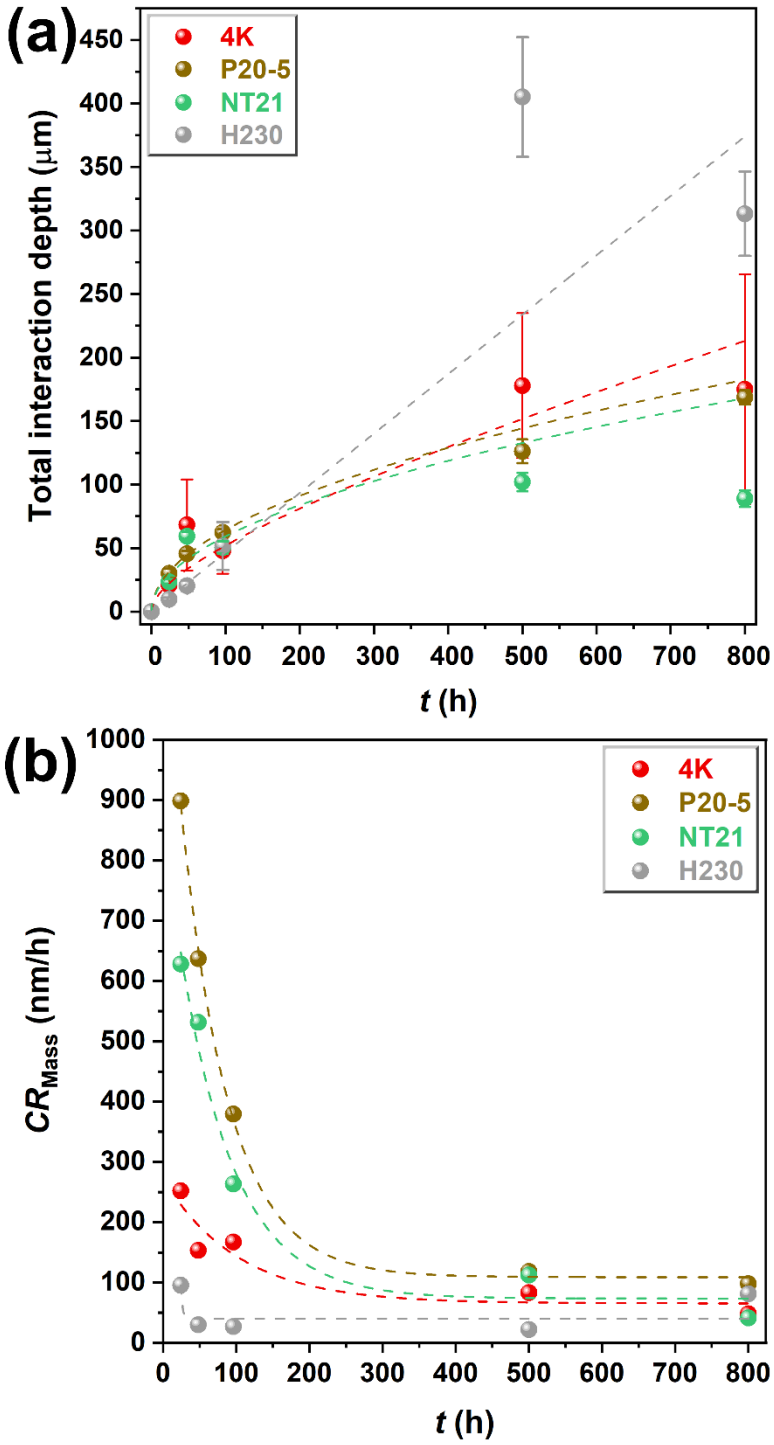

Figure 7.3. Kinetic study of 4K, NT21, P20-5, and Haynes 230 alloy up to 1000 h at 800℃ for the **(a)** total interaction depth (TID) and **(b)** mass corrosion rate. The TID was fitted to a two-parameter model ($TID = k_{lin}t + k_{par}\sqrt{t}$) to extract the linear and parabolic rate constants. The corrosion rate was fitted to an exponential decay ($CR_{Mass} = Ae^{\lambda t} + B$) to determine the limiting values.

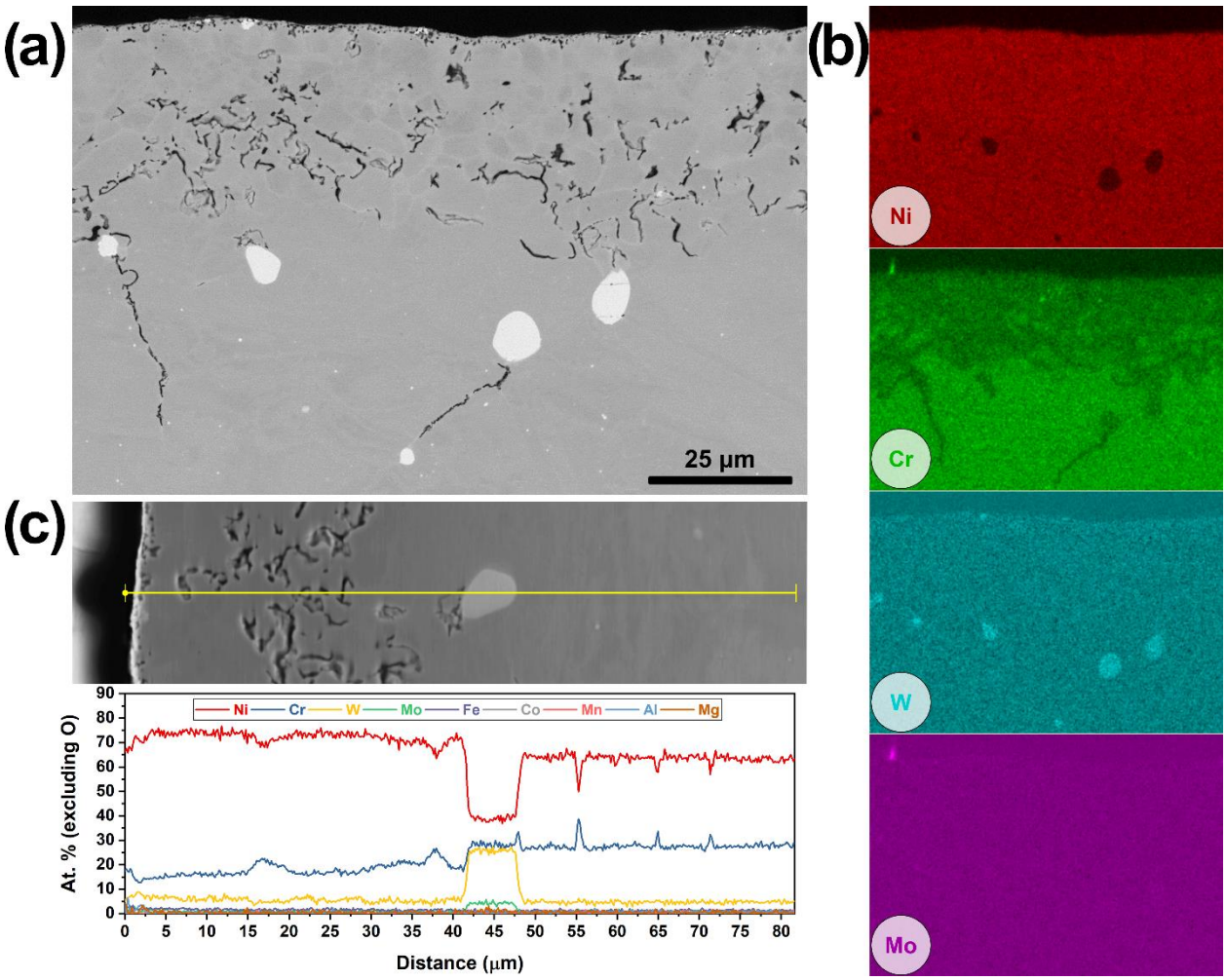

Figure 7.4. (a) Cross-section micrograph of Haynes 230 alloy and **(b)** the corresponding elemental maps. **(c)** Line scan elemental profile across the interaction region.

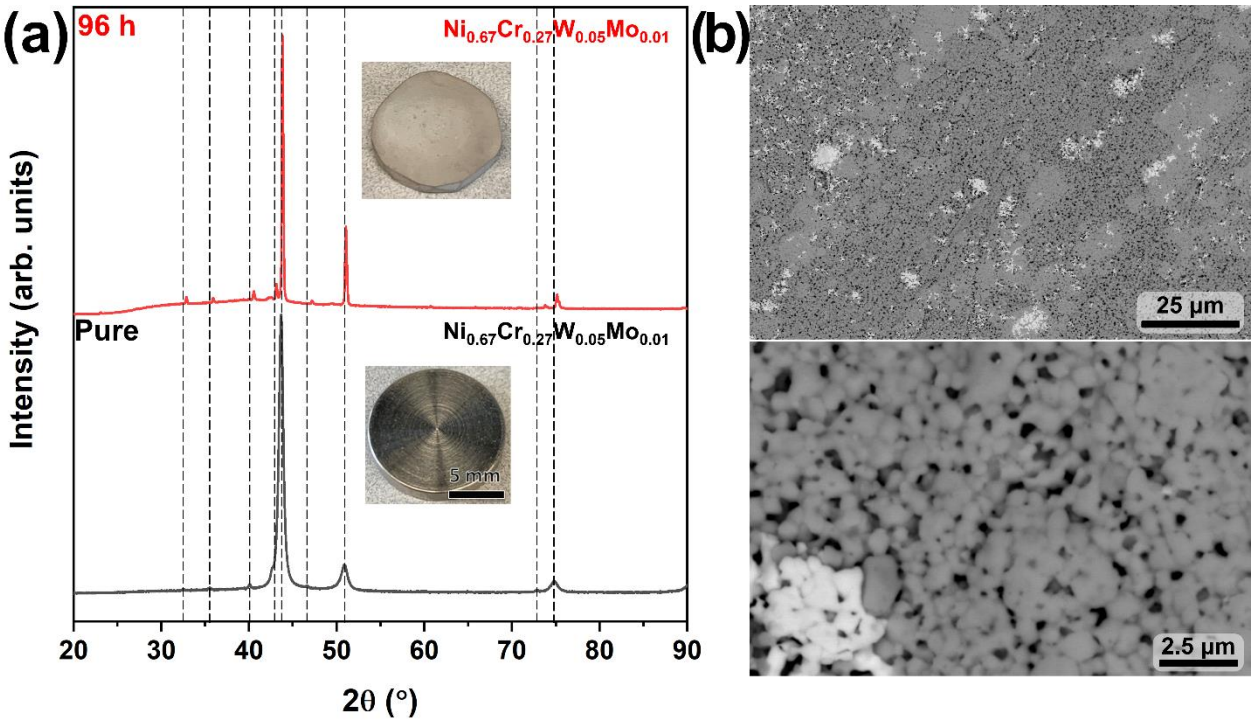

Figure 7.5. (a) XRD evolution of Haynes 230 alloy after the 96 *h* corrosion test. Along with a digital image of each pellet. Note that the pellet was ground on the edges prior to sealing so that the specimen could fit inside the quartz tube. This reduction in mass was accounted for. **(b)** Surface micrograph at low and high magnification of after the 96 *h* anneal.

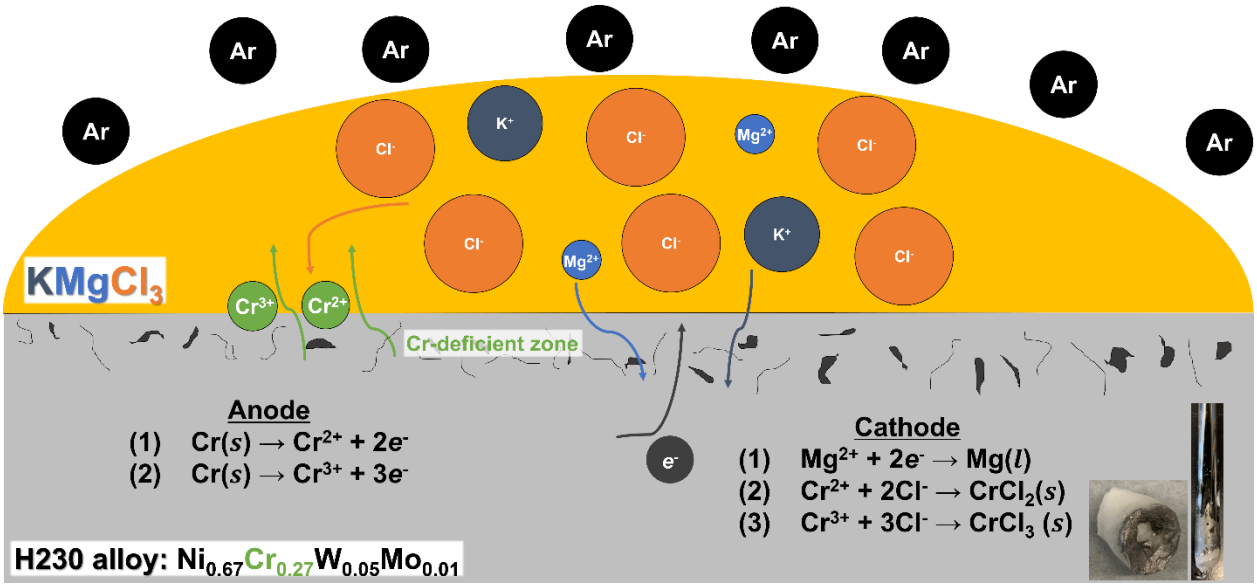

Figure 7.6. A schematic illustrating the proposed corrosion mechanism with Haynes 230 alloy. Cr is suggested to leach into the melt while the electrons reduce Mg^{2+} to metal. This was suggested from the observation of a metal layer on the surface of the residual salt after testing.

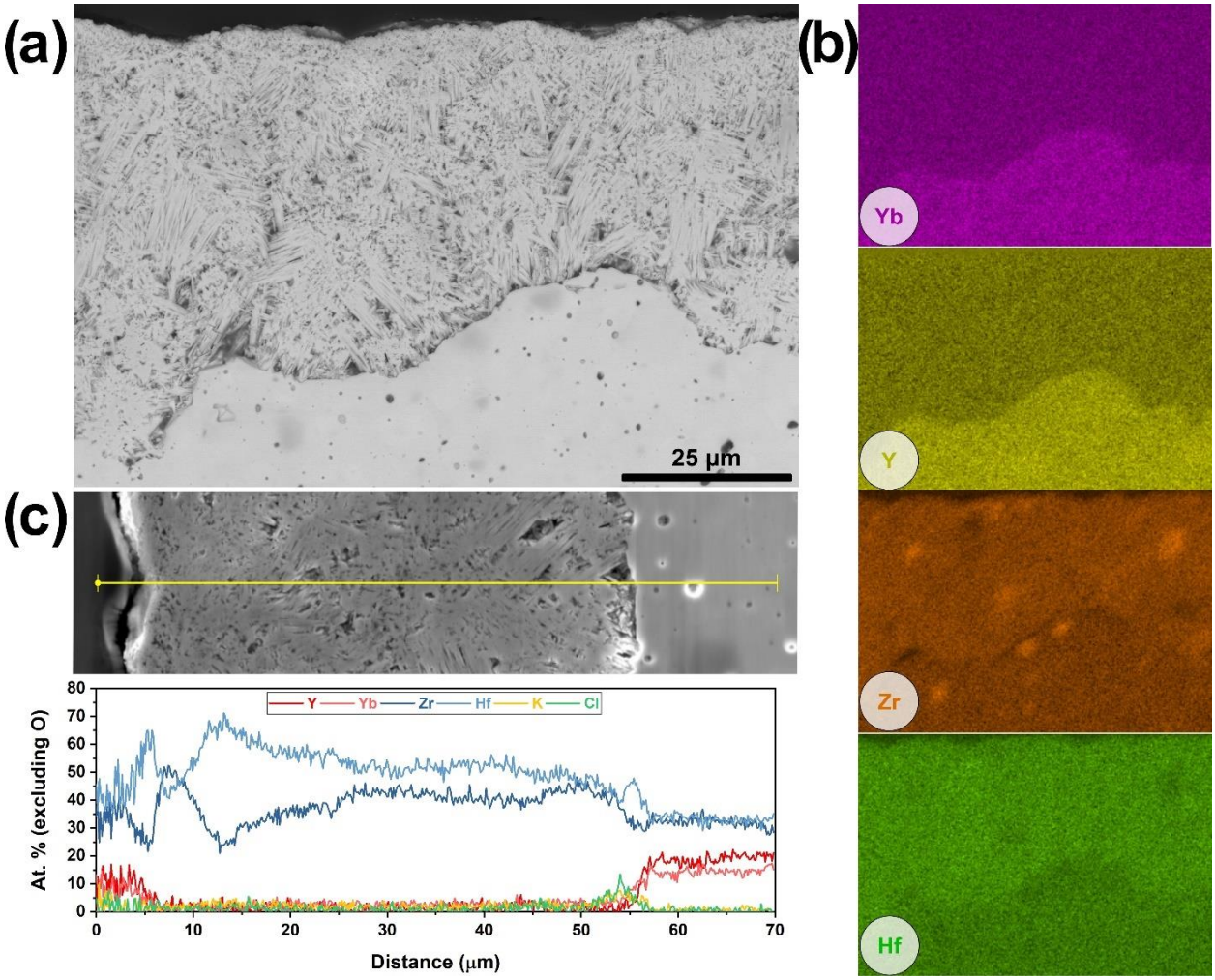

Figure 7.7. (a) Cross-section micrograph of CCFO 4K ($Y_{0.15}Yb_{0.15}Zr_{0.35}Hf_{0.35}O_{2-\delta}$) and **(b)** the corresponding elemental maps. Note the EDS map scan drifted slightly towards the top-right. **(c)** Line scan elemental profile across the interaction region.

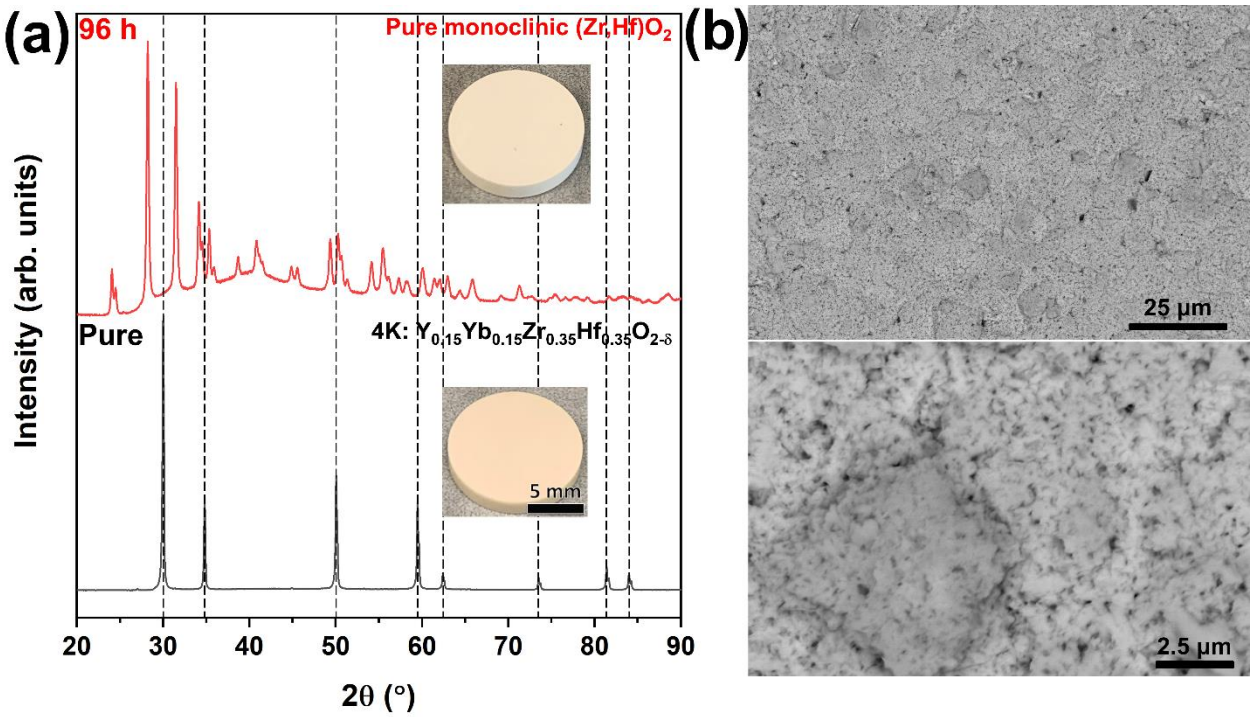

Figure 7.8. (a) XRD evolution of CCFO 4K after the 96 *h* corrosion test along with a digital image of each pellet. **(b)** Surface micrograph at low and high magnification after the 96 *h* anneal.

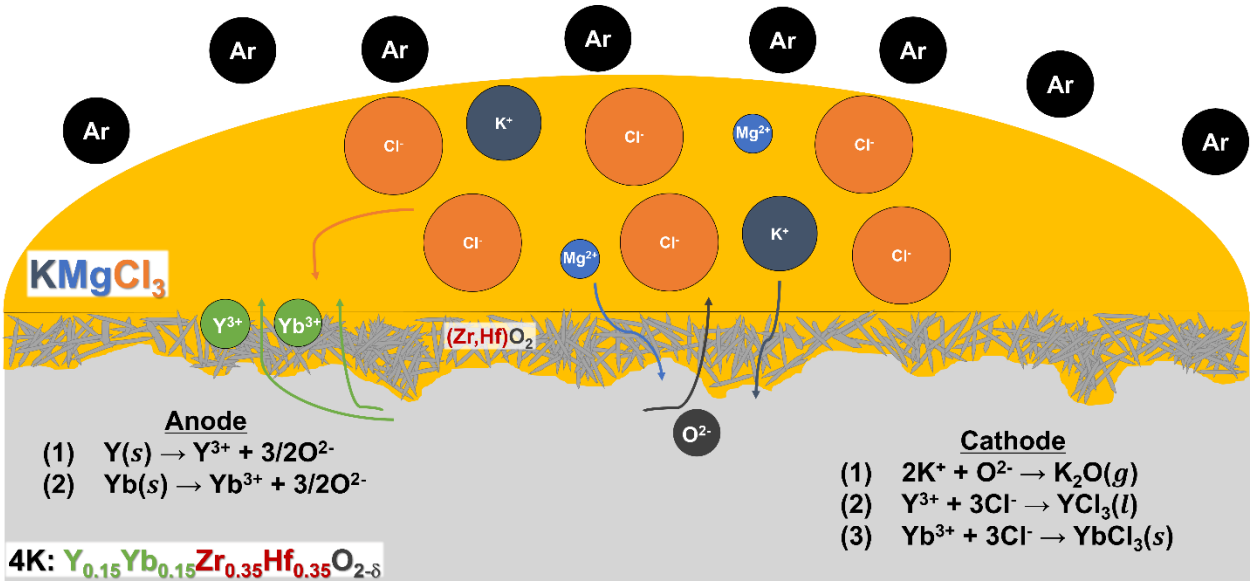

Figure 7.9. A schematic illustrating the proposed corrosion mechanism with CCFO 4K. The rare-earths (Y and Yb) are suggested to leach into the melt while the oxygen anions reduce K^+ to K_2O. This was suggested from the lack of observation of a MgO phase by XRD. A monoclinic $(Zr,Hf)O_2$ phase is leftover in the reaction layer.

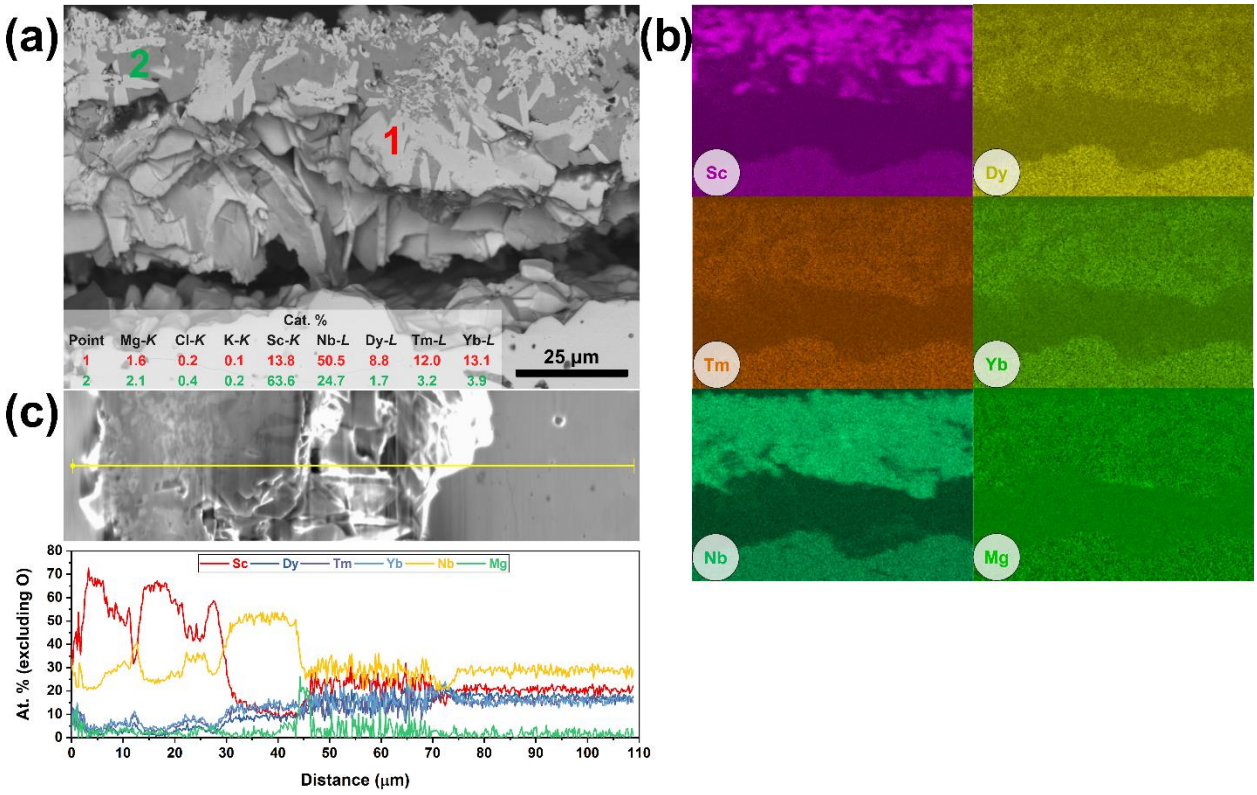

Figure 7.10. (a) Point EDS analysis of HENT NT21 ($(Sc_{0.266}Dy_{0.248}Tm_{0.246}Yb_{0.240})_3NbO_7$) and **(b)** an elemental map distribution. **(c)** Line scan elemental profile across the interaction region.

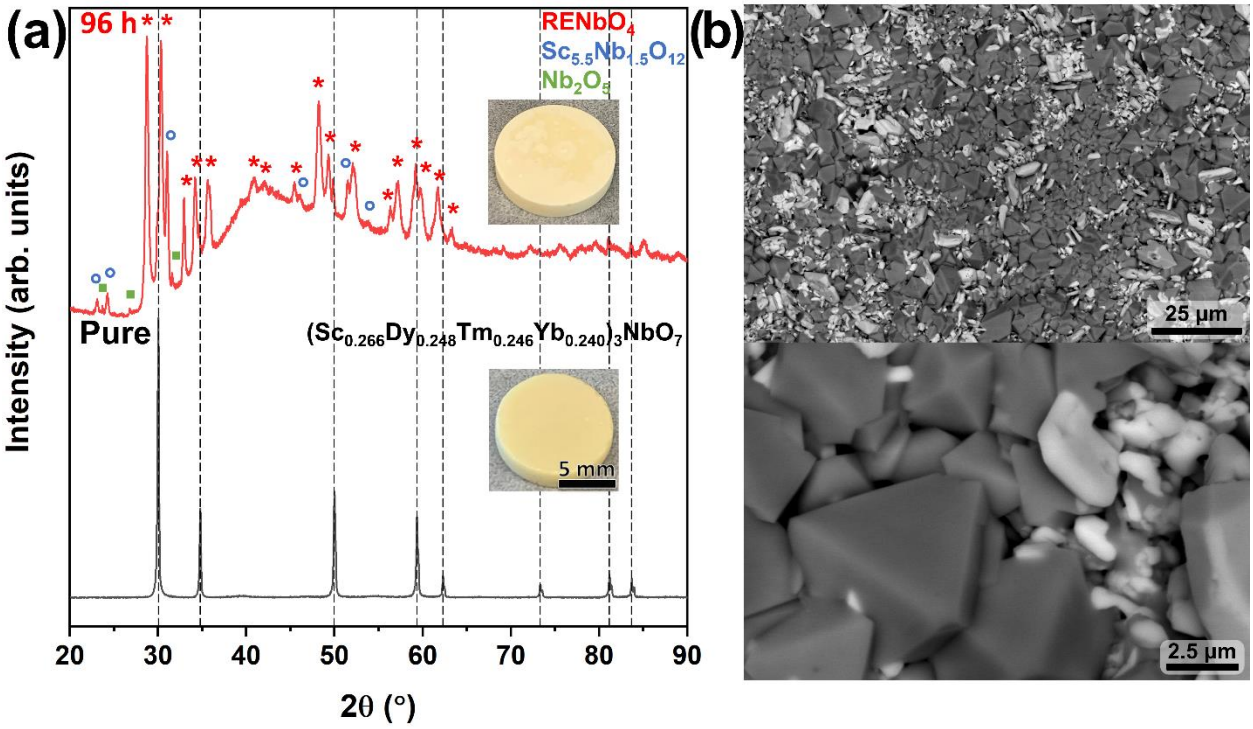

Figure 7.11. (a) XRD evolution of HENT NT21 after the 96 *h* corrosion test along with a digital image of each pellet. **(b)** Surface micrograph at low and high magnification after the 96 *h* anneal showing two phases, $Sc_{5.5}Nb_{1.5}O_{12}$ (darker) and $RENbO_4$ (lighter). RE: rare-earths.

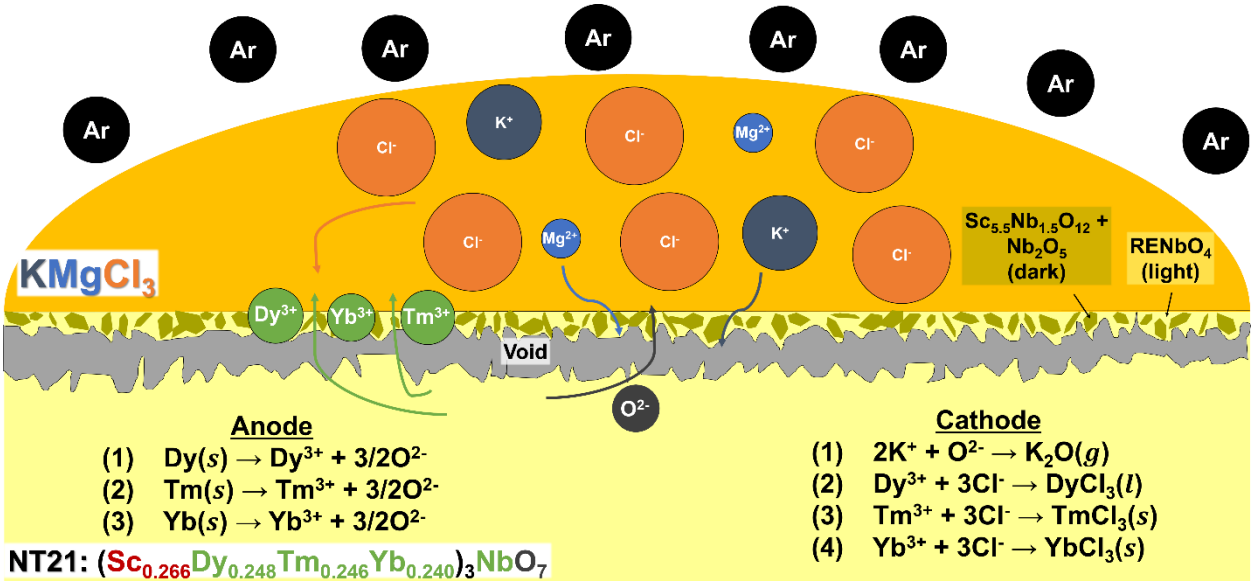

Figure 7.12. A schematic illustrating the proposed corrosion mechanism with HENT NT21. The rare-earths (Dy, Tm, and Yb) are suggested to leach into the melt while the oxygen anions reduce K^+ to K_2O. This was suggested from the lack of observation of a MgO phase by XRD.

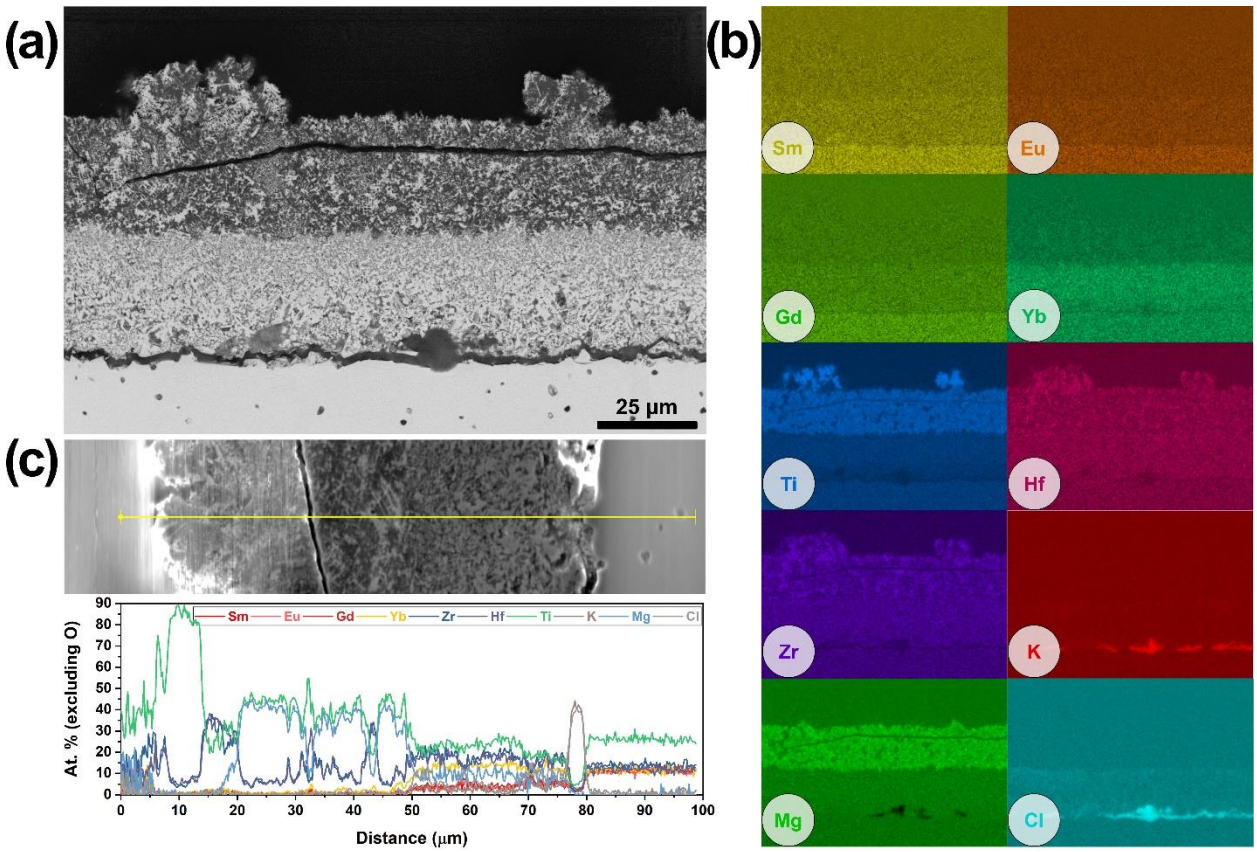

Figure 7.13. (a) Cross-section micrograph of HEP P20-5 ($(Sm_{0.25}Eu_{0.25}Gd_{0.25}Yb_{0.25})_2(Ti_{0.5}Hf_{0.25}Zr_{0.25})_2O_7$) and **(b)** the corresponding elemental maps. **(c)** Line scan elemental profile across the interaction region.

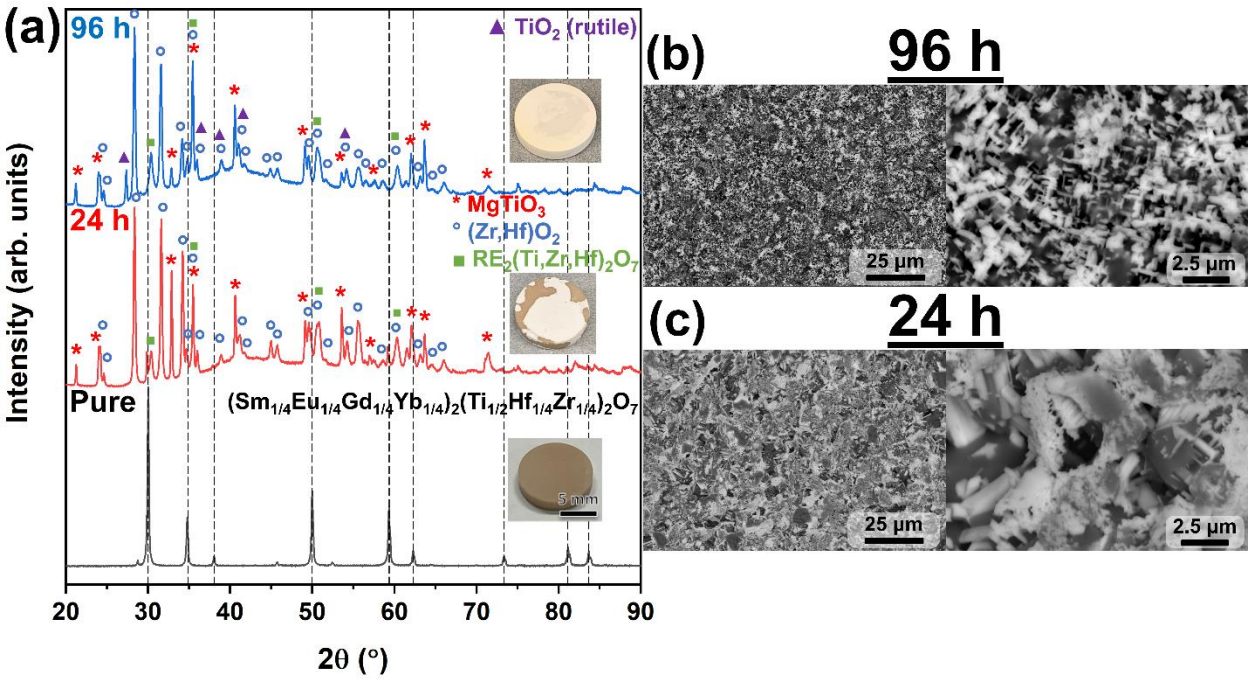

Figure 7.14. (a) XRD evolution of HEP P20-5 after the 24 *h* and 96 *h* corrosion test along with a digital image of each pellet. Surface micrograph at low and high magnification after the **(b)** 24 *h* and **(c)** 96 *h* anneal.

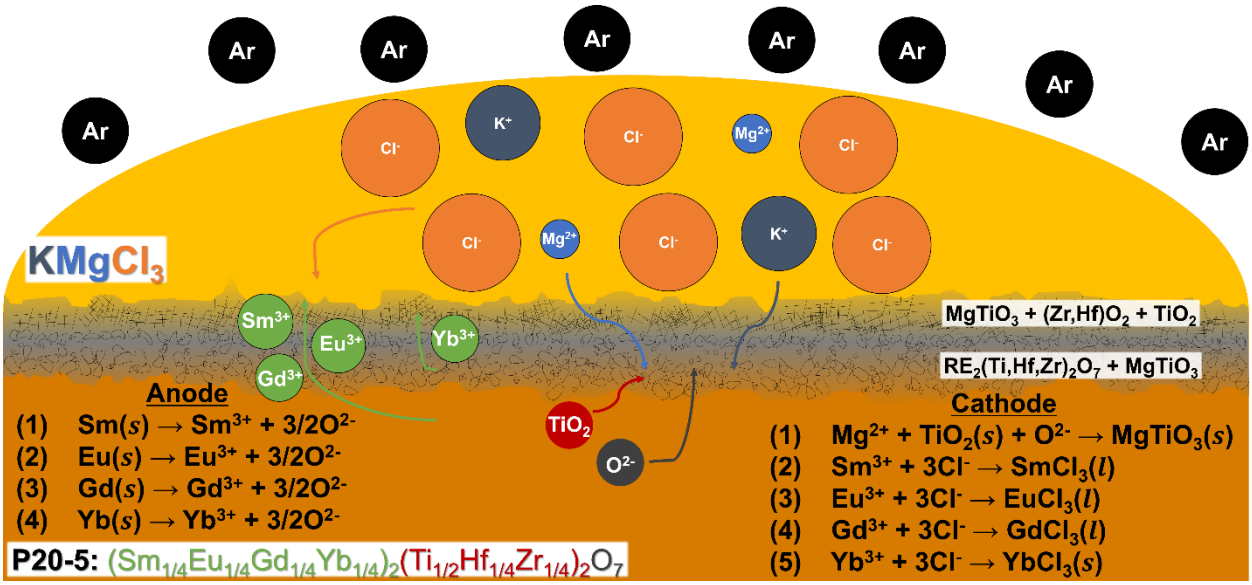

Figure 7.15. A schematic illustrating the proposed corrosion mechanism with HEP P20-5. The rare-earths (Sm, Eu, and Gd) are suggested to leach into the melt first. Yb appears to be stable in a fluorite or pyrochlore phase ($RE_2(Ti,Hf,Zr)_2O_7$) throughout the bottom layer. Mg^{2+} reacts with Ti and O^{2-} to form a $MgTiO_3$ phase. In the top layer, all the rare-earths leach into the melt and a monoclinic $(Zr,Hf)O_2$ phase and $MgTiO_3$ phase persist. Dispersed along with the top boundary are some round figures rich in TiO_2 and $(Zr,Hf)O_2$. RE: rare-earths.

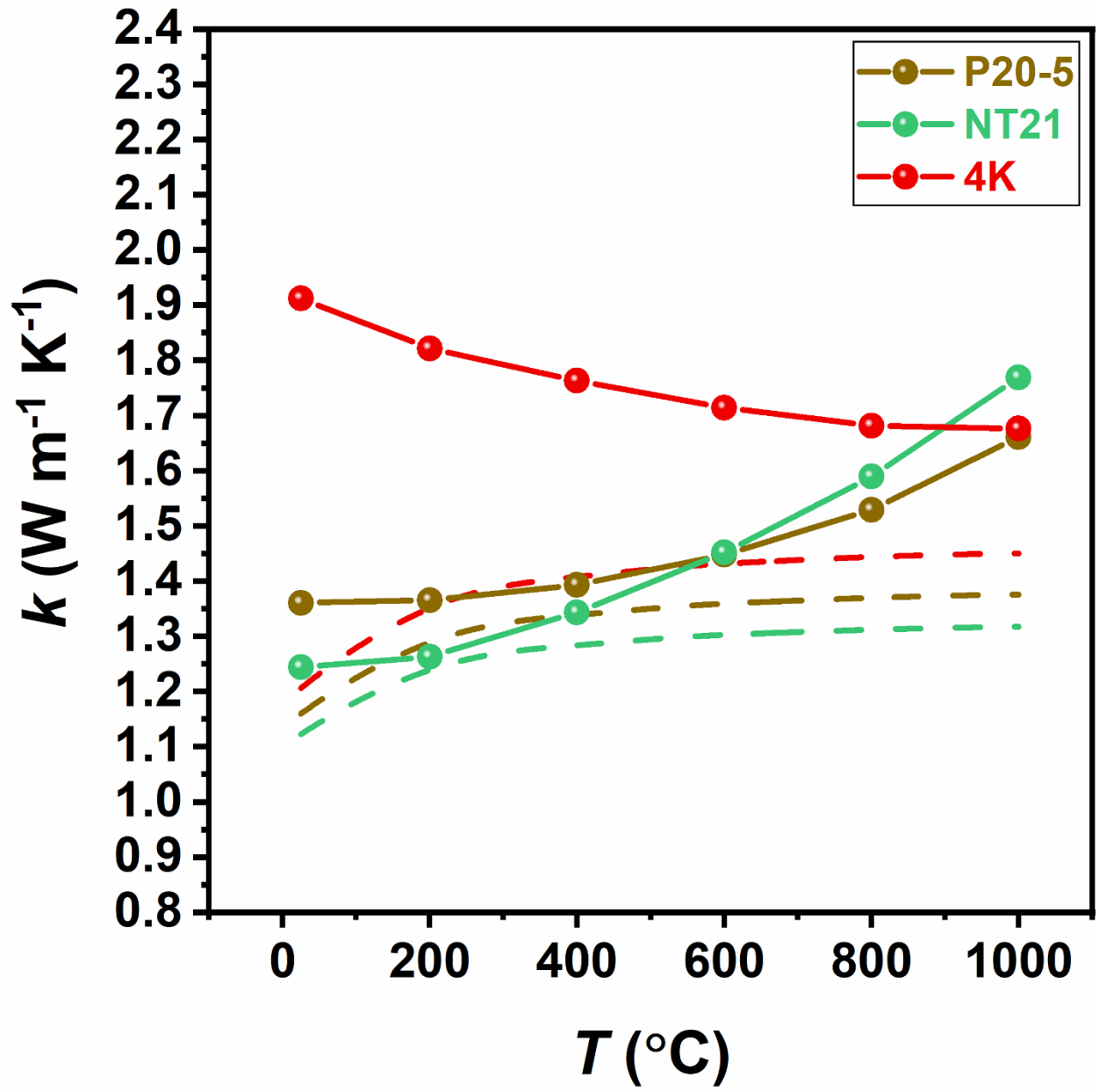

Figure 7.16. Temperature-dependent thermal conductivity of CCFO 4K ($Y_{0.15}Yb_{0.15}Zr_{0.35}Hf_{0.35}O_{2-\delta}$), HENT NT21 ($(Sc_{0.266}Dy_{0.248}Tm_{0.246}Yb_{0.240})_3NbO_7$), and HEP P20-5 ($(Sm_{0.25}Eu_{0.25}Gd_{0.25}Yb_{0.25})_2(Ti_{0.5}Hf_{0.25}Zr_{0.25})_2O_7$) from 25℃ – 1000℃. The phonon limit based on the Cahill model is also provided [46].

Table 7.2. Relevant corrosion performance values and thermomechanical properties for all 42 screened materials. *: multiphase material. Λ: optical basicity.

	Λ	Total interaction depth (μm)	Mass corrosion rate ($\mu m/h$)	k_{RT} ($W\ m^{-1}\ K^{-1}$)	$k_{800°C}$ ($W\ m^{-1}\ K^{-1}$)	E_{RT} (GPa)
		24 h	**24 h**			
Compositionally-Complex Fluorite Oxides (CCFOs)						
4F $(Y_{1/4}Sc_{1/4}Yb_{1/4}Gd_{1/4})_{0.2}(Hf_{1/2}Zr_{1/2})_{0.8}O_{2-\delta}$	0.849	29.2 ± 9.1	0.2	1.73 ± 0.02	1.76 ± 0.02	266.5 ± 2.7
4J $Y_{0.15}Yb_{0.15}Zr_{0.7}O_{2-\delta}$	0.880	24.6 ± 8.4	0.34	2.12 ± 0.17	1.95 ± 0.17	259.8 ± 2.0
4G $Y_{0.091}Yb_{0.091}Hf_{0.818}O_{2-\delta}$	0.799	23.4 ± 10.5	0.22	1.74 ± 0.02	1.81 ± 0.02	273.7 ± 2.8
4K $Y_{0.15}Yb_{0.15}Zr_{0.35}Hf_{0.35}O_{2-\delta}$	0.850	20.9 ± 7.0	0.25	1.91 ± 0.02	1.68 ± 0.02	265.9 ± 2.5
4M $(Hf_{0.284}Zr_{0.284}Ce_{0.284}Y_{0.074}Yb_{0.074})O_{2-\delta}$	0.888	38.2 ± 7.2	1.11	1.74 ± 0.05	1.71 ± 0.05	232.8 ± 2.2
4L $(Hf_{0.314}Zr_{0.314}Ce_{0.314}Y_{0.029}Yb_{0.029})O_{2-\delta}$	0.881	44.9 ± 3.6	0.49	1.78 ± 0.05	1.83 ± 0.05	201.2 ± 2.2
5M $(Hf_{0.284}Zr_{0.284}Ce_{0.284}Y_{0.074}Ca_{0.074})O_{2-\delta}$	0.889	28.5 ± 6.0	0.38	1.54 ± 0.05	1.50 ± 0.05	153.8 ± 2.3
7L $(Hf_{0.314}Zr_{0.314}Ce_{0.314}Y_{0.029}Gd_{0.029})O_{2-\delta}$	0.886	66.5 ± 10.1	1.01	1.74 ± 0.05	1.77 ± 0.05	199.4 ± 2.0
F1300 $(Hf_{0.3}Zr_{0.3}Ce_{0.3}Gd_{0.01}Tb_{0.01}Dy_{0.01}Ho_{0.01}Er_{0.01}Tm_{0.01}Yb_{0.01}Y_{0.01}Lu_{0.01}Ca_{0.01})O_{2-\delta}$	0.888	45.2 ± 10.5	0.53	1.65 ± 0.05	1.67 ± 0.05	217.5 ± 4.5
High-Entropy Fluorites (HEFs)						
F6 $(Hf_{1/5}Zr_{1/5}Ce_{1/5}Y_{1/5}Yb_{1/5})O_{2-\delta}$	0.909	26.3 ± 13.2	0.71	2.21 ± 0.07	1.66 ± 0.07	239.2 ± 5.2
F9* $(Hf_{1/5}Zr_{1/5}Ce_{1/5}Sc_{1/5}Gd_{1/5})O_{2-\delta}$	0.964	127.4 ± 53.9	1.03	--	--	--
F10 $(Hf_{1/5}Zr_{1/5}Ce_{1/5}Sc_{1/5}Y_{1/5})O_{2-\delta}$	0.934	50.4 ± 15.8	0.54	2.01 ± 0.06	1.57 ± 0.06	222.4 ± 4.1
F13 $(Hf_{1/5}Zr_{1/5}Ce_{1/5}Gd_{1/5}Tb_{1/5})O_{2-\delta}$	0.947	29.5 ± 15.1	0.92	1.92 ± 0.06	1.48 ± 0.06	227.9 ± 3.9
F14 $(Hf_{1/5}Zr_{1/5}Ce_{1/5}Gd_{2/5})O_{2-\delta}$	0.978	26.7 ± 6.7	0.61	2.04 ± 0.07	1.48 ± 0.07	231.8 ± 3.9
4E $(Yb_{1/2}Y_{1/2})_{0.6}(Hf_{1/3}Zr_{1/3}Ce_{1/3})_{0.4}O_{2-\delta}$	0.929	34.7 ± 19.0	1.31	2.29 ± 0.03	1.47 ± 0.03	214.6 ± 2.1
High-Entropy Pyrochlores (HEPs)						
LZO $La_2Zr_2O_7$	0.991	145.8 ± 7.0	0.65	2.14 ± 0.06	1.60 ± 0.06	236.2 ± 6.7

Table 7.2. Relevant corrosion performance values and thermomechanical properties for all 42 screened materials. *: multiphase material. Λ: optical basicity.

	Λ	Total interaction depth (μm)	Mass corrosion rate ($\mu m/h$)	k_{RT} ($W\ m^{-1}\ K^{-1}$)	$k_{800°C}$ ($W\ m^{-1}\ K^{-1}$)	E_{RT} (GPa)
		24 h	24 h			
SZO $Sm_2Zr_2O_7$	0.974	61.0 ± 16.4	0.83	2.04 ± 0.06	1.62 ± 0.06	220.1 ± 3.0
P1 $La_2(Hf_{1/2}Zr_{1/2})_2O_7$	0.969	394.6 ± 33.2	2.62	2.29 ± 0.06	1.80 ± 0.06	250.2 ± 4.2
P10 $(La_{1/3}Pr_{1/3}Nd_{1/3})_2(Hf_{1/2}Zr_{1/2})_2O_7$	0.983	119.7 ± 18.7	1.42	2.16 ± 0.06	1.66 ± 0.06	240.0 ± 4.3
P20-5 $(Sm_{1/4}Eu_{1/4}Gd_{1/4}Yb_{1/4})_2(Ti_{1/2}Hf_{1/4}Zr_{1/4})_2O_7$	0.944	30.2 ± 3.6	0.90	1.36 ± 0.04	1.53 ± 0.04	236.9 ± 2.4
P21 $(La_{1/5}Ce_{1/5}Nd_{1/5}Sm_{1/5}Eu_{1/5})_2Zr_2O_7$	0.956	357.4 ± 103.8	0.96	2.06 ± 0.06	1.86 ± 0.06	230.6 ± 2.9
High-Entropy Niobate/Tantalates (HENTs)						
NT0 Dy_3NbO_7	1.069	107.3 ± 29.5	2.93	1.10 ± 0.03	1.35 ± 0.03	201.8 ± 2.2
NT1 $(YDyErNb_{1/2}Ta_{1/2})O_7$	1.020	68.0 ± 16.8	2.49	1.11 ± 0.03	1.21 ± 0.03	226.5 ± 2.6
NT2 $(Dy_{1/3}Er_{1/3}Yb_{1/3})_3(Nb_{1/2}Ta_{1/2})O_7$	1.009	39.4 ± 14.6	1.48	1.10 ± 0.03	1.23 ± 0.03	223.9 ± 2.7
NT5 $(DyHoErNb)O_7$	1.048	68.4 ± 20.6	2.81	1.09 ± 0.03	1.28 ± 0.03	215.0 ± 2.5
NT20 $(Sc_{0.224}Er_{0.312}Tm_{0.244}Yb_{0.220})_3NbO_7$	1.029	38.7 ± 3.8	1.55	1.24 ± 0.02	1.51 ± 0.02	211.4 ± 1.9
NT21 $(Sc_{0.266}Dy_{0.248}Tm_{0.246}Yb_{0.240})_3NbO_7$	1.040	23.5 ± 2.1	0.63	1.24 ± 0.02	1.59 ± 0.02	214.1 ± 1.9
NT25 $(Sc_{0.22}Dy_{0.255}Ho_{0.262}Tm_{0.263})_3NbO_7$	1.052	51.8 ± 12.4	0.55	1.21 ± 0.03	1.34 ± 0.03	217.8 ± 1.7
Mixed Pyrochlore-Niobate/Tantalate (P-NT)						
P-NT20 75-25 $((Sm_{1/4}Eu_{1/4}Gd_{1/4}Yb_{1/4})_2(Ti_{1/2}Hf_{1/4}Zr_{1/4})_2O_7)_{0.75}((Sc_{0.224}Er_{0.312}Tm_{0.244}Yb_{0.220})_3NbO_7)_{0.25}$	0.965	29.6 ± 4.6	0.98	1.31 ± 0.02	1.59 ± 0.02	237.3 ± 2.1
P-NT20 50-50 $((Sm_{1/4}Eu_{1/4}Gd_{1/4}Yb_{1/4})_2(Ti_{1/2}Hf_{1/4}Zr_{1/4})_2O_7)_{0.50}((Sc_{0.224}Er_{0.312}Tm_{0.244}Yb_{0.220})_3NbO_7)_{0.50}$	0.986	37.1 ± 10.0	1.2	1.27 ± 0.02	1.51 ± 0.02	232.1 ± 2.4
P-NT20 10-90 $((Sm_{1/4}Eu_{1/4}Gd_{1/4}Yb_{1/4})_2(Ti_{1/2}Hf_{1/4}Zr_{1/4})_2O_7)_{0.10}((Sc_{0.224}Er_{0.312}Tm_{0.244}Yb_{0.220})_3NbO_7)_{0.90}$	1.021	10.0 ± 3.8	0.22	1.26 ± 0.02	1.56 ± 0.02	221.0 ± 2.1
P-NT21 98-2 $((Sm_{1/4}Eu_{1/4}Gd_{1/4}Yb_{1/4})_2(Ti_{1/2}Hf_{1/4}Zr_{1/4})_2O_7)_{0.98}((Sc_{0.266}Dy_{0.248}Tm_{0.246}Yb_{0.240})_3NbO_7)_{0.02}$	0.946	34.8 ± 3.1	0.81	1.34 ± 0.01	1.52 ± 0.01	241.1 ± 2.4

Table 7.2. Relevant corrosion performance values and thermomechanical properties for all 42 screened materials. *: multiphase material. Λ: optical basicity.

	Λ	Total interaction depth (μm)	Mass corrosion rate ($\mu m/h$)	k_{RT} ($W\ m^{-1}\ K^{-1}$)	$k_{800°C}$ ($W\ m^{-1}\ K^{-1}$)	E_{RT} (GPa)
		24 h	24 h			
P-NT21 90-10						
$((Sm_{1/4}Eu_{1/4}Gd_{1/4}Yb_{1/4})_2(Ti_{1/2}Hf_{1/4}Zr_{1/4})_2O_7)_{0.90}((Sc_{0.266}Dy_{0.248}Tm_{0.246}Yb_{0.240})_3NbO_7)_{0.10}$	0.953	39.5 ± 6.8	0.93	1.31 ± 0.01	1.51 ± 0.01	237.9 ± 2.4
P-NT21 10-90						
$((Sm_{1/4}Eu_{1/4}Gd_{1/4}Yb_{1/4})_2(Ti_{1/2}Hf_{1/4}Zr_{1/4})_2O_7)_{0.10}((Sc_{0.266}Dy_{0.248}Tm_{0.246}Yb_{0.240})_3NbO_7)_{0.90}$	1.030	43.8 ± 9.8	1.17	1.26 ± 0.01	1.55 ± 0.01	217.0 ± 1.9
P-NT25 98-2						
$((Sm_{1/4}Eu_{1/4}Gd_{1/4}Yb_{1/4})_2(Ti_{1/2}Hf_{1/4}Zr_{1/4})_2O_7)_{0.98}((Sc_{0.22}Dy_{0.255}Ho_{0.262}Tm_{0.263})_3NbO_7)_{0.02}$	0.946	15.7 ± 1.9	0.92	1.37 ± 0.05	1.63 ± 0.05	242.1 ± 2.2
P-NT25 90-10						
$((Sm_{1/4}Eu_{1/4}Gd_{1/4}Yb_{1/4})_2(Ti_{1/2}Hf_{1/4}Zr_{1/4})_2O_7)_{0.90}((Sc_{0.22}Dy_{0.255}Ho_{0.262}Tm_{0.263})_3NbO_7)_{0.10}$	0.954	15.9 ± 3.8	0.82	1.34 ± 0.05	1.60 ± 0.05	240.7 ± 2.1
P-NT25 75-25						
$((Sm_{1/4}Eu_{1/4}Gd_{1/4}Yb_{1/4})_2(Ti_{1/2}Hf_{1/4}Zr_{1/4})_2O_7)_{0.75}((Sc_{0.22}Dy_{0.255}Ho_{0.262}Tm_{0.263})_3NbO_7)_{0.25}$	0.971	38.9 ± 5.0	--	1.33 ± 0.05	1.59 ± 0.05	237.5 ± 2.0
P-NT25 50-50						
$((Sm_{1/4}Eu_{1/4}Gd_{1/4}Yb_{1/4})_2(Ti_{1/2}Hf_{1/4}Zr_{1/4})_2O_7)_{0.50}((Sc_{0.22}Dy_{0.255}Ho_{0.262}Tm_{0.263})_3NbO_7)_{0.50}$	0.998	58.0 ± 2.2	1.95	1.29 ± 0.05	1.57 ± 0.05	229.0 ± 2.0
P-NT25 25-75						
$((Sm_{1/4}Eu_{1/4}Gd_{1/4}Yb_{1/4})_2(Ti_{1/2}Hf_{1/4}Zr_{1/4})_2O_7)_{0.25}((Sc_{0.22}Dy_{0.255}Ho_{0.262}Tm_{0.263})_3NbO_7)_{0.75}$	1.025	35.8 ± 3.6	0.63	1.26 ± 0.04	1.64 ± 0.04	221.5 ± 2.1
P-NT25 10-90						
$((Sm_{1/4}Eu_{1/4}Gd_{1/4}Yb_{1/4})_2(Ti_{1/2}Hf_{1/4}Zr_{1/4})_2O_7)_{0.10}((Sc_{0.22}Dy_{0.255}Ho_{0.262}Tm_{0.263})_3NbO_7)_{0.90}$	1.041	28.5 ± 10.3	1.49	1.21 ± 0.04	1.60 ± 0.04	219.8 ± 2.5
P-NT25 2-98						
$((Sm_{1/4}Eu_{1/4}Gd_{1/4}Yb_{1/4})_2(Ti_{1/2}Hf_{1/4}Zr_{1/4})_2O_7)_{0.02}((Sc_{0.22}Dy_{0.255}Ho_{0.262}Tm_{0.263})_3NbO_7)_{0.98}$	1.050	35.3 ± 2.6	1.96	1.23 ± 0.04	1.74 ± 0.04	217.7 ± 2.0
P-NT31 50-50						
$((Sm_{0.25}Eu_{0.25}Gd_{0.25}Yb_{0.25})_2(Ti_{0.065}Hf_{0.234}Zr_{0.701})_2O_7)_{0.5}((Y_{0.266}Dy_{0.248}Tm_{0.246}Yb_{0.240})_3NbO_7)_{0.5}$	0.976	55.4 ± 23.1	2.14	1.36 ± 0.01	1.35 ± 0.01	247.0 ± 3.0

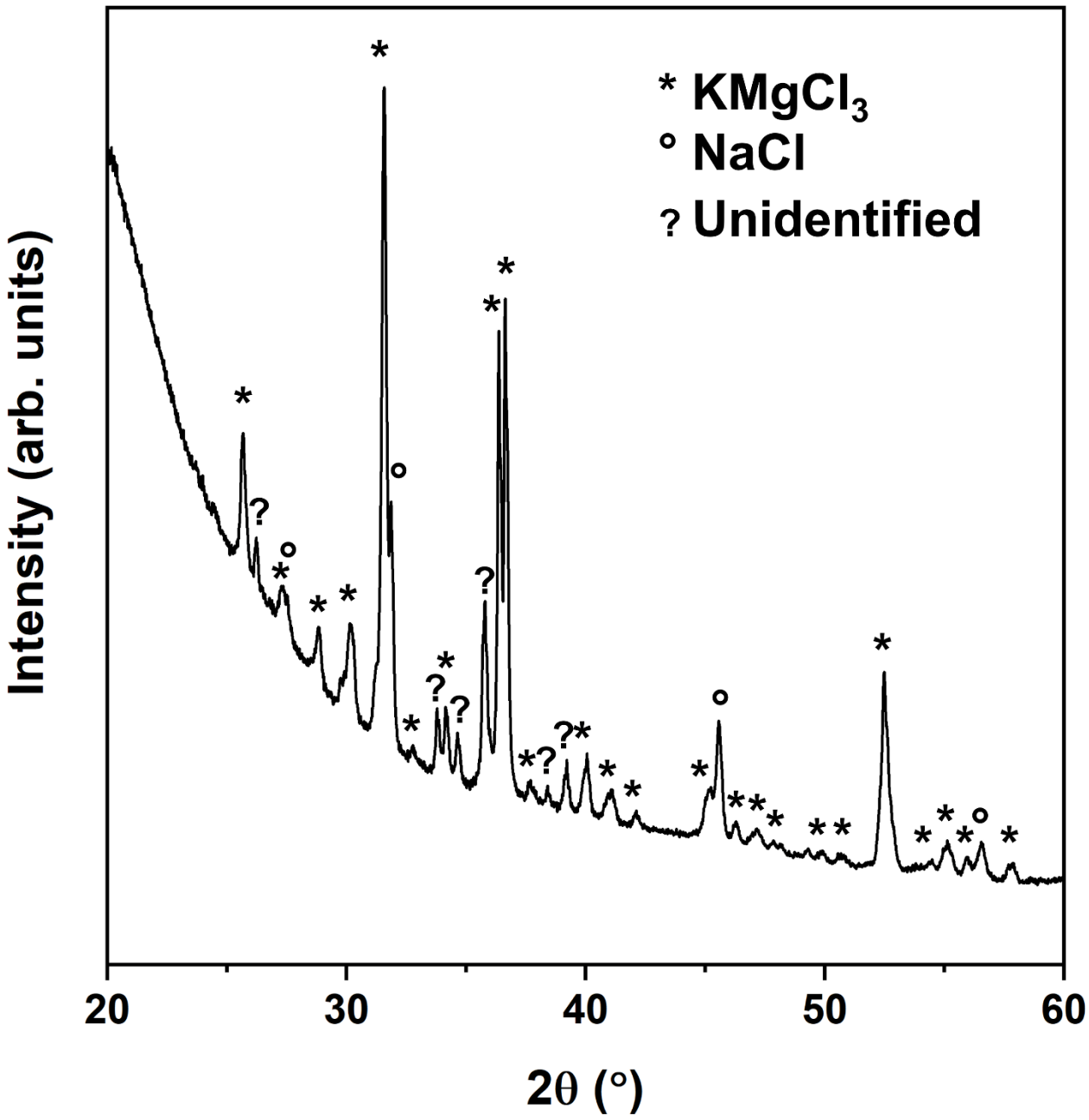

Figure 7.17. XRD pattern of $KMgCl_3$ salt used for corrosion testing. Large background comes from Kapton tape used to seal the powder.

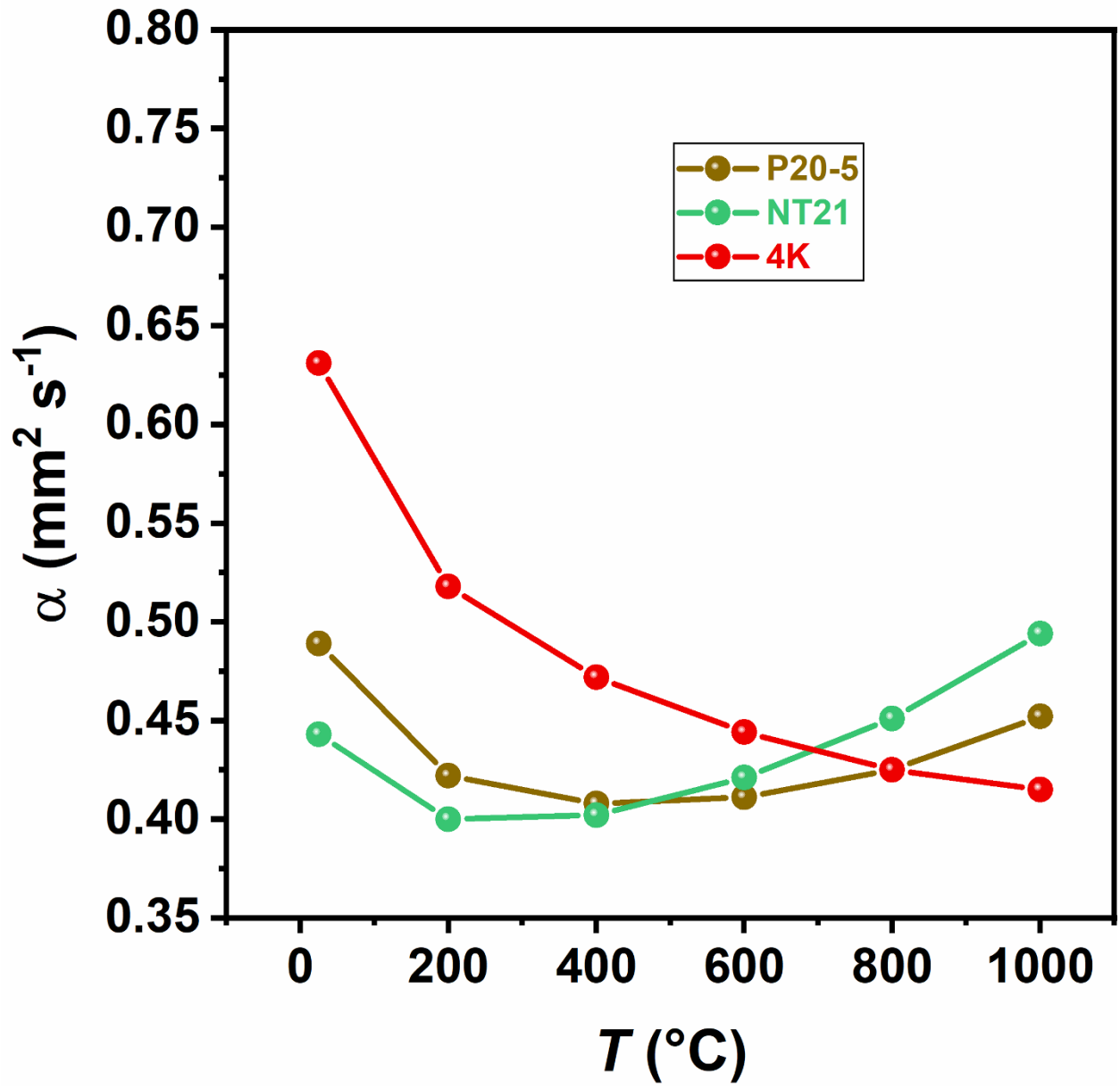

Figure 7.18. Temperature-dependent thermal diffusivity obtained from laser flash experiments used to calculate the thermal conductivity.

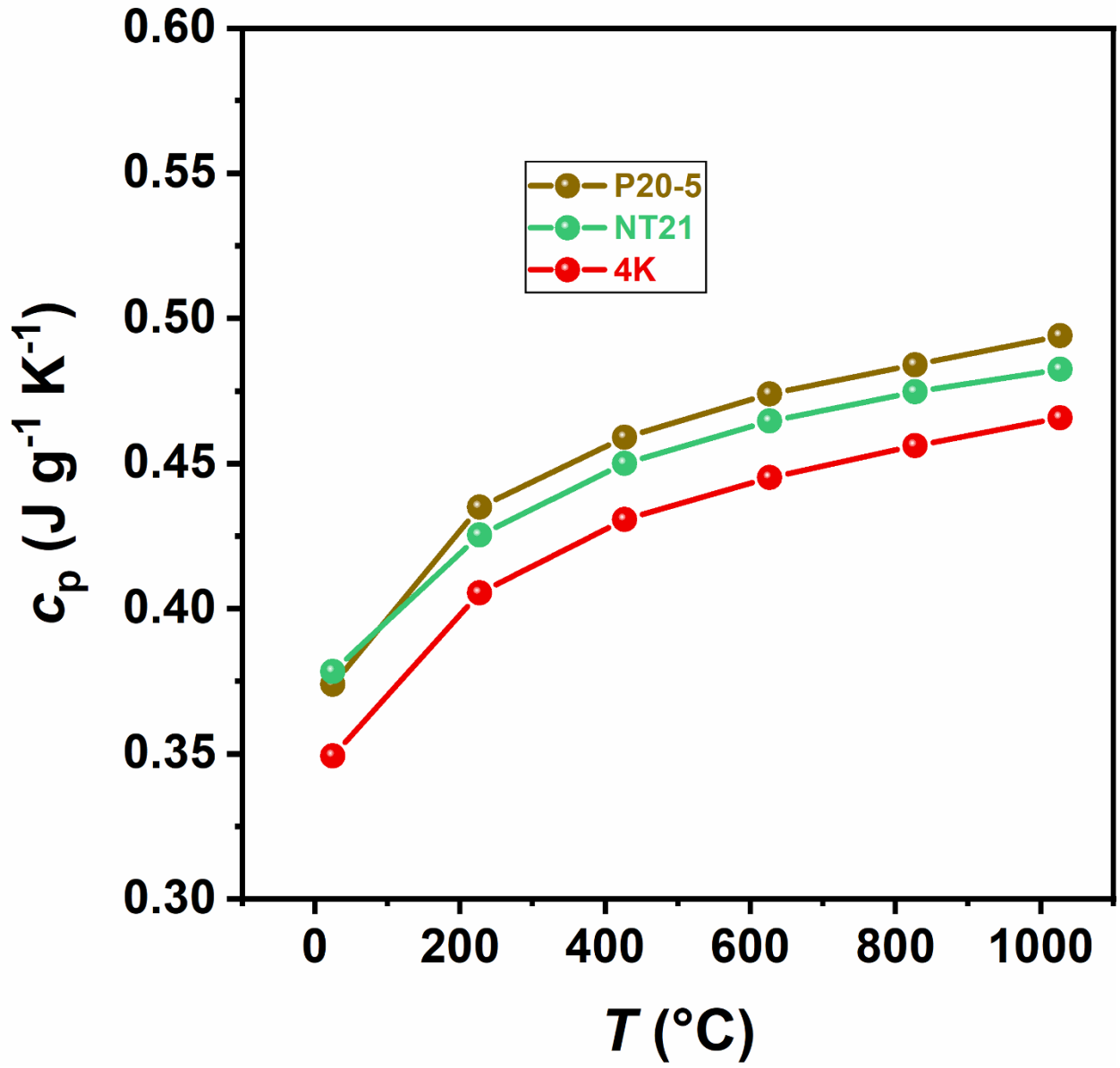

Figure 7.19. Temperature-dependent heat capacity used to calculate the thermal conductivity. Values are derived from Neumann-Kopp rule from tabulated measurements by I. Barin, Thermochemical Data of Pure Substances, VCH, Weinheim, 1995.

7.5 REFERENCES

[1] J.H. Perepezko, The hotter the engine, the better, Science (80-.). 326 (2009) 1068–1069. doi:10.1126/science.1179327.

[2] N.P. Padture, Advanced structural ceramics in aerospace propulsion, Nat. Mater. 15 (2016) 804–809. doi:10.1038/nmat4687.

[3] V. Lughi, V.K. Tolpygo, D.R. Clarke, Microstructural aspects of the sintering of thermal barrier coatings, Mater. Sci. Eng. A. 368 (2004) 212–221. doi:10.1016/j.msea.2003.11.018.

[4] V. Lughi, D.R. Clarke, High temperature aging of YSZ coatings and subsequent transformation at low temperature, Surf. Coatings Technol. 200 (2005) 1287–1291. doi:10.1016/j.surfcoat.2005.07.089.

[5] S. Guillot, A. Faik, A. Rakhmatullin, J. Lambert, E. Veron, P. Echegut, C. Bessada, N. Calvet, X. Py, Corrosion effects between molten salts and thermal storage material for concentrated solar power plants, Appl. Energy. 94 (2012) 174–181. doi:10.1016/j.apenergy.2011.12.057.

[6] Á.G. Fernández, L.F. Cabeza, Molten salt corrosion mechanisms of nitrate based thermal energy storage materials for concentrated solar power plants: A review, Sol. Energy Mater. Sol. Cells. 194 (2019) 160–165. doi:10.1016/j.solmat.2019.02.012.

[7] H.L. Zhang, J. Baeyens, J. Degrève, G. Cacères, Concentrated solar power plants: Review and design methodology, Renew. Sustain. Energy Rev. 22 (2013) 466–481. doi:10.1016/j.rser.2013.01.032.

[8] A. Hoshi, D.R. Mills, A. Bittar, T.S. Saitoh, Screening of high melting point phase change materials (PCM) in solar thermal concentrating technology based on CLFR, Sol. Energy. 79 (2005) 332–339. doi:10.1016/j.solener.2004.04.023.

[9] M.R. Winter, D.R. Clarke, Oxide materials with low thermal conductivity, J. Am. Ceram. Soc. 90 (2007) 533–540. doi:10.1111/j.1551-2916.2006.01410.x.

[10] D.R. Clarke, S.R. Phillpot, Thermal barrier coating materials, Mater. Today. 8 (2005) 22–29. doi:10.1016/S1369-7021(05)70934-2.

[11] D.L. Poerschke, R.W. Jackson, C.G. Levi, Silicate deposit degradation of engineered coatings in gas turbines: Progress toward models and materials solutions, Annu. Rev. Mater. Res. 47 (2017) 297–330. doi:10.1146/annurev-matsci-010917-105000.

[12] J.E. Indacochea, J.L. Smith, K.R. Litko, E.J. Karell, A.G. Raraz, High-Temperature Oxidation and Corrosion of Structural Materials in Molten Chlorides, Oxid. Met. 55 (2001) 1–16. doi:10.1023/A:1010333407304.

[13] J.C. Gomez-Vidal, R. Tirawat, Corrosion of alloys in a chloride molten salt (NaCl-LiCl) for solar thermal technologies, Sol. Energy Mater. Sol. Cells. 157 (2016) 234–244. doi:10.1016/j.solmat.2016.05.052.

[14] S.S. Raiman, R.T. Mayes, J.M. Kurley, R. Parrish, E. Vogli, Amorphous and partially-amorphous metal coatings for corrosion resistance in molten chloride salt, Sol. Energy Mater. Sol. Cells. 201 (2019) 110028. doi:10.1016/j.solmat.2019.110028.

[15] Y.J. Hsu, W.C. Chiang, J.K. Wu, Corrosion behavior of FeCoNiCrCux high-entropy alloys in 3.5% sodium chloride solution, Mater. Chem. Phys. 92 (2005) 112–117. doi:10.1016/j.matchemphys.2005.01.001.

[16] Y. Shi, B. Yang, P. Liaw, Corrosion-Resistant High-Entropy Alloys: A Review, Metals (Basel). 7 (2017) 43. doi:10.3390/met7020043.

[17] B. Gludovatz, A. Hohenwarter, K.V.S. Thurston, H. Bei, Z. Wu, E.P. George, R.O. Ritchie, Exceptional damage-tolerance of a medium-entropy alloy CrCoNi at cryogenic temperatures, Nat. Commun. 7 (2016) 1–8. doi:10.1038/ncomms10602.

[18] D.B. Miracle, O.N. Senkov, A critical review of high entropy alloys and related concepts, Acta Mater. 122 (2017) 448–511. doi:10.1016/j.actamat.2016.08.081.

[19] J. Gild, M. Samiee, J.L. Braun, T. Harrington, H. Vega, P.E. Hopkins, K. Vecchio, J. Luo, High-entropy fluorite oxides, J. Eur. Ceram. Soc. 38 (2018) 3578–3584. doi:10.1016/j.jeurceramsoc.2018.04.010.

[20] A.J. Wright, Q. Wang, C. Huang, A. Nieto, R. Chen, J. Luo, From high-entropy ceramics to compositionally-complex ceramics: A case study of fluorite oxides, J. Eur. Ceram. Soc. 40 (2020) 2120–2129. doi:10.1016/j.jeurceramsoc.2020.01.015.

[21] Y. Dong, K. Ren, Y. Lu, Q. Wang, J. Liu, Y. Wang, High-entropy environmental barrier coating for the ceramic matrix composites, J. Eur. Ceram. Soc. 39 (2019) 2574–2579. doi:10.1016/j.jeurceramsoc.2019.02.022.

[22] J.L. Braun, C.M. Rost, M. Lim, A. Giri, D.H. Olson, G.N. Kotsonis, G. Stan, D.W. Brenner, J.P. Maria, P.E. Hopkins, Charge-induced disorder controls the thermal conductivity of entropy-stabilized oxides, Adv. Mater. 30 (2018) 1805004. doi:10.1002/adma.201805004.

[23] A.J. Wright, Q. Wang, S.T. Ko, K.M. Chung, R. Chen, J. Luo, Size disorder as a descriptor for predicting reduced thermal conductivity in medium- and high-entropy pyrochlore oxides, Scr. Mater. 181 (2020) 76–81. doi:10.1016/j.scriptamat.2020.02.011.

[24] D.C. Tsai, M.J. Deng, Z.C. Chang, B.H. Kuo, E.C. Chen, S.Y. Chang, F.S. Shieu, Oxidation resistance and characterization of (AlCrMoTaTi)-Six-N coating deposited via magnetron sputtering, J. Alloys Compd. 647 (2015) 179–188. doi:10.1016/j.jallcom.2015.06.025.

[25] B. Ye, T. Wen, Y. Chu, High-temperature oxidation behavior of (Hf0.2Zr0.2Ta0.2Nb0.2Ti0.2)C high-entropy ceramics in air, J. Am. Ceram. Soc. 103 (2020) 500–507. doi:10.1111/jace.16725.

[26] W.J. Shen, M.H. Tsai, K.Y. Tsai, C.C. Juan, C.W. Tsai, J.W. Yeh, Y.S. Chang, Superior oxidation resistance of (Al0.34Cr0.22Nb 0.11Si0.11Ti0.22)50N50 high-entropy nitride, J. Electrochem. Soc. 160 (2013) 531–535. doi:10.1149/2.028311jes.

[27] J. Gild, Y. Zhang, T. Harrington, S. Jiang, T. Hu, M.C. Quinn, W.M. Mellor, N. Zhou, K. Vecchio, J. Luo, High-entropy metal diborides: A new class of high-entropy materials and a new type of ultrahigh temperature ceramics, Sci. Rep. 6 (2016) 37946. doi:10.1038/srep37946.

[28] X. Ren, Z. Tian, J. Zhang, J. Wang, Equiatomic quaternary (Y1/4Ho1/4Er1/4Yb1/4)2SiO5 silicate: A perspective multifunctional thermal and environmental barrier coating material, Scr. Mater. 168 (2019) 47–50. doi:10.1016/j.scriptamat.2019.04.018.

[29] L. Sun, Y. Luo, Z. Tian, T. Du, X. Ren, J. Li, W. Hu, J. Zhang, J. Wang, High temperature corrosion of (Er0.25Tm0.25Yb0.25Lu0.25)2Si2O7 environmental barrier coating material subjected to water vapor and molten calcium–magnesium–aluminosilicate (CMAS), Corros. Sci. (2020) 108881. doi:10.1016/j.corsci.2020.108881.

[30] A.J. Wright, C. Huang, M.J. Walock, A. Ghoshal, M. Murugan, J. Luo, Sand corrosion, thermal expansion, and ablation of medium- and high-entropy compositionally complex fluorite oxides, J. Am. Ceram. Soc. (2020). doi:10.1111/jace.17448.

[31] C.A. Schneider, W.S. Rasband, K.W. Eliceiri, NIH Image to ImageJ: 25 years of image analysis, Nat. Methods. 9 (2012) 671–675. doi:10.1038/nmeth.2089.

[32] B.H. Toby, R.B. Von Dreele, GSAS-II: The genesis of a modern open-source all purpose crystallography software package, J. Appl. Crystallogr. 46 (2013) 544–549. doi:10.1107/S0021889813003531.

[33] ASTM International, C373-18 Standard Test Methods for Determination of Water Absorption and Associated Properties by Vacuum Method for Pressed Ceramic Tiles and Glass Tiles and Boil Method for Extruded Ceramic Tiles and Non-tile Fired Ceramic Whiteware Products, West Conshohocken, PA, 2018. doi:10.1520/C0373-16.2.

[34] ASTM International, C1198-20 Standard Test Method for Dynamic Young's Modulus, Shear Modulus, and Poisson's Ratio for Advanced Ceramics by Sonic Resonance, West Conshohocken, PA, 2020. doi:10.1520/C1198-20.

[35] I. Barin, Thermochemical Data of Pure Substances, VCH, Weinheim, 1995. doi:10.1016/s0165-2427(96)05632-2.

[36] R.R. Reddy, Y. Nazeer Ahammed, K. Rama Gopal, P. Abdul Azeem, T.V.R. Rao, Correlation between optical basicity, electronegativity and electronic polarizability for some oxides and oxysalts, Opt. Mater. (Amst). 12 (1999) 425–428. doi:10.1016/S0925-3467(98)00083-4.

[37] J.A. Duffy, M.D. Ingram, Establishment of an optical scale for lewis basicity in inorganic oxyacids, molten salts, and glasses, J. Am. Chem. Soc. 93 (1971) 6448–6454. doi:10.1021/ja00753a019.

[38] G.C.C. Costa, D. Zhu, M.J. Kulis, W.A. Acosta, A. Ghoshal, Reactivity between rare-earth oxides based thermal barrier coatings and a silicate melt, J. Am. Ceram. Soc. 101 (2018) 3674–3693. doi:10.1111/jace.15516.

[39] Z. Tian, J. Zhang, L. Zheng, W. Hu, X. Ren, Y. Lei, J. Wang, General trend on the phase stability and corrosion resistance of rare earth monosilicates to molten calcium–magnesium–aluminosilicate at 1300°C, Corros. Sci. 148 (2019) 281–292. doi:10.1016/j.corsci.2018.12.032.

[40] A.R. Krause, B.S. Senturk, H.F. Garces, G. Dwivedi, A.L. Ortiz, S. Sampath, N.P. Padture, 2ZrO2·Y2O3 thermal barrier coatings resistant to degradation by molten CMAS: Part I, Optical basicity considerations and processing, J. Am. Ceram. Soc. 97 (2014) 3943–3949. doi:10.1111/jace.13210.

[41] N.P. Padture, Environmental degradation of high-temperature protective coatings for ceramic-matrix composites in gas-turbine engines, Npj Mater. Degrad. 3 (2019). doi:10.1038/s41529-019-0075-4.

[42] S. Krämer, J. Yang, C.G. Levi, Infiltration-inhibiting reaction of gadolinium zirconate thermal barrier coatings with CMAS melts, J. Am. Ceram. Soc. 91 (2008) 576–583. doi:10.1111/j.1551-2916.2007.02175.x.

[43] D.L. Poerschke, C.G. Levi, Effects of cation substitution and temperature on the interaction between thermal barrier oxides and molten CMAS, J. Eur. Ceram. Soc. 35 (2015) 681–691. doi:10.1016/j.jeurceramsoc.2014.09.006.

[44] B. Pieraggi, Calculations of parabolic reaction rate constants, Oxid. Met. 27 (1987) 177–185. doi:10.1007/BF00667057.

[45] E.R. Andrievskaya, Phase equilibria in the refractory oxide systems of zirconia, hafnia and yttria with rare-earth oxides, J. Eur. Ceram. Soc. 28 (2008) 2363–2388. doi:10.1016/j.jeurceramsoc.2008.01.009.

[46] D.G. Cahill, S.K. Watson, R.O. Pohl, Lower limit to the thermal conductivity of disordered crystals, Phys. Rev. B. 46 (1992) 6131–6140. doi:10.1103/PhysRevB.46.6131.

[47] W. Pan, S.R. Phillpot, C. Wan, A. Chernatynskiy, Z. Qu, Low thermal conductivity oxides, MRS Bull. 37 (2012) 917–922. doi:10.1557/mrs.2012.234.

[48] R. Vassen, X. Cao, F. Tietz, D. Basu, D. Stöver, Zirconates as New Materials for Thermal Barrier Coatings, J. Am. Ceram. Soc. 83 (2004) 2023–2028. doi:10.1111/j.1151-2916.2000.tb01506.x.

SUMMARY AND OUTLOOK

Over 100 novel high-entropy ceramics have been added to the blossoming field along with useful thermomechanical properties.

In Chapter 2, it is proposed to expand the standard high-entropy ceramics to include medium-entropy ceramics (MECs). MECs included non-equimolar compositions with five components distributed on one site or three-or four-component compositions in equimolar compositions. Leading the field in this direction, we demonstrate several novel compositions similar to yttria-stabilized zirconia yet show greatly reduced thermal conductivities.

In Chapter 3, another fluorite system is investigated, RE_3NbO_7. This class of materials represents ultra-low k and were build off the model composition of Dy_3NbO_7, which has a room temperature thermal conductivity approaching $1\ W\ m^{-1}\ K^{-1}$. 35 new high-entropy compositions were added to this class that all demonstrate low thermal conductivities. Additionally, a trend is found that when the size of the rare-earth cations is large, the thermal conductivity is lower. We explored this with neutron diffraction and modeling approaches and found the larger specimens have a higher tendency for short-range ordering, which effectively reduces the domain size. The domain size approaches the Ioffe-Regel limit (phonon mean free path $\sim$ lattice parameter) and transitions the predominant conduction mechanism to diffusons (instead of phonons or propagons). Lastly, the collapsed cells reveal a strong dependence of the O sublattices structure to be on the chemistry.

In Chapter 4, the pyrochlore structure was investigated. This related to the fluorite cell by being a $2 \times 2 \times 2$ ordered variant, which is stable when the ionic radius of the 3+ cations is more than 1.46 times larger than the 4+ cations. Within this class, we attributed over 20 new high-entropy compositions. We also found the root mean square size disorder of the two sites (A and

B) to accurately predict the room temperature thermal conductivity trend. Interestingly, the compositions containing Ti exhibited the lowest thermal conductivities and high moduli. Recent reports have determined Ti has a higher tendency for short-range ordering in the pyrochlore structure and locally distorts the lattice to form an orthorhombic structure.

In Chapter 5, the rare-earth niobates from Chapter 3 and the pyrochlores from Chapter 4 were mixed to for undenary compositions (11 cations + O) look at the order disorder transition. The compositions were uniquely designed so that lattice and density mismatch were negligible (only achievable through high entropy effects). The mixed composition displayed a single phase transition from the ordered pyrochlore to the disordered fluorite. A unique property found, is that the thermomechanical properties significantly deviate from the rule of mixtures (RoM). The Young's modulus is enhanced in all mixing ratios above the RoM presumably due to short-range ordering effects.

In Chapter 6, the corrosion performance of the MECs investigated in Chapter 2 against molten silicates was looked at. The materials were placed in contact with a synthetic sand and annealed for $24\ h$ at $1200 - 1500℃$. The harsh environment leads to significant corrosion in all ceramics, but the tendency for reaction is more prevalent as the concentration of the 3+ rare-earth stabilizers increases. This is one of the first studies on performance of MECs and HECs in molten silicate environments, so we provided an initial baseline. Additionally, the presence of significant reaction may be beneficial if our materials were tested as a coating since the reaction products can fill the pores and provide a dense passivating layer.

In Chapter, 7 we gathered approximately 40 specimens from all the previous chapters and subjected them to a molten chloride salt (85 wt. % $KMgCl_3$ and 15 wt. % NaCl). at $800℃$ for $24 - 1000\ h$. We compare their performance against a Haynes 230 structural alloy. It was found

that the structural alloy performs better than nearly all specimens at $24\ h$, which all tended to form oxide reaction products. However, we tested a few specimens at longer times (up to $1000\ h$) so to investigate the kinetics. Interestingly, the MECs and HECs all perform better than the structural alloy at times greater than $100\ h$. This is attributed to linear kinetics experience by the structural alloy due to the absence of any reaction, and thus passivating layer. The ceramics on the other hand all reaction to form a reaction layer that grows and densifies with time. This forces the salt to diffuse through the passivating layer to continue corrosion. This describes a parabolic rate constant, which is similar to the kinetics experienced in passivating layers in metals.

Overall, over 100 new compositions have been detailed, which likely represents one of the largest studies conduct on high-entropy ceramics so far. Since the compositional space is so vast in these materials, I set out to screen numerous compositions across multiple (but related) classes to identify simple descriptors that may be used to predict useful properties such as thermal conductivity. Overall size disorder was found to be the best general descriptor. However, size disorder is likely only a first-order approximation and may serve as a proxy for short-range ordering, which would be the direct phenomenon affecting the observed thermal conductivity. I have provided a large dataset, which may help computational work get a quick start in predicting new useful materials and may also fit the data with more sophisticated models such as machine learning and deep neural networks. Lastly, the corrosion performance presented here is to serve as a baseline to be built from and expanded to other material systems.

REFERENCES

[1] J.H. Perepezko, The hotter the engine, the better, Science (80-.). 326 (2009) 1068–1069. doi:10.1126/science.1179327.

[2] V. Lughi, V.K. Tolpygo, D.R. Clarke, Microstructural aspects of the sintering of thermal barrier coatings, Mater. Sci. Eng. A. 368 (2004) 212–221. doi:10.1016/j.msea.2003.11.018.

[3] V. Lughi, D.R. Clarke, High temperature aging of YSZ coatings and subsequent transformation at low temperature, Surf. Coatings Technol. 200 (2005) 1287–1291. doi:10.1016/j.surfcoat.2005.07.089.

[4] M.G. Dunn, A.J. Baran, J. Miatech, Operation of gas turbine engines in volcanic ash clouds, J. Eng. Gas Turbines Power. 118 (1996) 724–731. doi:10.1115/1.2816987.

[5] C.G. Levi, J.W. Hutchinson, M.H. Vidal-Sétif, C.A. Johnson, Environmental degradation of thermal-barrier coatings by molten deposits, MRS Bull. 37 (2012) 932–941. doi:10.1557/mrs.2012.230.

[6] A. Ghoshal, M. Murugan, M.J. Walock, A. Nieto, B.D. Barnett, M.S. Pepi, J.J. Swab, D. Zhu, K.A. Kerner, C.R. Rowe, C.Y. Shiao, D.A. Hopkins, G.A. Gazonas, Molten particulate impact on tailored thermal barrier coatings for gas turbine engine, J. Eng. Gas Turbines Power. 140 (2018) 022601. doi:10.1115/1.4037599.

[7] L. Li, N. Hitchman, J. Knapp, Failure of thermal barrier coatings subjected to CMAS attack, J. Therm. Spray Technol. 19 (2010) 148–155. doi:10.1007/s11666-009-9356-8.

[8] J. Wu, H. Guo, Y. Gao, S. Gong, Microstructure and thermo-physical properties of yttria stabilized zirconia coatings with CMAS deposits, J. Eur. Ceram. Soc. 31 (2011) 1881–1888. doi:10.1016/j.jeurceramsoc.2011.04.006.

[9] G. Pujol, F. Ansart, J.P. Bonino, A. Malié, S. Hamadi, Step-by-step investigation of degradation mechanisms induced by CMAS attack on YSZ materials for TBC applications, Surf. Coatings Technol. 237 (2013) 71–78. doi:10.1016/j.surfcoat.2013.08.055.

[10] J.W. Yeh, S.K. Chen, S.J. Lin, J.Y. Gan, T.S. Chin, T.T. Shun, C.H. Tsau, S.Y. Chang, Nanostructured high-entropy alloys with multiple principal elements: novel alloy design concepts and outcomes, Adv. Eng. Mater. 6 (2004) 299–303. doi:10.1002/adem.200300567.

[11] B. Cantor, I.T.H. Chang, P. Knight, A.J.B. Vincent, Microstructural development in equiatomic multicomponent alloys, Mater. Sci. Eng. A. 375 (2004) 213–218. doi:10.1016/j.msea.2003.10.257.

[12] D.B. Miracle, O.N. Senkov, A critical review of high entropy alloys and related concepts, Acta Mater. 122 (2017) 448–511. doi:10.1016/j.actamat.2016.08.081.

[13] D. Ma, M. Yao, K.G. Pradeep, C.C. Tasan, H. Springer, D. Raabe, Phase stability of non-equiatomic CoCrFeMnNi high entropy alloys, Acta Mater. 98 (2015) 288–296. doi:10.1016/j.actamat.2015.07.030.

[14] F. Otto, A. Dlouhý, C. Somsen, H. Bei, G. Eggeler, E.P. George, The influences of temperature and microstructure on the tensile properties of a CoCrFeMnNi high-entropy alloy, Acta Mater. 61 (2013) 5743–5755. doi:10.1016/j.actamat.2013.06.018.

[15] E.P. George, D. Raabe, R.O. Ritchie, High-entropy alloys, Nat. Rev. Mater. 4 (2019) 515–534. doi:10.1038/s41578-019-0121-4.

[16] B. Gludovatz, A. Hohenwarter, K.V.S. Thurston, H. Bei, Z. Wu, E.P. George, R.O. Ritchie, Exceptional damage-tolerance of a medium-entropy alloy CrCoNi at cryogenic temperatures, Nat. Commun. 7 (2016) 1–8. doi:10.1038/ncomms10602.

[17] A. Gali, E.P. George, Tensile properties of high- and medium-entropy alloys, Intermetallics. 39 (2013) 74–78. doi:10.1016/j.intermet.2013.03.018.

[18] Z. Li, D. Raabe, Strong and ductile non-equiatomic high-entropy alloys: Design, processing, microstructure, and mechanical properties, Jom. 69 (2017) 2099–2106. doi:10.1007/s11837-017-2540-2.

[19] C.M. Rost, E. Sachet, T. Borman, A. Moballegh, E.C. Dickey, D. Hou, J.L. Jones, S. Curtarolo, J.P. Maria, Entropy-stabilized oxides, Nat. Commun. 6 (2015) 1–8. doi:10.1038/ncomms9485.

[20] J. Gild, Y. Zhang, T. Harrington, S. Jiang, T. Hu, M.C. Quinn, W.M. Mellor, N. Zhou, K. Vecchio, J. Luo, High-entropy metal diborides: A new class of high-entropy materials and a new type of ultrahigh temperature ceramics, Sci. Rep. 6 (2016) 37946. doi:10.1038/srep37946.

[21] Y. Zhang, Z. Bin Jiang, S.K. Sun, W.M. Guo, Q.S. Chen, J.X. Qiu, K. Plucknett, H.T. Lin, Microstructure and mechanical properties of high-entropy borides derived from boro/carbothermal reduction, J. Eur. Ceram. Soc. 39 (2019) 3920–3924. doi:10.1016/j.jeurceramsoc.2019.05.017.

[22] Y. Zhang, W.M. Guo, Z. Bin Jiang, Q.Q. Zhu, S.K. Sun, Y. You, K. Plucknett, H.T. Lin, Dense high-entropy boride ceramics with ultra-high hardness, Scr. Mater. 164 (2019) 135–139. doi:10.1016/j.scriptamat.2019.01.021.

[23] J. Gild, K. Kaufmann, K. Vecchio, J. Luo, Reactive flash spark plasma sintering of high-entropy ultrahigh temperature ceramics, Scr. Mater. 170 (2019) 106–110.

doi:10.1016/j.scriptamat.2019.05.039.

[24] J. Zhou, J. Zhang, F. Zhang, B. Niu, L. Lei, W. Wang, High-entropy carbide: A novel class of multicomponent ceramics, Ceram. Int. 44 (2018) 22014–22018. doi:10.1016/j.ceramint.2018.08.100.

[25] X. Han, V. Girman, R. Sedlák, J. Dusza, E.G. Castle, Y. Wang, M. Reece, C. Zhang, Improved creep resistance of high entropy transition metal carbides, J. Eur. Ceram. Soc. (2019).

[26] T.J. Harrington, J. Gild, P. Sarker, C. Toher, C.M. Rost, O.F. Dippo, C. McElfresh, K. Kaufmann, E. Marin, L. Borowski, P.E. Hopkins, J. Luo, S. Curtarolo, D.W. Brenner, K.S. Vecchio, Phase stability and mechanical properties of novel high entropy transition metal carbides, Acta Mater. 166 (2019) 271–280. doi:10.1016/j.actamat.2018.12.054.

[27] X. Yan, L. Constantin, Y. Lu, J.F. Silvain, M. Nastasi, B. Cui, (Hf0.2Zr0.2Ta0.2Nb0.2Ti0.2)C high-entropy ceramics with low thermal conductivity, J. Am. Ceram. Soc. 101 (2018) 4486–4491. doi:10.1111/jace.15779.

[28] E. Castle, T. Csanádi, S. Grasso, J. Dusza, M. Reece, Processing and properties of high-entropy ultra-high temperature carbides, Sci. Rep. 8 (2018) 8609. doi:10.1038/s41598-018-26827-1.

[29] C. Heng, X. Huimin, D. Fu-Zhi, L. Jiachen, Z. Yanchun, High entropy (Yb0.25Y0.25Lu0.25Er0.25)2SiO5 with strong anisotropy in thermal expansion, J. Mater. Sci. Technol. (2019). doi:10.1016/j.jmst.2019.07.022.

[30] X. Ren, Z. Tian, J. Zhang, J. Wang, Equiatomic quaternary (Y1/4Ho1/4Er1/4Yb1/4)2SiO5 silicate: A perspective multifunctional thermal and environmental barrier coating material, Scr. Mater. 168 (2019) 47–50. doi:10.1016/j.scriptamat.2019.04.018.

[31] L. Sun, Y. Luo, Z. Tian, T. Du, X. Ren, J. Li, W. Hu, J. Zhang, J. Wang, High temperature corrosion of (Er0.25Tm0.25Yb0.25Lu0.25)2Si2O7 environmental barrier coating material subjected to water vapor and molten calcium–magnesium–aluminosilicate (CMAS), Corros. Sci. (2020) 108881. doi:10.1016/j.corsci.2020.108881.

[32] L. Sun, Y. Luo, X. Ren, Z. Gao, T. Du, Z. Wu, J. Wang, A multicomponent γ-type (Gd1/6Tb1/6Dy1/6Tm1/6Yb1/6Lu1/6)2Si2O7 disilicate with outstanding thermal stability, Mater. Res. Lett. 8 (2020) 424–430. doi:10.1080/21663831.2020.1783007.

[33] J. Gild, J. Braun, K. Kaufmann, E. Marin, T. Harrington, P. Hopkins, K. Vecchio, J. Luo, A high-entropy silicide: (Mo0.2Nb0.2Ta0.2Ti0.2W0.2)Si2, J. Mater. 5 (2019) 337–343. doi:10.1016/j.jmat.2019.03.002.

[34] Y. Qin, J.X. Liu, F. Li, X. Wei, H. Wu, G.J. Zhang, A high entropy silicide by reactive spark plasma sintering, J. Adv. Ceram. 8 (2019) 148–152. doi:10.1007/s40145-019-0319-

3.

[35] Y. Qin, J.-C. Wang, J.-X. Liu, X.-F. Wei, F. Li, G.-J. Zhang, C. Jing, J. Zhao, H. Wu, High-entropy silicide ceramics developed from (TiZrNbMoW)Si2 formulation doped with aluminum, J. Eur. Ceram. Soc. (2020). doi:10.1016/j.jeurceramsoc.2020.02.059.

[36] N. Zhou, S. Jiang, T. Huang, M. Qin, T. Hu, J. Luo, Single-phase high-entropy intermetallic compounds (HEICs): bridging high-entropy alloys and ceramics, Sci. Bull. 64 (2019) 856–864. doi:10.1016/j.scib.2019.05.007.

[37] X. Chen, Y. Wu, High-entropy transparent fluoride laser ceramics, J. Am. Ceram. Soc. 103 (2019) 750–756. doi:10.1111/jace.16842.

[38] T. Wang, H. Chen, Z. Yang, J. Liang, S. Dai, High-entropy perovskite fluorides: A new platform for oxygen evolution catalysis, J. Am. Chem. Soc. (2020). doi:10.1021/jacs.9b12377.

[39] Z. Zhao, H. Chen, H. Xiang, F.Z. Dai, X. Wang, Z. Peng, Y. Zhou, (La0.2Ce0.2Nd0.2Sm0.2Eu0.2)PO4: A high-entropy rare-earth phosphate monazite ceramic with low thermal conductivity and good compatibility with Al2O3, J. Mater. Sci. Technol. 35 (2019) 2892–2896. doi:10.1016/j.jmst.2019.08.012.

[40] Z. Zhao, H. Xiang, F.Z. Dai, Z. Peng, Y. Zhou, (TiZrHf)P2O7: An equimolar multicomponent or high entropy ceramic with good thermal stability and low thermal conductivity, J. Mater. Sci. Technol. 35 (2019) 2227–2231. doi:10.1016/j.jmst.2019.05.030.

[41] A. Sarkar, Q. Wang, A. Schiele, M.R. Chellali, S.S. Bhattacharya, D. Wang, T. Brezesinski, H. Hahn, L. Velasco, B. Breitung, High-entropy oxides: Fundamental aspects and electrochemical properties, Adv. Mater. 31 (2019) 1806236. doi:10.1002/adma.201806236.

[42] N. Qiu, H. Chen, Z. Yang, S. Sun, Y. Wang, Y. Cui, A high entropy oxide (Mg0.2Co0.2Ni0.2Cu0.2Zn0.2O) with superior lithium storage performance, J. Alloys Compd. 777 (2019) 767–774. doi:10.1016/j.jallcom.2018.11.049.

[43] Q. Wang, A. Sarkar, Z. Li, Y. Lu, L. Velasco, S.S. Bhattacharya, T. Brezesinski, H. Hahn, B. Breitung, High entropy oxides as anode material for Li-ion battery applications: A practical approach, Electrochem. Commun. 100 (2019) 121–125. doi:10.1016/j.elecom.2019.02.001.

[44] A. Sarkar, L. Velasco, D. Wang, Q. Wang, G. Talasila, L. de Biasi, C. Kübel, T. Brezesinski, S.S. Bhattacharya, H. Hahn, B. Breitung, High entropy oxides for reversible energy storage, Nat. Commun. 9 (2018) 3400. doi:10.1038/s41467-018-05774-5.

[45] B. Breitung, Q. Wang, A. Schiele, Đ. Tripković, A. Sarkar, L. Velasco, D. Wang, S.S.

Bhattacharya, H. Hahn, Breze, Gassing behavior of high-entropy oxide anode and oxyfluoride cathode probed using differential electrochemical mass spectrometry, Batter. Supercaps. (n.d.). doi:10.1002/batt.202000010.

[46] P. Sarker, T. Harrington, C. Toher, C. Oses, M. Samiee, J.P. Maria, D.W. Brenner, K.S. Vecchio, S. Curtarolo, High-entropy high-hardness metal carbides discovered by entropy descriptors, Nat. Commun. 9 (2018) 1–10. doi:10.1038/s41467-018-07160-7.

[47] B. Ye, T. Wen, D. Liu, Y. Chu, Oxidation behavior of (Hf0.2Zr0.2Ta0.2Nb0.2Ti0.2)C high-entropy ceramics at 1073-1473 K in air, Corros. Sci. 153 (2019) 327–332. doi:10.1016/j.corsci.2019.04.001.

[48] B. Ye, T. Wen, Y. Chu, High-temperature oxidation behavior of (Hf0.2Zr0.2Ta0.2Nb0.2Ti0.2)C high-entropy ceramics in air, J. Am. Ceram. Soc. 103 (2020) 500–507. doi:10.1111/jace.16725.

[49] H. Zhang, D. Hedman, P. Feng, G. Han, F. Akhtar, A high-entropy B4(HfMo2TaTi)C and SiC ceramic composite, Dalt. Trans. 48 (2019) 5161–5167. doi:10.1039/c8dt04555k.

[50] A.G. de la Obra, M.A. Avilés, Y. Torres, E. Chicardi, F.J. Gotor, A new family of cermets: Chemically complex but microstructurally simple, Int. J. Refract. Met. Hard Mater. 63 (2017) 17–25. doi:10.1016/j.ijrmhm.2016.04.011.

[51] J. Gild, A. Wright, K. Quiambao-tomko, M. Qin, A. John, S. Hoque, J.L. Braun, B. Bloomfield, D. Martinez, T. Harrington, K. Vecchio, P.E. Hopkins, J. Luo, Thermal conductivity and hardness of three single-phase high-entropy metal diborides fabricated by borocarbothermal reduction and spark plasma sintering, Ceram. Int. (2019). doi:10.1016/j.ceramint.2019.11.186.

[52] Z. Fan, H. Wang, Y. Wu, X. Liu, Z. Lu, Thermoelectric performance of PbSnTeSe high-entropy alloys, Mater. Res. Lett. 5 (2017) 187–194. doi:10.1080/21663831.2016.1244116.

[53] Z. Fan, H. Wang, Y. Wu, X.J. Liu, Z.P. Lu, Thermoelectric high-entropy alloys with low lattice thermal conductivity, RSC Adv. 6 (2016) 52164–52170. doi:10.1039/c5ra28088e.

[54] J.L. Braun, C.M. Rost, M. Lim, A. Giri, D.H. Olson, G.N. Kotsonis, G. Stan, D.W. Brenner, J.P. Maria, P.E. Hopkins, Charge-induced disorder controls the thermal conductivity of entropy-stabilized oxides, Adv. Mater. 30 (2018) 1805004. doi:10.1002/adma.201805004.

[55] K. Chen, X. Pei, L. Tang, H. Cheng, Z. Li, C. Li, X. Zhang, L. An, A five-component entropy-stabilized fluorite oxide, J. Eur. Ceram. Soc. 38 (2018) 4161–4164. doi:10.1016/j.jeurceramsoc.2018.04.063.

[56] R.-Z. Zhang, F. Gucci, H. Zhu, K. Chen, M.J. Reece, Data-driven design of ecofriendly thermoelectric high-entropy sulfides, Inorg. Chem. 57 (2018) 13027–13033.

doi:10.1021/acs.inorgchem.8b02379.

[57] H. Chen, H. Xiang, F.Z. Dai, J. Liu, Y. Lei, J. Zhang, Y. Zhou, High porosity and low thermal conductivity high entropy (Zr0.2Hf0.2Ti0.2Nb0.2Ta0.2)C, J. Mater. Sci. Technol. 35 (2019) 1700–1705. doi:10.1016/j.jmst.2019.04.006.

[58] J. Gild, M. Samiee, J.L. Braun, T. Harrington, H. Vega, P.E. Hopkins, K. Vecchio, J. Luo, High-entropy fluorite oxides, J. Eur. Ceram. Soc. 38 (2018) 3578–3584. doi:10.1016/j.jeurceramsoc.2018.04.010.

[59] K. Ren, Q. Wang, G. Shao, X. Zhao, Y. Wang, Multicomponent high-entropy zirconates with comprehensive properties for advanced thermal barrier coating, Scr. Mater. 178 (2020) 382–386. doi:10.1016/j.scriptamat.2019.12.006.

[60] Z. Zhao, H. Xiang, F.-Z. Dai, Z. Peng, Y. Zhou, (La0.2Ce0.2Nd0.2Sm0.2Eu0.2)2Zr2O7: A novel high-entropy ceramic with low thermal conductivity and sluggish grain growth rate, J. Mater. Sci. Technol. 35 (2019) 2647–2651. doi:10.1016/j.jmst.2019.05.054.

[61] F. Li, L. Zhou, J.-X. Liu, Y. Liang, G.-J. Zhang, High-entropy pyrochlores with low thermal conductivity for thermal barrier coating materials, J. Adv. Ceram. 8 (2019) 576–582. doi:10.1007/s40145-019-0342-4.

[62] R. Liu, H. Chen, K. Zhao, Y. Qin, B. Jiang, T. Zhang, G. Sha, X. Shi, C. Uher, W. Zhang, L. Chen, Entropy as a gene-like performance indicator promoting thermoelectric materials, Adv. Mater. 29 (2017) 1702712. doi:10.1002/adma.201702712.

[63] S. Shin, Q. Wang, J. Luo, R. Chen, Advanced materials for high-temperature thermal transport, Adv. Funct. Mater. (2019) 1904815. doi:10.1002/adfm.201904815.

[64] F. DeAngelis, M.G. Muraleedharan, J. Moon, H.R. Seyf, A.J. Minnich, A.J.H. McGaughey, A. Henry, Thermal transport in disordered materials, Nanoscale Microscale Thermophys. Eng. 23 (2019) 81–116. doi:10.1080/15567265.2018.1519004.

[65] W. Zhou, Y. Cheng, K. Chen, G. Xie, T. Wang, G. Zhang, Thermal conductivity of amorphous materials, Adv. Funct. Mater. (2019) 1903829. doi:10.1002/adfm.201903829.

[66] J. Callaway, H.C. Von Baeyer, Effect of point imperfections on lattice thermal conductivity, Phys. Rev. 120 (1960) 1149–1154. doi:10.1103/PhysRev.120.1149.

[67] R.E. Nettleton, Foundations of the callaway theory of thermal conductivity, Phys. Rev. 132 (1963) 2032–2038. doi:10.1103/PhysRev.132.2032.

[68] J. Callaway, Model for lattice thermal conductivity at low temperatures, Phys. Rev. 113 (1959) 1046–1051. doi:10.1103/PhysRev.113.1046.

[69] A.J. Wright, J. Luo, A step forward from high-entropy ceramics to compositionally

complex ceramics: a new perspective, J. Mater. Sci. (2020) 1–16. doi:10.1007/s10853-020-04583-w.

[70] C. Oses, C. Toher, S. Curtarolo, High-entropy ceramics, Nat. Rev. Mater. (2020) 1–15. doi:10.1038/s41578-019-0170-8.

[71] R.-Z. Zhang, M.J. Reece, Review of high entropy ceramics: design, synthesis, structure and properties, J. Mater. Chem. A. 7 (2019) 22148–22162. doi:10.1039/C9TA05698J.

[72] A.J. Wright, Q. Wang, S.T. Ko, K.M. Chung, R. Chen, J. Luo, Size disorder as a descriptor for predicting reduced thermal conductivity in medium- and high-entropy pyrochlore oxides, Scr. Mater. 181 (2020) 76–81. doi:10.1016/j.scriptamat.2020.02.011.

[73] P.K. Schelling, S.R. Phillpot, R.W. Grimes, Optimum pyrochlore compositions for low thermal conductivity, Philos. Mag. Lett. 84 (2004) 127–137. doi:10.1080/09500830310001646699.

[74] A.J. Wright, Q. Wang, C. Huang, A. Nieto, R. Chen, J. Luo, From high-entropy ceramics to compositionally-complex ceramics: A case study of fluorite oxides, J. Eur. Ceram. Soc. 40 (2020) 2120–2129. doi:10.1016/j.jeurceramsoc.2020.01.015.

[75] J.A. Duffy, M.D. Ingram, Establishment of an optical scale for lewis basicity in inorganic oxyacids, molten salts, and glasses, J. Am. Chem. Soc. 93 (1971) 6448–6454. doi:10.1021/ja00753a019.

[76] J.A. Duffy, Relationship between cationic charge, coordination number, and polarizability in oxidic materials, J. Phys. Chem. B. 108 (2004) 14137–14141. doi:10.1021/jp040330w.

[77] R.R. Reddy, Y. Nazeer Ahammed, K. Rama Gopal, P. Abdul Azeem, T.V.R. Rao, Correlation between optical basicity, electronegativity and electronic polarizability for some oxides and oxysalts, Opt. Mater. (Amst). 12 (1999) 425–428. doi:10.1016/S0925-3467(98)00083-4.

[78] C.P. Rodriguez, J.S. McCloy, M.J. Winschell, J.V. Crum, A. Schweiger, Optical basicity and nepheline crystallization in high alumina glasses, 2011.

[79] A.R. Krause, B.S. Senturk, H.F. Garces, G. Dwivedi, A.L. Ortiz, S. Sampath, N.P. Padture, 2ZrO2·Y2O3 thermal barrier coatings resistant to degradation by molten CMAS: Part I, Optical basicity considerations and processing, J. Am. Ceram. Soc. 97 (2014) 3943–3949. doi:10.1111/jace.13210.

[80] Y. Dong, K. Ren, Y. Lu, Q. Wang, J. Liu, Y. Wang, High-entropy environmental barrier coating for the ceramic matrix composites, J. Eur. Ceram. Soc. 39 (2019) 2574–2579. doi:10.1016/j.jeurceramsoc.2019.02.022.